The Cosmic Evolution of Atomic and Molecular Hydrogen in Galaxies

Danail Obreschkow

Lincoln College, Oxford

A thesis submitted to the

Mathematical, Physical and Life Sciences Division

for the degree of Doctor of Philosophy at the University of Oxford

Hilary Term 2009

Astrophysics,

University of Oxford

I dedicate this thesis to my grandmother, "Mömi",
who passed away towards the end of this work.
She was an angel to me and my family and
I am indebted to her for her
love and kindness.

The Cosmic Evolution of Atomic and Molecular Hydrogen in Galaxies

Danail Obreschkow

Lincoln College, Oxford

A thesis submitted to the
Mathematical, Physical and Life Sciences Division
for the degree of Doctor of Philosophy at the University of Oxford

Hilary Term 2009

Abstract

Neutral atomic hydrogen (HI) and molecular hydrogen (H_2) play a primordial role in the cosmic evolution of galaxies. However, little is known about the co-evolution of these two gas phases. This discrepancy and the design of future telescopes like the SKA and ALMA require theoretical models of the joint evolution of HI and H_2 in galaxies.

This thesis starts with a phenomenological analysis of the H_2/HI-ratios in a sample of 245 local galaxies. This analysis reveals a number of correlations between H_2/HI-ratios and other galaxy properties, and we demonstrate that these correlations can be understood in terms of the microscopic relation between the H_2/HI-ratio and the external gas pressure (Leroy et al., 2008). We subsequently use this relation to derive an analytic model for the column densities of HI and H_2, $\Sigma_{\rm HI}$ and $\Sigma_{\rm H_2}$ respectively, in arbitrary regular galaxies.

As a second step, we apply the model for $\Sigma_{\rm HI}$ and $\Sigma_{\rm H_2}$ to post-process approximately $3 \cdot 10^7$ virtual galaxies, whose cosmic evolution was simulated (Croton et al., 2006, De Lucia & Blaizot, 2007) on the evolving dark matter skeleton output by the Millennium Simulation (Springel et al., 2005). The post-processing of these galaxies allows us to (i) split their total cold gas masses between HI, H_2, and Helium, (ii) to assign realistic sizes to both the HI- and H_2-disks, and (iii) to evaluate the velocity profiles of HI and H_2. The resulting hydrogen simula-

tion successfully reproduces many local observations of HI and H_2, such as mass functions (MFs), mass–diameter relations, and mass–velocity relations.

A key prediction of this simulation is that the H_2/HI-ratio of regular galaxies increases dramatically with redshift z, leading to a scaling of $(1+z)^{1.6}$ for the ratio between the cosmic space densities of H_2 and HI. This evolution originates from the H_2/HI–pressure relation and the growth of galactic disks with cosmic time. The size evolution itself is driven by the cosmic increase in the volume/mass-ratio of dark haloes (Gunn & Gott, 1972), which translates into increasing disk sizes by the transfer of angular momentum (Fall & Efstathiou, 1980). The predicted cosmic decline in the H_2/HI-ratio offers a unified explanation for (i) the weak evolution of the cosmic HI-density inferred from Lyman-α absorption against quasars (e.g. Prochaska et al., 2005), (ii) the large molecular masses detected in regular galaxies at $z = 1.5$ (Daddi et al., 2008), and (iii) the recent cosmic decline in the density of star formation (Hopkins & Beacom, 2006).

As a third step, we introduce a heuristic model for the conversion of H_2-masses into observable CO-line luminosities for galaxies at all redshifts. We apply this model to our hydrogen simulation in order to predict the luminosity functions of the first 10 rotational transitions of CO in galaxies at redshift $z = 0$ to $z = 10$.

As a final step, we transform the simulated catalog of $3 \cdot 10^7$ evolving galaxies into a virtual observing cone, i.e. a catalog that lists the apparent HI- and CO-properties of millions of galaxies in a sky field with a comoving diameter of $500\,h^{-1}\,\mathrm{Mpc}$. This catalog represents a tangible contribution towards the design and operation of future telescopes, such as the SKA and ALMA. A key prediction is that HI will be significantly harder to detect at high z than predicted by a no-evolution model.

Supervisor: Prof. Steve Rawlings, University of Oxford

Int. Examiner: Prof. Joseph Silk, University of Oxford

Ext. Examiner: Prof. Roy Booth, Hartebeesthoek Radio Astronomy Observatory

D.Phil. Examination passed on Thursday 21st Mai 2009.

Acknowledgements

First and foremost, I would like to thank my supervisor Steve Rawlings. The healthy mixture of freedom and support I received from him has been both comfortable and very helpful in the course of my doctoral studies. I am indebted to Steve's high scientific standards, which were a significant source of inspiration. Moreover, his great logistic support made every observing trip and conference participation seem to be the easiest thing to organize. It was a serious pleasure to work with such an exceptional individual and I hope to continue collaborating with Steve in the future.

Over the course of my simulation work presented in this thesis, I had the opportunity to participate in numerous collaborations. In particular I want to thank my co-authors Darren Croton, Gabriella De Lucia, Sadegh Khochfar, Hans-Rainer Klöckner, and Ian Heywood. I like to extend this gratitude to a number of colleges, whom I had the chance to meet during my thesis. I got particularly inspired by the discussions with Carlton Baugh, Carlos Frenk, Scott Kay, Raul Angulo, Sarah Blyth, and Erwin de Blok. I further acknowledge the great scientific support and social frame provided by many collaborators of the Oxford SKADS team. A particularly warm thanks goes to Sascha Schediwy, Aris Karastergiou, Kristian Zarb Adami, Tom Mauch, François Levrier, Richard Wilman, Matt Jarvis, Roger Dean, Richard Armstrong, and, again, to Hans-Rainer Klöckner and Ian Heywood (the order is insignificant).

This thesis would not have been possible without great IT-support. I feel particularly indebted to Jonathan Patterson for his assistance and competence regarding our local SKA computing facility. Moreover, I would like to thank Gerard Lemson, whose continual assistance in accessing the Millennium databases in Munich was invaluable.

I thank Vanessa Ferraro-Wood, the administration assistant and PA to Steve Rawlings, for her unique efficiency and calm. Vanessa made any administrative task, no matter how intricate, seem solvable in a split-second.

Martin Bruderer and Shazrene Mohamed have been a great help in proof-reading this thesis. I like to thank them both for their generous contributions. Moreover, the Chapters 2–6 have greatly benefited from the fair comments of our anonymous referees, to whom I like to express my gratitude.

Over the course of my thesis, I have been involved in various research activities, which were not directly part of this thesis. Personally, I consider these projects as an invaluable enrichment of my scientific activities. I like to thank all my co-authors and collaborators in these projects, namely Nick Jones, Neil Johnson, Phillip Staniczenko, Philipp Podsiadlowski, Ben Fitzpatrick, Jocelyn Bell Burnell, Shazrene Mohamed, Philippe Kobel, Aurèle de Bosset, Nicolas Dorsaz, Mohamed Farhat, Claude Nicollier, and Marc-André Dupertuis.

I must express my deep gratitude to the Berrow Foundation for a generous scholarship over three years of my doctoral studies. The present thesis would not have been possible without this scholarship. Additionally, I like to thank the SKADS-funds for seven months of financial support, allowing the completion of this thesis. I am very graceful for the social and cultural frame offered by Lincoln College. Many of my friendships today originally arose from this sociable environment.

I certainly share a big thanks with my parents and my two sisters. Not only were they greatly supportive over the course of my thesis, but they also accepted my occasional abstractedness with humor and patience. Last but not least and with a touch of melancholy, I would like to thank Mirjam Belz for her warm support and for her great understanding for numerous research-related absences.

Danail Obreschkow, Oxford 2009

List of publications

Publications forming the content of this thesis

- D. Obreschkow and S. Rawlings. "Understanding the H_2/HI Ratio in Galaxies". Mon. Not. Roy. Astron. Soc., **394**, 1857-1874 (2009)

- D. Obreschkow, D. Croton, G. De Lucia, S. Khochfar, and S. Rawlings. "Simulation of the Cosmic Evolution of HI and $\mathbf{H_2}$ in Galaxies". Astrophys. J., **698**, 1467-1484 (2009)

- D. Obreschkow and S. Rawlings. "The Cosmic Decline in the H_2/HIRatio in Galaxies". Astrophys. J. Lett., **696**, L129-L132, (2009)

- D. Obreschkow and S. Rawlings. "Compactness of Cold Gas in High-Redshift Galaxies". Mon. Not. Roy. Astron. Soc., submitted

- D. Obreschkow, I. Heywood, H.-R. Klöckner, and S. Rawlings. "A Heuristic Prediction of the Cosmic Evolution of the CO-Luminosity Functions". Astrophys. J., accepted

- D. Obreschkow, I. Heywood, H.-R. Klöckner, F. Levrier, and S. Rawlings. "A Virtual Sky with Extragalactic HI- and CO-Lines for the SKA and ALMA". Astrophys. J., submitted

Publications related to this thesis

- D. Obreschkow. "Neutral Hydrogen in the Local Universe". AIP Conf. Proc., **1035**, 33-39 (2008)

- R. J. Wilman, L. Miller, M. Jarvis, T. Mauch, F. Levrier, F. B. Abdalla, S. Rawlings, H.-R. Klöckner, D. Obreschkow, D. Olteanu, and S. Young. "A

Semi-Empirical Simulation of the Extragalactic Radio Continuum Sky for Next Generation Radio Telescopes". Mon. Not. Roy. Astron. Soc. **388**, 1335-1348 (2008)

- M. Zatloukal, H.-J. Rser, S. Khochfar, D. Obreschkow, C. Wolf, S. Falter, and H. Hippelein. "Testing the Performance of the HIROCS Cluster Finder on the Millennium Simulation". Astron. Astrophys., submitted

Other peer-reviewed publications

- D. Obreschkow, P. Kobel, N. Dorsaz, A. de Bosset, C. Nicollier, and M. Farhat. "Cavitation Bubble Dynamics inside Liquid Drops in Microgravity". Phys. Rev. Lett. **97**, 094502 (2006)

- D. Obreschkow , F. Michelini, S. Dalessi, E. Kapon, and M.-A. Dupertuis. "Non-orthogonal Theory of Polarons and Application to Pyramidal Quantum Dots". Phys. Rev. B **76**, 035329 (2007)

- P. Kobel, D. Obreschkow, N. Dorsaz, A. de Bosset, M. Farhat. "Techniques for Generating Centimetric Drops in Microgravity and Application to Cavitation Studies". Experiments in Fluids, **47**, 39-48 (2009)

Contents

Chapter 1

Introduction : Neutral hydrogen – The play

1.1 Meet the actor : Neutral hydrogen in the Universe

"In the beginning was the hydrogen," is how the renowned scientific writer Hoimar von Ditfurth entitled one of his outstanding popular books (von Ditfurth, 1972). Even though hydrogen did not exist at the exact beginning of time, the formation of its nuclei, the protons, was completed only one second after the Big Bang. Ever since, hydrogen predominated the mass of baryonic matter and therefore represents one of the most fundamental constituents of the Universe. This leading role of hydrogen among the baryons was only marginally challenged by the synthesis of other elements via nuclear fusion. In fact, a few minutes into the cosmic expansion, the baryonic mass-fraction of hydrogen decreased to $\sim 75\%$ in the course of the primordial nucleosynthesis of Helium-4 (Wagoner, 1973). The subsequent nucleosynthesis in stars, which predominated the remaining 13 billion years of the Universe, could only reduce the share of hydrogen by $\sim 1\%$ (Hoyle, 1946). Hence, adopting a baryonic mass-fraction of $\sim 75\%$ for hydrogen is a robust assumption for nearly the entire life-time of the Universe.

Along the cosmic evolution of the Universe, hydrogen played a considerable dynamical role on many length-scales. In the currently favored ΛCDM-cosmogony (Springel et al., 2006), cosmic structure on the largest, supra-galactic scales arises from the action of gravity with a cosmological constant Λ on a fluid of cold dark matter (CDM) and baryons with a relative mass ratio of $\sim 5:1$. As the dominant baryon, hydrogen therefore makes a non-negligible contribution to the formation

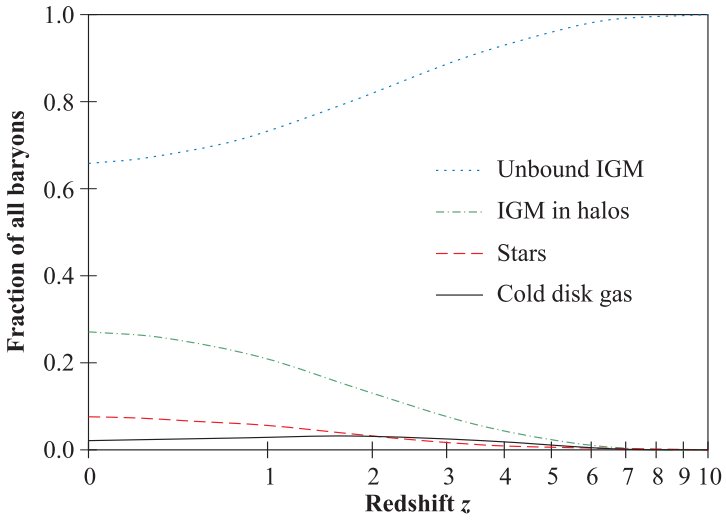

Figure 1.1. Predicted cosmic evolution of the fractional baryon mass in different phases, as extracted from the semi-analytic galaxy catalog (De Lucia & Blaizot, 2007) of the Millennium Simulation (Springel et al., 2005).

of cosmic structure. Within this structure, galaxies form when gas condenses at centers of gravitationally bound dark haloes (White & Rees, 1978). The neutral hydrogen thus acquired can exist in two phases: the atomic phase (HI) and the molecular phase (H_2)[1]. Only inside particularly dense regions can H_2 form, hence giving rise to molecular clouds (or sometimes disks, see Downes et al., 1993), embedded in a smooth distribution of HI. These molecular agglomerations are the sole crèches for the birth of new stars.

Computer models of galaxy evolution in a ΛCDM-cosmogony (Croton et al., 2006) suggest that today the bulk of hydrogen still resides in a hot ionized gas phase between galaxies and is accordingly called the intergalactic medium (IGM). Most of the IGM is predicted to be gravitationally unbound, while the self-bound remainder constitutes the haloes of galaxy clusters, galaxy groups, and isolated galaxies. Only a minor fraction of the hydrogen seems locked up in galaxies in

[1]Some authors use "neutral hydrogen" as a synonym for HI due to the historically assumed predominance of HI over H_2. However, this assumption seems problematic in light of the large molecular masses found in distant galaxies (e.g. Daddi et al., 2008) and with regard to our prediction that H_2 dominated over HI in the early Universe (see Chapter 4).

the form of neutral gas and stars. Fig. 1.1 shows the fractional baryon mass (or hydrogen mass) contained in each of these phases as a function of cosmic time, according to the computer simulation of De Lucia & Blaizot (2007). This cosmic evolution illustrates the incompleteness of the long-standing belief that all the baryons contained in stars today, were originally part of giant reservoirs of cold, neutral hydrogen associated with the individual galaxies. Historically, this closed galaxy model seemed first supported by early inferences from Lyman-α absorption against distant quasars (Storrie-Lombardi et al., 1996), but it finally had to be rejected in light of new cosmological models and improved measurements (see details in Zwaan, 2006). The modern conception of galaxy evolution is an open one, where the formation of new stars from neutral gas is sustained by the continual condensation of hot halo gas onto the cold disks, and the haloes themselves evolve under the ongoing accretion of new material from the unbound IGM.

Owing to this dynamic interdependence, *the cosmic co-evolution of HI and H_2* is currently considered as one of the most fundamental jigsaw pieces in the global picture of galaxy evolution. In principle, the *dynamic* process of star formation, HI $\rightarrow$ H_2 $\rightarrow$ stars, can be inferred from simultaneous *static* maps of HI, H_2, and star formation rates, in a large sample of galaxies at different redshifts. For small samples of nearby galaxies such maps have already been produced (e.g. Leroy et al., 2008). However, beyond the local Universe, such data cannot be obtained today (see Section 1.2), and hence the process of star formation in the early Universe remains virtually unknown from an observational point of view. Theoretically, some understanding of the cosmic evolution of HI and H_2 was achieved by simulations of individual galaxies (Combes et al., 1999, Greve & Sommer-Larsen, 2008, Robertson & Kravtsov, 2008). Yet, traditionally most galaxy simulations have represented HI and H_2 as a single fluid (e.g. Croton et al., 2006), thus masking the subtle interaction between the two phases. In fact, no large-scale simulation of a representative sample of galaxies with resolved HI- and H_2-properties is available today.

1.2 Meet the spectators : Observing neutral hydrogen

HI and H_2 are optically invisible. Therefore, the history of their study is short compared to that of optical astronomy. The first detection of HI was accomplished by Ewen & Purcell (1951). They detected the characteristic HI-emission line at 21 cm rest-frame wavelength, whose existence had already been predicted at the end of the second world war by van de Hulst (1945). Today, the prediction and subsequent first measurement of the HI-line are recognized as a corner stone in the history of 20th century astronomy.

By comparison with HI, detections of H_2 are impeded by the absence of lines in the radio or millimeter spectrum. The first direct detection of galactic H_2 was due to Carruthers (1970), who measured Lyman absorption lines of H_2 in the far-ultraviolet spectrum against the star ξ Persei from a space-borne spectrometer. Subsequent detections of ultraviolet lines and weak infrared lines stemming from electric quadrupole transitions showed some success in the study of nearby galaxies (see historical overview of Dalgarno, 2000). Occasionally, Lyman lines observed in absorption against distant quasars have also enabled the measurement of H_2 at high redshift, $z \approx 2-4$, (Ledoux et al., 2003, Noterdaeme et al., 2008). Despite this short list of direct detections, the bulk of H_2-mass estimates must rely on indirect tracers, typically rotational emission lines of carbon monoxide (CO), the second most abundant molecule in the Universe.

Observations of HI and H_2 (or CO) proved to be crucial for several lines of research. Firstly, the dynamic role of neutral hydrogen in galaxy growth and star formation (see Section 1.1) make detailed observations of HI and H_2 a primordial tool for describing the growth and evolution of galaxies. Secondly, the HI- and CO-emission lines trace the radial velocities and velocity dispersions of the interstellar medium (ISM), thereby allowing robust conclusions about a galaxy's dynamical state and mass-distribution. Thirdly, and particularly with regard to next-generation radio facilities, surveys of HI are also discussed as a powerful tool for the tomography of the large-scale structure of the Universe out to high

redshifts. While such large-scale surveys are currently dominated by the optical and higher frequency bands [e.g. Spitzer (Fang et al., 2005), SDSS (Eisenstein et al., 2005), DEEP2 (Davis et al., 2003), 2dFGRS (Cole et al., 2005), GALEX (Milliard et al., 2007), Chandra (Gilli et al., 2003)], they may be overtaken by future radio arrays, such as the Square Kilometre Array (SKA, Carilli & Rawlings, 2004). Fourthly, deep low frequency detections will presumably reveal HI in the neutral IGM of the cosmic epoch of reionization (Carilli et al., 2004) – one of the ultimate jigsaw pieces concatenating the radiation dominated early Universe with the matter dominated star-forming Universe.

In spite of the revolutionary role of HI- and CO-line observations, these detections remain essentially limited to a small number of galaxies in the local Universe. Less than 10^4 galaxies have been detected (and published) in HI-line emission (e.g. HI Parkes All Sky Survey, Meyer et al., 2004), and less than 10^3 galaxies have been detected in CO-line emission (e.g. FCRAO Extragalactic CO Survey, Keres et al., 2003). Both sample sizes are insignificant compared to the $\sim 10^6$ optically identified galaxies with spectroscopically measured redshifts (e.g. Sloan Digital Sky Survey, Adelman-McCarthy et al., 2008). At high redshift, the number of HI- and CO-line detections is even more limited. The only high-redshift sources detected in CO-emission are highly atypical objects, such as ultra luminous infrared galaxies (ULIRGs) or quasi stellar objects (QSOs), with the exception of two regular galaxies recently detected in CO(2–1)-emission at $z \approx 1.5$ (Daddi et al., 2008). So far, not a single trace of HI-emission has been detected at $z > 0.25$, this upper limit corresponding to a recent success in the study of cluster galaxies at the Arecibo telescope (Catinella et al., 2008). The only HI-systems at higher redshifts known today have been inferred from 21 cm absorption and Lyman-α absorption against distant quasars, and here the nature of the absorbing galaxies remains widely unknown.

These limitations of HI- and CO-line detections and their primordial astrophysical importance sketched out in Section 1.1, were the cause of many inde-

pendent calls for new radio and submillimeter telescopes with much higher sensitivity during the 1990s. The most prominent future telescopes arising from these early calls are the SKA and the Atacama Large Millimeter/submillimeter Array (ALMA), along with numerous pathfinders and extensions to existing telescopes.

Several original outlines of the SKA (Braun, 1991, Noordam et al., 1991, Swarup, 1991, Wilkinson, 1991) were conceived as exclusive HI telescopes, with apertures on the order of $10^6\,\mathrm{m}^2$. These early proposals evolved into a sophisticated multi-band radio array with strong continuum abilities, which can thus rely on the scientific and political support of a much broader community. A sub-committee of the SKA International Science Advisory Committee (ISAC, see Carilli & Rawlings, 2004 for details), established five "key science projects" (KSPs), two of which are centered around HI-line detections at moderate and high redshifts. The KSP IV, "Galaxy evolution and cosmology", features the SKA as the sole instrument able to probe the cosmic evolution of HI in regular galaxies. This KSP also aims at the tomography of cosmic structure. In fact, the sensitivity and survey speed characteristics of the SKA will allow the localization of $\sim 10^9$ galaxies in only a few years survey time. The cosmic structure hence revealed, especially the baryon acoustic oscillations (BAOs) manifest in the power spectrum, will, for example, constrain the equation of state of dark energy by an order of magnitude better than possible today (Abdalla et al., 2009, Abdalla & Rawlings, 2005). The KSP V, "Probing the dark ages", focuses on the detection of HI in the neutral IGM of the epoch of reionization.

The ALMA science case has traditionally been summarized in three very specific goals (De Breuck, 2005). The first of these goals explicitly aims at the detection of extragalactic molecular lines: "Detect spectral line emission from CO or [CII] in a normal galaxy like the Milky Way at a redshift of $z = 3$, in less than 24 hrs of observation." This goal presumes some knowledge of what the CO and [CII] emission lines of a Milky Way progenitor at $z = 3$ will look like – a challenging task, for which we can offer a partial solution (see Chapters 5 and 7).

1.3 Preparing the play : Simulating neutral hydrogen

The design and site for the SKA remain to be decided upon and it is expected to be fully operational by the mid 2020s. By contrast, the construction of ALMA is in an advanced stage with its completion being expected for 2012. The scientific communities affiliated with either of these telescopes recognize the significance of simulating the observable sky before they become operational. The purpose of such simulations is multiple:

1. Science simulations can assist in the definition of the science goals for a telescope, since they pinpoint the limits of our current knowledge.

2. Science simulations are required to optimize the design of a telescope.

3. Once the telescope is considered as given, science simulations help to test and optimize observational strategies.

4. Performing end-to-end simulations, i.e. simulations covering the whole process from generating virtual astrophysical sources to the reduction of virtual observing data, are an effective way to build a scientific community with the expertise necessary to handle the future telescope.

5. Predicting the results of unprecedented observations *before* they become possible, is the safest way to test of the predictive power of our current theories.

The term "science simulation" is as broad as the diversity of possible observations with generic instruments, such as the SKA and ALMA. In this thesis our interest is direct towards large-scale simulations of millions of galaxies, represented by a list of global properties of HI and H_2, such as masses, sizes, and circular velocities. These properties are those potentially detectable in large sky surveys with the SKA and ALMA, and they are the ones, which will most globally constrain the theories of galaxy evolution.

At present, such large-scale simulations of the cosmic evolution of galaxies are seriously challenged by the limited computational resources. No simulation today has succeeded in evolving millions of galaxies over 13 billion years of cosmic time, while simultaneously including gravitational, hydrodynamic, and radiative physics. An effective approximate solution to this numerical bottleneck can be achieved by using the hybrid model (Kauffmann et al., 1999), explained in detail in Chapter 3. The basic idea consists of separating the gravity-driven growth of large-scale structure from the more complex baryonic physics dictating the evolution of individual galaxies. The evolution of the large-scale structure is simulated first and assumed independent of the baryonic and radiative processes inside the galaxies. The latter can then be evolved on top of the preconstructed mass skeleton. Because the evolution of galaxies is often approached using a list of simplistic, half physical, half empirical prescriptions, the hybrid simulation approach is also referred to as the "semi-analytic" approach. This method currently represents the only way to simulate the cosmic co-evolution of millions of galaxies, and it will therefore be an important tool for this thesis.

1.4 The Plot: Organization and key results

The purpose of this thesis is to shed light on the cosmic co-evolution of HI and H_2 from a theoretical point of view. This purpose directly emerged from the two-fold necessity, highlighted above. Firstly, despite the primordial roles of HI and H_2 in the cosmic evolution of galaxies (Section 1.1), little is known about the co-evolution of these gas phases beyond the local Universe (Section 1.2). Secondly, future telescopes, such as the SKA or ALMA, require robust science simulations of HI and H_2 (Section 1.2).

The main part of this thesis is composed of six chapters, corresponding to six publications. These chapters can be interlinked in the structure displayed in Fig. 1.2. The backbone consists of the successive simulation layers (top to bottom) needed from an N-body dark matter simulation of cosmic structure down

to a simulation of atomic and molecular emission lines from the galaxies, which evolve inside the dense dark matter haloes (Section 1.1). The first two simulation layers, i.e. the dark matter simulation and a semi-analytic galaxy simulation, where all cold gas in galaxies is represented by a single gas phase, are adopted from previous work by Springel et al. (2005), Croton et al. (2006), and De Lucia & Blaizot (2007) (see details in Chapter 3). Building on these two simulation layers our work proceeds as follows.

Chapter 2 consists of a phenomenological description of the H_2/HI-ratios in a set of 245 local galaxies, drawn from the literature. Based on the correlations found between the H_2/HI-ratio and other galaxy properties, we introduce an empirical model for the H_2/HI-ratios in regular galaxies. We show that this model is consistent with the local HI-mass function (Zwaan et al., 2005a) and the local CO-luminosity function (Keres et al., 2003).

In Chapter 3, we construct an analytic model for the distribution of HI and H_2 in regular galaxies and use this model to assign HI- and H_2-properties to the galaxies simulated by De Lucia & Blaizot (2007) based on the Millennium Simulation (Springel et al., 2005) (see Fig. 1.2). The tangible product of this chapter is a catalog of $\sim 3 \cdot 10^7$ simulated galaxies with detailed evolving HI- and H_2-properties. This hydrogen simulation successfully reproduces many local observations of HI and H_2, such as MFs, mass–diameter relations, and mass–velocity relations. This success is quite surprising, since our model for HI and H_2 only introduced one additional free parameter to match the observed average space density of cold gas in the local Universe. We will argue that the simulation makes sensible predictions of the cosmic evolution of HI and H_2 in galaxies out to at least redshift $z = 5$.

Chapter 4 and Chapter 5 highlight two critical predictions of our simulation described in Chapter 3. The first prediction is that the H_2/HI-ratio in regular galaxies increases dramatically with redshift owing to the cosmic evolution of galaxy sizes. The second and related prediction is that the surface density of

HI remains approximately constant over cosmic time, while the surface density of H_2 decreases strongly with time. These predictions offer a unified explanation for (i) the weak evolution of the cosmic HI-density inferred from Lyman-α absorption against distant quasars, (ii) the strong molecular emission lines recently detected in regular galaxies at $z = 1.5$ (Daddi et al., 2008), and (iii) the strong evolution of the cosmic star formation density.

In Chapter 6, we introduce a heuristic model for the conversion between H_2-masses and CO-line luminosities for arbitrary rotational transitions. This model accounts for the possible overlap of molecular clouds, gas heating by black holes and star bursts, the cosmic evolution of metallicity, the cosmic microwave background, and nuclear molecular disks. We apply this model to our hydrogen simulation described in Chapter 3, which results in an updated catalog of the $\sim 3 \cdot 10^7$ virtual galaxies with additional properties for the millimeter/submillimeter emission lines of CO. In Chapter 7, we transform the simulated galaxy catalog into a virtual observing cone of extragalactic HI- and CO-sources in a sky field with a comoving diameter of $500\,h^{-1}\,\mathrm{Mpc}$.

While this introduction tried to narrow the frame of interest down to the particular content of this thesis, the conclusion in Chapter 8 focuses on the wider context. Firstly, I shall synthesize the results of this thesis and highlight the most significant contributions. Secondly, I will explain, how these results could interface with other fields in astronomy and with other simulations for the SKA and ALMA.

Finally, I note that in compiling this thesis I have chosen to exclude some less related or non-related research activities I have been involved in during my doctoral studies. For reference, these extracurricular projects are briefly summarized in Chapter 9.

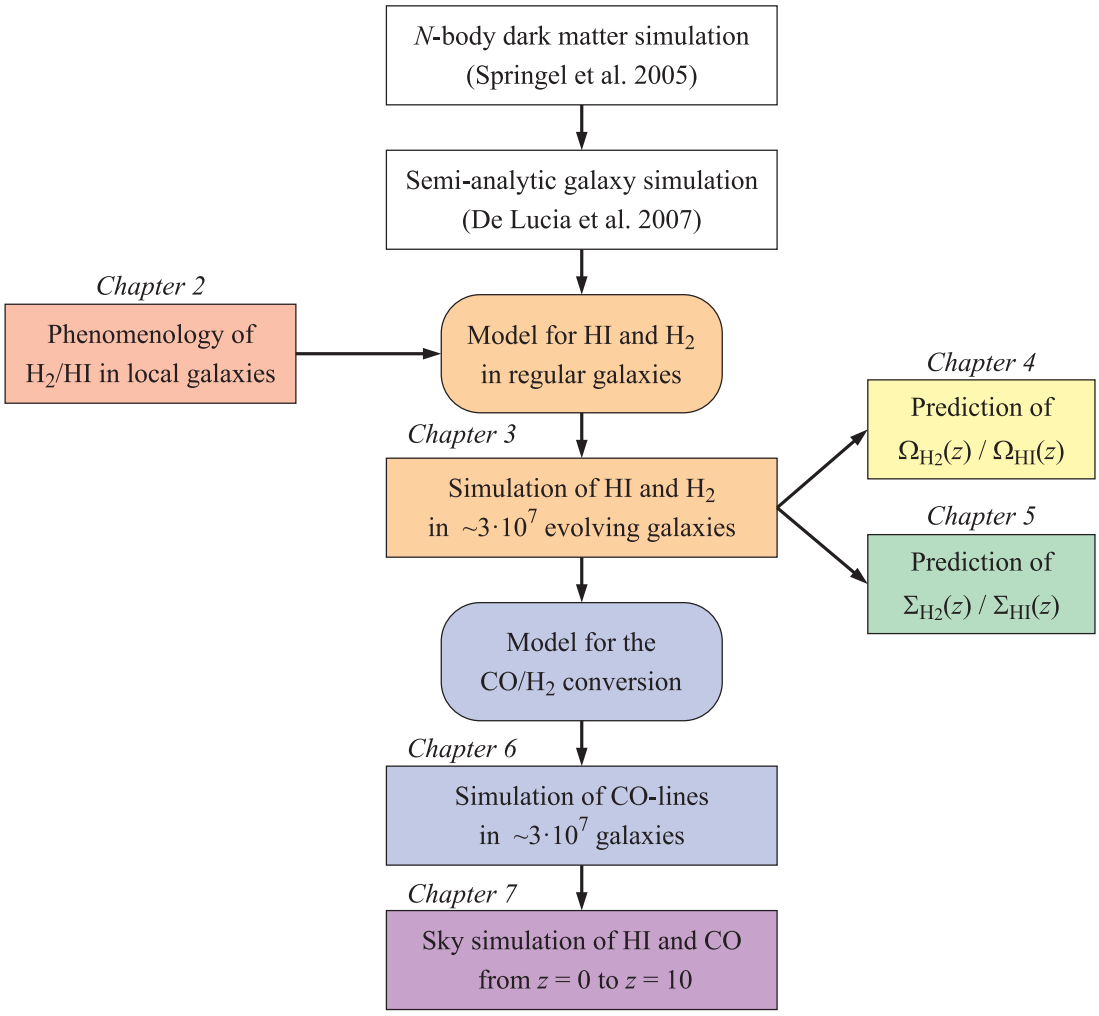

Figure 1.2. Skeleton of this thesis. Each of the six colors corresponds to one Chapter, i.e. one publication. The two white blocks show important previous work, which constitutes an important pilar of the galaxy simulation produced in the frame of this thesis.

Chapter 2

Phenomenology of the H_2/HI-ratio in local galaxies

D. Obreschkow and S. Rawlings

"Understanding the H_2/HI Ratio in Galaxies"

MNRAS, **394**, 1857-1874 (2009)

We revisit the mass ratio $R_{\rm mol}^{\rm galaxy}$ between molecular hydrogen (H_2) and atomic hydrogen (HI) in different galaxies from a phenomenological and theoretical viewpoint. First, the local H_2-mass function (MF) is estimated from the local CO-luminosity function (LF) of the FCRAO Extragalactic CO-Survey, adopting a variable CO-to-H_2 conversion fitted to nearby observations. This implies an average H_2-density $\Omega_{H_2} = (6.9 \pm 2.7) \cdot 10^{-5} h^{-1}$ and $\Omega_{H_2}/\Omega_{\rm HI} = 0.26 \pm 0.11$ in the local Universe. Second, we investigate the correlations between $R_{\rm mol}^{\rm galaxy}$ and global galaxy properties in a sample of 245 local galaxies. Based on these correlations we introduce four phenomenological models for $R_{\rm mol}^{\rm galaxy}$, which we apply to estimate H_2-masses for each HI-galaxy in the HIPASS catalog. The resulting H_2-MFs (one for each model for $R_{\rm mol}^{\rm galaxy}$) are compared to the reference H_2-MF derived from the CO-LF, thus allowing us to determine the Bayesian evidence of each model and to identify a clear best model, in which, for spiral galaxies, $R_{\rm mol}^{\rm galaxy}$ negatively correlates with both galaxy Hubble type and total gas mass. Third, we derive a theoretical model for $R_{\rm mol}^{\rm galaxy}$ for regular galaxies based on an expression for their axially symmetric pressure profile dictating the degree of molecularization. This model is quantitatively similar to the best phenomenological one at redshift $z = 0$, and hence represents a consistent generalization while providing a physical explanation for the dependence of $R_{\rm mol}^{\rm galaxy}$ on global galaxy properties. Applying the best phenomenological model for $R_{\rm mol}^{\rm galaxy}$ to the HIPASS sample, we derive the first integral cold gas-MF (HI+H_2+helium) of the local Universe.

2.1 Introduction

The Interstellar Medium (ISM) plays a vital role in galaxies as their primordial baryonic component and as fuel or exhaust of stars. Hydrogen constitutes 74 per cent of the mass of the ISM. When it is cold and neutral it coexists in the atomic phase (HI) and molecular phase (H_2). While the former follows a smooth distribution across large galactic substructures, the latter is found in dense molecular clouds (Drapatz & Zinnecker, 1984) acting as the sole crèches of newborn stars. The dissimilar but interlinked roles of HI and H_2 in substructure growth and star formation have caused a growing interest in simultaneous observations of both phases and cosmological simulations that distinguish between HI and H_2.

Extragalactic observations of HI often use its prominent 21-cm emission line, and currently comprise several thousand galaxies (HI Parkes All Sky Survey HIPASS, Barnes et al., 2001), and a maximum redshift of $z = 0.2$ (Verheijen et al., 2007). By contrast, most H_2-estimates must rely on indirect tracers, such as CO-lines, with uncertain conversion factors. Consequently, the phase ratio of neutral hydrogen $R_{\rm mol} \equiv {\rm d}M_{\rm H_2}/{\rm d}M_{\rm HI}$ and its value for entire galaxies $R_{\rm mol}^{\rm galaxy} \equiv M_{\rm H_2}/M_{\rm HI}$ remain debated, and estimates of the universal density ratio $R_{\rm mol}^{\rm universe} \equiv \Omega_{\rm H_2}/\Omega_{\rm HI}$ vary by an order of magnitude in the local Universe (e.g. 0.14, 0.42, 1.1 stated respectively by Boselli et al., 2002, Keres et al., 2003, Fukugita et al., 1998).

Ultimately, the uncertainties of H_2-measurements hinder the reconstruction of cold gas masses $M_{\rm gas} = (M_{\rm HI} + M_{\rm H_2})/\beta$, where $\beta \approx 0.74$ is the standard fraction of hydrogen in neutral gas with the rest consisting of helium (He) and a minor fraction of heavier elements. The limitations of comparing $M_{\rm HI}$ to $M_{\rm gas}$ caused by the measurement uncertainties of $M_{\rm H_2}$ culminate in severe difficulties to compare statistically tight cold gas-mass functions (MFs) of modern cosmological simulations with precise HI-MFs extracted from HI-surveys, such as HIPASS. Both simulations and surveys have reached statistical accuracies far better than any current model for $R_{\rm mol}^{\rm galaxy}$, and hence the comparison of observations with simulations is mainly limited by the uncertainty of $R_{\rm mol}^{\rm galaxy}$.

As an illustration, Fig. 2.1 displays the observed HI-MF from the HIPASS sample (Zwaan et al., 2005a) together with several simulated HI-MFs. The latter are based on the cold gas masses of the simulated galaxies produced by two different galaxy formation models applied to the Millennium Simulation (Bower et al., 2006, De Lucia & Blaizot, 2007). We have converted these cold gas masses into HI-masses using four models for $R_{\rm mol}^{\rm galaxy}$ from the literature (Boselli et al., 2002, Keres et al., 2003, Sauty et al., 2003, Young & Knezek, 1989). The figure adopts the Hubble constant of the Millennium Simulation, i.e. $h = 0.73$, where h is defined by $H_0 = 100\,h\,{\rm km\,s^{-1}\,Mpc^{-1}}$ with H_0 being the present-day Hubble constant. The differential gas density $\phi_{\rm HI}$ is defined as $\phi_{\rm HI} \equiv {\rm d}\rho_{\rm HI}/{\rm d}\log M_{\rm HI}$, where $\rho_{\rm HI}(M_{\rm HI})$ is the space density (i.e. number per volume) of HI-sources of mass $M_{\rm HI}$. In Fig. 2.1 different models for galaxy formation are distinguished by colour, while the models of $R_{\rm mol}^{\rm galaxy}$ are distinguished by line type. Clearly, any conclusion regarding the two galaxy formation models based on their HI-MFs is affected by the choice of the model for $R_{\rm mol}^{\rm galaxy}$.

This paper presents a state-of-the-art analysis of the galaxy-dependent phase ratio $R_{\rm mol}^{\rm galaxy}$, the H_2-MF and the integral cold gas-MF (HI+H_2+He), utilizing various observational constraints. In Section 2.2, the determination of H_2-masses via CO-lines is revisited and an empirical, galaxy-dependent model for the CO-to-H_2 conversion factor (X-factor) is derived from direct measurements of a few nearby galaxies (Boselli et al., 2002 and references therein). In Section 2.3, this model is applied to recover an *H_2-MF from the CO-luminosity function (LF)* by Keres et al. (2003). The resulting H_2-MF significantly differs from the one obtained by Keres et al. (2003) using a constant X-factor. Section 2.4 presents an independent derivation of the *H_2-MF from a HI-sample* with well characterized sample completeness (HIPASS, Barnes et al., 2001). This approach is less prone to completeness errors, but it premises an estimate of the H_2/HI-mass ratio $R_{\rm mol}^{\rm galaxy}$. Therefore, we propose four phenomenological models of $R_{\rm mol}^{\rm galaxy}$ (as functions of other galaxy properties) and compute their Bayesian evidence by

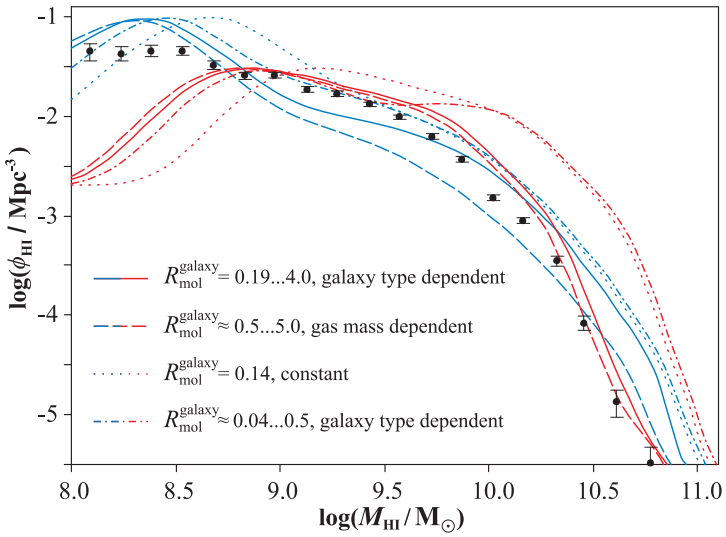

Figure 2.1. Dots represent the observed HI-MF by Zwaan et al. (2005a); lines represent simulated HI-MFs derived from the semi-analytic models by Bower et al. (2006, red lines) and De Lucia & Blaizot (2007, blue lines). The four models of $R_{\rm mol}^{\rm galaxy}$ were adopted or derived from Young & Knezek (1989, solid lines), Keres et al. (2003, dashed lines), Boselli et al. (2002, dotted lines), and Sauty et al. (2003, dash-dotted lines).

comparing the resulting H_2-MFs to the reference H_2-MF derived from the CO-LF. This empirical method is supported by Section 2.5, where we analytically derive a galaxy-dependent model for $R_{\rm mol}^{\rm galaxy}$ on the basis of the relation between $R_{\rm mol}$ and the pressure of the ISM (Leroy et al., 2008). A brief discussion and a derivation of an integral cold gas-MF (HI+H_2+He) are presented in Section 2.6. Section 2.7 concludes the paper with a summary and outlook.

2.2 The variable CO-to-H_2 conversion

2.2.1 Background: basic mass measurement of HI and H_2

HI emits rest-frame 1.42 GHz radiation ($\lambda = 0.21$ m) originating from the hyperfine spin-spin relaxation. Especially cold HI ($T \sim 50 - 100$ K, see Ferrière, 2001) also appears in absorption against background continuum sources or other

HI-regions, but makes up a negligible fraction in most galaxies. Within this assumption, HI can be considered as optically thin on galactic scales, and hence the HI-line intensity is a proportional mass tracer,

$$\frac{M_{\rm HI}}{\rm M_\odot} = 2.36 \cdot 10^5 \cdot \frac{S_{\rm HI}}{\rm Jy\,km\,s^{-1}} \cdot \left(\frac{D_{\rm l}}{\rm Mpc}\right)^2, \tag{2.1}$$

where $S_{\rm HI}$ is the integrated HI-line flux density and $D_{\rm l}$ is the luminosity distance to the source.

Unlike HI-detections, direct detections of H_2 in emission rely on weak lines in the infrared and ultraviolet bands (Dalgarno, 2000) and have so far been limited to the Milky Way and a few nearby galaxies (e.g. Valentijn & van der Werf, 1999). Occasionally, H_2 has also been detected at high redshift ($z \approx$2–4) through absorptions lines associated with damped Lyman α systems (Ledoux et al., 2003, Noterdaeme et al., 2008). All other H_2-mass estimates use indirect tracers, mostly rotational emission lines of carbon monoxide (CO) – the second most abundant molecule in the Universe. The most frequently used CO-emission line stems from the relaxation of the $J = 1$ rotational state of the predominant isotopomer $^{12}C^{16}O$. Radiation from this transition is referred to as CO(1–0)-radiation and has a rest-frame frequency of 115 GHz ($\lambda = 2.6 \cdot 10^{-3}$ m), detectable with millimeter telescopes. The conversion between CO(1–0)-radiation and H_2-masses is very subtle and generally expressed by the X-factor,

$$X \equiv \frac{N_{\rm H_2}/{\rm cm^{-2}}}{I_{\rm CO}/({\rm K\,km\,s^{-1}})} \cdot 10^{-20}, \tag{2.2}$$

where $N_{\rm H_2}$ is the column density of molecules and $I_{\rm CO}$ is the integrated CO(1–0)-line intensity per unit surface area defined via the surface brightness temperature T_ν in the Rayleigh-Jeans approximation. Explicitly, $I_{\rm CO} \equiv \int T_\nu {\rm d}V = \lambda \int T_\nu {\rm d}\nu$, where V is the radial velocity, ν is the frequency, and $\lambda = |{\rm d}V/{\rm d}\nu|$ is the wavelength. This definition of the X-factor implies a mass-luminosity relation analo-

gous to Eq. (2.1) (see review by Young & Scoville, 1991),

$$\frac{M_{\mathrm{H_2}}}{\mathrm{M_\odot}} = 580 \cdot X \cdot \left(\frac{\lambda}{\mathrm{mm}}\right)^2 \cdot \frac{S_{\mathrm{CO}}}{\mathrm{Jy\,km\,s^{-1}}} \cdot \left(\frac{D_{\mathrm{l}}}{\mathrm{Mpc}}\right)^2, \tag{2.3}$$

where $S_{\mathrm{CO}} \equiv \int S_{\mathrm{CO},\nu} \mathrm{d}V$ denotes the integrated CO(1–0)-line flux and D_{l} the luminosity distance. $S_{\mathrm{CO},\nu}$ is the flux density per unit frequency, for example expressed in Jy, and thus S_{CO} has units like $\mathrm{Jy\,km\,s^{-1}}$. Note that S_{CO} relates to the physical flux F, defined as power per unit surface, via a factor λ, i.e. $F \equiv \int S_{\mathrm{CO},\nu} \mathrm{d}\nu = \lambda^{-1} S_{\mathrm{CO}}$. CO-luminosities are often defined as $L_{\mathrm{CO}} \equiv 4\pi D_{\mathrm{l}}^2 S_{\mathrm{CO}}$ (giving units like $\mathrm{Jy\,km\,s^{-1}\,(h^{-1}\,Mpc)^2}$), thus relating to actual radiative power P_{CO} via $P_{\mathrm{CO}} = \lambda^{-1} L_{\mathrm{CO}}$. In the λ-dependent notation above, Eq. (2.3) remains valid for other molecular emission lines, as long as the X-factor is redefined with the respective intensities in the denominator of Eq. (2.2).

2.2.2 Variation of the X-factor among galaxies

The theoretical and observational determination of the X-factor is a highly intricate task with a long history, and it is perhaps one of the biggest challenges for future CO-surveys.

Theoretically, the difficulty to estimate X arises from the indirect mechanism of CO-emission and from the optical thickness of CO(1–0)-radiation. CO resides inside molecular clouds along with H_2 and acquires rotational excitations from H_2-CO collisions, which can subsequently decay via photon-emission. This mechanism implies that the CO(1–0)-luminosity per unit molecular mass a priori depends on three aspects: (i) the amount of CO per unit H_2, i.e. the CO/H_2-mass ratio; (ii) the thermodynamic state variables dictating the level populations of CO; (iii) the geometry of the molecular region influencing the degree of self-absorption.

The reason why the CO-luminosity can be used at all as a H_2-mass tracer is a statistical one. In fact, CO-luminosities are normally integrated over kiloparsec or larger scales, such as is inevitable given the spatial resolution of most extra-

galactic CO-surveys. Therefore, hundreds or thousands of molecular clouds are combined into one measurement, and cloud properties, such as geometries and thermodynamic state variables, probably tend towards a constant average, as long as most lines-of-sight to individual clouds do not pass through other clouds, where they would be affected by self-absorption. The latter assumption seems correct for all but nearly edge-on spiral galaxies (Ferrière, 2001, Wall, 2006). It is hence likely that the different geometries and thermodynamic variables of molecular clouds can be neglected in the variations of X and we expect X to depend most significantly on the average CO/H_2-mass ratio of the considered galaxy or galaxy part. However, the determination of the CO/H_2-ratio is itself difficult and its relation to the overall metallicity of the galaxy is uncertain.

Observational estimations of X require CO-independent H_2-mass measurements, which are limited to the Milky Way and a few nearby galaxies. Typical methods use the virial mass of giant molecular clouds assumed to be completely molecularized (Young & Scoville, 1991), the line ratios of different CO-isotopomers (Wild et al., 1992), mm-radiation from cold dust associated with molecular clouds (Guelin et al., 1993), and diffuse high energy γ-radiation caused by interactions of cosmic-rays with the ISM (Bertsch et al., 1993, Hunter et al., 1997).

Early measurements suggested a fairly constant X in the inner $2 - 10$ kpc of the Galaxy, leading several authors to the conclusion that X does not significantly depend on cloud properties and metallicity (e.g. Young & Scoville, 1991). This finding has recently been supported by Blitz et al. (2007), who analyzed five galaxies in the local group and found no clear trend between metallicity and X. The results of Young & Scoville (1991) and Blitz et al. (2007) rely on the assumption that molecular clouds are virialized. Using the same method Arimoto et al. (1996) detected strong variations of X amongst galaxies and galactic substructures, and they found the empirical power-law relation $X \propto (O/H)^{-1}$. Israel (2000) pointed out that molecular clouds cannot be considered as virialized

structures, and using far-infrared measurements rather than the virial theorem, Israel (1997) found an even tighter and steeper relation in a sample of 14 nearby galaxies, $X \propto (\mathrm{O/H})^{-2.7}$.

In summary, despite rigorous efforts to measure X and its relation to metallicity, the empirical findings remain uncertain and depend on the method used to measure X. Since we cannot overcome this issue, we shall use a model for X that relies on different methods to measure X, such as presented by Boselli et al. (2002). Their sample consists of 14 nearby galaxies covering an order of magnitude in O/H-metalicity. This sample includes early- and late-type spiral galaxies, as well as irregular objects and starbursts. For these galaxies X was determined from three different methods: the virial method, mm-data, and γ-ray data. Their data varies from $X = 0.88$ in the center of the face-on Sbc-spiral galaxy M 51 to $X \approx 60$ in NGC 55, a barred irregular galaxy seen edge-on. The high values ($X \gtrsim 10$) are often associated with dwarf galaxies and nearly edge-on spiral galaxies, thus consistent with the interpretation of increased CO(1–0) self-absorption in these objects. Typical values for non-edge-on galaxies lie around $X \approx 1 - 5$.

For the particular data set of Boselli et al. (2002), we shall check the validity of a constant-X model against variable models for X, by comparing their Bayesian evidence – a powerful tool for model selection (e.g. Sivia & Skilling, 2006). The underlying idea is that the probability $p(M|d)$ of a model M given the data set d is proportional to the probability $p(d|M)$ of d given M, provided the compared models are a priori equally likely (Bayes theorem). The probability $p(d|M)$ is also called the *Bayesian evidence* and can be computed as,

$$p(d|M) = \int_{\Omega} p(d|\theta, M)\pi(\theta|M)\mathrm{d}\theta \tag{2.4}$$

where θ denotes the vector of free parameters of model M and Ω the corresponding parameter space; $p(d|\theta, M)$ designates the probability of the data given a parameter choice θ and it typically includes measurement uncertainties of the data. The

Model for $\log(X)$	c_0	c_1	rms	$\ln B$
c_0	0.43 ± 0.15	-	0.45	0.0
$c_0 + c_1 \cdot \log(\mathrm{O/H})$	-2.90 ± 0.20	-1.02 ± 0.05	0.19	5.1
$c_0 + c_1 \cdot (M_\mathrm{B} - 5 \log\, h)$	3.67 ± 0.25	0.176 ± 0.006	0.29	3.3
$c_0 + c_1 \cdot \log(L_\mathrm{CO})$	1.85 ± 0.15	-0.288 ± 0.05	0.29	2.5

Table 2.1. Comparison of different models for the X-factor: c_0 and c_1 are the best parameters (Gaussian errors are coupled), rms is the rms-deviation of the data from the model, and B is the Bayes factor of each model with respect to the constant model (first row).

prior knowledge on the parameters is encoded in the probability density function $\pi(\theta|M)$, which satisfies the normalization condition $\int_\Omega \pi(\theta|M)\mathrm{d}\theta = 1$. Two competing models M_1 and M_2 are compared by their odds, commonly referred to as the *Bayes factor* $B \equiv p(d|M_1)/p(d|M_2)$. According to Jeffrey's scale (Jeffreys, 1961) for the strength of evidence, $|\ln B| < 1$ is *inconclusive*, while $|\ln B| = 1$ reveals *positive evidence* in favour of model M_1 (probability=0.750), $|\ln B| = 2.5$ depicts *moderate evidence* (probability=0.923), and $|\ln B| = 5$ expresses *strong evidence* (probability=0.993).

We consider the four models listed in Table 2.1: a constant model, where $\theta = (c_0)$, and three linear models, where $\theta = (c_0, c_1)$. The data are a sample of 14 nearby galaxies, for which X was measured (Table 2.2); X-factors and O/H-metallicities are taken from Boselli et al. (2002) and references therein, while M_B-magnitudes were taken from the HyperLeda database (Paturel et al., 2003), and CO(1–0)-luminosities L_CO were derived from the references indicated in Table 2.2.

For practical purposes we limit the parameter space Ω to $c_0 \in [-10, 10]$ and $c_1 \in [-2, 2]$ and take the prior probabilities as homogeneous within Ω, i.e. $\pi(\theta|M) = 1/|\Omega|$. The probability $p(d|\theta, M)$ in Eq. (2.4) is calculated as

Object	log(O/H) [a]	M_B [b] $-5 \log h$	log(L_{CO})	log(X) [a]
SMC	-3.96	-16.82	-2.04 [c]	1.00
NGC1569	-3.81	-15.94	-1.60 [d]	1.18
M31	-2.99	-20.23	-1.40 [e]	0.38 ± 0.21
IC10	-3.69	-15.13	-1.09 [f]	0.82 ± 0.12
LMC	-3.63	-17.63	-0.68 [g]	0.90
M81	-3	-19.90	-0.07 [h]	-0.15
M33	-3.22	-18.61	0.20 [i]	0.70 ± 0.11
M82	-3	-17.30	0.67 [d]	0.00
NGC4565	-	-21.74	1.12 [h]	0.00
NGC6946	-2.94	-20.12	1.24 [h]	0.26
NGC891	-	-19.43	1.48 [h]	0.18
M51	-2.77	-19.74	1.80 [h]	-0.22
Milky Way	-3.1	-19.63	-	0.19 ± 0.01
NGC6822	-3.84	-16.07	-	0.82 ± 0.20

Table 2.2. Observational data used for the derivation of a variable X-factor (Section 2.2.2). L_{CO} is given in units of $\mathrm{Jy\,km\,s^{-1}\,(h^{-1}\,Mpc)^2}$. (a) O/H-metallicities and X-factors from Boselli et al. (2002), (b) absolute, extinction-corrected B-Magnitudes from the HyperLeda database (Paturel et al., 2003), (c) Rubio et al. (1991), (d) Young et al. (1989), (e) Heyer et al. (2000), (f) Leroy et al. (2006), (g) Fukui et al. (1999), (h) Sage (1993), (i) Heyer et al. (2004).

the product,

$$p(d|\theta, M) = \prod_i \frac{1}{\sigma\sqrt{2\pi}} \exp\left\{\frac{[\log(X_i^{\mathrm{data}}) - \log(X_i^{\mathrm{model}})]^2}{2\,\sigma^2}\right\} \qquad (2.5)$$

where i labels the different galaxies listed in Table 2.2 and σ denotes the measurement uncertainty of log(X). We set σ equal the average value $\sigma = 0.13$, for all 14 galaxies. (In fact adopting the specific σ-values listed in Table 2.2 leads to very similar results, but could be potentially dangerous as the small value $\sigma = 0.01$ of the Milky Way is likely underestimated.)

The evidence integrals were solved numerically using a Monte Carlo sampling of the parameter space. The resulting Bayes factors (listed in Table 2.1) reveal moderate to strong Bayesian evidence for a variable X-factor given the X-factors

presented by Boselli et al. (2002). Among the different variable models for $\log(X)$, the best one depends linearly on log(O/H) (highest Bayes factor), as expected from the natural dependence of the CO/H_2 ratio on the O/H ratio. However, $\log(X)$ is also well correlated with M_B and $\log(L_{CO})$, and hereafter we will use those relations because of the widespread availability of M_B and L_{CO} data. In fact, a X-factor depending on L_{CO} simply translates to a non-linear conversion of CO-luminosities into H_2-masses. If the two linear regressions between $\log(X)$ and M_B and between $\log(X)$ and $\log(L_{CO})$ were determined independently, they would imply a third linear relation between M_B and $\log(L_{CO})$. The latter can, however, be determined more accurately from larger galaxy samples. The sample presented in Section 2.4.1 (245 galaxies) yields

$$\log(L_{CO}) \approx -4.5 - 0.52\,(M_B - 5\,\log\,h), \tag{2.6}$$

where L_{CO} is taken in units of $\mathrm{Jy\,km\,s^{-1}\,(h^{-1}\,Mpc)^2}$. To get the best result, we imposed this relation, while simultaneously minimizing the square deviations of the two regressions between $\log(X)$ and respectively M_B and $\log(L_{CO})$. In such a way we find

$$\log(X) = 1.97 - 0.308\,\log(L_{CO}) \pm \sigma_X, \tag{2.7}$$

$$\log(X) = 3.36 + 0.160\,(M_B - 5\,\log\,h) \pm \sigma_X. \tag{2.8}$$

These two relations are shown in Fig. 2.2 (red solid lines). For comparison, the independent regressions, obtained without imposing the relation given in Eq. (2.6), are plotted as dashed lines. These relations correspond to the parameters c_0 and c_1 given in Table 2.1. Other regressions found by Arimoto et al. (1996) and Boselli et al. (2002) are also displayed. Their approaches are similar, but Arimoto et al. (1996) used less galaxies (8 instead of 14). The 14 data points in Fig. 2.2 are scattered around the relations of Eqs. (2.7) and (2.8) with the same rms-deviation of 0.29 in $\log(X)$. Combined with the average measurement un-

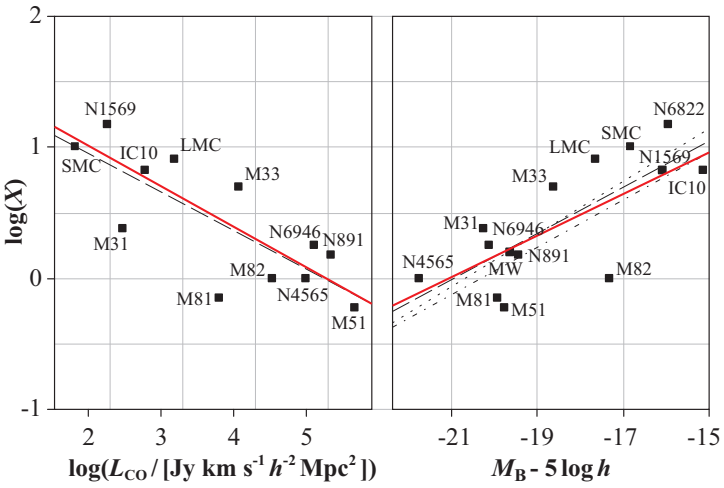

Figure 2.2. Points represent observed X-factors as a function of CO(1–0)-power L_{CO} and absolute blue magnitude M_{B} for 14 local galaxies. Red solid lines represent linear regressions respecting the mutual relation between L_{CO} and M_{B} given in Eq. (2.6); dashed lines represent independent linear regressions; the dotted line represents the linear fit found by Arimoto et al. (1996); and the dash-dotted line represents the linear fit found by Boselli et al. (2002).

certainty of $\sigma = 0.13$, this gives an estimated true physical scatter in $\log(X)$ of $\sigma_{\mathrm{X}} = (0.29^2 - 0.13^2)^{1/2} = 0.26$.

The variable models of X given in Eqs. (2.7) and (2.8) will be applied in Sections 2.3 and 2.4. In order to account for the uncertainties of X highlighted in the beginning of this section, we shall also present the results for a constant X-factor with random scatter in Section 2.3.

2.3 Deriving the H_2-MF from the CO-LF

Using the variable model for the X-factor of Eq. (2.7), we shall now recover the local H_2-mass function (H_2-MF) from the CO-LF presented by Keres et al. (2003). The latter is based on a far infrared-selected subsample of 200 galaxies from the FCRAO Extragalactic CO-Survey (Young et al., 1995), which successfully

reproduced the 60μm-LF, thus limiting the errors caused by the incompleteness of the sample. Keres et al. (2003) themselves derived a H_2-MF using a constant model $X = 3$, which probably leads to an overestimation of the H_2-abundance, especially in the high mass end, where the X-factors tend to be lower according to the data shown in Section 2.2.2.

We applied Eq. (2.7) with scatter $\sigma_X = 0.26$ to the individual data points of the CO-LF given by Keres et al. (2003). The resulting H_2-MF – hereafter the *reference H_2-MF* – is shown in Fig. 2.3 together with the *original H_2-MF* derived by Keres et al. (2003) using the constant factor $X = 3$ without scatter. To both functions we fitted a Schechter function (Schechter, 1976) of the form

$$\phi_{\mathrm{H_2}} = \ln(10) \cdot \phi^* \cdot \left(\frac{M_{\mathrm{H_2}}}{M^*}\right)^{\alpha+1} \exp\left[-\left(\frac{M_{\mathrm{H_2}}}{M^*}\right)\right] \tag{2.9}$$

by minimizing the weighted square deviations of all but the highest H_2-mass bin. Keres et al. (2003) argue that this bin may contain a CO-luminous subpopulation of starburst galaxies, similarly to the situation in the far infrared continuum (Yun et al., 2001). In any case the last bin only marginally contributes to the universal H_2-density. The Schechter function parameters are given in Table 2.3, as well as the reduced χ^2 of the fits, total H_2-densities $\rho_{\mathrm{H_2}}$ and $\Omega_{\mathrm{H_2}} \equiv \rho_{\mathrm{H_2}}/\rho_{\mathrm{crit}}$, and the average molecular ratio $R_{\mathrm{mol}}^{\mathrm{universe}} \equiv \Omega_{\mathrm{H_2}}/\Omega_{\mathrm{HI}}$. Both $\rho_{\mathrm{H_2}}$ and $\Omega_{\mathrm{H_2}}$ were evaluated from the fitted Schechter function rather than the binned data, and $\Omega_{\mathrm{HI}} = (2.6 \pm 0.3)\ h^{-1}10^{-4}$ was adopted from the HIPASS analysis by Zwaan et al. (2005a).

Our new reference H_2-MF is compressed in the mass-axis compared to the original one, and our estimate of $\rho_{\mathrm{H_2}}$ (Table 2.3) is 33 per cent smaller. The global H_2/HI-mass ratio drops to 0.26 ± 0.11, implying a total cold gas density of $\Omega_{\mathrm{gas}} = (4.4 \pm 0.8) \cdot 10^{-4}\ h^{-1}$. The composition of cold gas becomes: 59 ± 6 per cent HI, 15 ± 6 per cent H_2, 26 per cent He and metals, where the uncertainties of HI and H_2 are anti-correlated.

It is interesting to observe the quality of the Schechter function fits: the fit to

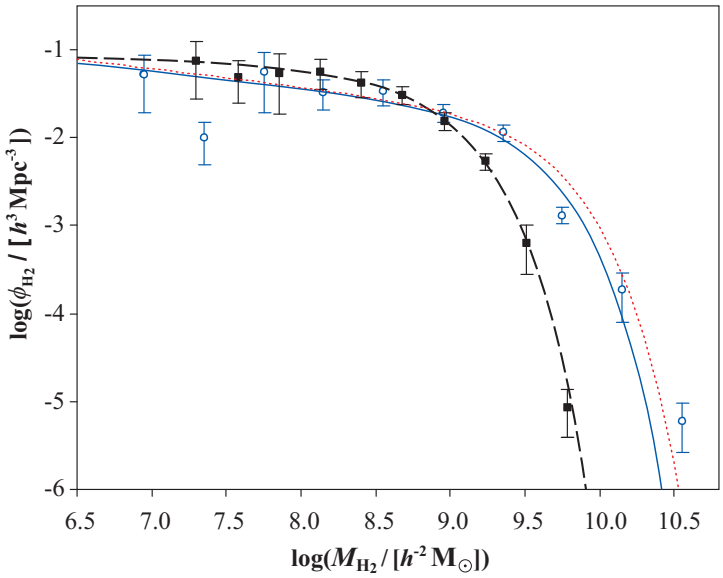

Figure 2.3. Filled squares represent our reference H_2-MF derived directly from the observed CO-LF (Keres et al., 2003) using the variable X-factor of Eq. (2.7) with scatter $\sigma_X = 0.26$. Open circles are the original H_2-MF obtained by Keres et al. (2003) using a constant factor $X = 3$ without scatter. The dashed and solid lines represent Schechter function fits to our reference H_2-MF and the original H_2-MF, while the dotted line represents the Schechter function corresponding to a constant X-factor $X = 3$ with scatter σ_X.

our reference H_2-MF is much better than the one to the original H_2-MF (Keres et al., 2003). Since the original MF is a simple shift of the CO-LF (constant X-factor), the Schechter function fit to our reference H_2-MF is also much better than the fit to the CO-LF. We could demonstrate that this difference is partially caused by the scatter $\sigma_X = 0.26$, applied to the variable X-factor when deriving the reference H_2-MF from the CO-LF. Scatter averages the densities in neighboring mass bins, hence smoothing the reference MF. Additionally, there is a fundamental reason for the rather poor Schechter function fit of the CO-LF: It is formally impossible to describe both the H_2-MF and the CO-LF with Schechter functions, if the two are interlinked via the linear transformation of Eq. (2.7).

	reference H_2-MF (variable X)	original H_2-MF (constant X)
M^*	$7.5 \cdot 10^8\, h^{-2}\, \mathrm{M}_\odot$	$2.81 \cdot 10^9\, h^{-2}\, \mathrm{M}_\odot$
α	-1.07	-1.18
ϕ^*	$0.0243\, h^3\, \mathrm{Mpc}^{-3}$	$0.0089\, h^3\, \mathrm{Mpc}^{-3}$
Red. χ^2	0.05	2.55
$\rho_{\mathrm{H_2}}$	$(1.9 \pm 0.7) \cdot 10^7\, h\, \mathrm{M}_\odot\, \mathrm{Mpc}^{-3}$	$(2.8 \pm 1.1) \cdot 10^7\, h\, \mathrm{M}_\odot\, \mathrm{Mpc}^{-3}$
$\Omega_{\mathrm{H_2}}$	$(0.69 \pm 0.27) \cdot 10^{-4}\, h^{-1}$	$(1.02 \pm 0.39) \cdot 10^{-4}\, h^{-1}$
$R_{\mathrm{mol}}^{\mathrm{universe}}$	0.26 ± 0.11	0.39 ± 0.16

Table 2.3. Schechter function parameters, reduced χ^2, and universal mass densities as obtained by integrating the Schechter functions. $R_{\mathrm{mol}}^{\mathrm{universe}} \equiv \Omega_{\mathrm{H_2}}/\Omega_{\mathrm{HI}}$ is the global H_2/HI-mass ratio of the local Universe. The very small reduced χ^2 of our reference H_2-MF arises from a spurious smoothing introduced by the scatter σ_{X}.

Yet, in analogy to the HI-MF (Zwaan et al., 2005a), it is likely that the H_2-MF is well matched by a Schechter function, hence implying that the CO-LF deviates from a Schechter function.

We finally note, that the faint end of the reference H_2-MF is nearly flat (i.e. $\alpha = -1$), such that the total H_2-mass is dominated by masses close to the Schechter function break at $M^* \approx 10^9 \mathrm{M}_\odot$. In particular, the faint end slope is flatter than for the HI-MF, where $\alpha = -1.37$ (Zwaan et al., 2005a), but it should be emphasized that this does not imply that small cold gas masses have a lower molecular fraction. In fact, the contrary is suggested by the observations shown in the Section 2.4.

For completeness, we re-derived the H_2-MF from the CO-LF using a constant X-factor $X = 3$ (like Keres et al., 2003) with the same Gaussian scatter $\sigma_{\mathrm{X}} = 0.26$ as used for our variable model of X. The best Schechter fit for the resulting H_2-MF is also displayed in Fig. 2.3. The difference between this H_2-MF and the original H_2-MF by Keres et al. (2003) demonstrates that the scatter of X stretches the high mass end towards higher masses.

2.4 Phenomenological models for the H_2/HI-mass ratio

In this section, we shall introduce four *phenomenological* models for the H_2/HI-mass ratio $R_{\rm mol}^{\rm galaxy}$ of individual galaxies. Each model will be used to recover a H_2-MF from the HIPASS HI-catalog (Barnes et al., 2001), thus demonstrating an alternative way to determine the H_2-MF to the CO-based approach. Comparing the H_2-MFs of this section with the reference H_2-MF derived from the CO-LF (Section 2.3) will allow us to determine the statistical evidence of the models for $R_{\rm mol}^{\rm galaxy}$.

2.4.1 Observed sample

The sample of galaxies used in this section is presented in Appendix 2.8 and consists of 245 distinct objects with simultaneous measurements of integrated HI-line fluxes and CO(1–0)-line fluxes. The latter were drawn from 9 catalogs in the literature, and, where not given explicitly, recomputed from indicated H_2-masses by factoring out the different X-factors used by the authors. HI line fluxes were taken from HIPASS via the optical cross-match catalog HOPCAT (Doyle et al., 2005). Both line fluxes were homogenized using h-dependent units, where they depend on the Hubble parameter h. Additional galaxy properties were adopted from the homogenous reference database "HyperLeda" (Paturel et al., 2003). These properties include numerical Hubble types T, extinction corrected blue magnitudes $M_{\rm B}$, and comoving distances $D_{\rm l}$ corrected for Virgo infall. In the few cases, where these properties were unavailable in the reference catalog, they were copied from the original reference for CO-fluxes. For each galaxy we calculated HI- and H_2-masses using respectively Eqs. (2.1) and (2.3). The variable X-factors were determined from the blue magnitudes according to Eq. (2.8). We chose to compute X from $M_{\rm B}$ rather than from $L_{\rm CO}$, because of the smaller measurement uncertainties of the $M_{\rm B}$ data. Finally, total cold gas masses $M_{\rm gas} = (M_{\rm HI} + M_{\rm H_2})/\beta$ and mass ratios $R_{\rm mol}^{\rm galaxy} = M_{\rm H_2}/M_{\rm HI}$ were calculated for each object. While the masses depend on the distances and hence on the Hubble

parameter h, the mass ratios $R_{\rm mol}^{\rm galaxy} = M_{\rm H_2}/M_{\rm HI}$ are independent of h.

This sample covers a wide range of galaxy Hubble types, masses, and environments, and has 49 per cent overlap with the subsample of the FCRAO Extragalactic CO-Survey used for the derivation of the reference H_2-MF in Section 2.3. We deliberately limited the sample overlap to 50 per cent in order to control possible sample biases.

We emphasize that this sample exhibits unknown completeness properties, which a priori presents a problem for any empirical model for $R_{\rm mol}^{\rm galaxy}$. However, as long as a proposed model is formally complete in the sense that it embodies the essential correlations with a set of free parameters, these parameters can be determined accurately even with an incomplete set of data points. The difficulty in the present case is that no reliable complete model for the molecular fraction $R_{\rm mol}^{\rm galaxy}$ has yet been established. We shall bypass this issue by proposing several models for $R_{\rm mol}^{\rm galaxy}$ that will be verified with hindsight (Section 2.4.2). Additional verification will become possible in Section 2.5, where we shall derive a physical model for $R_{\rm mol}^{\rm galaxy}$.

2.4.2 Phenomenological models for $R_{\rm mol}^{\rm galaxy}$

The galaxy sample of Section 2.4.1 reveals moderate correlations between $R_{\rm mol}^{\rm galaxy}$ and respectively T, $M_{\rm gas}$ and $M_{\rm B}$. These correlations motivate the models proposed below. Other correlations were looked at, such as a correlation between $R_{\rm mol}^{\rm galaxy}$ and environment, which may be suspected from stripping mechanisms acting differently on HI and H_2. However no conclusive trends could be identified given the observational scatter of $R_{\rm mol}^{\rm galaxy}$. All our models are first presented with free parameters, which are fitted to the data at the end of this section.

Model 0 ($R_{\rm mol,0}^{\rm galaxy}$) assumes a constant H_2/HI-ratio $R_{\rm mol}^{\rm galaxy}$, such as is often used in the literature,

$$\log(R_{\rm mol,0}^{\rm galaxy}) = q_0 + \sigma_{\rm phy,0}, \tag{2.10}$$

where q_0 is a constant and $\sigma_{\rm phy,0}$ denotes an estimate of the physical scatter of

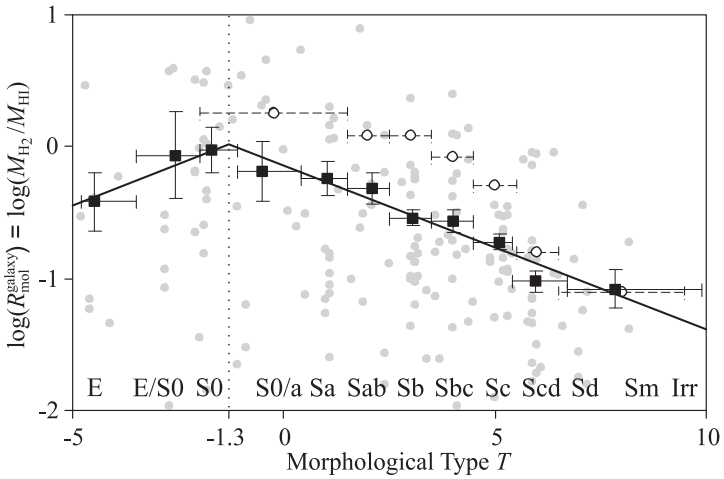

Figure 2.4. H_2/HI-mass ratio versus numerical Hubble type T. Grey dots represent the empirical data obtained by applying the variable X-factor of Eq. (2.8) with scatter to the CO-measurements. Black points represent the binned data; vertical bars represent statistical uncertainties obtained via bootstrapping, i.e. they depict a 1-σ confidence interval of the bin average obtained by examining 10^4 random half-subsets of the full data; horizontal bars represent the bin intervals. The solid line represents model 1 fitted to the data points. Open circles and dashed bars denote the binned data of the original paper by Young & Knezek (1989).

perfectly measured data relative to the model.

Model 1 is galaxy-type dependent, as suggested by earlier studies revealing a trend for $R_{\rm mol}^{\rm galaxy}$ to increase from late-type spiral galaxies to early-type ones (e.g. Sauty et al., 2003, Young & Knezek, 1989). The type dependence of our sample is displayed in Fig. 2.4. The binned data clearly show a monotonic increase of the molecular fraction by roughly an order of magnitude when passing from late-type spiral galaxies (Scd–Sd) to early-type spiral and lenticular galaxies (S0–S0/a). The unbinned data illustrate the importance of parameterizing the physical scatter. The Hubble type dependence can be widely explained by the effect of the bulge component on the disk size, as detailed in Section 2.5. Observationally, this dependence was first noted by Young & Knezek (1989), whose bins are also dis-

played in the figure. Their molecular fractions are generally higher, partly due to their rather high assumed X-factor of 2.8. The monotonic trend seems to break down between lenticular and elliptical galaxies, where the physical situation becomes more complex. In fact, many elliptical galaxies have molecular gas in their center with no detectable HI-counterpart, while others seem to have almost no H_2 (e.g. M 87, see Braine & Wiklind, 1993), or may even exhibit HI-dominated outer regions left over by mergers (e.g. NGC 5266, see Morganti et al., 1997). To account for the different behavior of $R_{\rm mol}^{\rm galaxy}$ in elliptical and spiral galaxies, we chose a piecewise power-law with different powers for the two populations,

$$\log(R_{\rm mol,1}^{\rm galaxy}) = \left\{ \begin{array}{ll} c_1^{\rm el} + u_1^{\rm el}\, T & \text{if } T < T_1^* \\ c_1^{\rm sp} + u_1^{\rm sp}\, T & \text{if } T \geq T_1^* \end{array} \right\} + \sigma_{\rm phy,1} \tag{2.11}$$

where $c_1^{\rm el}$, $u_1^{\rm el}$, $c_1^{\rm sp}$, $u_1^{\rm sp}$ are considered as the free parameters to be fitted to the data, and T_1^* is at the intersection of the two regressions, i.e. $c_1^{\rm el} + u_1^{\rm el}\, T_1^* \equiv c_1^{\rm sp} + u_1^{\rm sp}\, T_1^*$, thus ensuring that $R_{\rm mol,1}^{\rm galaxy}$ remains a continuous function of T at $T = T_1^*$.

Another correlation exists between $R_{\rm mol}^{\rm galaxy}$ and the total cold gas mass $M_{\rm gas}$ or between $R_{\rm mol}^{\rm galaxy}$ and the blue magnitude $M_{\rm B}$. In fact, these two correlations are closely related due to the mutual correlation between $M_{\rm gas}$ and $M_{\rm B}$, and hence we shall restrict our considerations to the correlation between $R_{\rm mol}^{\rm galaxy}$ and $M_{\rm gas}$. According to the roughly monotonic trend visible in Fig. 2.5, we choose a power-law between $R_{\rm mol}^{\rm galaxy}$ and $M_{\rm gas}$ for our model 2,

$$\log(R_{\rm mol,2}^{\rm galaxy}) = q_2 + k_2\, \log\left(\frac{M_{\rm gas}}{10^9\, h^{-2} {\rm M}_\odot}\right) + \sigma_{\rm phy,2}, \tag{2.12}$$

where q_2, k_2 are free parameters. A somewhat similar dependence was recently found between $R_{\rm mol}^{\rm galaxy}$ and $M_{\rm HI}$ (Keres et al., 2003), but this result is less conclusive, since $R_{\rm mol}^{\rm galaxy}$ and $M_{\rm HI}$ are naturally correlated by the definition of $R_{\rm mol}^{\rm galaxy}$, even if $M_{\rm HI}$ and $M_{\rm H_2}$ are completely uncorrelated.

Finally, we shall introduce a fourth model (model 3) for $R_{\rm mol}^{\rm galaxy}$ that simulta-

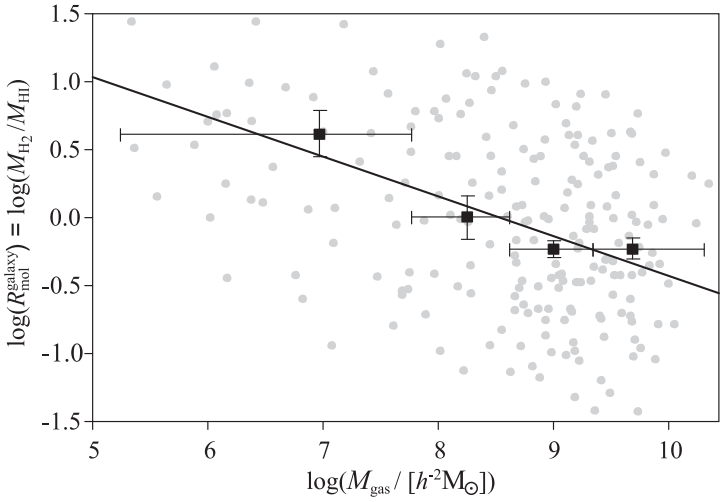

Figure 2.5. H_2/HI-mass ratio versus total cold gas mass $M_{\rm gas} \equiv (M_{\rm HI} + M_{\rm H_2})/\beta$. Grey dots represent the empirical data obtained by applying the variable X-factor of Eq. (2.8) with scatter to the CO-measurements. Black points represent the binned data; vertical bars represent the 1-σ confidence intervals; horizontal bars represent the bin intervals. The solid line represents model 2 fitted to the data points.

neously depends on galaxy Hubble type and cold gas mass,

$$\log(R_{\rm mol,3}^{\rm galaxy}) = \left\{ \begin{array}{ll} c_3^{\rm el} + u_3^{\rm el}\, T & (\text{if T} < \text{T}_3^*) \\ c_3^{\rm sp} + u_3^{\rm sp} T & (\text{if T} \geq \text{T}_3^*) \end{array} \right\} + k_3 \, \log\left(\frac{M_{\rm gas}}{10^9\, h^{-2}{\rm M}_\odot}\right) + \sigma_{\rm phy,3}\,, \tag{2.13}$$

where $c_3^{\rm el}$, $u_3^{\rm el}$, $c_3^{\rm sp}$, $u_3^{\rm sp}$, k_3 are free parameters and T_3^* is defined as $c_3^{\rm el} + u_3^{\rm el}\, T_3^* \equiv c_3^{\rm sp} + u_3^{\rm sp}\, T_3^*$, thus making $R_{\rm mol,3}^{\rm galaxy}$ a continuous function of T at $T = T_3^*$. Comparing this model with models 1 and 2, will also allow us to study a possible degeneracy between model 1 and model 2 caused by a dependence between cold gas mass and galaxy Hubble type.

The free parameters of the above models were determined by minimizing the rms-deviation between the model predictions and the 245 observed values

Model $\log(R_{\rm mol,i}^{\rm galaxy})$	$i=0$	$i=1$	$i=2$	$i=3$
$q_{\rm i}$	$-0.58^{+0.16}_{-0.23}$	-	$-0.51^{+0.03}_{-0.04}$	-
$c_{\rm i}^{\rm el}$	-	$+0.18^{+0.40}_{-0.22}$	-	$-0.01^{+0.25}_{-0.16}$
$u_{\rm i}^{\rm el}$	-	$+0.12^{+0.14}_{-0.05}$	-	$+0.13^{+0.07}_{-0.04}$
$c_{\rm i}^{\rm sp}$	-	$-0.14^{+0.10}_{-0.07}$	-	$-0.02^{+0.10}_{-0.09}$
$u_{\rm i}^{\rm sp}$	-	$-0.12^{+0.01}_{-0.02}$	-	$-0.13^{+0.02}_{-0.02}$
$k_{\rm i}$	-	-	$-0.24^{+0.05}_{-0.05}$	$-0.18^{+0.06}_{-0.07}$
$T_{\rm i}^{*}$	-	$-1.3^{+1.2}_{-0.5}$	-	$-0.1^{+1.2}_{-0.6}$
$\sigma_{\rm data,i}$	0.71	0.66	0.67	0.62
$\sigma_{\rm phy,i}$	0.39	0.27	0.30	0.15

Table 2.4. The upper panel lists the most likely parameters and 1-σ confidence intervals of the four models $R_{\rm mol,i}^{\rm galaxy}$ $(i=0,...,3)$. The bottom panel shows the rms-deviations $\sigma_{\rm data,i}$ of the data from the model predictions and the estimated physical scatter $\sigma_{\rm phy,i}$ for each model i.

of $\log(R_{\rm mol}^{\rm galaxy})$ (Appendix 2.8). Optimization in log-space is the most sensible choice since $R_{\rm mol}^{\rm galaxy}$ is subject to Gaussian scatter in log-space as will be shown in the Section 2.4.3. The most probable values of all parameters are shown in Table 2.4 together with the corresponding 1-σ confidence intervals. The latter were obtained using a bootstrapping method that uses 10^4 random half-sized subsamples of the full data set and determines the model-parameters for every one of them. The resulting distribution of values for each free parameter was approximated by a Gaussian distribution and its standard deviation σ was divided by $\sqrt{2}$ in order to find the 1-σ confidence intervals for the full data set. Note that in some cases the parameter uncertainties are coupled, i.e. a change in one parameter can be accommodated by changing the others, such that the model remains nearly identical. For models 1 and 2, the best fits are displayed in Figs. 2.4 and 2.5 as solid lines.

Table 2.4 also shows different scatters that will be explained in Section 2.4.3.

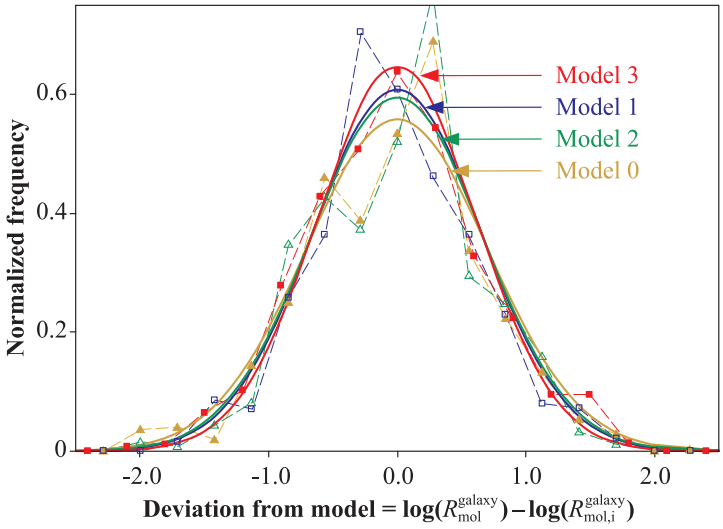

Figure 2.6. Distributions of the deviations between the observed values of $\log(R_{\rm mol}^{\rm galaxy})$ and the model-values $\log(R_{\rm mol,i}^{\rm galaxy})$ $(i = 1, ..., 3)$. Data points and dashed lines represent the actual distribution of the data; solid lines represent Gaussian distributions with equal standard deviations.

2.4.3 Scatter and uncertainty

The empirical values of $R_{\rm mol}^{\rm galaxy}$ scatter around the model predictions according to the distributions shown in Fig. 2.6 (dashed lines). The close similarity of these distributions to Gaussian distributions in log-space (solid lines) allows us to consider the rms-deviations of the data $\sigma_{\rm data}$ as the standard deviations of Gaussian distributions. This exhibits the advantage that $\sigma_{\rm data}$ can be decomposed in model-independent observational scatter $\sigma_{\rm obs}$ and model-dependent physical scatter $\sigma_{\rm phy}$ via the square-sum relation $\sigma_{\rm data,i}^2 = \sigma_{\rm obs}^2 + \sigma_{\rm phy,i}^2$, $i = 0, ..., 3$.

The major contribution to $\sigma_{\rm data,i}$ comes from observational scatter, as suggested by the close similarity of the different values of $\sigma_{\rm data,i}$. Indeed, the observational scatter inferred from the $R_{\rm mol}^{\rm galaxy}$ values of the 22 repeated sources in our data is $\sigma_{\rm obs} \approx 0.6$. This scatter is a combination of CO-flux measurement uncertainties, uncertain CO/H_2-conversions and HI-flux uncertainties (in decreasing significance). Since $\sigma_{\rm obs}$ is only marginally smaller than $\sigma_{\rm data,i}$ for all models,

the estimation of the physical scatters $\sigma_{\rm phy,i}$ (given in Table 2.4) is uncertain. Nevertheless, we shall include these best guesses of the physical scatter, when constructing the H_2-MFs in Section 2.4.4.

2.4.4 Recovering the H_2-MF and model evidence

Given a model for $R_{\rm mol}^{\rm galaxy}$, H_2-masses of arbitrary HI-galaxies can be estimated. We shall apply this technique to the 4315 sources in the HIPASS catalog using our four models of $R_{\rm mol,i}^{\rm galaxy}$, $i = 0, ..., 3$. For each model, the resulting H_2-catalog with 4315 objects will be converted into a H_2-MF, which can be compared to our reference H_2-MF derived directly from the CO-LF (Section 2.3).

For the models $R_{\rm mol,1}^{\rm galaxy}(T)$ and $R_{\rm mol,3}^{\rm galaxy}(M_{\rm gas}, T)$ Hubble types T were drawn from the HyperLeda database for each galaxy in the HIPASS catalog by means of the galaxy identifiers given in the optical cross-match catalog HOPCAT (Doyle et al., 2005). H_2-masses were then computed via $M_{\rm H_2} = R_{\rm mol,i}^{\rm galaxy}\, M_{\rm HI}$, $i = 0, ..., 3$. This equation is implicit in case of the mass-dependent models $R_{\rm mol,2}^{\rm galaxy}(M_{\rm gas})$ and $R_{\rm mol,3}^{\rm galaxy}(M_{\rm gas}, T)$, where $M_{\rm gas} = (M_{\rm HI} + M_{\rm H_2})/\beta$. All four models were applied with scatter, randomly drawn from a Gaussian distribution with the model-specific scatter $\sigma_{\rm phy,i}$, listed in Table 2.4.

In order to reconstruct a H_2-MF for each model, we employed the $1/V_{\rm max}$ method (Schmidt, 1968), where $V_{\rm max}$ was calculated from the analytic completeness function for HIPASS that depends on the HI peak flux density $S_{\rm p}$, the integrated HI line flux $S_{\rm int}$, and the flux limit of the survey (Zwaan et al., 2004). After ensuring that we can accurately reproduce the HI-MF derived by Zwaan et al. (2005a), we evaluated the four H_2-MFs (one for each model $R_{\rm mol,i}^{\rm galaxy}$) displayed in Fig. 2.7 (dots). The uncertainties of $\log(\phi_{\rm H_2})$ vary around $\sigma = 0.03 - 0.1$. Each function was fitted by a Schechter function by minimizing the weighted rms-deviation (colored solid lines).

The comparison of these four H_2-MFs with the reference H_2-MF derived from the CO-LF allows us to qualify the different models $R_{\rm mol,i}^{\rm galaxy}$, $i = 0, ..., 3$, against

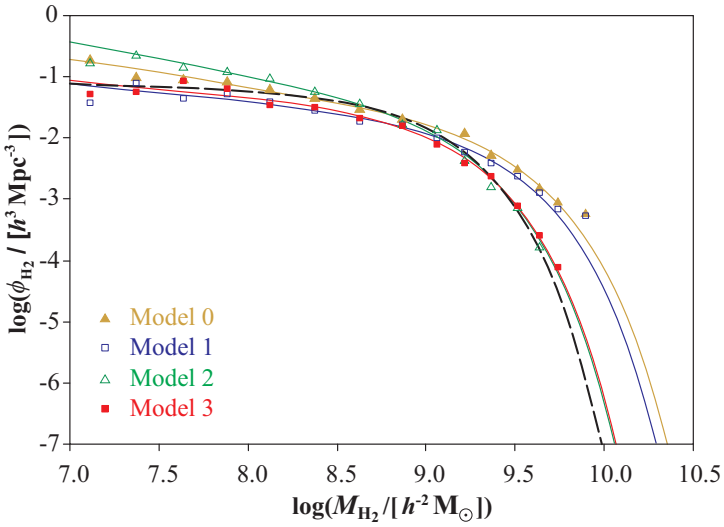

Figure 2.7. H_2-MFs constructed from the HIPASS HI-catalog using the different phenomenological models for the HI/H_2 ratio. The black dashed line is the reference H_2-MF derived from the CO-LF in Section 2.3.

each other. We ask: "What are the odds of model $R_{\rm mol,i}^{\rm galaxy}$ against model $R_{\rm mol,j}^{\rm galaxy}$ if the reference H_2-MF derived from the CO-LF is correct?" This question takes us back to the Bayesian framework of model selection applied in Section 2.2.2: If the models are a priori equally likely, their odds are equal to the Bayes factor, defined as the ratio between the model evidences. When computing these evidences, we take the "observational" data d to be the reference H_2-MF (with scatter), while the "model" data is the H_2-MF reproduced by applying a model $R_{\rm mol,i}^{\rm galaxy}$ to the HIPASS data. The free parameters θ (vector) are listed in Table 2.4 for each model (e.g. $c_1^{\rm el}$, $u_1^{\rm el}$, $c_1^{\rm sp}$, $u_1^{\rm sp}$ for model $R_{\rm mol,1}^{\rm galaxy}$). The prior probability density $\pi(\theta|M_{\rm i})$ in the evidence integral of Eq. (2.4) is taken as the multi-dimensional parameter probability distribution function obtained from the 245 galaxies studied in Section 2.4.2 (see Table 2.4). The second piece in the evidence integral, i.e. the probability density $p(d|\theta, M_{\rm i})$, is calculated as the product,

$$p(d|\theta, M_{\rm i}) = \prod_{\rm k} \frac{1}{\sigma\sqrt{2\pi}} \exp\left[\frac{(\phi_{\rm k}^{\rm ref} - \phi_{\rm k}^{\rm model,i})^2}{2\,\sigma^2}\right] \qquad (2.14)$$

where k labels the different bins of the H_2-MF (Fig. 2.7), and $\phi_{\rm k}^{\rm ref}$ and $\phi_{\rm k}^{\rm model,i}$ respectively denote the differential mass densities of the reference H_2-MF and the H_2-MFs reconstructed from HIPASS using the models $R_{\rm mol,i}^{\rm galaxy}$, $i = 0, ..., 3$. σ denotes the combined statistical uncertainties of $\phi_{\rm k}^{\rm ref}$ and $\phi_{\rm k}^{\rm model,i}$, theoretically given by $\sigma^2 = {\sigma_{\rm k}^{\rm ref}}^2 + {\sigma_{\rm k}^{\rm model,i}}^2$. However, we shall neglect the contribution of $\sigma_{\rm k}^{\rm model,i}$, since $\sigma_{\rm k}^{\rm ref}$ is about $3-4$ times larger due to the small size of the FCRAO sample of CO-galaxies compared to the HIPASS sample of HI-galaxies. Furthermore, we assume that σ is independent of the bin k and adopt an average uncertainty equal to $\sigma = 0.15$ dex. This is the mean scatter of the binned data of the reference H_2-MF (see Fig. 2.3). Assuming a constant scatter for the whole reference MF artificially increases the weight of the low and high mass ends, where the scatter is indeed closer to 0.3 dex, and reduces the weight of the central part, where the scatter equals 0.1 dex. We argue that this is a reasonable choice, since the central part of the reference H_2-MF suffers most from systematical uncertainties of the X-factor and the low and high mass ends encode much of the physics that could discriminate our models for $R_{\rm mol}^{\rm galaxy}$ against each other. In any case, the outcome of this evidence analysis is only weakly affected by the choice of scatter.

The integration of the evidence integral is computationally expensive: for *each* choice of model-parameters the following three steps need to be performed: (i) evaluation of the H_2-masses for each galaxies in the HIPASS sample, (ii) computation of the H_2-MF from that sample, (iii) computation of the product in Eq. (2.14). We applied a Monte Carlo method to sample the parameter spaces of the different models. About 10^6 integration steps had to be performed in total to reach a 2 per cent convergence of the Bayes factors.

The Bayes factor between each model $R_{\rm mol,i}^{\rm galaxy}$, $i = 0, ..., 3$, and $R_{\rm mol,0}^{\rm galaxy}$ is shown in Table 2.5: We find strong evidence for all variable models ($R_{\rm mol,1}^{\rm galaxy}$, $R_{\rm mol,2}^{\rm galaxy}$, $R_{\rm mol,3}^{\rm galaxy}$) against the constant one ($R_{\rm mol,0}^{\rm galaxy}$), and there is even stronger evidence of the bilinear model ($R_{\rm mol,3}^{\rm galaxy}$) against all others. The H_2-MF associated with this model is indeed the only one providing a simultaneous fit to the low and high

Model	$R^{\rm galaxy}_{\rm mol,0}$	$R^{\rm galaxy}_{\rm mol,1}$	$R^{\rm galaxy}_{\rm mol,2}$	$R^{\rm galaxy}_{\rm mol,3}$
Nb. of free param.	1	4	2	5
$\ln B$	0.0	7.3	8.2	22

Table 2.5. Comparison of different models for H_2/HI-mass ratios of entire galaxies; the first row shows the number of free parameters, while the second row shows the model evidence in terms of the Bayes factor between that model and the constant model $R^{\rm galaxy}_{\rm mol,0}$.

mass ends of the reference MF (see Fig. 2.7), and the agreement is very good (reduced $\chi^2 = 0.8$).

On a physical level, there are good reasons for the partial failure of the other models in reproducing the extremities of the reference H_2-MF. Model $R^{\rm galaxy}_{\rm mol,1}(T)$ overestimates the space density of galaxies with high H_2-masses by overestimating $R^{\rm galaxy}_{\rm mol}$ for the gas-richest early-type spiral galaxies. In reality, the latter have a very low molecular fraction (see data, model $R^{\rm galaxy}_{\rm mol,2}$, theory in Section 2.5), but they are a minority within otherwise gas-poor but molecule-rich early-type spirals. Hence, a model depending on Hubble type alone is likely to miss out such objects, resulting in an increased density of high H_2-masses. While model $R^{\rm galaxy}_{\rm mol,2}(M_{\rm gas})$ overcomes this issue and produces the right density of high H_2-masses, it fails by a factor $3-4$ in the low-mass end ($M_{\rm H_2} \lesssim 10^8 {\rm M}_\odot$). This is a direct manifestation of assigning high molecular fractions to all gas-poor galaxies, which neglects small young spirals with a dominant atomic phase. Finally, model $R^{\rm galaxy}_{\rm mol,0}$ seems to suffer from limitations at both ends of the H_2-MF.

The clear statistical evidence for model 3 shall be supported by the theoretical derivation of $R^{\rm galaxy}_{\rm mol}$ presented in Section 2.5.

2.5 Theoretical model for the H_2/HI-mass ratio

So far, we have approached the galactic H_2/HI-mass ratios $R^{\rm galaxy}_{\rm mol}$ with a set of *phenomenological* models, limited to the local Universe. By contrast, we have

recently derived a *physical* model for the H_2/HI-ratios in regular galaxies, which potentially extends to high redshift (Obreschkow et al., 2009a). This model relies on the theoretically and empirically established relation between interstellar gas pressure and local molecular fraction (Blitz & Rosolowsky, 2006, Elmegreen, 1993, Krumholz et al., 2009, Leroy et al., 2008). In this section, we will show that the physical model predicts H_2/HI-ratios consistent with our phenomenological model 3 given in Eq. (2.13). Hence, the physical (or "theoretical") model provides a reliable explanation for the global phenomenology of the H_2/HI-ratio in galaxies.

2.5.1 Background: the $R_{\rm mol}$–pressure relation

Understanding the observed continuous variation of $R_{\rm mol}$ within individual galaxies (e.g. Leroy et al., 2008) requires some explanation, since, fundamentally, there is no mixed thermodynamic equilibrium of HI and H_2. To first order, the ISM outside molecular clouds is atomic, while a cloud-region in local thermodynamic equilibrium (LTE) is either fully atomic or fully molecular, depending on the local state variables. The apparent continuous variation of $R_{\rm mol}$ is the combined result of (i) a non-resolved conglomeration of fully atomic and fully molecular clouds, (ii) clouds with molecular cores and atomic shells in different LTE, and (iii) some cloud regions off LTE with actual transient mixtures of HI and H_2. However, a time-dependent model for off-equilibrium clouds (Goldsmith et al., 2007) revealed that the characteristic time taken between the onset of cloud compression and full molecularization is of the order of 10^7 yrs, much smaller than the typical age of molecular clouds, and hence the fraction of these clouds is small. Therefore, averaged over galactic parts (hundreds or thousands of clouds), $R_{\rm mol}$ is dictated by clouds in LTE, entirely defined by a number of state variables.

A theoretical frame exploiting the LTE of molecular clouds was introduced by Elmegreen (1993), who considered an idealized double population of homogeneous diffuse clouds and isothermal self-gravitating clouds, both of which can have atomic and molecular shells. In this model the molecular mass fraction

$f_{\rm mol} = {\rm d}M_{\rm H_2}/{\rm d}(M_{\rm HI} + M_{\rm H_2})$ of each cloud depends on the density profile and the photodissociative radiation density from stars j, corrected for self-shielding by the considered cloud, mutual shielding among different clouds, and dust extinction. Since the shielding from this radiation depends on the gas pressure, Elmegreen (1993) finds that $f_{\rm mol}$ essentially scales with the external pressure P and photodissociative radiation density j, approximately following $f_{\rm mol} \propto P^{2.2}\, j^{-1}$ with an asymptotic flattening towards $f_{\rm mol} = 1$ at high P and low j. This implies approximately $R_{\rm mol} \equiv {\rm d}M_{\rm H_2}/{\rm d}M_{\rm HI} \propto P^{2.2}\, j^{-1}$. Assuming that j is proportional to the surface density of stars $\Sigma_{\rm stars}$ and that the stellar velocity dispersion $\sigma_{\rm stars}$ varies radially as $\Sigma_{\rm stars}^{0.5}$, Wong & Blitz (2002) and Blitz & Rosolowsky (2004, 2006) find roughly $j \propto P$ and hence $R_{\rm mol} \propto P^{\,\alpha}$ with $\alpha = 1.2$. Recently, Krumholz et al. (2009) have presented a more elaborate theory concluding that $\alpha \approx 0.8$. However, the exponent α remains uncertain, thus requiring an empirical determination.

Observationally, Blitz & Rosolowsky (2004, 2006) were the first ones to reveal a surprisingly tight power-law relation between pressure and molecular fraction based on a sample of 14 nearby galaxies including dwarf galaxies, HI-rich galaxies, and H_2-rich galaxies. Perhaps the richest observational study published so far is the one by Leroy et al. (2008), who analyzed 23 galaxies of The HI Nearby Galaxy Survey (THINGS, Walter et al., 2008), for which H_2-densities had been derived from CO-data and star formation densities. This analysis confirmed the power-law relation

$$R_{\rm mol} = (P/P_*)^{\alpha}, \tag{2.15}$$

where P is the local, kinematic midplane pressure of the gas, and P_* and α are free parameters, whose best fit to the data is given by $P_* = 2.35 \cdot 10^{-13}$ Pa and $\alpha = 0.8$.

2.5.2 Physical model for the H_2/HI-ratio in galaxies

We shall now consider the consequence of the model given in Eq. (2.15) for the H_2/HI-ratio of entire galaxies. To this end, we adopt the models and methods

presented in Obreschkow et al. (2009a), restricting this paragraph to an overview.

First, we note that most cold gas of regular galaxies is normally contained in a disc. This even applies to bulge-dominated early-type galaxies, such as suggested by recently presented CO-maps of five nearby elliptical galaxies (Young, 2002). Hence, the HI- and H_2-distributions of all regular galaxies can be well described by surface density profiles $\Sigma_{\rm HI}(r)$ and $\Sigma_{\rm H_2}(r)$. We assume that the disk is composed of axially symmetric, thin layers of stars and gas, which follow an exponential density profile with a generic scale length $r_{\rm disk}$, i.e.

$$\Sigma^{\rm disk}_{\rm stars}(r) \sim \Sigma_{\rm gas}(r) \sim \Sigma_{\rm HI}(r) + \Sigma_{\rm H_2}(r) \sim \exp(-r/r_{\rm disk}), \tag{2.16}$$

where r is the galactocentric radius and Σ denotes the mass column densities of the different components. Next, we adopt the phenomenological relation of Eq. (2.15), i.e.

$$\frac{\Sigma_{\rm HI}(r)}{\Sigma_{\rm H_2}(r)} = [P(r)/P_*]^\alpha, \tag{2.17}$$

and substitute the kinematic midplane pressure $P(r)$ for (Elmegreen, 1989)

$$P(r) = \frac{\pi}{2}\, G\, \Sigma_{\rm gas}(r) \Big(\Sigma_{\rm gas}(r) + f\, \Sigma^{\rm disk}_{\rm stars}(r) \Big), \tag{2.18}$$

where G is the gravitational constant and $f \equiv \sigma_{\rm gas,z}/\sigma_{\rm stars,z}$ is the ratio between the vertical velocity dispersions of gas and stars. We adopt $f = 0.4$ according to Elmegreen (1989).

Eqs. (2.16, 2.17) can be solved for $\Sigma_{\rm HI}(r)$ and $\Sigma_{\rm H_2}(r)$. In Obreschkow et al. (2009a), we demonstrate that the resulting surface profiles are consistent with the empirical data of the two nearby spiral galaxies NGC 5055 and NGC 5194 (Leroy et al., 2008). Integrating $\Sigma_{\rm HI}(r)$ and $\Sigma_{\rm H_2}(r)$ over the exponential disk gives the gas masses $M_{\rm HI}$ and $M_{\rm H_2}$, hence providing an estimate of their ratio $R^{\rm galaxy}_{\rm mol}$. Analytically, $R^{\rm galaxy}_{\rm mol}$ is given by an intricate expression, which is well

approximated (relative error < 0.05 for all galaxies) by the double power-law

$$R_{\rm mol,th}^{\rm galaxy} = \left(3.44\, {R_{\rm mol}^{\rm c}}^{-0.506} + 4.82\, {R_{\rm mol}^{\rm c}}^{-1.054}\right)^{-1}, \tag{2.19}$$

where

$$R_{\rm mol}^{\rm c} = \left[11.3\,{\rm m}^4\,{\rm kg}^{-2}\,{\rm r}_{\rm disk}^{-4}\,{\rm M}_{\rm gas}\left({\rm M}_{\rm gas} + 0.4\,{\rm M}_{\rm stars}^{\rm disk}\right)\right]^{0.8}. \tag{2.20}$$

$R_{\rm mol}^{\rm c}$ is a dimensionless parameter, which can be interpreted as the H_2/HI-ratio at the center of a pure disk galaxy. For typical cold gas masses of average galaxies ($M_{\rm gas} = 10^8 - 10^{10}{\rm M}_\odot$) and corresponding stellar masses and scale radii, $R_{\rm mol}^{\rm c}$ calculated from Eq. (2.20) varies roughly between 0.1 and 50. Hence, $R_{\rm mol}^{\rm galaxy}$ given in Eq. (2.19) varies roughly between 0.01 and 1.

In summary, Eqs. (2.19, 2.20) represent a theoretical model for $R_{\rm mol}^{\rm galaxy}$, which uses three input parameters: the disk stellar mass $M_{\rm stars}^{\rm disk}$, the cold gas mass $M_{\rm gas}$, and the exponential scale radius $r_{\rm disk}$ (see Obreschkow et al., 2009a for a detailed discussion).

2.5.3 Mapping between theory and phenomenology

We shall now show that our theoretical model for galactic H_2/HI-mass ratios given in Eqs. (2.19, 2.20) closely matches the best phenomenological model given in Eq. (2.13). The mapping between the two models uses a list of empirical relations derived from observations of nearby spiral galaxies, and hence the comparison of the models is a priori restricted to spiral galaxies in the local Universe.

First, we note that Eq. (2.19) can be well approximated by the power-law

$$R_{\rm mol,th}^{\rm galaxy} \approx 0.1\, {R_{\rm mol}^{\rm c}}^{0.8}. \tag{2.21}$$

As shown in Fig. 2.8, this approximation is accurate to about 10 per cent over the whole range $R_{\rm mol}^{\rm c} = 0.1, ..., 50$, covering most regular galaxies in the local Universe.

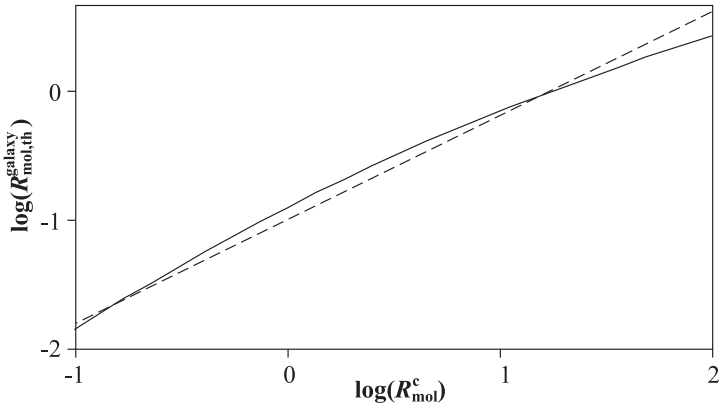

Figure 2.8. Visualization of the function $R^{\rm galaxy}_{\rm mol,th}(R^{\rm c}_{\rm mol})$. The solid line represents the nearly exact function given in Eq. (2.19), while the dashed line is the power-law fit of Eq. (2.21).

Substituting $R^{\rm c}_{\rm mol}$ in Eq. (2.21) for Eq. (2.20), yields the approximate relation

$$R^{\rm galaxy}_{\rm mol,th} = \left[0.31\,{\rm m}^4\,{\rm kg}^{-2}\,{\rm r}^{-4}_{\rm disk}\,{\rm M}_{\rm gas}\left({\rm M}_{\rm gas}+0.4\,{\rm M}^{\rm disk}_{\rm stars}\right)\right]^{0.64}. \qquad (2.22)$$

In order to compare the theoretical model of $R^{\rm galaxy}_{\rm mol}$ to the empirical models of Section 2.4.2, we need to eliminate the formal dependence of $R^{\rm galaxy}_{\rm mol,th}$ on $r_{\rm disk}$ and $M^{\rm disk}_{\rm stars}$. To this end, we use two approximate empirical relations, derived from samples of nearby spiral galaxies (see Appendix 2.9),

$$\log\left(\frac{M^{\rm disk}_{\rm stars}}{h^{-2}{\rm M}_\odot}\right) = \gamma_1+\alpha_1\,\log\left(\frac{M_{\rm gas}}{2\cdot10^9\,h^{-2}\,{\rm M}_\odot}\right), \qquad (2.23)$$

$$\log\left(\frac{r_{\rm disk}}{h^{-1}{\rm kpc}}\right) = \gamma_2+\alpha_2\,\log\left(\frac{M^{\rm disk}_{\rm stars}}{5\cdot10^9\,h^{-2}\,{\rm M}_\odot}\right)+\delta\,\tilde{T}, \qquad (2.24)$$

where $\tilde{T}\equiv(10-T)/16$ is the normalized Hubble type, which varies between $\tilde{T}=0$ (pure disk galaxies) to $\tilde{T}=1$ (pure spheroids).

The parameters corresponding to the best χ^2 fit (Appendix 2.9) are $\alpha_1 = 1.46\pm0.1$, $\gamma_1 = 9.80\pm0.05$, $\alpha_2 = 0.45\pm0.05$, $\gamma_2 = 0.97\pm0.05$, $\delta = -1.07\pm0.1$. The given intervals are the 1-σ confidence intervals of the parameters; they do

not characterize the scatter of the data. The units on the right hand side of Eqs. (2.23, 2.24) were chosen such as to minimize the correlations between the uncertainties of $\alpha_{\rm i}$ and $\gamma_{\rm i}$.

Physical reasons for the empirical relations in Eqs. (2.23, 2.24) are discussed in Appendix 2.9. Substituting Eqs. (2.23, 2.24) into Eq. (2.22) reduces $R^{\rm galaxy}_{\rm mol,th}$ to a pure function of $M_{\rm gas}$ and T of the form

$$\begin{aligned} \log\left[R^{\rm galaxy}_{\rm mol,th}(M_{\rm gas},T)\right] &= \log\left[R^{\rm galaxy}_{\rm mol,th}(M_{\rm gas},10)\right] \\ &\quad +\delta(0.16\,T-1.6), \end{aligned} \tag{2.25}$$

where $R^{\rm galaxy}_{\rm mol,th}(M_{\rm gas},10)$ is the theoretical H_2/HI-ratio of a pure disk galaxy, i.e. $T=10$. The function $R^{\rm galaxy}_{\rm mol,th}(M_{\rm gas},10)$ is displayed in Fig. 2.9 together with the 1-σ uncertainty implied by the uncertainties of the four parameters α_1, α_2, γ_1, γ_2. We approximate this relation by the power-law

$$\log\left[R^{\rm galaxy}_{\rm mol,th}(M_{\rm gas},10)\right] = c + s\cdot\log\left(\frac{M_{\rm gas}}{10^9\,h^{-2}\,{\rm M}_\odot}\right). \tag{2.26}$$

The parameters minimizing the rms-deviation on the mass-interval $\log(M_{\rm gas}/[{\rm M}_\odot h^{-2}]) = 7.5-10.5$ are $c=-1.79\pm0.04$ and $s=-0.24\pm0.05$. The given uncertainties approximate the propagated uncertainties of α_1, α_2, γ_1, γ_2.

The simplified theoretical model for the H_2/HI-ratio given in Eqs. (2.25, 2.26) exhibits exactly the formal structure of our best phenomenological model 3. Setting $R^{\rm galaxy}_{\rm mol,th}(M_{\rm gas},T)$ in Eq. (2.25) equal to $R^{\rm galaxy}_{\rm mol,3}(M_{\rm gas},T)$ in Eq. (2.13) for spiral galaxies, yields the following mapping between the theoretical and empirical model-parameters,

$$\begin{aligned} c_3^{\rm sp} &= c-1.6\,\delta\,, \\ u_3^{\rm sp} &= s\,, \\ k_3 &= 0.16\,\delta\,. \end{aligned} \tag{2.27}$$

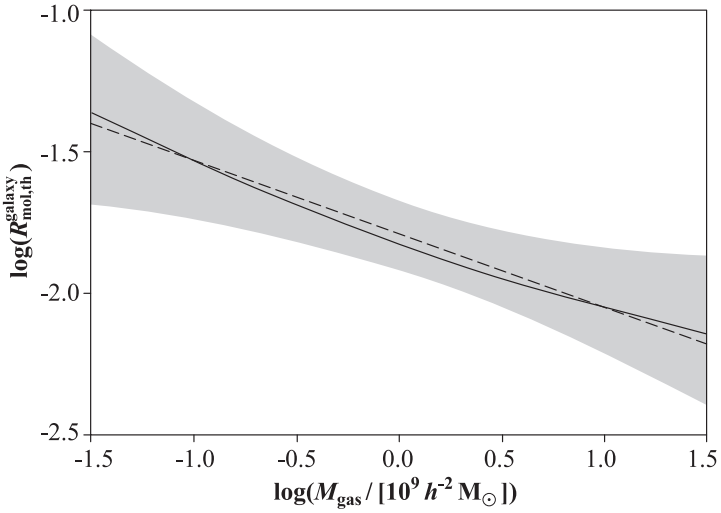

Figure 2.9. Relation between $R^{\rm galaxy}_{\rm mol,th}$ and $M_{\rm gas}$ for flat disks ($T = 10$). The solid line represents the relation obtained from Eq. (2.22), when expressing $r_{\rm disk}$ and $M^{\rm disk}_{\rm stars}$ as functions of $M_{\rm gas}$ using Eqs. (2.23, 2.24). The shaded zone represents the 1-σ uncertainty implied by the uncertainties of the empirical parameters in Eqs. (2.23, 2.24). The dashed line represents the best power-law fit for the displayed mass interval as given in Eq. (2.26).

The probability distributions of the empirical model-parameters on the left hand side of Eqs. (2.27) were derived in Section 2.4 and their 1-σ uncertainties are given in Table 2.4. The corresponding probability distributions of the theoretical model-parameters on the right hand side of Eqs. (2.27) can be estimated from the Gaussian uncertainties given for the parameters c, s, δ. The empirical and theoretical parameter distributions are compared in Fig. 2.10 and reveal a surprising consistency.

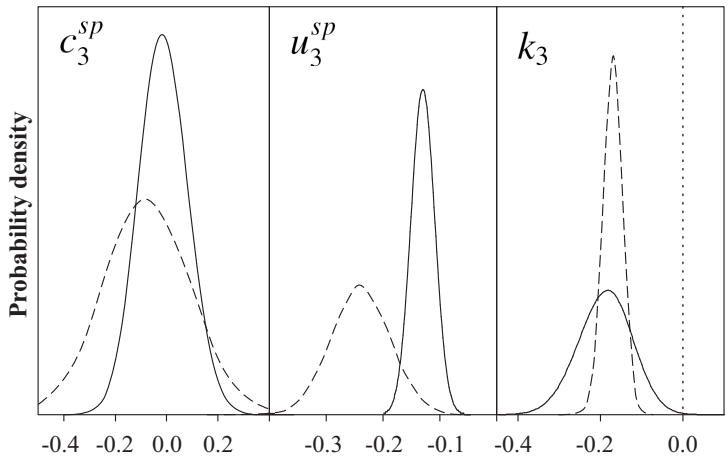

Figure 2.10. Probability distributions of the three parameters in our model 3 (Eq. 2.13) for the H_2/HI-mass ratio $R_{\rm mol}^{\rm galaxy}$ of spiral galaxies. Solid lines represent phenomenologically determined probability distributions given in Table 2.4; dashed lines represent the corresponding theoretical probability distributions, obtained when using Eqs. (2.27) with the respective distributions for c, s, and δ.

2.6 Discussion

2.6.1 Theoretical versus phenomenological model

The dependence of $R_{\rm mol}^{\rm galaxy}$ on galaxy Hubble type T and cold gas mass $M_{\rm gas}$ was first considered on a purely phenomenological level, and described by the empirical models in Section 2.4. The best empirical model for spiral galaxies could be quantitatively reproduced by the subsequently derived theoretical model for regular galaxies in Section 2.5. Hence, the latter provides a tool for understanding the variations of $R_{\rm mol}^{\rm galaxy}$.

In fact, according to Eq. (2.22), $R_{\rm mol}^{\rm galaxy}$ seems most directly dictated by the scale radius $r_{\rm disk}$ and the masses $M_{\rm gas}$ and $M_{\rm stars}^{\rm disk}$. The dependence of $R_{\rm mol}^{\rm galaxy}$ on T is clearly due to the trend for smaller values of $r_{\rm disk}$ (for a given mass) in bulge-rich galaxies. Several physical reasons for the influence of the bulge on $r_{\rm disk}$ are mentioned in Appendix 2.9.2.

From Eq. (2.22), one might naively expect that $R_{\rm mol}^{\rm galaxy}$ and $M_{\rm gas}$ are positively correlated. However, the disk scale radius $r_{\rm disk}$ increases with $M_{\rm gas}$ as $r_{\rm disk} \propto M_{\rm gas}^{0.66}$ by virtue of Eqs. (2.23, 2.24). Taking this scaling into account, the H_2/HI-ratio $R_{\rm mol}^{\rm galaxy}$ effectively decreases with increasing $M_{\rm gas}$. The physical picture is that more massive galaxies are less dense due to their larger sizes, and hence their molecular fraction is lower.

The 'best' phenomenological model is by definition the one that, when applied to the galaxies in the HIPASS sample, exhibits the H_2-MF that best fits the reference H_2-MF derived from the CO-LF. The close agreement between the best model defined in this way and the theoretical model therefore supports the accuracy of the CO-LF (Keres et al., 2003), which could a priori be affected by the poorly characterized completeness of the CO-sample. Confirmingly, Keres et al. (2003) argued that the CO-LF does not substantially suffer from incompleteness by analyzing the FIR-LF produced from the same sample.

2.6.2 Brief word on cosmic evolution

The theoretical model $R_{\rm mol,th}^{\rm galaxy}$ given in Eqs. (2.19, 2.20) potentially extends to high redshift, as it only premises the invariance of the relation between pressure and $R_{\rm mol}$ and a few assumptions with weak dependence on redshift (but see discussion in Obreschkow et al., 2009a). However, we emphasize that the transition from the theoretical model $R_{\rm mol,th}^{\rm galaxy}$ to the phenomenological model $R_{\rm mol,3}^{\rm galaxy}$ uses a set of relations extracted from observations in the local Universe. Most probably $R_{\rm mol,3}^{\rm galaxy}$ underestimates the molecular fraction at higher redshift, predominantly due to the evolution in the mass–diameter relation of Eq. (2.24). Indeed, scale radii are smaller at higher redshift for identical masses, thus increasing the pressure and molecular fraction. Bouwens et al. (2004) found $r_{\rm disk} \propto (1+z)^{-1}$ from observations in the Ultra Deep Field, consistent with the theoretical prediction by Mo et al. (1998). According to Eq. (2.22), where $R_{\rm mol}^{\rm galaxy} \propto r_{\rm disk}^{-2.6}$, this implies $R_{\rm mol}^{\rm galaxy} \propto (1+z)^{2.6}$. In other words, the phenomenological model 3 (Eq. 2.13)

for the H_2/HI-mass ratio should be multiplied by roughly a factor $(1+z)^{2.6}$. However, this conclusion only applies if we consider galaxies with constant stellar and gas masses. For the cosmic evolution of the universal H_2/HI-ratio $R_{\rm mol}^{\rm universe}$, we also require a model for the evolution of the stellar and gas mass functions, and it may even be important to consider different scenarios for the evolution of the scale radius for different masses. A more elaborate model for the evolution of $R_{\rm mol}^{\rm universe}$ can be obtained from cosmological simulations (e.g. Obreschkow et al., 2009a and forthcoming publications).

2.6.3 Application: The local cold gas-MF

We finally apply our best phenomenological model for the H_2/HI-mass ratio (i.e. $R_{\rm mol,3}^{\rm galaxy}$ given in Eq. 2.13) to derive an integral cold gas-MF (HI+H_2+He) from the HIPASS catalog. In fact, the cold gas-MF cannot be inferred solely from the HI-MF (e.g. Zwaan et al., 2005a) and the H_2-MF (e.g. Section 2.3), but only from a sample of galaxies with simultaneous HI- and H_2-data. Presently, there is no such sample with a large number of galaxies and an accurate completeness function. Therefore, we prefer using the HIPASS data, which have both sufficient size (4315 galaxies) and well described completeness (Zwaan et al., 2004), and we estimate the corresponding H_2-masses using our model $R_{\rm mol,3}^{\rm galaxy}$. Details of the computation of the H_2-masses were given in Section 2.4.4.

The resulting cold gas-MF is shown in Fig. 2.11 together with the HI-MF from Zwaan et al. (2005a) and the reference H_2-MF derived in Section 2.3. The displayed continuous functions are best fitting Schechter functions. The respective Schechter function parameters for the cold gas-MF are $M^* = 7.21\cdot10^9\,h^{-2}\,{\rm M}_\odot$, $\alpha = -1.37$, and $\phi^* = 0.0114\,h^3$ Mpc^{-3}. The total cold gas density in the local Universe derived by integrating this Schechter function is $\Omega_{\rm gas} = 4.2\cdot10^{-4}\,h^{-1}$, closely matching the value $(4.4\pm0.8)\cdot10^{-4}\,h^{-1}$ obtained when summing up the empirical HI-density (Zwaan et al., 2005a), the H_2-density (Section 2.3), and the corresponding He-density.

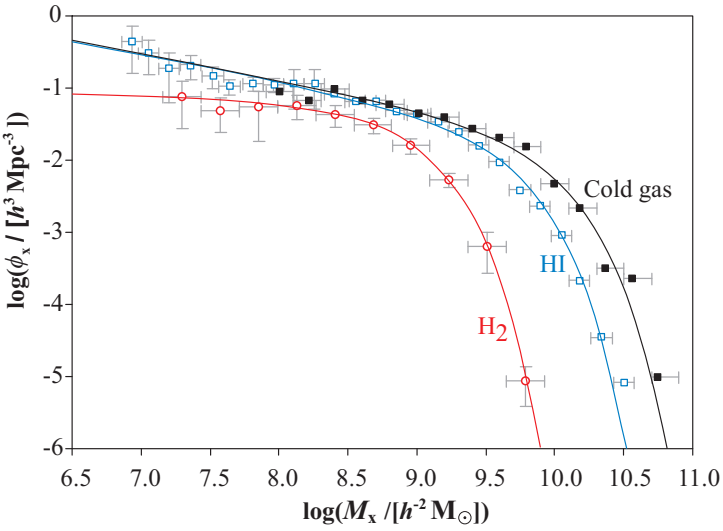

Figure 2.11. Filled squares represent the integral cold gas-MF (HI+H_2+He) derived from the HIPASS data using our best phenomenological model for the H_2/HI-mass ratio (Eq. 2.13); empty squares represent the observed HI-MF (Zwaan et al., 2005a) and empty circles represent our best estimate of the H_2-MF (Section 2.3). Solid lines are best fitting Schechter functions.

2.7 Conclusion

In this paper, we established a coherent picture of the H_2/HI-ratio in galaxies based on a variety of extragalactic observations and theoretical considerations. Some important jigsaw pieces are:

1. Measurements of the X-factor (summarized in Boselli et al., 2002) were combined with more recent CO-flux measurements and extinction-corrected optical M_B-magnitudes, resulting in a working model for X.

2. This model for X was applied to the CO-LF by Keres et al. (2003) in order to derive the first local H_2-MF based on a variable X-factor.

3. Nine samples of local galaxies (245 objects in total) with simultaneous measurements of M_{HI} and L_{CO} were combined to fit a set of empirical models

for galactic H_2/HI-mass ratios $R_{\rm mol}^{\rm galaxy}$.

4. These models were applied to the large HI-sample of the HIPASS catalog, which permitted the derivation of a H_2-MF for each model for $R_{\rm mol}^{\rm galaxy}$. A comparison of these H_2-MFs with the one derived directly from the CO-LF allowed us to determine the statistical evidence of each model and to uncover a clear 'best model'.

5. Based on the relation between pressure and the local H_2/HI-ratio $R_{\rm mol}$ (Leroy et al., 2008), we established a theoretical model for the H_2/HI-ratio $R_{\rm mol}^{\rm galaxy}$ of regular galaxies, which potentially extends to high redshifts.

6. We could show that the best empirical model for $R_{\rm mol}^{\rm galaxy}$ found before is an excellent approximation of the theoretical model in the local Universe.

The factual results standing out of this analysis are

1. an empirical H_2-MF obtained by combining the CO-LF of Keres et al. (2003) with a variable X-factor (see Fig. 2.3 and parameters in Table 2.3),

2. an empirical model for $R_{\rm mol}^{\rm galaxy}$ (Eq. 2.13), which accurately reproduces the above H_2-MF, when applied to the HI-sample of the HIPASS catalog,

3. a theoretical model for $R_{\rm mol}^{\rm galaxy}$ (Eqs. 2.19, 2.20), which provides a source for physical understanding and generalizes to high redshift,

4. a quasi-empirical integral cold gas-MF (HI+H_2+He) based on the HIPASS data.

Self-consistency argues in favour of the interlinked picture established in this paper. However, all quantitative results remain subjected to the uncertainties of the X-factor. The latter appears as a scaling factor, affecting in the same way the reference H_2-MF derived from the CO-LF, the phenomenological models of $R_{\rm mol}^{\rm galaxy}$ and hence the H_2-MFs derived from HIPASS, as well as the P–$R_{\rm mol}$ relation

and thus the theoretical model for $R_{\rm mol}^{\rm galaxy}$. In the future it may therefore be necessary to re-scale the quantitative results of this paper using a more accurate determination of X.

Acknowledgements

This effort/activity is supported by the European Community Framework Programme 6, Square Kilometre Array Design Studies (SKADS), contract no 011938. We further acknowledge the usage of the HyperLeda database (http://leda.univ-lyon1.fr) and we thank the anonymous referee for the helpful suggestions.

2.8 Appendix A : Homogenized data

This section presents the data (245 galaxies) used for the derivation of the models of $R_{\rm mol}^{\rm galaxy}$ in section 2.4.

CO-luminosities were drawn from 10 smaller samples: 17 nearby ($\lesssim$ 10 Mpc) lenticulars and ellipticals (Sage & Welch, 2006, Welch & Sage, 2003), 4 late-type spirals (Matthews et al., 2005), 68 isolated late-type spirals (Sauty et al., 2003), 6 ellipticals (Georgakakis et al., 2001), 17 spirals of all types (Andreani et al., 1995), 48 nearby ($\lesssim$ 10 Mpc) spirals of all types (Sage, 1993), 12 ellipticals (Lees et al., 1991), 18 lenticulars and ellipticals (Thronson et al., 1989), 77 spirals of all types (Young & Knezek, 1989). These 267 objects contained 22 repeated galaxies. In each case of repetition, the older reference was removed, such as to remain with the 245 distinct sources listed in Table 2.6. The CO-luminosities were homogenized by making them independent of different X-factors and Hubble constants. All other properties listed in the table were taken from homogenized reference catalogs, such as described in Section 2.4.1.

Table 2.6: Homogenized galaxy sample based on data drawn from the literature. T is the numerical Hubble type (see online help of the HyperLeda database), D_l the luminosity distance, M_B is the extinction corrected absolute blue magnitude, and X is the variable X-factor derived from M_B (eq. 2.8) without addition of Gaussian scatter. The references for H_2-masses are: [1] Sage & Welch (2006), Welch & Sage (2003), [2] Matthews et al. (2005), [3] Sauty et al. (2003), [4] Georgakakis et al. (2001), [5] Andreani et al. (1995), [6] Sage (1993), [7] Lees et al. (1991), [8] Thronson et al. (1989), [9] Young & Knezek (1989).

Object	T	D_l/ $[h^{-1}\,\mathrm{Mpc}]$	M_B- $5\log h$	X	$\log M_{H_2}$/ $[X\,h^{-2}\,M_\odot]$	Ref.	$\log M_{HI}$/ $[h^{-2}\,M_\odot]$
NGC 404	-2.8	1.7	-15.86	6.66	6.06	1	7.51
NGC 2787	-1.1	9.5	-18.87	2.21	6.58	1	8.58
NGC 3115	-2.8	6.4	-19.27	1.91	5.60	1	6.75
NGC 3384	-2.7	9.2	-19.06	2.06	5.87	1	5.94
NGC 3489	-1.3	7.7	-18.45	2.58	6.12	1	6.46
NGC 3607	-3.1	10.3	-19.23	1.94	8.34	1	6.93
NGC 3870	-2.0	9.9	-16.56	5.15	7.44	1	8.08
NGC 3941	-2.0	11.0	-19.04	2.08	7.15	1	8.81
NGC 4026	-1.8	12.1	-18.82	2.25	7.27	1	7.86
NGC 4150	-2.1	6.8	-17.66	3.44	6.91	1	6.88
NGC 4203	-2.7	12.7	-18.86	2.22	6.21	1	8.41
NGC 4310	-1.0	10.8	-16.86	4.61	6.96	1	7.10
NGC 4460	-0.9	7.3	-17.04	4.32	6.45	1	8.26
NGC 4880	-1.5	14.8	-17.92	3.13	6.27	1	6.02
NGC 7013	0.5	9.6	-18.79	2.28	7.30	1	8.70
NGC 7077	-3.9	12.0	-16.13	6.03	6.09	1	7.60

Object	T	$D_{\rm l}$/ $[h^{-1}\,{\rm Mpc}]$	$M_{\rm B}-$ 5 log h	X	log $M_{\rm H_2}$/ $[X\,h^{-2}\,{\rm M}_\odot]$	Ref.	log $M_{\rm HI}$/ $[h^{-2}\,{\rm M}_\odot]$
NGC 7457	-2.6	9.6	-18.29	2.73	5.85	1	5.88
NGC 100	5.9	9.0	-17.61	3.51	5.91	2	8.87
UGC 2082	5.9	7.7	-17.72	3.37	5.89	2	8.80
UGC 3137	4.2	12.5	-17.05	4.30	6.20	2	9.11
UGC 6667	6.0	12.1	-17.06	4.29	5.73	2	8.54
UGC 5	3.9	74.4	-20.98	1.02	8.76	3	9.82
NGC 7817	4.1	24.1	-20.42	1.25	8.44	3	9.30
IC 1551	3.6	136.0	-22.17	0.66	8.94	3	9.34
NGC 237	4.5	42.0	-19.81	1.57	8.53	3	9.75
NGC 575	5.3	32.3	-19.10	2.03	8.04	3	9.18
NGC 622	3.4	52.1	-19.93	1.50	8.24	3	9.54
UGC 1167	5.9	43.6	-19.18	1.97	8.85	3	9.61
UGC 1395	3.1	52.3	-19.90	1.51	8.43	3	9.25
UGC 1587	3.7	57.4	-20.38	1.27	7.86	3	9.59
UGC 1706	5.8	49.4	-19.82	1.56	7.96	3	9.17
IC 302	4.1	59.6	-21.33	0.90	8.43	3	10.19
IC 391	4.9	18.3	-18.91	2.18	7.46	3	8.89
UGC 3420	3.1	54.5	-20.96	1.03	8.03	3	10.01
UGC 3581	5.2	53.2	-20.30	1.31	8.24	3	9.56
NGC 2344	4.4	11.3	-17.91	3.14	6.73	3	8.66
UGC 3863	1.1	62.2	-20.53	1.20	8.32	3	9.30
UGC 4684	7.2	24.9	-17.92	3.13	6.82	3	9.11
NGC 2746	1.1	73.7	-20.65	1.15	8.65	3	9.64
UGC 4781	5.9	14.4	-16.54	5.19	6.46	3	8.90
UGC 5055	3.1	79.4	-20.19	1.36	8.79	3	10.02
NGC 2900	5.9	54.3	-19.51	1.75	8.57	3	9.69

Object	T	D_l/ $[h^{-1}\,\mathrm{Mpc}]$	M_B- 5 log h	X	log M_{H_2}/ $[X\,h^{-2}\,M_\odot]$	Ref.	log M_{HI}/ $[h^{-2}\,M_\odot]$
NGC 2977	3.2	33.5	-19.95	1.49	8.31	3	8.83
NGC 3049	2.5	15.0	-17.86	3.20	7.24	3	8.86
IC 651	8.2	45.2	-20.37	1.28	8.54	3	9.53
NGC 3526	5.2	14.5	-18.68	2.37	7.73	3	8.64
UGC 6568	8.2	60.8	-19.86	1.54	8.12	3	9.14
UGC 6769	3.0	88.2	-20.66	1.15	9.10	3	9.96
UGC 6780	6.4	17.3	-16.79	4.73	7.29	3	9.28
UGC 6879	7.1	24.1	-18.78	2.28	7.82	3	8.83
UGC 6903	5.9	19.3	-17.69	3.40	7.46	3	9.07
NGC 4348	4.1	20.3	-19.49	1.76	8.10	3	9.01
NGC 4617	3.1	49.6	-20.70	1.13	8.56	3	9.90
NGC 4635	6.5	10.9	-17.28	3.96	6.73	3	8.23
NGC 5377	1.1	20.6	-19.83	1.55	7.81	3	8.91
NGC 5375	2.4	26.0	-19.54	1.73	7.60	3	9.24
NGC 5584	5.9	17.1	-19.06	2.06	7.22	3	9.27
NGC 5690	5.4	18.4	-19.88	1.53	8.15	3	9.33
NGC 5768	5.3	20.3	-18.74	2.32	7.90	3	9.11
NGC 5772	3.1	52.3	-20.41	1.26	8.25	3	9.49
NGC 5913	1.3	20.8	-19.00	2.11	8.22	3	8.44
NGC 6012	1.9	20.1	-19.00	2.11	7.73	3	9.26
IC 1231	5.8	55.9	-20.71	1.13	8.04	3	9.14
UGC 10699	4.4	65.5	-20.19	1.36	8.60	3	9.11
UGC 10743	1.1	27.2	-18.75	2.31	7.52	3	8.78
NGC 6347	3.1	64.3	-20.46	1.23	8.57	3	9.48
UGC 10862	5.3	18.2	-17.81	3.26	7.21	3	9.07
NGC 6389	3.6	33.1	-20.37	1.28	8.30	3	9.93

Object	T	$D_{\rm l}$/ $[h^{-1}\,{\rm Mpc}]$	$M_{\rm B}-$ 5 log h	X	log $M_{\rm H_2}$/ $[X\,h^{-2}\,{\rm M}_\odot]$	Ref.	log $M_{\rm HI}$/ $[h^{-2}\,{\rm M}_\odot]$
UGC 11058	3.2	50.6	-20.48	1.22	8.51	3	9.40
NGC 6643	5.2	17.8	-20.31	1.30	8.35	3	9.27
NGC 6711	4.0	50.1	-20.18	1.37	8.77	3	9.14
UGC 11635	3.7	51.8	-21.05	0.99	8.95	3	9.88
UGC 11723	3.1	50.1	-19.87	1.53	8.48	3	9.57
NGC 7056	3.6	55.8	-20.53	1.20	8.67	3	9.11
NGC 7156	5.9	40.8	-20.12	1.40	8.43	3	9.32
UGC 11871	3.1	82.9	-20.38	1.27	9.22	3	9.43
NGC 7328	2.1	29.2	-19.31	1.88	8.34	3	9.45
NGC 7428	1.1	31.0	-18.85	2.23	7.72	3	9.44
UGC 12304	5.2	35.3	-19.40	1.82	8.01	3	8.88
UGC 12372	4.0	57.7	-19.94	1.49	8.65	3	9.49
NGC 7514	4.3	51.1	-20.62	1.16	8.18	3	9.16
UGC 12474	1.1	53.5	-20.53	1.20	8.80	3	8.87
NGC 7664	5.1	36.3	-20.03	1.44	8.51	3	9.91
UGC 12646	3.0	83.7	-20.84	1.07	8.68	3	9.70
NGC 7712	1.6	31.9	-18.94	2.15	7.84	3	9.10
IC 1508	7.2	43.8	-20.07	1.42	8.45	3	9.75
UGC 12776	3.0	51.8	-19.88	1.53	8.31	3	9.99
IC 5355	5.7	50.8	-19.56	1.72	8.26	3	9.05
UGC 12840	-1.8	71.3	-20.27	1.32	7.97	3	9.43
NGC 2623	2.0	57.2	-20.59	1.18	9.02	4	9.01
NGC 2865	-4.1	26.0	-20.01	1.46	7.35	4	8.79
NGC 3921	0.0	61.9	-21.00	1.01	8.82	4	9.46
NGC 4649	-4.6	12.1	-20.70	1.13	7.15	4	8.35
NGC 7252	-2.1	47.0	-20.73	1.12	8.83	4	9.29

Object	T	D_l/ $[h^{-1}\,\mathrm{Mpc}]$	M_B- 5 log h	X	log M_{H_2}/ $[X\,h^{-2}\,M_\odot]$	Ref.	log M_{HI}/ $[h^{-2}\,M_\odot]$
NGC 7727	1.1	17.9	-19.98	1.47	7.27	4	8.45
NGC 142	3.1	81.4	-20.46	1.23	9.36	5	9.43
IC 1553	5.4	28.0	-18.75	2.31	7.69	5	9.10
ESO 473-27	4.4	193.6	-21.12	0.97	9.78	5	9.75
NGC 232	1.1	66.7	-19.82	1.56	9.50	5	9.21
ESO 475-16	2.1	70.7	-20.44	1.24	9.01	5	9.74
NGC 578	5.0	14.8	-19.73	1.61	7.97	5	9.52
ESO 478-6	4.1	52.6	-20.64	1.16	8.96	5	9.23
NGC 1187	5.0	12.2	-19.39	1.83	8.69	5	9.33
NGC 1306	2.8	12.7	-16.85	4.63	7.34	5	8.64
NGC 1385	5.9	13.1	-19.56	1.72	8.59	5	9.07
ESO 549-23	1.2	40.8	-19.42	1.81	8.45	5	8.88
ESO 483-12	0.3	41.0	-19.18	1.97	8.27	5	8.83
NGC 1591	1.9	39.5	-19.65	1.66	8.51	5	9.04
NGC 7115	3.4	34.1	-19.53	1.73	8.26	5	9.52
NGC 7225	-0.5	47.9	-20.09	1.41	9.29	5	9.07
NGC 7314	4.0	13.2	-19.71	1.62	8.05	5	9.24
NGC 628	5.2	6.9	-19.84	1.55	8.55	6	9.73
NGC 672	6.0	5.1	-19.03	2.08	6.60	6	9.07
NGC 891	3.0	6.7	-19.43	1.80	8.97	6	9.72
NGC 925	7.0	6.6	-19.32	1.87	8.04	6	9.57
NGC 1058	5.3	6.3	-17.78	3.29	7.42	6	8.93
NGC 1560	7.0	2.3	-15.91	6.53	5.88	6	8.47
NGC 2403	6.0	3.2	-18.89	2.19	7.31	6	9.54
NGC 2683	3.1	5.2	-19.53	1.73	7.63	6	8.54
NGC 2903	4.0	6.3	-20.16	1.38	8.39	6	9.01

Object	T	$D_{\rm l}$/ $[h^{-1}\,{\rm Mpc}]$	$M_{\rm B}-$ 5 log h	X	log $M_{\rm H_2}$/ $[X\,h^{-2}\,{\rm M}_\odot]$	Ref.	log $M_{\rm HI}$/ $[h^{-2}\,{\rm M}_\odot]$
NGC 2976	5.3	1.6	-17.35	3.86	6.42	6	7.49
NGC 3031	2.4	2.4	-19.90	1.51	7.42	6	9.15
NGC 3184	5.9	7.7	-19.11	2.02	8.35	6	9.11
NGC 3344	4.0	6.9	-18.89	2.19	7.74	6	9.01
NGC 3351	3.0	8.3	-19.46	1.78	8.08	6	8.67
NGC 3368	1.8	9.4	-20.12	1.40	8.18	6	8.95
NGC 3486	5.2	8.2	-18.84	2.23	7.50	6	9.03
NGC 3521	4.0	8.0	-20.31	1.30	8.75	6	9.63
NGC 3593	-0.4	6.9	-17.50	3.65	7.62	6	7.75
NGC 3623	1.0	8.9	-20.17	1.37	7.62	6	8.27
NGC 3627	3.0	7.9	-20.40	1.26	8.55	6	8.56
NGC 3628	3.1	9.2	-20.67	1.14	8.62	6	9.33
NGC 4020	6.9	9.2	-17.31	3.91	6.60	6	8.05
NGC 4062	5.3	9.4	-18.78	2.28	7.63	6	8.47
NGC 4096	5.3	7.9	-19.49	1.76	7.75	6	8.86
NGC 4144	6.0	3.1	-15.93	6.48	6.31	6	8.09
NGC 4244	6.1	2.3	-18.06	2.97	6.62	6	8.72
NGC 4245	0.1	10.5	-17.97	3.07	7.39	6	6.61
NGC 4274	1.7	10.9	-19.33	1.87	8.27	6	8.75
NGC 4288	7.1	7.5	-16.32	5.62	6.67	6	8.52
NGC 4314	1.0	11.5	-19.02	2.09	7.69	6	6.43
NGC 4359	5.0	14.3	-17.49	3.66	6.55	6	8.44
NGC 4414	5.1	8.9	-19.25	1.92	8.48	6	8.90
NGC 4448	1.8	8.2	-17.86	3.20	7.39	6	7.38
NGC 4490	7.0	8.0	-20.93	1.04	7.45	6	9.54
NGC 4437	6.0	11.6	-20.70	1.13	8.14	6	7.90

Object	T	D_l/ $[h^{-1}\,\mathrm{Mpc}]$	M_B- 5 log h	X	log M_{H_2}/ $[X\,h^{-2}\,M_\odot]$	Ref.	log M_{HI}/ $[h^{-2}\,M_\odot]$
NGC 4525	5.9	13.5	-18.11	2.92	6.57	6	7.86
NGC 4559	6.0	9.8	-20.35	1.28	8.26	6	9.57
NGC 4565	3.2	13.8	-21.74	0.77	8.62	6	9.48
NGC 4605	4.9	3.0	-17.58	3.54	6.82	6	8.05
NGC 4631	6.6	7.9	-21.46	0.86	8.03	6	9.58
NGC 4736	2.4	5.3	-19.27	1.91	7.86	6	8.23
NGC 4826	2.4	5.5	-19.86	1.54	7.79	6	8.07
NGC 5055	4.0	7.3	-20.43	1.25	8.80	6	9.40
NGC 5194	4.0	7.0	-19.74	1.61	9.29	6	9.21
NGC 5457	5.9	5.0	-20.26	1.33	8.50	6	9.79
NGC 6503	5.9	4.6	-17.77	3.31	7.35	6	8.86
NGC 6946	5.9	4.1	-20.12	1.40	8.74	6	9.55
NGC 7640	5.3	5.5	-18.75	2.31	6.93	6	9.62
NGC 185	-4.8	0.7	-13.83	14.00	4.81	7	5.18
NGC 205	-4.7	0.7	-13.61	15.18	4.95	7	5.57
NGC 855	-4.6	6.9	-16.23	5.81	5.33	7	7.62
NGC 3265	-4.8	15.7	-17.28	3.96	7.13	7	7.95
NGC 3928	-4.5	12.1	-17.35	3.86	7.36	7	8.22
NGC 5128	-2.1	5.3	-20.59	1.17	8.16	7	8.28
NGC 5666	6.4	23.6	-18.90	2.19	8.00	7	8.63
NGC 1819	-1.9	44.8	-20.23	1.34	9.10	7	9.13
NGC 3032	-1.8	16.7	-18.14	2.89	7.72	7	7.76
NGC 4138	-0.9	10.9	-17.97	3.07	7.13	7	8.54
NGC 7465	-1.9	20.6	-18.57	2.47	8.11	7	9.20
NGC 3413	-1.8	7.9	-16.66	4.96	7.21	8	7.95
NGC 5866	-1.2	9.5	-19.23	1.94	7.81	8	8.15

Object	T	$D_{\rm l}$/ $[h^{-1}\,{\rm Mpc}]$	$M_{\rm B}-$ 5 log h	X	log $M_{\rm H_2}$/ $[X\,h^{-2}\,{\rm M}_\odot]$	Ref.	log $M_{\rm HI}$/ $[h^{-2}\,{\rm M}_\odot]$
NGC 4710	-0.8	13.8	-19.02	2.09	8.25	8	7.20
NGC 4459	-1.4	13.3	-19.37	1.84	8.30	8	6.70
NGC 4526	-1.9	6.7	-18.63	2.41	8.30	8	7.05
NGC 693	0.1	15.5	-18.08	2.95	7.53	8	8.74
NGC 2685	-1.1	11.0	-18.32	2.70	7.45	8	8.79
NGC 2273	1.0	20.7	-19.47	1.77	8.26	8	8.90
NGC 3611	1.1	16.1	-18.67	2.38	8.42	8	8.75
NGC 4457	0.4	9.4	-18.31	2.71	8.63	8	8.27
NGC 4383	1.0	18.3	-19.01	2.10	7.91	8	9.15
NGC 7625	1.2	17.2	-18.38	2.64	8.56	8	8.98
NGC 23	1.2	47.4	-20.84	1.07	9.30	9	9.69
NGC 253	5.1	1.7	-20.19	1.36	8.32	9	9.04
NGC 520	0.8	21.5	-19.90	1.51	9.35	9	9.50
NGC 828	1.0	55.9	-20.95	1.03	9.75	9	9.80
NGC 834	3.9	48.1	-20.32	1.30	9.13	9	9.47
NGC 864	5.1	15.4	-19.80	1.57	8.49	9	9.78
NGC 877	4.8	39.7	-21.15	0.96	9.34	9	10.08
NGC 1055	3.2	9.3	-18.97	2.13	9.37	9	9.39
IC 342	5.9	2.3	-19.85	1.54	8.70	9	9.68
NGC 1530	3.1	27.5	-20.70	1.13	9.10	9	9.76
NGC 1569	9.6	2.4	-15.94	6.46	5.89	9	8.09
NGC 1614	4.9	47.2	-20.64	1.16	9.36	9	9.28
NGC 2146	2.3	11.6	-20.34	1.29	9.04	9	9.50
NGC 2339	4.0	22.9	-20.02	1.45	9.27	9	9.45
NGC 2276	5.4	27.2	-20.80	1.09	9.31	9	9.50
NGC 2532	5.2	54.5	-21.00	1.01	9.10	9	9.92

Object	T	D_l/ $[h^{-1}\,\mathrm{Mpc}]$	M_B- 5 log h	X	log M_{H_2}/ $[X\,h^{-2}\,M_\odot]$	Ref.	log M_{HI}/ $[h^{-2}\,M_\odot]$
NGC 2633	3.0	24.5	-19.47	1.77	8.83	9	9.41
NGC 2775	1.7	13.5	-19.83	1.55	8.30	9	8.16
NGC 2841	3.0	8.3	-20.07	1.42	8.61	9	9.20
NGC 3034	8.0	1.7	-17.30	3.93	8.16	9	8.54
NGC 3079	6.6	13.5	-20.68	1.14	9.16	9	9.57
NGC 3147	3.9	31.1	-21.43	0.86	9.65	9	9.52
NGC 3221	5.6	42.5	-19.86	1.54	9.24	9	9.81
NGC 3310	4.0	12.2	-19.26	1.92	7.81	9	9.33
NGC 3437	5.2	13.8	-19.03	2.08	7.91	9	9.03
NGC 3504	2.1	16.8	-19.68	1.64	8.50	9	8.37
NGC 3556	6.0	9.3	-19.89	1.52	8.37	9	9.35
NGC 3893	5.1	12.0	-20.13	1.39	8.35	9	9.29
NGC 4192	2.5	10.0	-20.83	1.08	8.57	9	9.33
NGC 4194	9.7	27.3	-19.87	1.53	8.61	9	8.96
NGC 4254	5.2	25.2	-21.82	0.75	9.07	9	9.39
NGC 4303	4.0	16.2	-21.05	0.99	8.95	9	9.38
NGC 4321	4.0	16.8	-21.29	0.91	9.12	9	9.06
NGC 4388	2.8	26.2	-21.16	0.95	7.96	9	8.33
NGC 4394	2.9	10.3	-18.65	2.39	8.04	9	8.22
NGC 4402	3.3	10.0	-17.18	4.09	8.39	9	8.23
NGC 4419	1.1	10.0	-18.43	2.60	8.56	9	7.62
NGC 4424	1.2	5.1	-15.75	6.91	7.34	9	7.89
NGC 4438	0.7	10.0	-19.99	1.47	7.92	9	8.26
NGC 4449	9.8	2.6	-16.83	4.66	6.60	9	9.10
NGC 4450	2.3	20.7	-21.10	0.98	8.25	9	7.95
NGC 4501	3.4	23.9	-22.33	0.62	8.94	9	8.91

Object	T	$D_{\rm l}$/ $[h^{-1}\,{\rm Mpc}]$	$M_{\rm B}-$ 5 log h	X	log $M_{\rm H_2}$/ $[X\,h^{-2}\,{\rm M}_\odot]$	Ref.	log $M_{\rm HI}$/ $[h^{-2}\,{\rm M}_\odot]$
NGC 4527	4.0	17.9	-20.75	1.11	8.85	9	9.35
NGC 4535	5.0	20.3	-21.18	0.95	8.79	9	9.41
NGC 4536	4.2	18.6	-21.02	1.01	8.46	9	9.23
NGC 4548	3.1	6.0	-20.01	1.46	8.33	9	8.68
NGC 4569	2.4	10.0	-20.33	1.29	8.77	9	8.32
NGC 4571	6.3	10.0	-17.53	3.60	8.17	9	8.49
NGC 4579	2.8	16.1	-20.91	1.05	8.55	9	8.38
NGC 4647	5.2	14.9	-19.02	2.09	8.37	9	8.33
NGC 4651	5.2	9.1	-18.86	2.22	8.14	9	9.21
NGC 4654	5.9	11.4	-19.86	1.54	8.46	9	9.15
NGC 4689	4.7	17.2	-19.92	1.50	8.44	9	8.30
NGC 5236	5.0	4.5	-19.99	1.46	9.41	9	9.86
NGC 5936	3.2	42.2	-20.29	1.31	9.15	9	8.90
NGC 6207	4.9	10.9	-19.11	2.02	7.52	9	8.97
NGC 6574	3.9	24.6	-20.12	1.40	9.13	9	8.87
NGC 7217	2.5	11.2	-19.70	1.63	8.41	9	8.65
NGC 7331	3.9	9.9	-20.81	1.09	9.22	9	9.77
NGC 7469	1.1	50.4	-21.00	1.01	9.50	9	9.30
NGC 7479	4.4	24.6	-20.93	1.04	9.35	9	9.77
NGC 7541	4.7	27.2	-20.78	1.10	9.34	9	10.01
NGC 7674	3.8	91.6	-21.17	0.95	9.66	9	10.11

2.9 Appendix B : Diverse phenomenological relations

This section summarizes the two phenomenological relations given in Eqs. (2.23) and (2.24).

2.9.1 Stellar mass versus gas mass

From the galaxy sample presented in Appendix 2.8, we extracted all 25 Scd/Sd-type galaxies ($6 \leq T \leq 9$), that is all objects approximating pure discs. For these objects the total gas masses $M_{\rm gas}$ were calculated via $M_{\rm gas} = (M_{\rm HI} + M_{\rm H_2})/\beta$. Additionally, we estimated the stellar mass $M_{\rm stars}$ of each galaxy from the I-band magnitude $M_{\rm I}$ via (Mo et al., 1998),

$$\log(M_{\rm stars}/{\rm M}_\odot) = 1.66 + \log(\Upsilon_{\rm I}) - M_{\rm I}/2.5, \tag{2.28}$$

where the mass/light-ratio $\log(\Upsilon_{\rm I}) = 1.2$ has been adopted from McGaugh & de Blok (1997).

The resulting data points displayed in Fig. 2.12 reveal an approximate power-law relation between $M_{\rm gas}$ and $M_{\rm stars}$. We have fitted the corresponding free parameters α_1, γ_1 to the data points by minimizing the x-y-weighted rms-deviations. 1-σ errors for these parameters were obtained via a bootstrapping method that uses 10^3 random half-sized subsamples of the 25 galaxies and determines the power-law parameters for every one of them. The standard deviations of the distributions for α_1 and γ_1 are then divided by $\sqrt{2}$ to estimate 1-σ confidence intervals for the full data set. The best power-law fit and its 1-σ confidence interval are displayed in Fig. 2.13, while explicit numerical values are given in Section 2.5.3.

To first order, one would expect that $M_{\rm stars}$ depends linearly on $M_{\rm gas}$, if both masses scale linearly with the mass of the parent haloe. The over-proportional growth of $M_{\rm stars}$ ($\alpha_1 = 1.46 \pm 0.10 > 1$) could be explained by the fact that more massive galaxies are generally older and therefore could convert a larger fraction

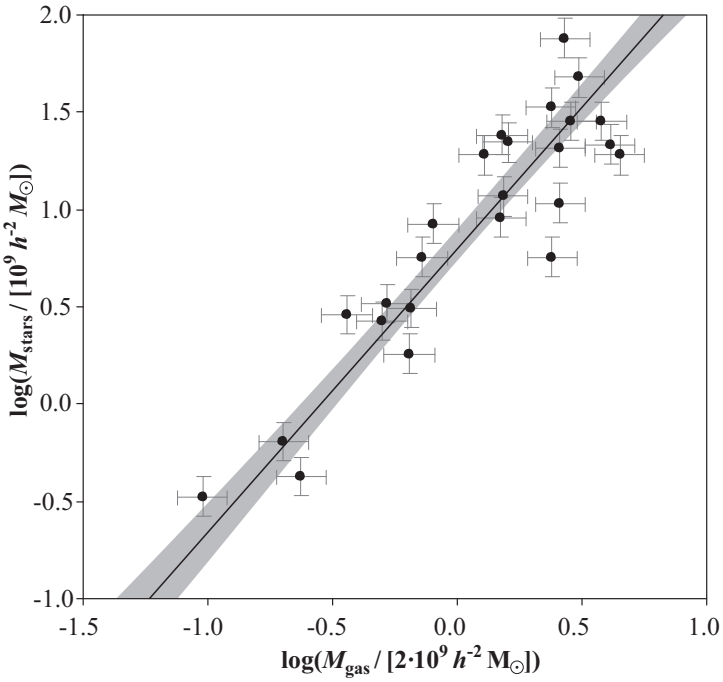

Figure 2.12. Data points (subsample of the data shown in Appendix 2.8) represent the observed relation between disk stellar mass $M_{\rm stars}^{\rm disk}$ and cold gas mass $M_{\rm gas}$. The solid line shows the best power-law fit and the shaded envelope its 1-σ uncertainty. This power-law is given in Eq. (2.23) and has a slope of $\alpha_1 = 1.46 \pm 0.10$.

of hydrogen gas into stars.

2.9.2 Scale radius versus stellar mass

Kregel et al. (2002) investigated a sample of 34 nearby edge-on spiral galaxies, drawn from the ESO-LV catalog (Lauberts & Valentijn, 1989) using four selection criteria: (i) inclination $i \geq 87\,\mathrm{deg}$, (ii) blue diameter $D_{25}^{\rm B} > 2.2$ arcmin, (iii) Hubble type from S0–Sd, (iv) only regular field galaxies, i.e. no interacting systems, no warped or lopsided systems. This sample is complete in terms of sample selection (see Davies, 1990, Kregel et al., 2002), but the sample volume is too small to contain rare objects. For each galaxy in the sample Kregel et al. (2002) determined the scale radius $r_{\rm disk}$ of the stellar disk from the I-band lu-

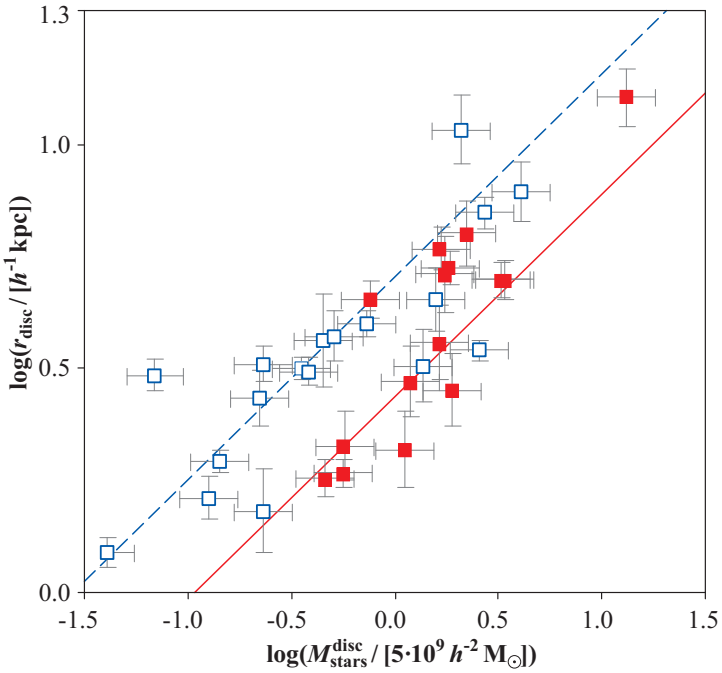

Figure 2.13. Relation between disk scale radius $r_{\rm disk}$ and disk stellar mass $M_{\rm stars}^{\rm disk}$. Squares represent 34 nearby spiral galaxies observed by Kregel et al. (2002). Filled squares correspond to Sa/Sb-type galaxies, and empty squares represent Sc/Sd-type galaxies. These data were used to fit the free parameters of the model in Eq. (2.24). The solid line shows this model for $T = 2$ (i.e. Sab-type galaxies), while the dashed line shows the model for $T = 6$ (i.e. Scd-type galaxies). The slope of these power-laws is $\alpha_2 = 0.45 \pm 0.05$, consistent with a Freeman law (McGaugh et al., 1995).

minosity profiles. They also obtained the morphological Hubble type T for each source from the Lyon/Meudon Extragalactic Database (LEDA). Additionally, we estimated the disk stellar masses $M_{\rm stars}^{\rm disk}$ from the I-band magnitudes of the disk components according to Eq. (2.28).

Using these data, we investigated the relations between $M_{\rm stars}^{\rm disk}$, $r_{\rm disk}$ and T. The data points shown in Fig. 2.13 suggest the approximate power-law with Hubble type correction of Eq. (2.24). The best fitting parameters α_2, γ_2, and δ were obtained as in Section 2.9.1 and explicit numerical values with errors are given in Section 2.5.3.

To first order, the $r_{\rm disk}$–$M_{\rm stars}^{\rm disk}$ relation can be understood in terms of a dark matter halo with an isothermal, singular, and spherical structure (e.g. Mo et al., 1998). This model predicts that the virial radius $r_{\rm vir}$ is proportional to the cubic root of the dark matter mass $M_{\rm DM}$ at any fixed cosmic time. If $r_{\rm disk}$ were proportional to $r_{\rm vir}$ and $M_{\rm stars}^{\rm disk}$ were proportional to $M_{\rm DM}$, one would expect $r_{\rm disk}$ to scale as $(M_{\rm stars}^{\rm disk})^{1/3}$. Our empirical result, $\alpha_2 = 0.45 \pm 0.05$, shows a slightly stronger scaling, consistent with the empirical Freeman law ($\alpha_2 = 0.5$), according to which disk galaxies have approximately constant surface brightness (McGaugh et al., 1995).

The secondary dependence of the $r_{\rm disk}$–$M_{\rm stars}^{\rm disk}$ relation on the Hubble type T probably has multiple reasons: (i) early-type galaxies have more massive stellar bulges, which present an additional central potential that contracts the disc; (ii) bulges often form from disk instabilities, occurring preferably in systems with relatively low angular momentum, and hence early-type galaxies are biased towards smaller angular momenta and smaller scale radii; (iii) larger bulges, such as the ones of lenticular and elliptical galaxies, often arise from galaxy mergers, which tend to reduce the specific angular momenta and scale radii (see also Obreschkow et al., 2009a).

Chapter 3

Simulation of HI and H_2 in $3 \cdot 10^7$ evolving galaxies

D. Obreschkow, D. Croton, G. De Lucia, S. Khochfar, and S. Rawlings

"Simulation of the Cosmic Evolution of HI and H_2 in Galaxies"

ApJ, **698**, 1467–1484 (2009)

We present a simulation of the cosmic evolution of the atomic and molecular phases of the cold hydrogen gas in about $3 \cdot 10^7$ galaxies, obtained by post-processing the virtual galaxy catalog produced by De Lucia & Blaizot (2007) on the Millennium Simulation of cosmic structure (Springel et al., 2005). Our method uses a set of physical prescriptions to assign neutral atomic hydrogen (HI) and molecular hydrogen (H_2) to galaxies, based on their total cold gas masses and a few additional galaxy properties. These prescriptions are specially designed for large cosmological simulations, where, given current computational limitations, individual galaxies can only be represented by simplistic model-objects with a few global properties. Our recipes allow us to (i) split total cold gas masses between HI, H_2, and Helium, (ii) assign realistic sizes to both the HI- and H_2-disks, and (iii) evaluate the corresponding velocity profiles and shapes of the characteristic radio emission lines. The results presented in this paper include the local HI- and H_2-mass functions, the CO-luminosity function, the cold gas mass–diameter relation, and the Tully–Fisher relation (TFR), which all match recent observational data from the local Universe. We also present high-redshift predictions of cold gas diameters and the TFR, both of which appear to evolve markedly with redshift.

3.1 Introduction

Observations of gas in galaxies play a vital role in many fields of astrophysics and cosmology. Detailed studies of atomic and molecular material now possible in the local Universe with radio and millimeter telescopes will, over the coming decades, be extended to high redshifts as new facilities come on line.

Firstly, hydrogen is the prime fuel for galaxies, when it condenses from the hot ionized halo onto the galactic disks. The fresh interstellar medium (ISM) thus acquired mainly consists of atomic hydrogen (HI), but in particularly dense regions, called molecular clouds, it can further combine to molecular hydrogen (H_2). Only inside these clouds can new stars form. Mapping HI and H_2 in individual galaxies therefore represents a key tool for understanding their growth and evolution. Secondly, the characteristic HI-radio line permits the measurement of the radial velocity and velocity dispersion of the ISM with great accuracy, thereby leading to solid conclusions about galaxy dynamics and matter density profiles. Thirdly, and particularly with regard to next-generation radio facilities, surveys of HI are also discussed as a powerful tool for investigating the large scale structure of the Universe out to high redshifts. While such large scale surveys are currently dominated by the optical and higher frequency bands [e.g. Spitzer (Fang et al., 2005), SDSS (Eisenstein et al., 2005), DEEP2 (Davis et al., 2003), 2dFGRS (Cole et al., 2005), GALEX (Milliard et al., 2007), Chandra (Gilli et al., 2003)], they may well be overtaken by future radio arrays, such as the Square Kilometre Array (SKA, Carilli & Rawlings, 2004). The latter features unprecedented sensitivity and survey speed characteristics regarding the HI-line and could allow the construction of a three-dimensional map of $\sim 10^9$ HI-galaxies in just a few years survey time. The cosmic structure hence revealed, specifically the baryon acoustic oscillations (BAOs) manifest in the power spectrum, will, for example, constrain the equation of state of dark energy an order of magnitude better than possible nowadays (Abdalla et al., 2009, Abdalla & Rawlings, 2005). Fourthly, deep low frequency detections will presumably reveal HI in the intergalactic space of the

dark ages (Carilli et al., 2004) – one of the ultimate jigsaw pieces concatenating the radiation dominated early Universe with the matter dominated star-forming Universe.

Typically, HI- and H_2-observations are considered part of radio and millimeter astronomy, as they rely on the characteristic radio line of HI at a rest-frame frequency of $\nu = 1.42$ GHz and several carbon monoxide (CO) radio lines, indirectly tracing H_2-regions, in the $\nu = 10^2 - 10^3$ GHz band. Such line detections will soon undergo a revolution with the advent of new radio facilities such as the SKA and the Atacama Large Millimeter/submillimeter Array (ALMA). These observational advances regarding HI and H_2 premise equally powerful theoretical predictions for both the optimal design of the planned facilities and for the unbiased analysis of future detections.

This is the first paper in a series of papers aiming at predicting basic HI- and H_2-properties in a large sample of evolving galaxies. Here, we introduce a suite of tools to assign HI- and H_2-properties, such as masses, disk sizes, and velocity profiles, to simulated galaxies. These tools are subsequently applied to the $\sim 3 \cdot 10^7$ simulated evolving galaxies in the galaxy-catalog produced by De Lucia & Blaizot (2007) (hereafter the "DeLucia-catalog") for the Millennium Simulation of cosmic structure (Springel et al., 2005). In forthcoming publications, we will specifically investigate the cosmic evolution of HI- and H_2-masses and -surface densities predicted by this simulation, and we will produce mock-observing cones, from which predictions for the SKA and the ALMA will be derived.

Section 3.2 provides background information about the DeLucia-catalog. In particular, we highlight the hybrid simulation scheme that separates structure formation from galaxy evolution, and discuss the accuracy of the cold gas masses of the DeLucia-catalog. In section 3.3, we derive an analytic model for the H_2/HI-ratio in galaxies in order to split the hydrogen of the cold gas of the DeLucia-catalog between HI and H_2. We compare the resulting mass functions (MFs) and the CO-luminosity function (LF) with recent observations. Sections 3.4 and 3.5

explain our model to assign diameters and velocity profiles to HI- and H_2-disks. The simulation results are compared to observations from the local Universe and high-redshift predictions are presented. In Section 3.6, we discuss some consistency aspects and limitations of the approaches taken in this paper. Section 3.7 concludes the paper with a brief summary and outlook.

3.2 Background: simulated galaxy catalog

N-body simulations of cold dark matter (CDM) on supra-galactic scales proved to be a powerful tool to analyze the non-linear evolution of cosmic structure (e.g. Springel et al., 2006). Starting with small primordial perturbations in an otherwise homogeneous part of a model-universe, such simulations can quantitatively reproduce the large-scale structures observed in the real Universe, such as galaxy clusters, filaments, and voids. These simulations further demonstrate that most dark matter aggregations, especially the self-bound haloes, grow hierarchically, that is through successive mergers of smaller progenitors. Hence, each halo at a given cosmic time can be ascribed a "merger tree" containing all its progenitors. One of the most prominent simulations is the "Millennium run" (Springel et al., 2005), which followed the evolution of $2160^3 \approx 10^{10}$ particles of mass $8.6{\cdot}10^8\,\mathrm{M}_\odot/h$ over a redshift range $z = 127 \rightarrow 0$ in a cubic volume of $(500\,\mathrm{Mpc}/h)^3$ with periodic boundary conditions. The dimensionless Hubble parameter h, defined as $H_0 = 100\,h\,\mathrm{km\,s^{-1}\,Mpc^{-1}}$, was set equal to $h = 0.73$, and the other cosmological parameters were chosen as $\Omega_{\mathrm{matter}} = 0.25$, $\Omega_{\mathrm{baryon}} = 0.045$, $\Omega_\Lambda = 0.75$, $\sigma_8 = 0.9$.

Despite impressive results, modern N-body simulations of CDM in comoving volumes of order $(500\,\mathrm{Mpc}/h)^3$ cannot simultaneously evolve the detailed substructure of individual galaxies. The reasons are computational limitations, which restrict both the mass-resolution and the degree to which baryonic and radiative physics can be implemented. Nevertheless, an efficient approximate solution for the cosmic evolution of galaxies can be achieved by using a hybrid model that separates CDM-dominated structure growth from more complex baryonic physics

(Kauffmann et al., 1999). The idea is to first perform a purely gravitational large-scale N-body simulation of CDM and to reduce the evolving data cube to a set of halo merger trees. These dark matter merger trees are assumed independent of the baryonic and radiative physics taking place on smaller scales, but they constitute the mass skeleton for the formation and evolution of galaxies. As a second step, each merger tree is populated with a list of galaxies, which are represented by simplistic model-objects with a few global properties (stellar mass, gas mass, Hubble type, star formation rate, etc.). The galaxies are formed and evolved according to a set of physical prescriptions, often of a "semi-analytic" nature, meaning that galaxy properties evolve analytically unless a merger occurs. This hybrid approach tremendously reduces the computational requirements compared to hydro-gravitational N-body simulations of each galaxy.

Croton et al. (2006) were the first to apply this hybrid scheme to the Millennium Simulation, thus producing a catalog with $\sim 1.1 \cdot 10^9$ galaxies in 64 time steps, corresponding to about $\sim 3 \cdot 10^7$ evolving galaxies. This catalog was further improved by De Lucia & Blaizot (2007), giving rise to the DeLucia-catalog used in this paper. The underlying semi-analytic prescriptions to form and evolve galaxies account for the most important mechanisms known today. In brief, the hot gas associated with the parent halo is converted into galactic cold gas according to a cooling rate that scales with redshift and depth of the halo potential. Stars form at a rate proportional to the excess of the cold gas density above a critical density, below which star formation is suppressed. In return, supernovae reheat some fraction of the cold gas, and, if the energy injected by supernovae is large enough, their material can escape from the galaxy and later be reincorporated into the hot gas. In addition, when galaxies become massive enough, cooling gas can be reheated via feedback from active galaxy nuclei (AGNs) associated with continuous or merger-based black hole mass accretion. These basic mechanisms are completed with additional prescriptions regarding merger-related starbursts, morphology changes, metal enrichment, dust evolution and change of

photometric properties (see Croton et al., 2006, De Lucia & Blaizot, 2007). The free parameters in this model were adjusted such that the simulated galaxies at redshift $z = 0$ fit the joint luminosity/color/morphology distribution of observed low-redshift galaxies (Cole et al., 2001, Huang et al., 2003, Norberg et al., 2002). A good first order accuracy of the model is suggested by its ability to reproduce the observed bulge-to-black hole mass relation (Häring & Rix, 2004), the Tully–Fisher relation (Giovanelli et al., 1997), and the cold gas metallicity as a function of stellar mass (Tremonti et al., 2004, see also Figs. 4 and 6 in Croton et al., 2006).

Some galaxies in the DeLucia-catalog have no corresponding halo in the Millennium Simulation. Such objects can form during a halo merger, where the resulting halo is entirely ascribed to the most massive progenitor galaxy. In the model, the other galaxies continue to exist as "satellite galaxies" without haloes. These galaxies are identified as "type 2" objects in the DeLucia-catalog. If the halo properties of a satellite galaxy are required, they must be extrapolated from the original halo of the galaxy or estimated from the baryonic properties of the galaxy.

We emphasize that the semi-analytic recipes of the DeLucia-catalog are simplistic and may require an extension or readjustment, when new observational data become available. In particular, recent observations (Bigiel et al., 2008, Leroy et al., 2008) suggest that star formation laws based on a surface density threshold are suspect, especially in low surface density systems. Moreover, galaxies in the DeLucia-catalog with stellar masses $M_{\rm stars}$ below $4 \cdot 10^9\,{\rm M}_\odot$ typically sit at the centers of haloes with less than 100 particles, whose merging history could only be followed over a few discrete cosmic time steps. It is likely that the physical properties of these galaxies are not yet converged. Croton et al. (2006) noted that especially the morphology (colors and bulge mass) of galaxies with $M_{\rm stars} \lesssim 4 \cdot 10^9\,{\rm M}_\odot$ is poorly resolved, since, according to the model, the bulge formation directly relies on the galaxies' merging history and disk insta-

Catalog	$\Omega_{\rm gas}^{\rm sim}$	$\Omega_{\rm gas}^{\rm sim}/\Omega_{\rm gas}^{\rm obs}$
De Lucia & Blaizot (2007)	$8.7 \cdot 10^{-4}$	1.45
Bower et al. (2006)	$14.8 \cdot 10^{-4}$	2.45
Bertone et al. (2007)	$9.0 \cdot 10^{-4}$	1.50

Table 3.1. Normalized cold gas densities at $z = 0$ of three different semi-analytic galaxy simulations applied to the Millennium Simulation of cosmic structure. The rightmost column shows the multiplicative offset from the observed value as determined by Obreschkow & Rawlings (2009c).

bilities. Nevertheless, the simulated cosmic space densities of stars in early-type and late-type galaxies at redshift $z = 0$ and the cosmic star formation history are consistent with observations (see figures and references in Croton et al., 2006). It is therefore probable that at least the more massive galaxies in the simulation are not significantly affected by the mass-resolution and the simplistic law for star formation.

In this paper, we post-process the DeLucia-catalog to estimate realistic HI- and H_2-properties for each galaxy. Our prescriptions will make use of the cold gas masses given for each galaxy in the DeLucia-catalog, and hence it is crucial to verify these cold gas masses against current observations. Based on a new estimation of the H_2-MF, we have recently calculated the normalized density of cold neutral gas in the local Universe as $\Omega_{\rm gas}^{\rm obs} = (4.4 \pm 0.8) \cdot 10^{-4}\ h^{-1}$, hence $\Omega_{\rm gas}^{\rm obs} \approx 6.0 \cdot 10^{-4}$ for $h = 0.73$ (Obreschkow & Rawlings, 2009c). This value was obtained by integrating the best fitting Schechter functions of the local HI-MF and H_2-MF and therefore it includes an extrapolation towards masses below the respective detection limits of HI and H_2. The simulated local cold gas density $\Omega_{\rm gas}^{\rm sim}$ of the DeLucia-catalog, obtained from the sum of the cold gas masses of all galaxies at redshift $z = 0$, exceeds the observed value by a factor $\zeta = \Omega_{\rm gas}^{\rm sim}/\Omega_{\rm gas}^{\rm obs} = 1.45$, as shown in Table 3.1. For comparison, this table also lists the cold gas densities of other galaxy catalogs produced for the Millennium Simulation, using different semi-analytic recipes (Bertone et al., 2007) and different schemes for the construction of dark matter merger trees (Bower et al., 2006).

There are plausible reasons for the excess of cold gas in the DeLucia-catalog compared to observations. Most importantly, the semi-analytic recipes only distinguish between two gas phases: the hot ($T \approx 10^6 - 10^7$ K) and ionized material located in the halo of the galaxy or group of galaxies, and the cold ($T \approx 10^2 - 10^3$ K) gas in galactic disks. However, recent observations have clearly revealed that some hydrogen in the disk of the Milky Way is warm ($T \approx 10^4$ K) and ionized, too. For example, Reynolds (2004) analyzed faint optical emission lines from hydrogen, helium, and trace atoms, leading to the conclusion that about 1/3 of all the hydrogen gas in the Local Interstellar Cloud (LIC) is ionized. If this were true for all the gas in disk galaxies, one would expect a correction factor around 1.5 between simulated disk gas and cold neutral gas. Justified by this considerations, we decided to divide all the cold gas masses in the DeLucia-catalog $M_{\rm gas}^{\rm DeLucia}$ by the constant $\zeta = 1.45$ in order to obtain more realistic estimates,

$$M_{\rm gas} \equiv \zeta^{-1} M_{\rm gas}^{\rm DeLucia}. \tag{3.1}$$

3.3 Gas masses and mass functions

In this section we establish a physical prescription to subdivide the cold and neutral hydrogen mass $M_{\rm H} = M_{\rm HI} + M_{\rm H_2}$ of a galaxy into its atomic (HI) and molecular (H_2) component based on the observed and theoretically confirmed relation between local gas pressure and local molecular fraction (Blitz & Rosolowsky, 2006, Elmegreen, 1993, Krumholz et al., 2009, Leroy et al., 2008). This prescription shall be applied to the DeLucia-catalog. The resulting simulated HI- and H_2-mass functions (MFs) and the related CO-luminosity function (LF) will be compared to observations in the local Universe.

3.3.1 Prescription for subdividing cold gas

Before addressing the sub-composition of cold hydrogen, we note that the total cold hydrogen mass $M_{\rm H}$ can be inferred from the total cold gas mass $M_{\rm gas}$ by a

constant factor $M_{\rm H} = 0.74\,M_{\rm gas}$, which corresponds to the universal abundance of hydrogen (e.g. Arnett, 1996) that changes insignificantly with cosmic time. The remaining gas is composed of helium (He) and a minor fraction of heavier elements, collectively referred to as metals (Z). The DeLucia-catalog gives an estimate for the metal mass in cold gas $M_{\rm Z}$, and hence we shall compute the masses of cold hydrogen and He as

$$\begin{aligned} M_{\rm H} &= (M_{\rm gas} - M_{\rm Z}) \cdot \beta, \\ M_{\rm He} &= (M_{\rm gas} - M_{\rm Z}) \cdot (1 - \beta), \end{aligned} \tag{3.2}$$

where the hydrogen fraction $\beta = 0.75$ is chosen slightly above 0.74 to account for the subtraction of the 1–2% metals in Eqs. (3.2).

The subdivision of the cold hydrogen mass $M_{\rm H} = M_{\rm HI} + M_{\rm H_2}$ depends on the galaxy and evolves with cosmic time. We shall tackle this complexity using the variable $\rm H_2$/HI-ratio $R_{\rm mol}^{\rm galaxy} \equiv M_{\rm H_2}/M_{\rm HI}$, hence

$$\begin{aligned} M_{\rm HI} &= M_{\rm H} \cdot (1 + R_{\rm mol}^{\rm galaxy})^{-1}, \\ M_{\rm H_2} &= M_{\rm H} \cdot (1 + R_{\rm mol}^{\rm galaxy\,-1})^{-1}. \end{aligned} \tag{3.3}$$

Detailed observations of HI and CO in nearby regular spiral galaxies revealed that virtually all cold gas of these galaxies resides in flat, often approximately axially symmetric, disks (e.g. Leroy et al., 2008, Walter et al., 2008). CO-maps recently obtained for five nearby elliptical galaxies (Young, 2002) show that even these galaxies, who carry most of their stars are in a spheroid, have most of their cold gas in a disk. There is also empirical evidence, that most cold gas in high-redshift galaxies resides in disks (e.g. Tacconi et al., 2006). Based on these findings, we assume that galaxies generally carry their cold atomic and molecular cold gas in flat disks with axially symmetric surface density profiles $\Sigma_{\rm HI}(r)$ and $\Sigma_{\rm H_2}(r)$, where r denotes the galactocentric radius in the plane of the disk. Using

these functions, $R_{\rm mol}^{\rm galaxy}$ can be expressed as

$$R_{\rm mol}^{\rm galaxy} = \frac{2\pi \int_0^\infty {\rm d}r\, r\, \Sigma_{\rm H_2}(r)}{2\pi \int_0^\infty {\rm d}r\, r\, \Sigma_{\rm HI}(r)}. \tag{3.4}$$

To solve Eq. (3.4), we shall now derive an analytic model for $\Sigma_{\rm HI}(r)$ and $\Sigma_{\rm H_2}(r)$. To this end, we analyzed the observed density profiles $\Sigma_{\rm HI}(r)$ and $\Sigma_{\rm H_2}(r)$ presented by Leroy et al. (2008) for 12 nearby spiral galaxies of The HI Nearby Galaxy Survey (THINGS)[1]. In general, the surface density of the total hydrogen component (HI+H_2) is well fitted by a single exponential profile,

$$\Sigma_{\rm HI}(r) + \Sigma_{\rm H_2}(r) = \tilde{\Sigma}_{\rm H} \exp(-r/r_{\rm disk}), \tag{3.5}$$

where $r_{\rm disk}$ is a scale length and $\tilde{\Sigma}_{\rm H} \equiv M_{\rm H}/(2\pi r_{\rm disk}^2)$ is a normalization factor, which can be interpreted the maximal surface density of the cold hydrogen disk.

Eq. (3.5) can be solved for $\Sigma_{\rm HI}(r)$ and $\Sigma_{\rm H_2}(r)$, if we know the local H_2/HI-ratio in the disk, i.e. the radial function $R_{\rm mol}(r) \equiv \Sigma_{\rm H_2}(r)/\Sigma_{\rm HI}(r)$. Following the theoretical prediction that $R_{\rm mol}(r)$ scales as some power of the gas pressure (Elmegreen, 1993), Blitz & Rosolowsky (2006) presented compelling observational evidence for this power-law based on 14 nearby spiral galaxies of various types. Perhaps the most complete empirical study of $R_{\rm mol}(r)$ today has recently been published by Leroy et al. (2008), who analyzed the correlations between $R_{\rm mol}(r)$ and various disk properties in 23 galaxies of the THINGS catalog. This study confirmed the power-law relation between $R_{\rm mol}(r)$ and pressure. On theoretical grounds, Krumholz et al. (2009) argued that $R_{\rm mol}(r)$ is most fundamentally driven by density rather than pressure. However, by virtue of the thermodynamic relation between pressure and density, it is, in the context of this paper, irrelevant which quantity is considered, and the density-law for $R_{\rm mol}(r)$ by Krumholz et al. (2009) is indeed consistent with the pressure-laws by Blitz & Rosolowsky (2006)

[1]In total Leroy et al. (2008) analyzed 23 galaxies. Here, we only use the 12 galaxies, for which radial density profiles are provided for both HI and H_2 (based on CO(2–1) or CO(1–0) measurements), and we subtract the Helium-fraction included by Leroy et al. (2008).

and Leroy et al. (2008). Here, we shall apply the pressure-law

$$R_{\rm mol}(r) = [P(r)/P_*]^{\alpha}, \tag{3.6}$$

where $P(r)$ is the kinematic midplane pressure outside molecular clouds, and $P_* = 2.35 \cdot 10^{-13}$ Pa and $\alpha = 0.8$ are empirical values adopted from Leroy et al. (2008).

Elmegreen (1989) showed that the equations of hydrostatic equilibrium for an infinite thin disk with gas and stars exhibit a simple approximate solution for the macroscopic kinematic midplane-pressure $P(r)$ of the ISM,

$$P(r) = \frac{\pi}{2}\, G\, \Sigma_{\rm gas}(r) \Big(\Sigma_{\rm gas}(r) + f_\sigma(r)\, \Sigma^{\rm disk}_{\rm stars}(r) \Big), \tag{3.7}$$

where G is the gravitational constant, $\Sigma_{\rm gas}(r)$ is the surface density of the total cold gas component (HI+H_2+He+metals), $\Sigma^{\rm disk}_{\rm stars}(r)$ is the surface density of stars in the disk (thus excluding the bulge stars of early-type spiral galaxies and elliptical galaxies), and $f_\sigma(r) \equiv \sigma_{\rm gas,z}/\sigma_{\rm stars,z}$ is the ratio between the vertical velocity dispersions of gas and stars. The impact of supernovae and other small-scale effects on the gas pressure are implicitly included in Eq. (3.7) via the velocity dispersion $\sigma_{\rm gas,z}$. For $\Sigma^{\rm disk}_{\rm stars} = 0$, Eq. (3.7) reduces to $P(r) = 0.5\, \pi\, G\, \Sigma_{\rm gas}(r)^2$, which is sometimes used as an approximation for the ISM pressure in gas-rich galaxies (e.g. Crosthwaite & Turner, 2007).

To simplify Eq. (3.7), we note that $\Sigma_{\rm gas}(r)$ can be expressed as $\Sigma_{\rm gas}(r) = M_{\rm gas}/(2\pi\, r^2_{\rm disk}) \exp(-r/r_{\rm disk})$, which is identical to Eq. (3.5) up to the constant factor correcting for helium and metals. To find a similar expression for $\Sigma^{\rm disk}_{\rm stars}(r)$, we analyzed the stellar surface densities $\Sigma_{\rm stars}(r)$ of the 12 THINGS galaxies mentioned before. In agreement with many other studies (e.g. Courteau et al., 1996), we found that $\Sigma_{\rm stars}(r)$ is generally well approximated by a double exponential profile, i.e. the sum of an exponential profile $\Sigma^{\rm bulge}_{\rm stars}$ for the bulge and an exponential profile $\Sigma^{\rm disk}_{\rm stars}$ for the disk. On average, the scale length of the stellar disk

$\tilde{r}_{\rm disk}$ is 30%–50% smaller than the gas scale length $r_{\rm disk}$, which traces the fact that stars form in the more central H_2-dominated parts of galaxies. Indeed, several observational studies revealed that the stellar scale length is nearly identical to that of molecular gas (e.g. Leroy et al., 2008, Regan et al., 2001, Young et al., 1995), and hence smaller than the scale length of HI or the scale length $r_{\rm disk}$ of the total cold gas component. For simplicity, we shall here assume $r_{\rm disk} = 2\,\tilde{r}_{\rm disk}$ for all galaxies, such that $\Sigma^{\rm disk}_{\rm stars}(r) = 4\,M_{\rm stars}/(2\pi\,r^2_{\rm disk})\exp(-2\,r/r_{\rm disk})$. Finally, we approximate the dispersion ratio $f_\sigma(r)$ as $f_\sigma(r) = f^0_\sigma\,\exp(r/r_{\rm disk})$, where f^0_σ is a constant. This approximation is motivated by empirical evidence that the gas dispersion $\sigma_{\rm gas,z}$ remains approximately constant across galactic discs (e.g. Boulanger & Viallefond, 1992, Dickey et al., 1990, Leroy et al., 2008), combined with theoretical and observational studies showing that the stellar velocity dispersion $\sigma_{\rm stars,z}$ decreases approximately exponentially with a scale length twice that of the stellar surface density (e.g. Bottema, 1993). Within those approximations Eq. (3.7) reduces to

$$P(r) \approx \frac{G\,M_{\rm gas}}{8\pi\,r^4_{\rm disk}}\left(M_{\rm gas}+f_\sigma M^{\rm disk}_{\rm stars}\right)\exp(-2\,r/r_{\rm disk}), \tag{3.8}$$

where $f_\sigma \equiv 4f^0_\sigma$ is a constant, which can be interpreted as the average value of $f_\sigma(r)$ weighted by the stellar surface density, since $\int 2\pi\,r\,\Sigma^{\rm disk}_{\rm stars}(r) f_\sigma(r)/M^{\rm disk}_{\rm stars} = 4f^0_\sigma$.

Substituting $P(r)$ in Eq. (3.6) for Eq. (3.8), we obtain

$$\frac{\Sigma_{\rm H_2}(r)}{\Sigma_{\rm HI}(r)} \equiv R_{\rm mol}(r) = R^{\rm c}_{\rm mol}\,\exp(-1.6\,r/r_{\rm disk}) \tag{3.9}$$

with

$$R^{\rm c}_{\rm mol} = \left[K\,r^{-4}_{\rm disk}\,M_{\rm gas}\left(M_{\rm gas} + f_\sigma\,M^{\rm disk}_{\rm stars}\right)\right]^{0.8}, \tag{3.10}$$

where $K \equiv G/(8\pi\,P_*) = 11.3\,{\rm m^4\,kg^{-2}}$. Eq. (3.9) reveals that the H_2/HI-ratio $R_{\rm mol}(r)$ is described by an exponential profile with scale length $r_{\rm disk}/1.6$. It should be emphasized that the central value $R^{\rm c}_{\rm mol}$ does not necessarily correspond to the

H_2/HI-ratio measured at the center of real galaxies due to an additional H_2-enrichment caused by the central stellar bulge. However, $R_{\rm mol}^{\rm c}$ represents the extrapolated cental H_2/HI-ratio of the exponential profile, which approximates $R_{\rm mol}(r)$ in the outer, disk-dominated galaxy parts.

We can now solve Eqs. (3.5, 3.9) for the atomic and molecular surface density profiles, i.e.

$$\Sigma_{\rm HI}(r) = \frac{\tilde{\Sigma}_{\rm H}\,\exp(-r/r_{\rm disk})}{1+R_{\rm mol}^{\rm c}\exp(-1.6\,r/r_{\rm disk})}\,, \tag{3.11}$$

$$\Sigma_{\rm H_2}(r) = \frac{\tilde{\Sigma}_{\rm H}\,R_{\rm mol}^{\rm c}\,\exp(-2.6\,r/r_{\rm disk})}{1+R_{\rm mol}^{\rm c}\exp(-1.6\,r/r_{\rm disk})}\,, \tag{3.12}$$

These model-profiles can be checked against the observed HI- and H_2-density profiles of the nearby galaxies analyzed by Leroy et al. (2008). In particular, we can test the limitations implied by our assumption that $r_{\rm disk} = 2\,\tilde{r}_{\rm disk}$. To this end, we selected two observed regular spiral galaxies with $r_{\rm disk} \approx 2\,\tilde{r}_{\rm disk}$ (NGC 3184) and $r_{\rm disk} \approx \tilde{r}_{\rm disk}$ (NGC 5505). To evaluate Eqs. (3.11, 3.12) for those galaxies, we require the quantities $M_{\rm stars}^{\rm disk}$, $M_{\rm gas}$, $r_{\rm disk}$, and f_σ. $M_{\rm stars}^{\rm disk}$, $M_{\rm gas}$, and $r_{\rm disk}$ were determined by fitting a single exponential profile to the total cold gas component and a double exponential profile (bulge and disk) to the stellar component, and f_σ was chosen as $f_\sigma = 0.4$, i.e. the value given by Elmegreen (1993) for nearby galaxies. As shown in Fig. 3.1, the resulting model-profiles $\Sigma_{\rm HI}(r)$ and $\Sigma_{\rm H_2}(r)$ approximately match the empirical data. The fact that the fit is rather good for both galaxies demonstrates that the quality of the model-predictions does not sensibly depend on the goodness of the model-assumption $r_{\rm disk} \approx 2\,\tilde{r}_{\rm disk}$. Similarly good fits are indeed found for most of the 12 THINGS-galaxies, for which Leroy et al. (2008) published radial HI- and H_2-density profiles.

Eqs. (3.11, 3.12) can be solved for the maximal surface densities of HI and H_2. $\Sigma_{\rm HI}(r)$ exhibits its maximum at the radius $r_{\rm HI}^{\rm max} = 0.625\,r_{\rm disk}\,\ln(3/5\cdot R_{\rm mol}^{\rm c})$, as long as $R_{\rm mol}^{\rm c} > 5/3$. Galaxies in this category show an HI-drop towards their center, such as observed in most galaxies in the THINGS catalog (Walter et al., 2008).

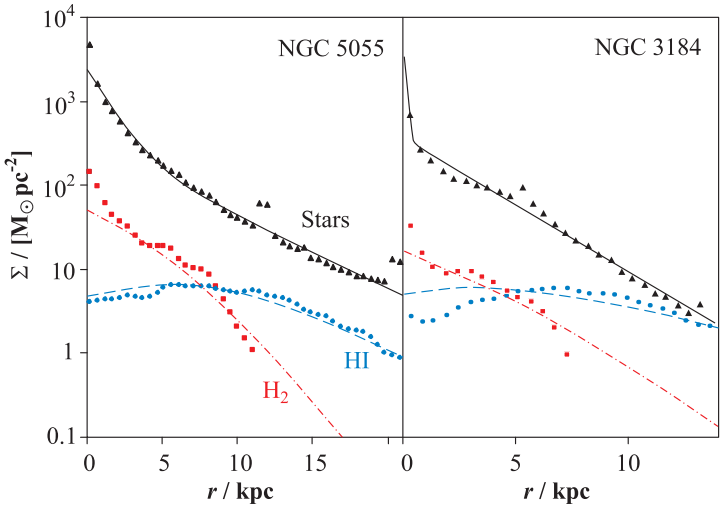

Figure 3.1. Column density profiles of two nearby spiral galaxies. Filled triangles, circles, and squares respectively represent the measured column density profiles of stars, HI, and H_2 (Leroy et al., 2008). Solid lines show the best-fitting double-exponential functions for the stellar densities. Dashed lines and dash-dotted lines represent the predictions of our pressure-based model given in Eqs. (3.11, 3.12).

By contrast, disk galaxies with $R_{\rm mol}^{\rm c} \leq 5/3$ have HI-density profiles peaking at the center, $r_{\rm HI}^{\rm max} = 0$. Galaxies with such small values of $R_{\rm mol}^{\rm c}$ have low gas densities by virtue of Eq. (3.10), such as the irregular galaxies NGC 4214 and NGC 3077 (see profiles in Leroy et al., 2008). $\Sigma_{\rm H_2}(r)$ given in Eq. (3.12) always peaks at the disk center, $r_{\rm H_2}^{\rm max} = 0$.

The maximal values of $\Sigma_{\rm HI}(r)$ and $\Sigma_{\rm H_2}(r)$, called $\Sigma_{\rm HI}^{\rm max} \equiv \Sigma_{\rm HI}(r_{\rm HI}^{\rm max})$ and $\Sigma_{\rm H_2}^{\rm max} \equiv \Sigma_{\rm H_2}(r_{\rm H_2}^{\rm max})$, can be computed as

$$\Sigma_{\rm HI}^{\rm max}/\tilde{\Sigma}_{\rm H} = \begin{cases} 1/(1+R_{\rm mol}^{\rm c}) & \text{if } {\rm R}_{\rm mol}^{\rm c} \leq 5/3 \\ 0.516\, {R_{\rm mol}^{\rm c}}^{-5/8} & \text{if } {\rm R}_{\rm mol}^{\rm c} > 5/3 \end{cases} \tag{3.13}$$

$$\Sigma_{\rm H_2}^{\rm max}/\tilde{\Sigma}_{\rm H} = R_{\rm mol}^{\rm c}/(1+R_{\rm mol}^{\rm c}). \tag{3.14}$$

The density profiles of Eqs. (3.11, 3.12) can be substituted into Eq. (3.4). The

exact solution of Eq. (3.4) is quite unhandy, but $R_{\rm mol}^{\rm galaxy}$ only depends on $R_{\rm mol}^{\rm c}$ and an excellent approximation, accurate to better than 5% over the nine orders of magnitude $R_{\rm mol}^{\rm c} = 10^{-3} - 10^{6}$ (covering the most extreme values at all redshifts), is given by

$$R_{\rm mol}^{\rm galaxy} = \left(3.44\, {R_{\rm mol}^{\rm c}}^{-0.506} + 4.82\, {R_{\rm mol}^{\rm c}}^{-1.054}\right)^{-1}. \tag{3.15}$$

Eqs. (3.10, 3.15) constitute a physical prescription to estimate the H_2/HI-ratio of any regular galaxy based on four global quantities: the disk stellar mass $M_{\rm stars}^{\rm disk}$, the cold gas mass $M_{\rm gas}$, the scale radius of the cold gas disk $r_{\rm disk}$, and the dispersion parameter f_σ. In Obreschkow & Rawlings (2009c), we showed that the H_2/HI-ratios inferred from this model are consistent with observations of nearby galaxies. Moreover, this model presumably extends to high redshifts, since it essentially relies on the fundamental relation between pressure and molecular fraction and on a few other physical assumptions with weak or absent dependence on cosmic epoch. However, a critical discussion of the limitations of this model is presented in Sections 3.6.2 and 3.6.3.

3.3.2 Application to the DeLucia-catalog

We applied the model given in Eqs. (3.10, 3.15) together with Eqs. (3.2, 3.3) to the DeLucia-catalog in order to assign HI-, H_2-, and He-masses to the simulated galaxies. The quantities $M_{\rm stars}^{\rm disk}$ and $M_{\rm Z}$ used in these Eqs. are directly contained in the DeLucia-catalog, and $M_{\rm gas}$ was inferred from the given cold gas masses via the correction of Eq. (3.1). The dispersion parameter f_σ is approximated by the constant $f_\sigma = 0.4$, consistent with the local observational data used by Elmegreen (1989) (but see discussion in Section 3.6.3).

The remaining and most subtle ingredient for our prescription of Eqs. (3.10, 3.15) is the scale radius $r_{\rm disk}$. This radius can be estimated from the virial radius $r_{\rm vir}$ of the parent halo, but their relation is intricate. Even modern N-body plus SPH simulations of galaxy formation cannot reproduce observed disk diameters (Kaufmann et al., 2007), and hence the more simplistic semi-analytic approaches

are likely to require some empirical adjustment. Mo et al. (1998) studied the case of a flat exponential disk in an isothermal singular halo. When assuming that the disk's mass can be neglected for its rotation curve, they find

$$r_{\rm disk} = \frac{\lambda \cdot \xi}{\sqrt{2}} r_{\rm vir}, \tag{3.16}$$

where λ is the spin parameter of the halo and ξ is the ratio between the specific angular momentum of the disk (angular momentum per unit mass) and the specific angular momentum of the halo. The model behind Eq. (3.16) does not distinguish between different scale radii for stars and cold gas, but it assumes a single exponential disk in hydrostatic equilibrium without including the effects of star formation. It is therefore natural to identify $r_{\rm disk}$ in Eq. (3.16) with the cold gas scale radius $r_{\rm disk}$ of Eqs. (3.10–3.12).

In the Millennium Simulation, $r_{\rm vir}$ was calculated from the virial mass $M_{\rm vir}$ using the relation

$$M_{\rm vir} = \frac{4\pi}{3} r_{\rm vir}^3 \cdot 200\ \rho_{\rm c}(z) \tag{3.17}$$

where $\rho_{\rm c}(z)$ is the critical density for closure $\rho_{\rm c}(z) = 3H^2(z)/(8\pi G)$ and $M_{\rm vir}$ the virial mass of the halo. For central haloes, $M_{\rm vir}$ was approximated as M_{200}, i.e. the mass in the region with an average density equal to 200 $\rho_{\rm c}(z)$; and for sub-haloes, $M_{\rm vir}$ was approximated as the total mass of the gravitationally bound simulation-particles.

The spin parameter λ was calculated directly from the N-body Millennium Simulation according to the definition $\lambda \equiv J_{\rm halo} {E_{\rm halo}}^{1/2} G^{-1} {M_{\rm halo}}^{-5/2}$, where $J_{\rm halo}$ denotes the angular momentum of the halo, $E_{\rm halo}$ its energy, and $M_{\rm halo}$ its total mass. For the satellite galaxies in the DeLucia-catalog, i.e. the ones without halo (see Section 3.2), the value of $\lambda \cdot r_{\rm vir}$ was approximated as the respective value of the original galaxy halo before its disappearance.

The only missing parameter for the calculation of $r_{\rm disk}$ via Eq. (3.16) is the angular momentum ratio ξ. It is of order unity for evolved disk-galaxies (e.g. Fall

& Efstathiou, 1980, Zavala et al., 2008), but its exact value is uncertain because of the difficulty of measuring the spin of dark matter haloes and convergence issues in numerical simulations. For example, Kaufmann et al. (2007) showed that N-body plus SPH simulations with as many as 10^6 particles per galaxy do not reach convergence in angular momentum, because of the difficulties to model the transport of angular momentum.

Here, we shall chose ξ, such that our simulation reproduces the empirical relation between the galaxy baryon mass $M_{\rm bary}$ and the stellar scale radius $\tilde{r}_{\rm disk} \approx r_{\rm disk}/2$, measured in the local Universe. To ensure consistency with Section 3.3.1, we use again the data from the THINGS-galaxies analyzed by (Leroy et al., 2008). Of the 23 galaxies in this sample, we reject the 6 irregular objects, since our model for HI and H_2 assumes regular galaxies. The remaining 17 galaxies cover all spiral types and include HI-rich and H_2-rich galaxies. For each galaxy, we adopted the stellar scale radii $\tilde{r}_{\rm disk}$ and baryon masses $M_{\rm bary} = M_{\rm stars} + M_{\rm HI} + M_{\rm H_2}$ directly from the data presented in (Leroy et al., 2008)[2]. The Hubble-types T, i.e. the numerical stage indexes along the revised Hubble sequence of the RC2 system (de Vaucouleurs et al., 1976), were drawn from the HyperLeda database (Paturel et al., 2003).

The resulting empirical relation between $M_{\rm bary}$ and $\tilde{r}_{\rm disk}$ is displayed in Fig. 3.2. The scatter of these data probably underestimates the true scatter caused by all galaxies, since we exclusively considered non-interacting regular spiral galaxies. The zero-point of the mean relation between $M_{\rm bary}$ and $\tilde{r}_{\rm disk}$ depends on the morphological galaxy type, as is revealed by the distinction of early-type and late-type spiral galaxies in Fig. 3.2. Given identical baryon masses, the stellar scale radii of early-type galaxies tend to be smaller than the radii of late-type galaxies. This trend was also detected in other data samples (e.g. data from Kregel et al., 2002 shown in Obreschkow & Rawlings, 2009c). Several reasons could ex-

[2]Stellar masses $M_{\rm stars}$ rely on 3.6 μm-maps (SINGS, Kennicutt et al., 2003); HI-masses use the 21 cm-maps from THINGS (Walter et al., 2008), H_2-masses rely on CO-maps (CO(2–1) from HERACLES, Leroy et al., 2008; CO(1–0) from BIMA SONG, Helfer et al., 2003).

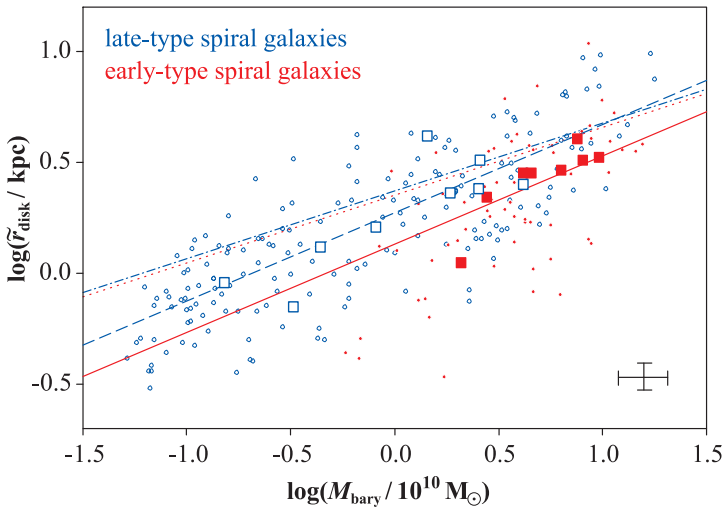

Figure 3.2. Relation between the baryon mass (stars+cold gas) and the stellar scale radius of disk galaxies. The filled and empty squares, respectively, represent observed early- and late-type spiral galaxies (Leroy et al., 2008). Typical 1-σ error bars are shown in the bottom right corner. The empirical fit given in Eq. (3.19) is represented by a solid line for early-type spiral galaxies ($T = 2$) and by a dashed line for late-type spiral galaxies ($T = 10$). The dotted and dash-dotted lines represent the respective relations of the simulated galaxies in the DeLucia-catalog, if $\xi = 1$. In order for the simulation to maximally align with the observations, ξ must be chosen according to Eq. (3.20). For the latter case, 10^2 random early- and late-type spiral galaxies of the DeLucia-catalog at $z = 0$ are represented by filled and empty dots, respectively.

plain this finding: (i) early-type galaxies have more massive stellar bulges, which present an additional central potential that contracts the disk; (ii) bulges often form from disk instabilities, occurring preferably in systems with relatively low angular momentum, and hence early-type galaxies are biased towards smaller angular momenta and smaller scale radii; (iii) larger bulges like those of lenticular and elliptical galaxies, often arise from galaxy mergers, which tend to reduce the specific angular momenta and scale radii.

To parameterize the dependence of the scale radius on the morphological galaxy type, the latter shall be quantified using the stellar mass fraction of the bulge, $\mathcal{B} \equiv M_{\rm stars}^{\rm bulge}/M_{\rm stars}$. In the observed sample, the values of $\mathcal{B}$ can be approximately inferred from the Hubble type T. Here we shall use the relation

$$\mathcal{B} = (10 - T)^2/256, \tag{3.18}$$

which approximately parameterizes the mean behavior of 146 moderately inclined barred and unbarred local spiral galaxies analyzed by Weinzirl et al. (2009). Eq. (3.18) satisfies the boundary conditions $\mathcal{B} = 1$ for $T = -6$ (i.e. pure spheriods) and $\mathcal{B} = 0$ for $T = 10$ (pure disks).

We shall approximate the relation between $M_{\rm bary}$ and $\tilde{r}_{\rm disk}$ as a power-law with an additional term for the observed secondary dependence on morphological type,

$$\log\left(\frac{\tilde{r}_{\rm disk}}{\rm kpc}\right) = a_0 + a_1 \log\left(\frac{M_{\rm bary}}{10^{10}{\rm M}_\odot}\right) + a_2\,\mathcal{B}, \tag{3.19}$$

where a_0, a_1, and a_2 are free parameters. The best fit to the empirical data in terms of a maximum-likelihood approach is given by the choice $a_0 = 0.3$, $a_1 = 0.4$, $a_2 = -0.6$.

The fit of Eq. (3.19) is displayed in Fig. 3.2 for early-type spiral galaxies ($T = 2 \leftrightarrow \mathcal{B} = 0.25$, solid line) and for late-type spiral galaxies ($T = 10 \leftrightarrow \mathcal{B} = 0$, dashed line). For comparison, the mean power-law relations for the early- and late-type spiral galaxies in the DeLucia-catalog at $z = 0$ are displayed as dotted and dash-dotted lines for the choice $\xi = 1$. The simulated scale radii using $\xi = 1$ are consistent with the observed ones for very massive galaxies ($M_{\rm bary} \approx 10^{11}\,{\rm M}_\odot$), but less massive galaxies in the simulation turn out slightly too large if $\xi = 1$. Furthermore, the morphological dependence of the simulation is too small compared to the observations. This can be corrected ad hoc by

introducing a variable ξ that depends on both $M_{\rm bary}$ and $\mathcal{B}$, i.e.

$$\log(\xi) = b_0 + b_1 \log\left(\frac{M_{\rm bary}}{10^{10}{\rm M}_\odot}\right) + b_2\,\mathcal{B}, \tag{3.20}$$

where b_0, b_1, and b_2 are free parameters. The parameters minimizing the rms-deviation between the simulated galaxies and the empirical model of Eq. (3.19) are $b_0 = -0.1$, $b_1 = 0.3$, $b_2 = -0.6$. In addition, we chose a lower limit for ξ equal to 0.5, in order to prevent unrealistically small scale radii.

We emphasize that Eq. (3.20) is merely an empirical correction; this choice of ξ should not be considered as an estimate of the true ratio between the specific angular momenta of the disk and the halo, but it also accounts for the imperfection of the simplistic halo model by Mo et al. (1998), for missing physics in the semi-analytic modeling, and for possible systematic errors in the spin parameters λ of the Millennium Simulation. The average value of Eq. (3.20) over all galaxies in the DeLucia-catalog is $\langle\xi\rangle = 0.7$ (with $\sigma = 0.2$), which is approximately consistent with $\xi \approx 1$ of modern high-resolution simulations of galaxy formation (e.g. Zavala et al., 2008), even though the latter still suffer from issues with the transport of angular momentum as mentioned above.

Using Eqs. (3.16, 3.20) we estimated a scale radius $r_{\rm disk}$ for each galaxy in the DeLucia-catalog. A sample of 10^2 simulated early- and late-type spiral galaxies at $z = 0$ is shown in Fig. 3.2. Given $r_{\rm disk}$ as well as $M_{\rm stars}$, $M_{\rm gas}$, and $f_\sigma = 0.4$, we then applied Eqs. (3.2, 3.3, 3.10, 3.15) in order to subdivide the non-metallic cold gas mass ($M_{\rm gas} - M_{\rm Z}$) of each galaxy into HI, H_2, and He.

3.3.3 Atomic and molecular mass functions

We shall now compare the HI- and H_2-masses predicted by our model of Sections 3.3.1 and 3.3.2 to recent observations in the local Universe. From the viewpoint of the simulation, a fundamental output are the mass functions (MFs) of HI and H_2, while the available observational counterparts are the luminosity functions (LFs) of the HI-emission line (Zwaan et al., 2005a) and the CO(1–0)-emission line

(Keres et al., 2003). Therefore, either the simulated data or the observed data need a luminosity-to-mass (or vice versa) conversion to compare the two. Section 3.3.3 focuses on the MFs, adopting the standard luminosity-to-mass conversion for HI used by Zwaan et al. (2005a) and the CO-luminosity-to-H_2-mass conversion of Obreschkow & Rawlings (2009c). As a complementary approach, Section 3.3.4 will focus on the LFs, which will require a model for the conversion of simulated H_2-masses into CO-luminosities.

We define the MFs as $\phi_{\rm x}(M_{\rm x}) \equiv {\rm d}\rho_{\rm x}/{\rm d}\log M_{\rm x}$, where $\rho_{\rm x}(M_{\rm x})$ is the space density (number per comoving volume) of galaxies containing a mass $M_{\rm x}$ of the constituent x (HI, H_2, He, etc.). Given a mass, such as $M_{\rm HI}$, for each galaxy in the DeLucia-catalog, the derivation of the corresponding MF only requires the counting of the number of sources per mass interval. We chose 60 mass intervals, logarithmically spaced between $10^8\,{\rm M}_\odot$ and $10^{11}\,{\rm M}_\odot$, giving about $\sim 10^6$ galaxies per mass interval in the central mass range, while keeping the mass error relatively small ($\Delta\log(M) < 0.05$). Since MFs combine units of mass and length, they generally depend on the Hubble constant H_0, or the dimensionless Hubble parameter h, defined as $H_0 = 100\,h\,{\rm km\,s^{-1}\,Mpc^{-1}}$. Although MFs are often plotted in units making no assumption on h (e.g. ${\rm M}_\odot\,h^{-2}$ for the mass scale), this is impossible when observations are compared to cosmological simulations. The reason is that simulated masses in the Millennium Simulation scale to first order as h^{-1}, whereas empirical masses, when determined from electromagnetic fluxes, are proportional to the square of the distance and hence scale as h^{-2}. For all plots in this paper we shall therefore use $h = 0.73$, which corresponds to the value adopted by the Millennium Simulation (see Section 3.2).

Fig. 3.3 displays the HI- and H_2-MF of our simulation (solid lines), as well as the corresponding empirical MFs for the local Universe (points with error bars). The empirical HI-MF was obtained by Zwaan et al. (2005a) based on 4315 galaxies of the HI-Parkes All Sky Survey (HIPASS) and the empirical H_2-MF was derived in Obreschkow & Rawlings (2009c) from the CO-luminosity function

(LF) presented by Keres et al. (2003). Both empirical MFs approximately match the simulated data. We note, however, that the consistency between observation and simulation decreases if we skip the overall correction of the cold gas masses in the DeLucia-catalog by the constant factor ζ (dotted lines), which, as argued in Section 3.2 can be justified by a fraction of the disk gas being electronically excited or ionized.

Our simulation slightly over-predicts the observed number of the largest HI- and H_2-masses, i.e. the ones in the exponential tail of the MFs in Fig. 3.3. These tails contain the most massive systems, whose emergent luminosities are most likely to be biased by opacity and thermal effects. Including these effects would probably correct the space density of massive systems towards the simulated MFs. Additionally, we note that the presented empirical MFs neglect mass measurement errors, which might have an important effect on the slope of the exponential tails. Another difference between observations and simulation are the spurious bumps in the low mass range of the simulated MFs, i.e. $\log(M_{\rm HI}) \approx 8.5$ and $\log(M_{\rm H_2}) \approx 8.0$, where the number density is about doubled compared to observations. This feature can also be seen in the optical b_J-band LF shown by Croton et al. (2006) and stems from an imprecision in the number density of the smallest galaxies in the DeLucia-catalog, where the mass-resolution of the Millennium Simulation implies a poorly resolved merger history. The over-density of sources around this resolution limit roughly balances the mass of even smaller galaxies, i.e. $\log(M_{\rm HI}/{\rm M}_\odot) \ll 8.0$, that are missing in the simulation.

The universal gas densities of the simulation, expressed relative to the critical density for closure, are $\Omega_{\rm HI}^{\rm sim} = 3.4 \cdot 10^{-4}$ and $\Omega_{\rm H_2}^{\rm sim} = 1.1 \cdot 10^{-4}$, in good agreement with the observations $\Omega_{\rm HI}^{\rm obs} = (3.6 \pm 0.4) \cdot 10^{-4}$ (Zwaan et al., 2005a) and $\Omega_{\rm H_2}^{\rm obs} = (0.95 \pm 0.37) \cdot 10^{-4}$ (Obreschkow & Rawlings, 2009c).

Fig. 3.4 shows our simulated HI-MF and H_2-MF together with the MF for the cold gas metals given in the original DeLucia-catalog and the MF for He as trivially derived using Eq. (3.2). This picture reveals that in the cold gas of the

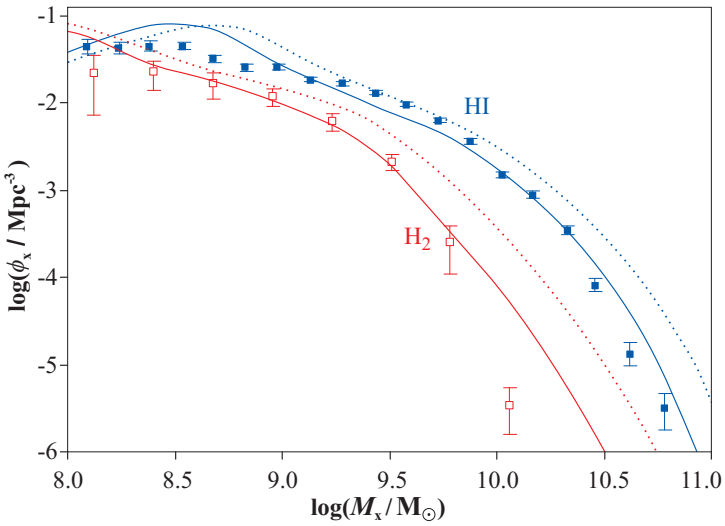

Figure 3.3. Simulated galaxy MFs for HI and H_2 with (solid lines) and without (dotted lines) the constant correction for all cold gas masses given in Eq. (3.1). Filled and open squares with error bars represent the corresponding empirical MFs from Zwaan et al. (2005a) and Obreschkow & Rawlings (2009c).

local Universe He is probably more abundant than H_2, but less abundant than HI.

We shall now consider the HI-masses in elliptical and spiral galaxies separately. This division is based on the Hubble type T, where we consider galaxies with $T < 0$ as "ellipticals" and galaxies with $T \geq 0$ as "spirals" – a rough separation that neglects other types like irregular galaxies as well as various subclassifications. In the simulation, T is computed from the bulge mass fraction according to Eq. (3.18).

The simulated HI-MFs of both elliptical and spiral galaxies are shown in Fig. 3.5. In order to determine the observational counterparts, we split the HIPASS galaxy sample into elliptical and spiral galaxies according to the Hubble types provided in the HyperLeda reference database (Paturel et al., 2003). For both subsamples, the HI-MF was evaluated using the $1/V_{\rm max}$ method (Schmidt, 1968), where $V_{\rm max}$ was estimated from the analytic completeness function for

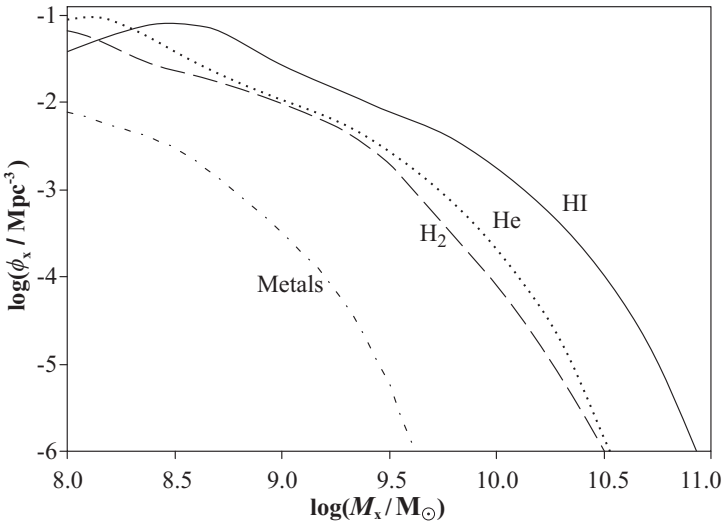

Figure 3.4. Simulated galaxy MFs for HI (solid line), H_2 (dashed line), cold He (dotted line), and cold gas metals (dash-dotted line). The HI-MF and H_2-MF are identical to the solid lines in Fig. 3.3.

HIPASS, which characterizes the completeness of each source given its HI-peak flux density S_p and integrated HI-line flux S_int (Zwaan et al., 2004). In order to estimate the uncertainties of the MFs, we derived them for 10^4 random half-sized subsets of the HIPASS sample – a bootstrapping approach. The standard deviation of the 10^4 values of $\log(\phi_\mathrm{HI})$ for each mass bin was divided by $\sqrt{2}$ to estimate the 1-σ errors of $\log(\phi_\mathrm{HI})$ for the full sample.

Fig. 3.5 demonstrates that our simulation successfully reproduces the HI-masses of both spiral and elliptical galaxies for HI-masses greater than $\sim 10^9\,\mathrm{M}_\odot$, although the nearly perfect match between simulation and observation may be somewhat coincidental due to the uncertainties of the Hubble types T calculated via Eq. (3.18). For HI-masses smaller than $10^9\,\mathrm{M}_\odot$, the morphological separation seems to breakdown (shaded zone in Fig. 3.5). Indeed the HI-mass range $M_\mathrm{HI} \lesssim 10^9\,\mathrm{M}_\odot$ approximately corresponds to the stellar mass range $M_\mathrm{stars} \lesssim 4 \cdot 10^9\,\mathrm{M}_\odot$, for which morphology properties are poorly resolved (see Section 3.2).

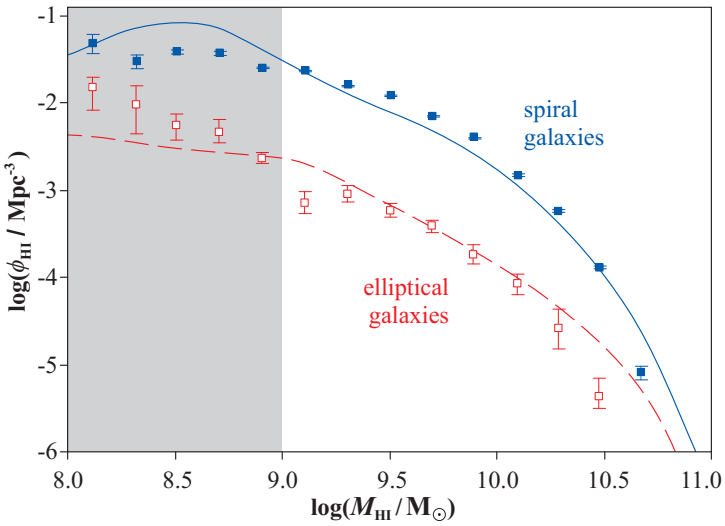

Figure 3.5. HI-MFs for elliptical and spiral galaxies. The solid line and dashed line respectively represent the simulated result, where the galaxies have been divided in ellipticals and spirals according to their Hubble type estimated using Eq. (3.18). Filled and open dots with error bars represent the corresponding empirical HI-MFs, which we derived from the HIPASS sample. The shaded zone represents the HI-mass range $M_{\rm HI} \lesssim 10^9\,{\rm M}_\odot$, approximately corresponding to the simulated galaxies with poorly resolved morphologies.

3.3.4 Observable HI- and CO-luminosities

The characteristic radio line of HI stems from the hyperfine energy level splitting of the hydrogen atom and lies at 1.42 GHz rest-frame frequency. The velocity-integrated luminosity of this line $L_{\rm HI}$ can be calculated from the HI-mass via

$$\frac{M_{\rm HI}}{{\rm M}_\odot} = 1.88 \cdot 10^4 \cdot \frac{L_{\rm HI}}{{\rm Jy\,km\,s^{-1}\,Mpc^2}}. \qquad (3.21)$$

Eq. (3.21) neglects HI-self absorption effects, but this is likely to be a problem only for the largest disk galaxies observed edge-on (Rao et al., 1995). The strict proportionality between $L_{\rm HI}$ and $M_{\rm HI}$ assumed in Eq. (3.21) means that the HI-LF is geometrically identical to the HI-MF.

By contrast, the H_2-masses used for the empirical H_2-MFs in Figs. 3.3 and 3.4 rely on measurements of the CO(1–0)-line, i.e. the 115 GHz radio line stemming from the fundamental rotational relaxation of the most abundant CO-isotopomer $^{12}C^{16}O$. Here we only consider this line, but luminosities of other CO-lines can be estimated using approximate empirical line ratios (e.g. Braine et al., 1993, Righi et al., 2008).

The CO(1–0)-to-H_2 conversion generally depends on the galaxy and the cosmic epoch, and it is often represented by the dimensionless factor

$$X \equiv \frac{N_{\rm H_2}/{\rm cm}^{-2}}{I_{\rm CO}/({\rm K\,km\,s}^{-1})} \cdot 10^{-20}, \tag{3.22}$$

where $N_{\rm H_2}$ is the column density of H_2-molecules and $I_{\rm CO}$ is the integrated CO(1–0)-line intensity per unit surface area defined via the surface brightness temperature in the Rayleigh-Jeans approximation. The definition of Eq. (3.22) implies the mass–luminosity relation (e.g. review by Young & Scoville, 1991)

$$\frac{M_{\rm H_2}}{{\rm M}_\odot} = 313 \cdot X \cdot \frac{L_{\rm CO}}{{\rm Jy\,km\,s}^{-1}\,{\rm Mpc}^2}, \tag{3.23}$$

where $L_{\rm CO}$ is the velocity-integrated luminosity of the CO(1–0) line.

As discussed in Obreschkow & Rawlings (2009c), the theoretical and observational determination of the X-factor is a subtle task with a long history. Most present-day studies assume a constant X-factor $X_{\rm c}$, such as

$$X_{\rm c} = 2, \tag{3.24}$$

which is typical for spiral galaxies in the local Universe (Leroy et al., 2008). By contrast, Arimoto et al. (1996) and Boselli et al. (2002) suggested that X is variable, $X_{\rm v}$, and approximately inversely proportional to the metallicity O/H, i.e. the ratio between the number of oxygen ions and hydrogen ions in the hot

ISM. Using their data, we found that (Obreschkow & Rawlings, 2009c)

$$\log(X_{\rm v}) = (-2.9 \pm 0.2) - (1.02 \pm 0.05) \log(O/H). \tag{3.25}$$

At first sight, the empirical negative dependence of X on the metallicity seems to contradict the fact that $^{12}C^{16}O$ is optically thick for 115 GHz radiation. Indeed, the radiated luminosity should not depend on the density of metals, as long as the latter is high enough for the radiation to remain optically thick (Kutner & Leung, 1985). However, detailed theoretical investigations (e.g. Maloney & Black, 1988) of the sizes and temperatures of molecular clumps were indeed able to explain, and in fact predict, the negative dependence of X on metallicity.

Eq. (3.25) links the metallicity of the hot ISM to the X-factor of cold molecular clouds, and it is likely a consequence of a more fundamental relation between cold gas metallicity and X. To uncover such a relation, we assume that the O/H metallicity of the cold ISM in local galaxies is approximated by O/H of the hot ISM. Given an atomic mass of 16 for Oxygen, the fact that hydrogen makes up a fraction 0.74 of the total baryon mass, and assuming that Oxygen accounts for a fraction of 0.4 of the mass of all metals (based on Arnett, 1996, Kobulnicky & Zaritsky, 1999), Eq. (3.25) translates to

$$X_{\rm v} \approx 0.04\, M_{\rm gas}/M_{\rm Z}, \tag{3.26}$$

where $M_{\rm gas}$ is the total cold gas mass and $M_{\rm Z}$ is the mass of metals in cold gas. Eq. (3.26) only relates cold gas properties to each other and therefore is more fundamental than Eq. (3.25).

To evaluate Eq. (3.26) for each galaxy in the simulation, we used the cold gas metal masses $M_{\rm Z}$ given in the DeLucia-catalog. Those masses are reasonably accurate as demonstrated by De Lucia et al. (2004) and Croton et al. (2006) through a comparison of the simulated stellar mass–metallicity relation to the empirical mass–metallicity relation obtained from 53,000 star forming galaxies in

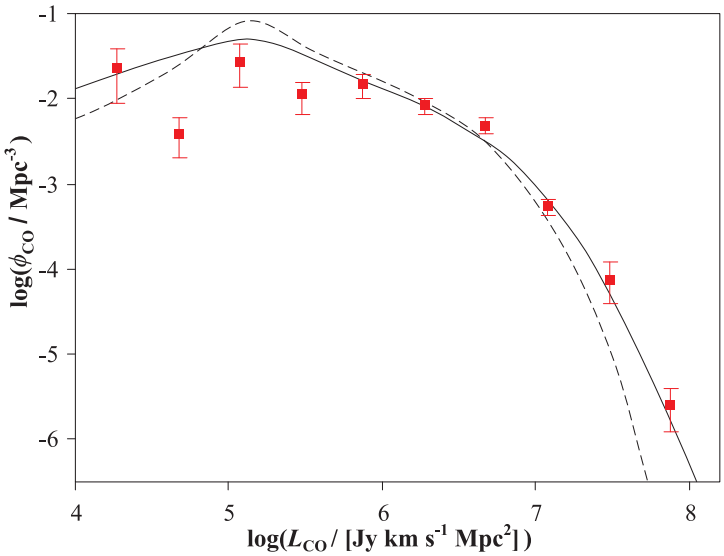

Figure 3.6. Luminosity function of CO(1–0)-emission (CO-LF) in the local Universe. The solid line represents the simulated CO-LF, obtained using the variable conversion factor $X_{\rm v}$ of Eq. (3.26), and the dashed line represents the CO-LF, obtained using the constant conversion factor $X_{\rm c}$ of Eq. (3.24). Square dots and error bars represent the empirical CO-LF determined by Keres et al. (2003).

the Sloan Digital Sky Survey (Tremonti et al., 2004). For most galaxies at $z = 0$ the simulation yields metal fractions $M_{\rm Z}/M_{\rm gas} \approx 0.01 - 0.04$ in the local Universe, thus implying $X_{\rm v} \approx 1 - 4$ in agreement with observed values (e.g. Boselli et al., 2002).

Fig. 3.6 displays the simulated CO-LF for the variable X-factor $X_{\rm v}$ (solid line) and the constant X-factor $X_{\rm c}$ (dashed line) together with the empirical CO-LF (Keres et al., 2003), adjusted to $h = 0.73$. The comparison supports the variable X-factor of Eq. (3.26) against $X_{\rm c} = 2$ (and the same conclusion is found for other constant values of $X_{\rm c}$). Using Eq. (3.26) also has the advantage that the cosmic evolution of the X-factor due to the evolution of metallicity is implicitly accounted for. Nevertheless Eq. (3.26) may not be appropriate at high redshift as discussed in Section 3.6.3.

3.4 Cold gas disk sizes

Using the axially symmetric surface density profiles for HI and H_2 given in Eqs. (3.11, 3.12), we can define the HI-radius $r_{\rm HI}$ and H_2-radius $r_{\rm H_2}$ of an axially symmetric galaxy as the radii corresponding to a detection limit Σ_0, i.e.

$$\Sigma_{\rm HI}(r_{\rm HI}) \equiv \Sigma_0\,, \tag{3.27}$$

$$\Sigma_{\rm H_2}(r_{\rm H_2}) \equiv \Sigma_0\,. \tag{3.28}$$

In this paper, we chose $\Sigma_0 = 1\,{\rm M_\odot pc^{-2}}$, corresponding to the deep survey of the Ursa Major group by Verheijen (e.g. 2001), but any other value could be adopted. In general Eqs. (3.27, 3.28) do not have explicit closed-form solutions and must be solved numerically for each galaxy.

Results for $r_{\rm HI}$ and $r_{\rm H_2}$ at three epochs are displayed in Fig. 3.7. Each graph shows 10^3 simulated galaxies, drawn randomly from the catalog with a probability proportional to their cold gas mass. This selection rule ensures that rare objects at the high end of the MF are included. The arithmetic average of the points in each graph can be interpreted as the cold gas mass-weighted average of the displayed quantities. This average is marked in each graph to emphasize changes with redshift. The data in Fig. 3.7a are shown again in Fig. 3.8 together with measurements of 39 spiral galaxies in the Ursa Major group (Verheijen, 2001).

Figs. 3.7 and 3.8 reveal several features, which we shall discuss hereafter: (i) the mass–radius relation for HI is a nearly perfect power-law with surprisingly small scatter; (ii) in general, radii become smaller with increasing redshift; (iii) the evolution of the mass–radius relation is completely different for HI and H_2.

The first result, i.e. the strict power-law relation between $M_{\rm HI}$ and $r_{\rm HI}$, is strongly supported by measurements in the Ursa Major group (Verheijen, 2001, see Fig. 3.8). The best power-law fit to the simulation is

$$\frac{M_{\rm HI}}{\rm M_\odot} = 12 \cdot \left(\frac{r_{\rm HI}}{\rm pc}\right)^{2.0}. \tag{3.29}$$

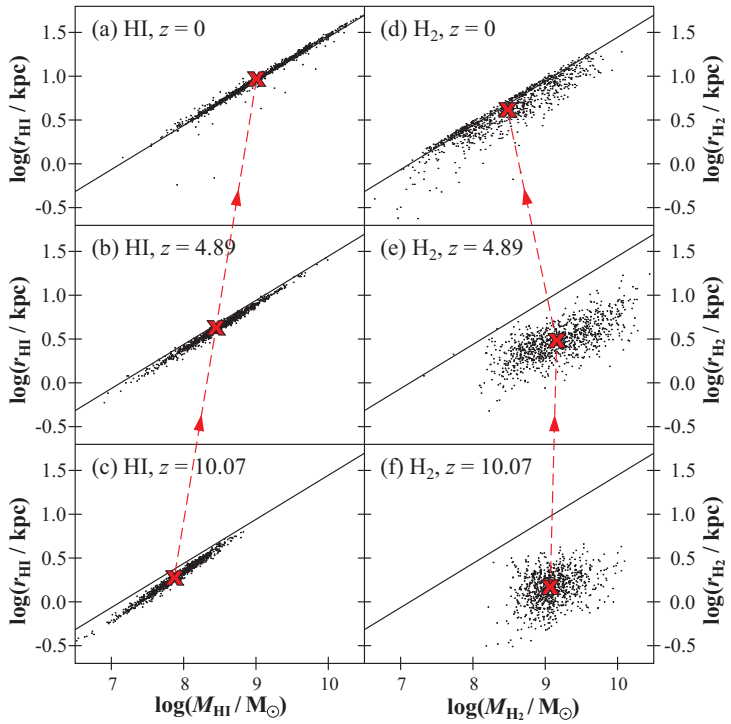

Figure 3.7. Simulated mass–radius relations for HI and H_2 at redshifts $z = 0, 4.89, 10.07$, corresponding to the simulation snapshots 63, 21, 12. Black dots represent 10^3 simulated galaxies and the solid lines show the power-law regression for the data in Fig. 3.7a (i.e. HI at $z = 0$). The red crosses represent the cold gas mass-weighted averages of ($M_{\rm HI}$,$r_{\rm HI}$) and ($M_{\rm H_2}$,$r_{\rm H_2}$) in the simulation at each of the three redshifts.

The rms-scatter of the simulated data around Eq. (3.29) is $\sigma = 0.03$ in log-space, while the rms-scatter of the observations by Verheijen (2001) is $\sigma = 0.06$. This small scatter is particularly surprising as the more fundamental relation between $M_{\rm bary}$ and $\tilde{r}_{\rm disk}$ shown in Fig. 3.2 exhibits a much larger scatter of $\sigma = 0.26$. The square-law form of the power-law in Eq. (3.29) implies that the average HI-surface density inside the radius $r_{\rm HI}$ is nearly identical for all galaxies, which have most of their HI-mass inside the radius $r_{\rm HI}$,

$$\langle \Sigma_{\rm HI} \rangle_{r \leq r_{\rm HI}} \approx \frac{M_{\rm HI}}{r_{\rm HI}^2 \pi} \approx 3.8\,{\rm M}_\odot\ {\rm pc}^{-2}. \tag{3.30}$$

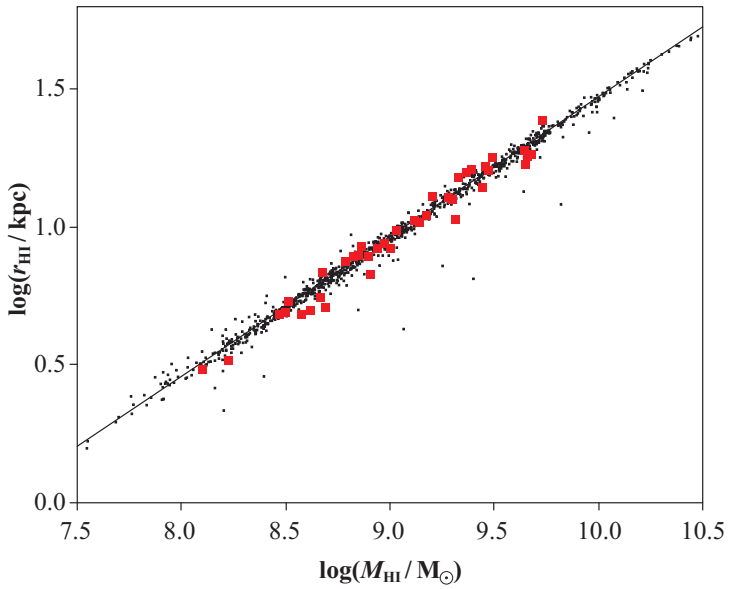

Figure 3.8. Relation between HI-mass $M_{\rm HI}$ and HI-radius $r_{\rm HI}$ for galaxies at redshift $z = 0$. The black dots represent 10^3 simulated galaxies and the solid line their linear regression. The slope of this power-law is 0.5, thus indicating a universal average HI-surface density for all disk galaxies. The simulated data are identical to those plotted in Fig. 3.7a. Red squares show measurements in the Ursa Major group by Verheijen (2001), who used the same definition of $r_{\rm HI}$ as this paper.

The existence of such a constant average density of HI can to first order be interpreted as a consequence of the fact that HI transforms into H_2 and stars as soon as its density and pressure are raised. In fact, observations show that $\Sigma_{\rm HI}$ saturates at about $6-10\,{\rm M}_\odot\ {\rm pc}^{-2}$ (Blitz & Rosolowsky, 2006, Leroy et al., 2008) and that higher cold gas densities are generally dominated by $\Sigma_{\rm H_2}$. Therefore, HI maintains a constant surface density during the evolution of any isolated galaxy as long as enough HI is supplied from an external source, e.g. by cooling from a hot medium as assumed in the recipes of the DeLucia-catalog. This also explains why the power-law relation between $M_{\rm HI}$ and $r_{\rm HI}$ remains nearly constant towards higher redshift in the simulation (Fig. 3.7a–c). About 1% of the simulated galaxies at redshift $z = 0$ lie far off the power-law relation (i.e. are

outside 5-σ of the best fit), typically towards smaller radii (see Fig. 3.8). One might first expect that these objects have a higher HI-surface density, while, in fact, the contrary applies. These galaxies have very flat HI-profiles with most of the HI-mass lying outside the radius $r_{\rm HI}$, and therefore they would require a lower sensitivity limit than $1\,{\rm M}_\odot\ {\rm pc}^{-2}$ for a useful definition of $r_{\rm HI}$. Such galaxies are indeed very difficult to map due to observational surface brightness limitations.

The radii $r_{\rm HI}$ and $r_{\rm H_2}$ become smaller towards higher redshift. This is a direct consequence of the cosmic evolution of the virial radii $r_{\rm vir}$ of the haloes in the Millennium Simulation, which affects the disk scale radius $\tilde{r}_{\rm disk}$ in Eq. (3.16). As shown by Mo et al. (1998), $r_{\rm vir}$ scales as $(1+z)^{-1.5}$ for a fixed circular velocity or as $(1+z)^{-1}$ for a fixed halo mass, consistent with high-redshift observations ($z = 2.5-6$) in the Hubble Ultra Deep Field (UDF) by Bouwens et al. (2004). Their selection criteria include all but the reddest starburst galaxies in the UDF and some evolved galaxies. It should be emphasized that the phenomenological size evolution of galaxies is not properly understood, and even modern N-body/SPH-simulation cannot yet accurately reproduce the sizes of galaxies.

In analogy to the mass–radius power-law relation for HI, our simulation predicts a similar relation, again nearly a square-law, for H_2 at redshift $z = 0$ (see Fig. 3.7d). This power-law is consistent with observations of the two face-on spiral galaxies M 51 (Schuster et al., 2007) and NGC 6946 (Crosthwaite & Turner, 2007). For the small H_2/HI-ratios found in the local Universe the $M_{\rm H_2}$–$r_{\rm H_2}$ relation is linked to the $M_{\rm HI}$–$r_{\rm HI}$ relation, because both $M_{\rm H_2}$ and $r_{\rm H_2}$ can be regarded as a fraction (< 1) of, respectively, $M_{\rm HI}$ and $r_{\rm HI}$. However, there is no fundamental reason for a constant surface density of H_2 and the smaller sizes of high-redshift galaxies implies a higher pressure of the ISM and thus a much higher molecular fraction by virtue of Eqs. (3.10, 3.15). Therefore, H_2-masses become uncorrelated to HI and tend to increase with redshift out to $z \approx 5$, while $r_{\rm H_2}$ decreases. Hence, the $M_{\rm H_2}$–$r_{\rm H_2}$ relation must move away from the power-law $M_{\rm H_2} \sim r_{\rm H_2}^2$ found at $z = 0$ (see Figs. 3.7d–f).

3.5 Realistic velocity profiles

In this section we derive circular velocity profiles and atomic and molecular-radio line profiles for the simulated galaxies in the DeLucia-catalog. Circular velocity profiles $V_c(r)$ for various galaxies are derived over the Sections 3.5.1–3.5.3 and transcribed to radio line profiles for edge-on galaxies in Section 3.5.4. Results for the local and high-redshift Universe are presented in Section 3.5.5.

3.5.1 Velocity profile of a spherical halo

To account for the narrowness of the emission lines observed in the central gas regions of many galaxies (e.g. Sauty et al., 2003), we require a halo model with vanishing velocity at the center, as opposed to, for example, the commonly adopted singular isothermal sphere with a density $\rho_{\rm halo}(r) \sim r^{-2}$ and a constant velocity profile. We chose the Navarro–Frenk–White (NFW, Navarro et al., 1995, 1996) model, which relies on high resolution numerical simulations of dark matter haloes in equilibrium. These simulations revealed that haloes of all masses in a variety of dissipation-less hierarchical clustering models are well described by the spherical density profile

$$\rho_{\rm halo}(r) = \rho_0 \left[(r/r_{\rm s})(1 + r/r_{\rm s})^2 \right]^{-1}, \tag{3.31}$$

where ρ_0 is a normalization factor and $r_{\rm s}$ is the characteristic scale radius of the halo. This profile is also supported by the Hubble Space Telescope analysis of the weak lensing induced by the galaxy cluster MS 2053-04 at redshift $z = 0.58$ (Hoekstra et al., 2002). $\rho_{\rm halo}(r)$ varies as r^{-1} at the halo center and continuously steepens to r^{-3} for $r \to \infty$. It passes through the equilibrium profile of the self-gravitating isothermal sphere, i.e. $\rho_{\rm halo}(r) \sim r^{-2}$, at $r = r_{\rm s}$.

The definition of $r_{\rm vir}$ in the Millennium Simulation given in Eq. (3.17) implies that

$$\rho_0 = \frac{200}{3} \frac{\rho_{\rm c}\, c_{\rm halo}^3}{\ln(1 + c_{\rm halo}) - c_{\rm halo}/(1 + c_{\rm halo})}, \tag{3.32}$$

where $c_{\rm halo} \equiv r_{\rm vir}/r_{\rm s}$ is referred to as the halo concentration parameter. Most

numerical models predict that $c_{\rm halo}$ scales with the virial mass $M_{\rm vir}$, defined as the mass inside the radius $r_{\rm vir}$, according to a power-law (e.g. Bullock et al., 2001, Dolag et al., 2004, Hennawi et al., 2007, Navarro et al., 1997). Here we shall use the result of Hennawi et al. (2007),

$$c_{\rm halo} = \frac{12.3}{1+z} \left(\frac{M_{\rm vir}}{1.3 \cdot 10^{13}\, h^{-1} {\rm M}_\odot} \right)^{-0.13}, \tag{3.33}$$

which is consistent with recent empirical values of the matter concentration in galaxy clusters derived from X-ray measurements and strong lensing data (Comerford & Natarajan, 2007).

For a spherical halo, the circular velocity profile is given by ${V_{\rm c}^{\rm halo}}^2(r) = GM_{\rm halo}(r)/r$ with $M_{\rm halo}(r) = 4\pi \int_0^r {\rm d}\tilde{r}\, \tilde{r}^2\, \rho_{\rm halo}(\tilde{r})$. Using Eqs. (3.31, 3.32), this implies that

$${V_{\rm c}^{\rm halo}}^2(x) = \frac{GM_{\rm vir}}{r_{\rm vir}} \times \frac{\ln(1+c_{\rm halo}X) - \frac{c_{\rm halo}X}{1+c_{\rm halo}X}}{X[\ln(1+c_{\rm halo}) - \frac{c_{\rm halo}}{1+c_{\rm halo}}]}, \tag{3.34}$$

where $X \equiv r/r_{\rm vir}$ (thus $c_{\rm halo}X = r/r_{\rm s}$). This velocity vanishes at the halo center, then climbs to a maximal value $V_{\rm max} = 1.65\, r_{\rm s}\sqrt{G\rho_0}$ at $r = 2.16\, r_{\rm s}$, from where it decreases monotonically with r, typically reaching $0.65 - 0.95\, V_{\rm max}$ at $r = r_{\rm vir}$ ($X = 1$) with the extremes corresponding, respectively, to $c_{\rm halo} = 25$ and $c_{\rm halo} = 5$. For larger radii, the velocity asymptotically approaches the point-mass velocity profile ${V_{\rm c}^{\rm halo}}^2(r) = GM_{\rm vir}/r$.

3.5.2 Velocity profile of a flat disk

For simplicity, we assume in this section that the galactic disk is described by a single exponential surface density for stars and cold gas,

$$\Sigma^{\rm disk}(r) = \frac{M^{\rm disk}}{2\pi\, r_{\rm disk}^2} \exp\left(-\frac{r}{r_{\rm disk}}\right), \tag{3.35}$$

where $M^{\rm disk}$ is the total disk mass, taken as the sum of the cold gas mass and the stellar mass in the disk. In most real galaxies the stellar surface densities, are

slightly more compact (see Section 3.3.1), but we found that including this effect does not significantly modify the shape of the atomic and molecular emission lines. In fact, the radius, which maximally contributes to the disk mass, i.e. the maximum of $r\,\Sigma^{\rm disk}(r)$, is $r = r_{\rm disk}$. Therefore, we expect the gravitational potential to differ significantly from the point-mass potential only for r of order $r_{\rm disk}$ or smaller. Applying Poisson's equation to the surface density of Eq. (3.35), the gravitational potential in the plane of the disk becomes

$$\varphi_{\rm disk}(r) = -\frac{GM^{\rm disk}}{2\pi r_{\rm disk}^2} \iint_D \frac{\exp(-\tilde{r}/r_{\rm disk})\,\tilde{r}\,{\rm d}\tilde{r}\,{\rm d}\theta}{(r^2+\tilde{r}^2-2r\tilde{r}\cos\theta)^{1/2}}, \tag{3.36}$$

where the integration surface D is given by $\tilde{r} \in [0,\infty)$, $\theta = [0, 2\pi)$.

The velocity profile for circular orbits in the plane of the disk can be calculated as ${V_{\rm c}^{\rm disk}}^2 = r\,{\rm d}\varphi_{\rm disk}/{\rm d}r$. The integral in Eq. (3.36) is elliptic, and hence there are no exact closed-from expressions for $\varphi_{\rm disk}$ and $V_{\rm c}^{\rm disk}$. However, in this study we numerically found that an excellent approximation is given by

$${V_{\rm c}^{\rm disk}}^2(x) \approx \frac{GM^{\rm disk}}{r_{\rm vir}} \times \frac{c_{\rm disk} + 4.8 c_{\rm disk}\exp[-0.35 c_{\rm disk}X - 3.5/(c_{\rm disk}X)]}{c_{\rm disk}X + (c_{\rm disk}X)^{-2} + 2(c_{\rm disk}X)^{-1/2}}, \tag{3.37}$$

where $c_{\rm disk} \equiv r_{\rm vir}/r_{\rm disk}$ is the disk concentration parameter in analogy to the halo concentration parameter $c_{\rm halo}$ of Section 3.5.1. Eq. (3.37) is accurate to less than 1% over the whole range $r = 0 - 10\,r_{\rm disk}$ and it correctly converges towards the circular velocity of a point-mass potential, ${V_{\rm c}^{\rm halo}}^2(r) = GM^{\rm disk}/r$, for $r \to \infty$.

Like in Section 3.3.2, we shall use Eq. (3.16) to compute $r_{\rm disk}$ and $c_{\rm disk}$ in the DeLucia-catalog. This approach is slightly inconsistent because Eq. (3.16) was derived by Mo et al. (1998) under the assumption that the disk is supported by an isothermal halo with $\rho_{\rm halo}(r) \sim r^{-2}$, while in Section 3.5.1 we have assumed the more complex NFW-profile. We argue, however, that Eq. (3.16) with the empirical correction of Eq. (3.20) is sufficiently accurate, as it successfully reproduces the observed relation between $M_{\rm bary}$ and $r_{\rm disk}$ (see Fig. 3.2) as well as the relation between $M_{\rm HI}$ and $r_{\rm HI}$ (see Fig. 3.8). It can also be shown that, for realistic val-

ues of the halo concentration $c_{\rm halo}$ ($10 - 20$ for one-galaxy systems) and the spin parameter λ ($0.05 - 0.1$, e.g. Mo et al., 1998), the scale radius of the halo $r_{\rm s}$ and the disk radius $r_{\rm disk}$ are similar. Hence, the main mass contribution of the disk comes indeed from galactocentric radii, where the halo profile is approximately isothermal, thus justifying the assumption made by Mo et al. (1998) to derive Eq. (3.16).

3.5.3 Velocity profile of the bulge

Many models for the surface brightness or surface density profiles of bulges have been proposed (e.g. overview by Balcells et al., 2001). A rough consensus seems established that no single surface density profile can describe a majority of the observed bulges, but that they are generally well matched by the class of Sérsic-functions (Sersic, 1968), $\Sigma^{\rm bulge}(r) \sim \exp[-(r/r_{\rm bulge})^{1/n}]$, where the exponent n depends on the morphological type (Andredakis et al., 1995), such that $n \approx 4$ for lenticular/early-type galaxies (de Vaucouleurs-profile) and $n \approx 1$ for the bulges of late-type galaxies (exponential profile). Courteau et al. (1996) find slightly steeper profiles with $n = 1 - 2$ for nearly all spirals in a sample of 326 spiral galaxies using deep optical and IR photometry, and they show that by imposing $n = 1$ for all late-type galaxies, the ratio between the exponential scale radius of the bulge $r_{\rm bulge}$ and the scale radius of the disk $r_{\rm disk}$ is roughly constant, $r_{\rm bulge} \approx 0.1\,\tilde{r}_{\rm disk} \approx 0.05\,r_{\rm disk}$. We shall therefore assume that all bulges have an exponential projected surface density,

$$\Sigma^{\rm bulge}(r) = \frac{M^{\rm bulge}}{2\pi\, r_{\rm bulge}^2}\, \exp\left(-\frac{r}{r_{\rm bulge}}\right) \tag{3.38}$$

with $r_{\rm bulge} = 0.05\,r_{\rm disk}$.

For simplicity, we assume that the bulges of all galaxies are spherical and thus described by a radial space density function $\rho_{\rm bulge}(r)$. This function is linked to the projected surface density via $\Sigma^{\rm bulge}(r) = \int_{-\infty}^{\infty} {\rm d}z\, \rho_{\rm bulge}\big[(r^2 + z^2)^{1/2}\big]$. Numerically, we find that this model for $\rho_{\rm bulge}(r)$ is closely approximated by the Plummer

model (Plummer, 1911), more often used in the context of clusters,

$$\rho_{\rm bulge}(r) \approx \frac{3\,M^{\rm bulge}}{4\pi\,\tilde{r}^3_{\rm bulge}} \left[1 + \left(\frac{r}{\tilde{r}_{\rm bulge}}\right)^2\right]^{-5/2}, \tag{3.39}$$

with a characteristic Plummer radius $\tilde{r}_{\rm bulge} \approx 1.7\,r_{\rm bulge}$. The circular velocity profile $V_{\rm c}^{\rm bulge}$ corresponding to Eq. (3.39) is given by ${V_{\rm c}^{\rm bulge}}^2(r) = GM^{\rm bulge}(r)/r$ with $M^{\rm bulge}(r) = 4\pi \int_0^r {\rm d}\tilde{r}\,\tilde{r}^2\,\rho_{\rm bulge}(\tilde{r})$. This solves to

$${V_{\rm c}^{\rm bulge}}^2(x) = \frac{GM^{\rm bulge}}{r_{\rm vir}} \times \frac{(c_{\rm bulge}x)^2 c_{\rm bulge}}{[1 + (c_{\rm bulge}x)^2]^{3/2}}, \tag{3.40}$$

where $c_{\rm bulge} \equiv r_{\rm vir}/\tilde{r}_{\rm bulge} \approx 12\,c_{\rm disk}$ is the bulge concentration parameter.

3.5.4 Line shapes from circular velocities

The addition rule for gravitational potentials implies that the circular velocity profile of the combined halo–disk–bulge system in the plane of the disk is given by

$$V_{\rm c}^2(x) = {V_{\rm c}^{\rm halo}}^2(x) + {V_{\rm c}^{\rm disk}}^2(x) + {V_{\rm c}^{\rm bulge}}^2(x), \tag{3.41}$$

where $x \equiv r/r_{\rm vir}$ as in Sections 3.5.1–3.5.3. According to Eqs. (3.34, 3.37, 3.40), this profile is determined by six parameters: the three form-parameters $c_{\rm halo}$, $c_{\rm disk}$, $c_{\rm bulge}$ and the three mass-scales $M_{\rm vir}/r_{\rm vir}$, $M^{\rm disk}/r_{\rm vir}$, $M^{\rm bulge}/r_{\rm vir}$. The form-parameters were calculated as explained in Sections 3.5.1–3.5.3, while the mass-scales were directly adopted from the DeLucia-catalog. For the satellite galaxies with no resolved halo (see Section 3.2), $M_{\rm vir}$ and $r_{\rm vir}$ were approximated as the corresponding quantities of the original galaxy halo just before its disappearance. An exemplar circular velocity profile for a galaxy in the DeLucia-catalog at redshift $z = 0$ is shown in Fig. 3.9.

In order to evaluate the profile of a radio emission line associated with any velocity profile $V_{\rm c}(r)$, we shall first consider the line profile of a homogeneous flat ring with constant circular velocity $V_{\rm c}$ and a total luminosity of unity. If

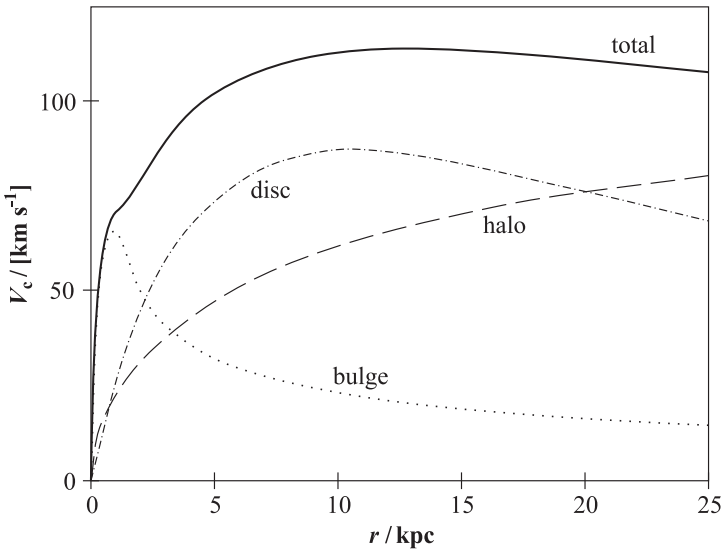

Figure 3.9. Circular velocity profile of a typical simulated galaxy with a small bulge at redshift $z = 0$. The total circular velocity (solid line) is given by the circular velocity of the halo (dashed line), the disk (dash-dotted line), and the bulge (dotted line) via Eq. (3.41).

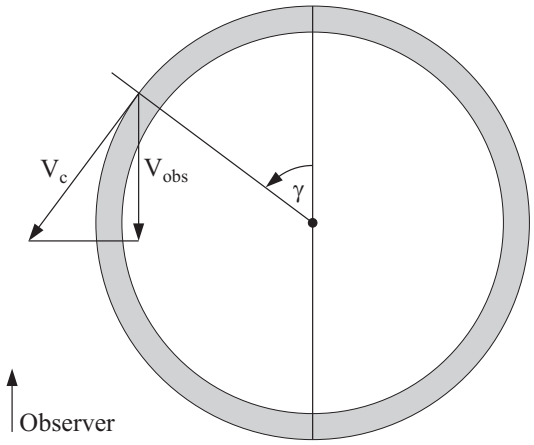

Figure 3.10. Apparent velocity $V_{\rm obs}$ induced by the infinitesimal ring element at the angle γ.

a point of the ring is labeled by the angle γ it forms with the line-of-sight (see Fig. 3.10), the apparent projected velocity of that point is given by $V_{\rm obs} = V_{\rm c} \sin\gamma$.

The ensemble of all angles $\gamma \in [0, 2\pi)$ therefore spans a continuum of apparent velocities $V_{\rm obs} \in (-V_{\rm c}, V_{\rm c})$ with a luminosity density distribution $\tilde{\psi}(V_{\rm obs}, V_{\rm c}) \sim {\rm d}\gamma/{\rm d}V_{\rm obs}$. Imposing the normalization condition $\int {\rm d}V_{\rm obs}\tilde{\psi}(V_{\rm obs}) = 1$, we find that the edge-on line profile of the ring is given by

$$\tilde{\psi}(V_{\rm obs}, V_{\rm c}) = \begin{cases} \frac{1}{\pi\sqrt{V_{\rm c}^2 - V_{\rm obs}^2}} & \text{if } |V_{\rm obs}| < V_{\rm c} \\ 0 & \text{otherwise.} \end{cases} \tag{3.42}$$

This profile exhibits spurious divergent singularities at $|V_{\rm obs}| \to V_{\rm c}$, which, in reality, are smoothed by the random, e.g. turbulent, motion of the gas. We assume that this velocity dispersion is given by the constant $\sigma_{\rm gas} = 8\,{\rm km\ s^{-1}}$, which is consistent with the velocity dispersions observed across the disks of several nearby galaxies (e.g. Burton, 1971, Dickey et al., 1990, Shostak & van der Kruit, 1984). The smoothed velocity profile is then given by

$$\psi(V_{\rm obs}, V_{\rm c}) = \frac{\sigma_{\rm gas}^{-1}}{\sqrt{2\pi}} \int {\rm d}V \exp\left[\frac{(V_{\rm obs} - V)^2}{-2\sigma_{\rm gas}^2}\right] \tilde{\psi}(V, V_{\rm c}), \tag{3.43}$$

which conserves the normalization $\int {\rm d}V_{\rm obs}\psi(V_{\rm obs}) = 1$. Some examples of the functions $\tilde{\psi}(V_{\rm obs}, V_{\rm c})$ and $\psi(V_{\rm obs}, V_{\rm c})$ are plotted in Fig. 3.11.

From the edge-on line profile $\psi(V_{\rm obs}, V_{\rm c})$ of a single ring and the face-on surface densities of atomic and molecular gas, $\Sigma_{\rm HI}(r)$ and $\Sigma_{\rm H_2}(r)$, we can now evaluate the edge-on profiles of emission lines associated with the entire HI- and H_2-disks, respectively. Since H_2-densities are most commonly inferred from CO-detections, we shall hereafter refer to all molecular emission lines as "the CO-line". The edge-on line profiles (or "normalized luminosity densities") $\Psi_{\rm HI}(V_{\rm obs})$ and $\Psi_{\rm CO}(V_{\rm obs})$ are given by

$$\Psi_{\rm HI}(V_{\rm obs}) = \frac{2\pi}{M_{\rm HI}} \int_0^\infty {\rm d}r\, r\, \Sigma_{\rm HI}(r)\, \psi\big(V_{\rm obs}, V_{\rm c}(r)\big), \tag{3.44}$$

$$\Psi_{\rm CO}(V_{\rm obs}) = \frac{2\pi}{M_{\rm H_2}} \int_0^\infty {\rm d}r\, r\, \Sigma_{\rm H_2}(r)\, \psi\big(V_{\rm obs}, V_{\rm c}(r)\big). \tag{3.45}$$

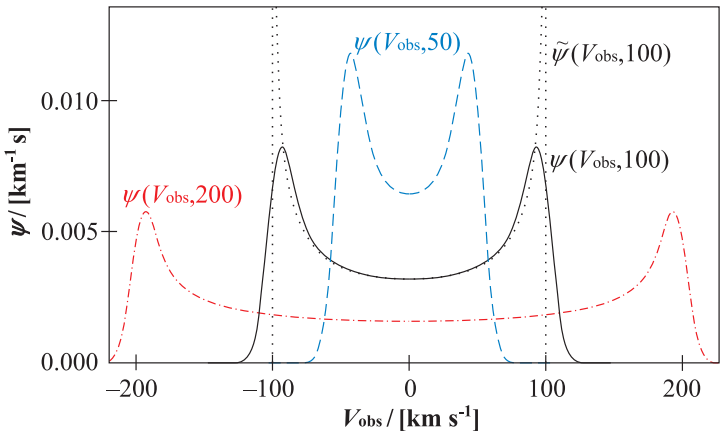

Figure 3.11. Illustration of the functions ψ (Eq. 3.43) and $\tilde{\psi}$ (Eq. 3.42), which represent the normalized emission line of a homogeneous edge-on disk or ring with constant circular velocity.

These two functions satisfy the normalization conditions $\int \mathrm{d}V_{\mathrm{obs}} \Psi_{\mathrm{HI}}(V_{\mathrm{obs}}) = 1$ and $\int \mathrm{d}V_{\mathrm{obs}} \Psi_{\mathrm{CO}}(V_{\mathrm{obs}}) = 1$. To obtain intrinsic luminosity densities, $\Psi_{\mathrm{HI}}(V_{\mathrm{obs}})$ must be multiplied by the integrated luminosity of the HI-line [see Eq. (3.21)] and $\Psi_{\mathrm{CO}}(V_{\mathrm{obs}})$ must be multiplied by the integrated luminosity of the considered molecular emission line, e.g. the integrated luminosity of the CO(1–0)-line given in Eq. (3.23).

Fig. 3.12 displays the line profiles $\Psi_{\mathrm{HI}}(V_{\mathrm{obs}})$ and $\Psi_{\mathrm{CO}}(V_{\mathrm{obs}})$ for the exemplar galaxy with the velocity profile shown in Fig. 3.9. All line profiles produced by our model are mirror-symmetric, but they can, in principle, differ significantly from the basic double-horned function $\psi(V_{\mathrm{obs}})$. Especially for CO, where the emission from the bulge can play an important role, several local maxima can sometimes be found in the line profile, in qualitative agreement with various observations (e.g. Lavezzi & Dickey, 1998).

3.5.5 Results and discussion

For every galaxy in the DeLucia-catalog, we computed the edge-on line profiles $\Psi_{\mathrm{HI}}(V_{\mathrm{obs}})$ and $\Psi_{\mathrm{CO}}(V_{\mathrm{obs}})$, from which we extracted the line parameters indicated

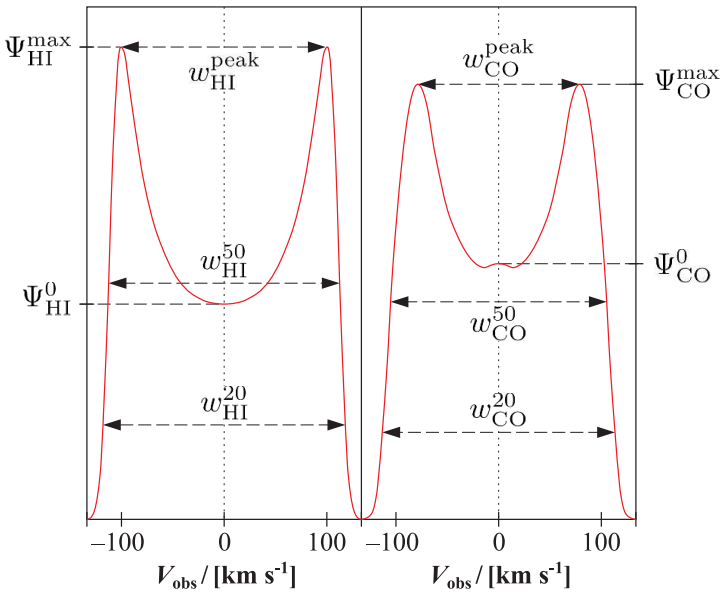

Figure 3.12. Simulated edge-on HI- and CO-emission lines for the exemplar galaxy, for which the circular velocity profile is shown in Fig. 3.9. The line profiles have been computed using Eq. (3.44).

in Fig. 3.12. $\Psi_{\rm HI}^0 \equiv \Psi_{\rm HI}(0)$ and $\Psi_{\rm CO}^0 \equiv \Psi_{\rm CO}(0)$ are the luminosity densities at the line center, and $\Psi_{\rm HI}^{\rm max}$ and $\Psi_{\rm CO}^{\rm max}$ are the peak luminosity densities, i.e. the absolute maxima of $\Psi_{\rm HI}(V_{\rm obs})$ and $\Psi_{\rm CO}(V_{\rm obs})$. $w_{\rm HI}^{\rm peak}$ and $w_{\rm CO}^{\rm peak}$ are the line widths measured between the left and the right maximum. These values vanish if the line maxima are at the line center, such as found, for example, in slowly rotating systems. $w_{\rm HI}^{50}$, $w_{\rm CO}^{50}$, $w_{\rm HI}^{20}$, and $w_{\rm CO}^{20}$ are the line widths measured at, respectively, the 50-percentile level or the 20-percentile level of the peak luminosity densities – the two most common definitions of observed line widths.

We shall now check the simulated line widths against observations by analyzing their relation to the mass of the galaxies. Here, we shall refer to all line width versus mass relations as Tully–Fisher relations (TFRs), since they are generalized versions of the original relation between line widths and optical magnitudes of spiral galaxies (Tully & Fisher, 1977). A variety of empirical TFRs have been published, such as the stellar mass-TFR and the baryonic-TFR (McGaugh et al.,

2000). The latter relates the baryon mass (stars+gas) of spiral disks to their line widths (or circular velocities) and is probably the most fundamental TFR detected so far, obeying a single power-law over five orders of magnitude in mass. We have also investigated the less fundamental empirical TFR between $M_{\rm HI}$ and $w_{\rm HI}^{50}$ – hereafter the HI-TFR – using the spiral galaxies of the HIPASS catalog. Assuming no prior knowledge on the inclinations of the HIPASS-galaxies, but taking an isotropic distribution of their axes as given, we found that the most-likely relation is

$$\log\left(\frac{M_{\rm HI}}{\rm M_\odot}\right) = 2.86 + 2.808 \cdot \log\left(\frac{w_{\rm HI}^{50}}{\rm km\ s^{-1}}\right) \tag{3.46}$$

for the Hubble parameter $h = 0.73$. Relative to Eq. (3.46) the HIPASS data exhibit a Gaussian scatter with $\sigma = 0.38$ in $\log(M_{\rm HI})$. Our method to find Eq. (3.46) will be detailed in a forthcoming paper (Obreschkow et al. in prep.), especially dedicated to the HI-TFR.

Figs. 3.13a–d show four TFRs at redshift $z = 0$. Each figure represents 10^3 simulated galaxies (black), randomly drawn from the simulation with a probability proportional to their cold gas mass in order to include the rare objects in the high end of the MF. Spiral and elliptical galaxies are distinguished as black dots and open circles.

Fig. 3.13a shows the simulated HI-TFR together with the empirical counterpart given in Eq. (3.46). This comparison reveals good consistency between observation and simulation for spiral galaxies. However, the elliptical galaxies lie far off the HI-TFR. In fact, simulated elliptical galaxies generally have a significant fraction of their cold hydrogen in the molecular phase, consistent with the galaxy-type dependence of the H_2/HI-ratio first identified by Young & Knezek (1989). Therefore, HI is a poor mass tracer for elliptical galaxies, both in simulations and observations, leading to their offset from the TFR when only HI-masses are considered. There seems to be no direct analog to the HI-TFR for elliptical galaxies.

Figs. 3.13b, c respectively display the simulated stellar mass-TFR and the

baryonic-TFR, together with the observed data of McGaugh et al. (2000) corrected for $h = 0.73$. These data include various galaxies from dwarfs to giant spirals, whose edge-on line widths were estimated from the observed ones using the inclinations determined from the optical axis ratios. Figs. 3.13b, c reveal a surprising consistency between simulation and observation. In Fig. 3.13b, both the simulated and observed data show a systematic offset from the power-law relation for all galaxies with $w_{\rm HI}^{20} \lesssim 200\ {\rm km\,s^{-1}}$. Yet, the power-law relation is restored as soon as the cold gas mass is added to the stellar mass (Fig. 3.13c), thus confirming that the TFR is indeed fundamentally a relation between mass and circular velocity.

It is interesting to consider the prediction of the simulation for the most fundamental TFR, i.e. the one between the total dynamical mass, taken as the virial mass $M_{\rm vir}$, and the circular velocity, represented by the line width $w_{\rm HI}^{20}$. This relation is shown in Fig. 3.13d and reveals indeed a 2–3 times smaller scatter in log(mass) than the baryonic-TFR, hence confirming its fundamental character.

Although the simulated elliptical galaxies shown in Figs. 3.13b–d roughly align with the respective TFRs for spiral galaxies, their scatter is larger. This is caused by the mass-domination of the bulge, which leads to steep circular velocity profiles $V_{\rm c}(r)$ with a poorly defined terminal velocity. Therefore, line widths obtained by averaging over the whole elliptical galaxy are weak tracers of its spin. This picture seems to correspond to observed elliptical galaxies, where the central line widths, corresponding to the velocity dispersion in the bulge dominated parts, are more correlated to the stellar mass than the line widths of the whole galaxy (see Faber-Jackson relation, e.g. Faber & Jackson, 1976).

Kassin et al. (2007) noted that $S_{0.5} \equiv (0.5\,V_{\rm c}^2 + \sigma_{\rm gas}^2)^{1/2}$ is a better kinematic estimator than the circular velocity $V_{\rm c}$, in the sense that it markedly reduces the scatter in the stellar mass-TFR. However, since our model assumes a constant gas velocity dispersion $\sigma_{\rm gas}$ for all galaxies, it is not possible to investigate this estimator.

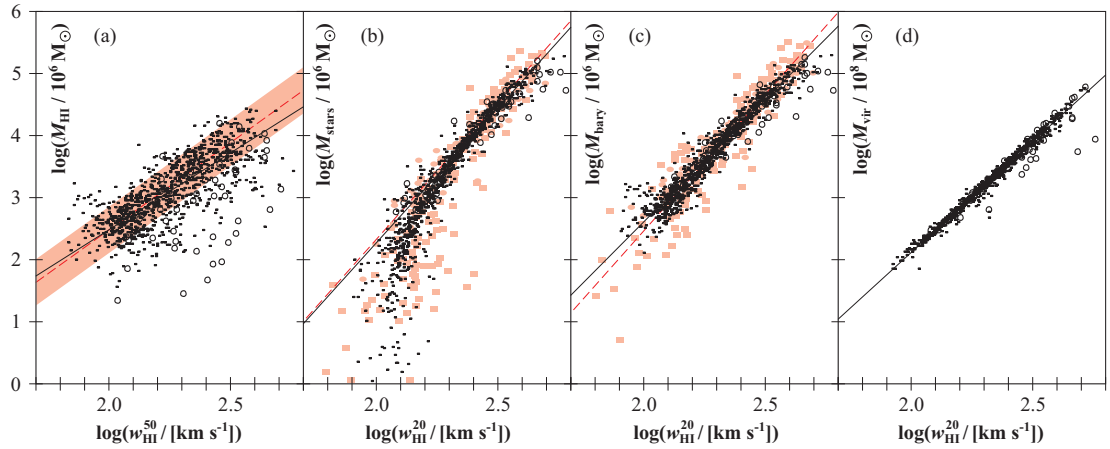

Figure 3.13. Relations between edge-on line widths and different mass tracers for galaxies in the local Universe. 10^3 simulated galaxies are represented by black dots (spiral galaxies) and black circles (elliptical galaxies). The solid lines represent power-law fits to the simulated spiral galaxies; their slopes are respectively $\alpha_{\rm HI} = 2.5$, $\alpha_{\rm stars} = 4.3$, $\alpha_{\rm bary} = 3.9$, and $\alpha_{\rm vir} = 3.6$. In case of Fig. 3.13b, this fit only includes galaxies with $M_{\rm stars} > 10^9\,{\rm M}_\odot$. Fig. 3.13d does not include satellite galaxies without haloes (see Section 3.2), for which $M_{\rm vir}$ is poorly defined. The dashed red line and shaded zone in Fig. 3.13a represent our observational determination and 1-σ scatter of the HI-TFR from the HIPASS data (see Section 3.5.5). The rose dots and dashed lines in Figs. 3.13b, c are the observational data and power-law regressions from McGaugh et al. (2000) and references therein; this sample include low surface brightness galaxies. The slopes of these empirical power-laws are respectively $\alpha_{\rm HI} = 2.8$ (see Eq. 3.46), $\alpha_{\rm stars} = 4.4$, and $\alpha_{\rm bary} = 4.4$.

The predicted evolution of the four TFRs in Figs. 3.13a–d is shown in Figs. 3.14a–d. In all four cases, the simulation predicts two important features: (i) galaxies of identical mass (respectively $M_{\rm HI}$, $M_{\rm stars}$, $M_{\rm bary}$, $M_{\rm vir}$) have broader lines (and larger circular velocities) at higher redshift, and (ii) the scatter of the TFRs generally increases with redshift. The first feature is mainly a consequence of the mass–radius–velocity relation of the dark matter haloes assumed in the Millennium Simulation (see Croton et al., 2006, Mo et al., 1998). This relation predicts

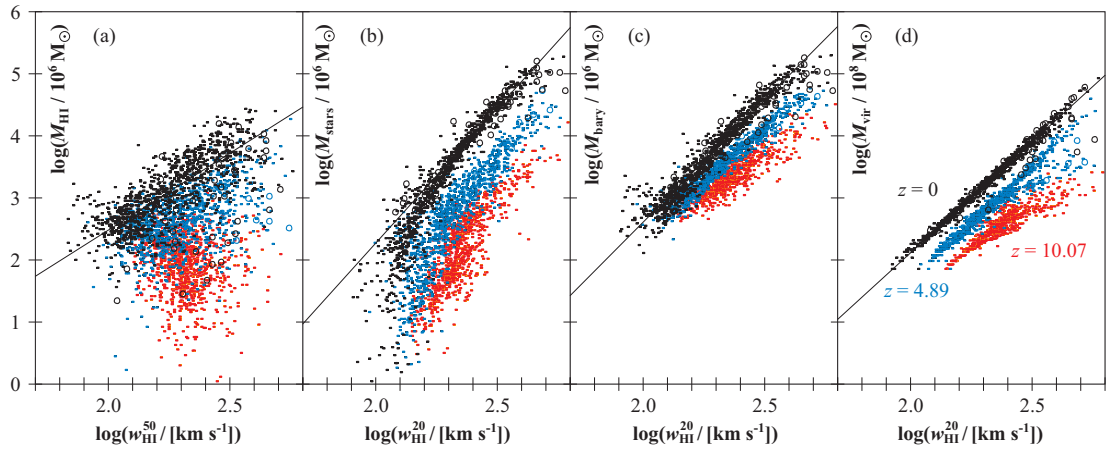

Figure 3.14. Simulated cosmic evolution of the different line width–mass relations shown in Fig. 3.13. Spiral and elliptical galaxies are respectively represented by dots and circles. Black color corresponds to redshift $z = 0$ (identically to Fig. 3.13), while blue and red color respectively represent $z = 4.89$ and $z = 10.07$. The solid black lines are power-law fits to the spiral galaxies at $z = 0$, where in case of Fig. 3.14b only galaxies with $M_{\rm stars} > 10^9\,{\rm M}_\odot$ have been considered. The number of elliptical galaxies decreases with redshift – a consequence of the merger- and instability-driven prescriptions for bulge formation in the DeLucia-catalog.

that, given a constant halo mass, $V_{\rm c}$ scales as $(1+z)^{1/2}$ for large z. Furthermore, the ratios $M_{\rm HI}/M_{\rm vir}$ and $M_{\rm stars}/M_{\rm vir}$ on average decrease with increasing redshift, explaining the stronger evolution found in Figs. 3.14a,b relative to Figs. 3.14c,d.

The increase of scatter in the TFRs with redshift is a consequence of the lower degree of virialization at higher redshifts, which, in the model, is accounted for via the spin parameter λ of the haloes. λ is more scattered at high redshift due to the young age of the haloes and the higher merger rates. More scatter in λ leads to more scatter in the radius $r_{\rm disk}$ via Eq. (3.16) and thus to more scatter in the circular velocity $V_{\rm c}$ via Eqs. (3.37, 3.40).

Current observational databases of resolved CO-line profiles are much smaller than HI-databases and their signal/noise characteristics are inferior. Nevertheless efforts to check the use of CO-line widths for probing TFRs (e.g. Lavezzi &

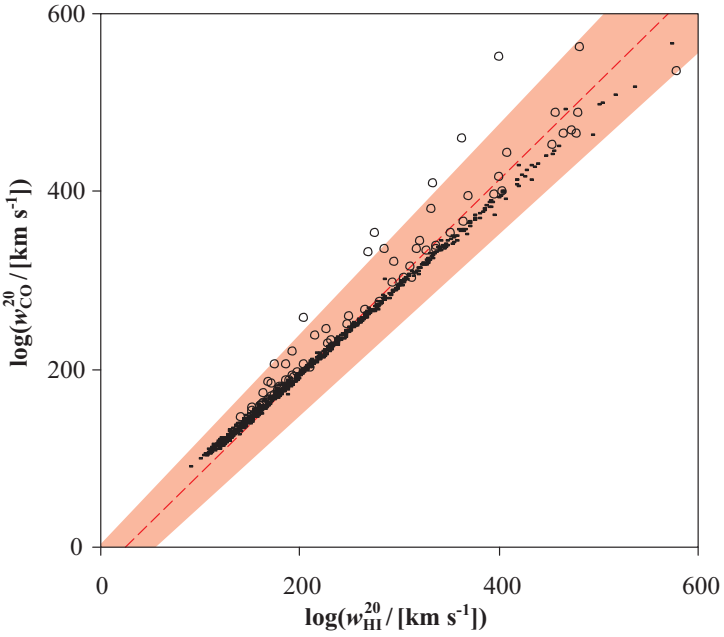

Figure 3.15. Relation between line widths of HI and CO. 10^3 simulated galaxies are represented by black dots (spiral galaxies) and black circles (elliptical galaxies). The red dashed line and rose-shaded zone represent the best fit and its 1-σ confidence interval to observations of 44 galaxies in clusters presented by Lavezzi & Dickey (1998).

Dickey, 1998) have led to the conclusion that in most spiral galaxies the CO-line widths are very similar to HI-line widths, even though the actual line profiles may radically differ. Fig. 3.15 shows our simulated relation between $w_{\rm HI}^{20}$ and $w_{\rm CO}^{20}$, as well as the linear fit to observations of 44 galaxies in different clusters (Lavezzi & Dickey, 1998). These observations are consistent with the simulation. The simulated elliptical galaxies tend to have higher $w_{\rm CO}^{20}/w_{\rm HI}^{20}$-ratios than the spiral ones, due to the high circular velocity of the bulge.

The line profiles considered in this section correspond to galaxies observed edge-on. First order corrections for spiral galaxies seen at an inclination $i \neq 90\,\mathrm{deg}$ can be obtained by dividing the normalized luminosity densities $\Psi_{\rm HI}^{0}$, $\Psi_{\rm HI}^{\rm max}$, $\Psi_{\rm CO}^{0}$, $\Psi_{\rm CO}^{\rm max}$ by $\sin i$, and multiplying the line widths $w_{\rm HI}^{50}$, $w_{\rm HI}^{20}$, $w_{\rm HI}^{\rm peak}$, $w_{\rm CO}^{50}$, $w_{\rm CO}^{20}$, $w_{\rm CO}^{\rm peak}$ by $\sin i$. More elaborate corrections, accounting for the isotropy of the velocity dispersion $\sigma_{\rm gas}$, are given in Obreschkow et al. (2009c).

3.6 Discussion

We used a list of physical prescriptions to post-process the DeLucia-catalog and showed that many simulation results match the empirical findings from the local Universe. However, this approach raises two major questions: (i) Are the applied prescriptions consistent with the DeLucia-catalog in the sense that they represent a compatible extension of the semi-analytic recipes used by De Lucia & Blaizot (2007) and Croton et al. (2006)? (ii) What are the limitations of our prescriptions at low and high redshifts?

3.6.1 Consistency of the model

The consistency question arises, because the DeLucia-catalog relies on a simplified version of a Schmidt–Kennicutt law (Kennicutt, 1998, Schmidt, 1959), i.e. a prescription where the star formation rate (SFR) scales as some power of the surface density of the ISM. However, in a smaller-scaled picture, new stars are bred inside molecular clouds, and hence it must be verified whether our prescription to assign H_2-masses to galaxies is compatible with the macroscopic Schmidt–Kennicutt law. Our prescription exploited the empirical power-law between the pressure of the ISM and its molecular content, as first presented by Blitz & Rosolowsky (2004, 2006). Based on this power-law relation, Blitz & Rosolowsky (2006) themselves formulated an alternative model for the computation of SFRs in galaxies, which seems more fundamental than the Schmidt–Kennicutt law. Applying both models for star formation to six molecule-rich galaxies in the local Universe, they showed that their new pressure-based law predicts SFRs nearly identical to the ones predicted by the Schmidt–Kennicutt law. Therefore, our choice to divide cold hydrogen in HI and H_2 according to pressure is indeed consistent with the prescription for SFRs used by De Lucia & Blaizot (2007) and Croton et al. (2006).

3.6.2 Accuracy and limitations at $z = 0$

A first limitation of our simulation comes from the assumption that the surface densities of HI and H_2 are axially symmetric (no spiral structures, no central bars, no warps, no satellite structures). In general, our model describes all galaxies as regular galaxies – as do all semi-analytic models for the Millennium Simulation. Hence, the simulation results cannot be used to predict the HI- and H_2-properties of irregular galaxies.

While our models allowed us to reproduce the observed relation between $M_{\rm HI}$ and $r_{\rm HI}$ remarkably well for various spiral galaxies (e.g. Fig. 3.8), it tends to underestimate the size of HI-distributions in elliptical galaxies. For example observations by Morganti et al. (1997) show that 7 nearby E- and S0-type galaxies all have very complex HI-distributions, often reaching far beyond the corresponding radius of a mass-equivalent disk galaxies. The patchy HI-distributions found around elliptical galaxies are probably due to mergers and tidal interactions, which could not be modeled in any of the semi-analytic schemes for the Millennium Simulation.

Another limitation arises from neglecting stellar bulges as an additional source of disk-pressure in Eq. (3.7) (Elmegreen, 1989). Especially the heavier bulges of early-type spiral galaxies could introduce a positive correction of the central pressure and hence increase the molecular fraction, thus leading to very sharp H_2-peaks in the galaxy centers, such as observed, for example, in the SBb-type spiral galaxy NGC 3351 (Leroy et al., 2008). Our model for the H_2-surface density of Eq. (3.12) fails at predicting such sharp peaks, although the predicted total HI- and H_2-mass and the corresponding radii and line profiles are not significantly affected by this effect.

3.6.3 Accuracy and limitations at $z > 0$

Additional limitations are likely to occur at higher redshifts, where our models make a number of assumptions based on low-redshift observations. Furthermore,

the underlying DeLucia-catalog itself may suffer from inaccuracies at high redshift, but we shall restrict this discussion to possible issues associated with the models in this paper.

Regarding the subdivision of hydrogen into atomic and molecular material (Section 3.3), our most critical assumption is the treatment of all galactic disks as regular exponential structures in hydro-gravitational equilibrium. This model is very likely to deviate more from the reality at high redshift, where galaxies were generally less virialized and mergers were much more frequent (de Ravel et al., 2008). Less virialized disks are thicker, which would decrease the average pressure and fraction of molecules compared to our model. Yet, galaxy mergers counteract this effect by creating complex shapes with locally increased pressures, where H_2 forms more efficiently, giving rise to merger-driven starbursts. Therefore, it is unclear whether the assumption of regular disks tends to underestimate or overestimate the H_2/HI-ratios.

Another critical assumption is the high-redshift validity of the local relation between the H_2/HI-ratio $R_{\rm mol}$ and the external gas pressure P (Eq. 3.6). This relation is not a fundamental thermodynamic relation, but represents the effective relation between the average H_2/HI-ratio and P, resulting from complex physical processes like cloud formation, H_2-formation on metallic grains, and H_2-destruction by the photodissociative radiation field of stars and supernovae. Therefore, the $R_{\rm mol}-P$ relation could be subjected to a cosmic evolution resulting from the cosmic evolution of the cold gas metallicity or the cosmic evolution of the photodissociative radiation field. However, the metallicity evolution is likely to be problem only at the highest redshifts ($z \gtrsim 10$). Observations in the local Universe show that spiral galaxies with metallicities differing by a factor 5 fall on the same $R_{\rm mol} - P$ relation (Blitz & Rosolowsky, 2006). Yet, the average cold gas metallicity of the galaxies in the DeLucia-catalog is only a factor 1.9 (3.6) smaller at $z = 5$ ($z = 10$) than in the local Universe. These predictions are consistent with observational evidence from the Sloan Digital Sky Survey (SDSS)

that stellar metallicities were at most a factor 1.5–2 smaller at $z \approx 3$ than today (Panter et al., 2008). The effect of the cosmic evolution of the photodissociative radiation field on the $R_{\rm mol} - P$ relation is difficult to assess. Blitz & Rosolowsky (2006) argued that the ISM pressure and the radiation field both correlate with the surface density of stars and gas, and therefore the radiation field is correlated to pressure. This is supported by observations in the local Universe showing that the $R_{\rm mol} - P$ relation holds true for dwarf galaxies and spiral galaxies spanning almost three orders of magnitude in SFR. For those reasons, the $R_{\rm mol} - P$ relation could indeed extend surprisingly well to high redshifts.

In the expression for the disk-pressure in Eq. (3.7) (Elmegreen, 1989), we assumed a constant average velocity dispersion ratio f_σ. Observations suggest that $V_{\rm c}/\sigma_{\rm gas}$ decreases significantly with redshift (Förster Schreiber et al., 2006, Genzel et al., 2008), and therefore f_σ perhaps increases. This would lead to even higher H_2/HI-ratios than predicted by our model. However, according to Eq. (3.10) this is likely to be a problem only for galaxies with $M_{\rm stars} > M_{\rm gas}$, while most galaxies in the simulation at $z > 2$ are indeed gas dominated.

Regarding cold gas geometries and velocity profiles, the most important limitation of our model again arises from the simplistic treatment of galactic disks as virialized exponential structures. Very young galaxies ($\lesssim 10^8$ yrs) or galaxies undergoing a merger do not conform with this model, and therefore the predicted velocity profiles may be unreal and the disk radii may be meaningless. This is not just a limitation of the simulation, but it reveals a principal difficulty to describe galaxy populations dominated by very young or merging objects with quantities such as $r_{\rm HI}$ or $w_{\rm HI}^{50}$, which are common and useful for isolated systems in the local Universe.

The radio line widths predicted by our model (Section 3.5.4) may be underestimated at high redshift, due to the assumption of a constant random velocity dispersion $\sigma_{\rm gas}$. Förster Schreiber et al. (2006) found $V_{\rm c}/\sigma_{\rm gas} \approx 2 - 4$ for 14 UV-selected galaxies at redshift $z \approx 2$. This result suggests that radio lines at $z \approx 2$

should be about 20%-30% broader than predicted by our model, and therefore the evolution of the TFRs could be slightly stronger than shown in Fig. 3.14.

In summary, the HI- and H_2-properties predicted for galaxies at high redshift are generally uncertain, even though no significant, systematic trend of the model-errors could be identified. Perhaps the largest deviations from the real Universe occur for very young galaxies or merging objects, while isolated field galaxies, typically late-type spiral systems, might be well described by the model at all redshifts.

In Section 3.3.4, we ascribed CO(1–0)-luminosities to the H_2-masses using the metallicity dependent X-factor of Eq. (3.26). This model neglects several important aspects: (i) the projected overlap of molecular clouds, which is negligible in the local Universe, may become significant at high redshifts, where galaxies are denser and richer in molecules; (ii) the temperature of the cosmic microwave background (CMB) increases with redshift, hence changing the level population of the CO-molecule (Combes et al., 1999, Silk & Spaans, 1997); (iii) the CMB presents a background against which CO-sources are detect; (iv) the molecular material in the very dense galaxies, such as Ultra Luminous Infrared Galaxies, may be distributed smoothly rather than in clouds and clumps (Downes et al., 1993); (v) the higher SFRs in early galaxies probably led to higher gas temperatures, hence changing the CO-level population[3]. Combes et al. (1999) presented a simplistic simulation of the cosmic evolution of X, taking the cosmic evolution of metallicity and points (i) and (ii) into account. They found that for an H_2-rich disk galaxy $\langle X \rangle$ increases by a factor 1.8 from redshift $z = 0$ to $z = 5$. This value approximately matches the average increase of X by a factor 2 predicted by our simulation using the purely metallicity-based model of Eq. (3.26). This indicates that the effects of (i) and (ii) approximately balance each other. If a more elaborate model for X becomes available, the latter can be directly applied to correct our CO-predictions. In fact, the X-factor only affects the CO(1–0)-luminosity

[3]This list is not exhaustive, see Maloney & Black (1988), Wall (2007) for an overview of the physical complexity behind the X-factor.

$L_{\rm CO}$ calculated via Eq. (3.23), but has no effect on the line properties considered in this paper, namely the line widths $w_{\rm CO}^{\rm peak}$, $w_{\rm CO}^{50}$, $w_{\rm CO}^{20}$ and the normalized luminosity densities $\Psi_{\rm CO}^{0}$, $\Psi_{\rm CO}^{\rm max}$.

3.7 Conclusion

In this paper, we presented the first attempt to incorporate detailed cold gas properties in a semi-analytic simulation of galaxies in a large cosmological volume. To this end, we introduced a series of physical prescriptions to evaluate relevant properties of HI and H_2 in simulated model-galaxies.

When applied to the DeLucia-galaxy catalog for the Millennium Simulation, our recipes introduce only one free parameter in addition to the 9 free parameters of the semi-analytic model of the DeLucia-catalog (see Table 1 in Croton et al., 2006). This additional parameter, i.e. the cold gas correction factor ζ (Section 3.2), was tuned to the cosmic space density of cold gas in the local Universe. The additional parameter ξ, describing the transfer of angular momentum from the halo to the disk (Section 3.3.2), is not a free parameter for the hydrogen simulation, since it is fixed by the baryon mass–scale radius relation. In fact, we deliberately did not adjust ξ to match the observed HI-mass–HI-radius relation of Verheijen (2001), in order to check the reliability of our models against this observation.

Based on the DeLucia-catalog, we produced a virtual catalog of $\sim 3 \cdot 10^7$ per redshift-snapshot with various cold gas properties. This catalog represents an extension of the DeLucia-catalog, and it can be used to investigate a broad variety of questions related to HI, H_2, CO and their cosmic evolution. The results presented in this paper have been restricted to some important examples, most of which could be compared directly to available observations and hence constitute key results for the verification of our simulation:

1. Based on a pressure-model for the molecular content of cold gas, the simulation simultaneously reproduces the HI-MF and the H_2-MF (resp. the

CO-LF) observed in the local Universe within the measurement uncertainties (Fig. 3.3).

2. The simulated HI-MFs for spiral and elliptical galaxies considered individually also match the observations for simulated galaxies with well-defined galaxy types (Fig. 3.5).

3. The simulated HI-radii, imply a mass–radius relation for HI that matches the empirical counterpart (Fig. 3.8), thus confirming that the relation between $M_{\rm HI}$ and $r_{\rm HI}$ is such that the average HI-density inside $r_{\rm HI}$ is $3.8\,{\rm M}_\odot\,{\rm pc}^{-2}$ for all galaxies in the local Universe, although this value sensibly depends on the definition of $r_{\rm HI}$.

4. The simulation predicts that the mass–radius relations for HI and H_2 are similar in the local Universe, but that their high-redshift evolution is completely different (Fig. 3.7).

5. The simulated widths of the HI-radio emission lines of spiral galaxies are consistent with the empirical HI-TFR derived from the HIPASS spiral galaxies (Fig. 3.13a); and the simulation predicts that there is no analog HI-TFR for elliptical galaxies.

6. The simulated the stellar mass-TFR and the baryonic TFR reveal good agreement with the empirical TFRs for both spiral and elliptical galaxies in the simulation (Figs. 3.13b, c).

7. These TFRs are observable manifestations of a more fundamental relation between circular velocity and total dynamical mass, as suggested by the small scatter in the relation between $w_{\rm HI}^{20}$ and $M_{\rm vir}$ (Fig. 3.13d).

8. At higher redshift, the simulation predicts that the above TFRs remain valid (except for HI at $z \approx 10$), but that their scatter increases and their zero-point is shifted towards higher velocities at fixed mass – a fundamental prediction of hierarchical growth (Fig. 3.14).

The good match between simulation and observation regarding gas masses, disk sizes, and velocity profiles supports the models and recipes established in this paper. It also validates the semi-analytic recipes used by De Lucia & Blaizot (2007) and supports the Millennium Simulation (Springel et al., 2005) as a whole.

In forthcoming investigations the presented extension of the DeLucia-catalog towards cold gas properties could be used to investigate more elaborate questions. For example, what is the bias of the cosmic structure, for example of the power spectrum, revealed in HI-surveys or CO-surveys compared to the underlying dark matter structure? How many HI-sources can we expect to detect in future experiments performed by the SKA? Or how does the global H_2/HI-ratio evolve with redshift and how does it relate to the observed evolution of the SFR density?

Acknowledgements

This effort/activity is supported by the European Community Framework Programme 6, Square Kilometre Array Design Studies (SKADS), contract no 011938. The Millennium Simulation databases and the web application providing online access to them were constructed as part of the activities of the German Astrophysical Virtual Observatory. D. O. thanks Gerard Lemson for his help in accessing the simulation data, as well as Erwin de Blok, Scott Kay, Raul Angulo, Carlton Baugh, and Carlos Frenk for fruitful discussions. Finally, we thank the anonymous referee for the helpful suggestions.

Chapter 4

The cosmic decline in the H_2/HI-ratio in galaxies

D. Obreschkow and S. Rawlings

"The Cosmic Decline in the H_2/HI-Ratio in Galaxies"

ApJ, **696**, L129–L132 (2009)

We use a pressure-based model for splitting cold hydrogen into its atomic (HI) and molecular (H_2) components to tackle the co-evolution of HI, H_2, and star formation rates (SFR) in $\sim 3 \cdot 10^7$ simulated galaxies in the Millennium Simulation. The main prediction is that galaxies contained similar amounts of HI at redshift $z \approx 1-5$ than today, but substantially more H_2, in quantitative agreement with the strong molecular line emission already detected in a few high-redshift galaxies and approximately consistent with inferences from studies of the damped Lyman-α absorbers seen in the spectra of quasars. The cosmic H_2/HI-ratio is predicted to evolve monotonically as $\Omega_{H_2}/\Omega_{HI} \propto (1+z)^{1.6}$. This decline of the H_2/HI-ratio as a function of cosmic time is driven by the growth of galactic disks and the progressive reduction of the mean cold gas pressure. Finally, a comparison between the evolutions of HI, H_2, and SFRs reveals two distinct cosmic epochs of star formation: an early epoch ($z \gtrsim 3$), driven by the evolution of $\Omega_{HI+H_2}(z)$, and a late epoch ($z \lesssim 3$), driven by the evolution of $\Omega_{H_2}(z)/\Omega_{HI}(z)$.

4.1 Introduction and key idea

Neutral hydrogen is the fuel for the formation of stars. The cosmic star formation rate (SFR) density as inferred from ultraviolet, far-infrared, and submillimeter observations increases by an order of magnitude from redshift $z = 0$ to $z = 2$ (Hopkins, 2007). Hence, neutral hydrogen in early galaxies was either more abundant or transformed into stars more efficiently than today.

A useful quantity in this context is the star formation efficiency (SFE) of a galaxy, defined as the SFR divided by the gas mass. The weak cosmic evolution of the density of neutral atomic hydrogen (HI), derived from Lyman-alpha absorption against distant quasars (Lah et al., 2007, Pontzen & Pettini, 2009), indicates a strongly increased SFE at high z. But recent detections of strong molecular line emission in ordinary galaxies at $z = 1.5$ (Daddi et al., 2008) suggest that the SFEs of these galaxies are similar to those seen today. The seeming contradiction between these two conclusions arises from the conceptual confusion of SFEs inferred from galactic HI with those inferred from H_2. In fact, it is crucial to distinguish between the two quantities $\mathrm{SFE_{HI}} \equiv \mathrm{SFR}/M_{\mathrm{HI}}$ and $\mathrm{SFE_{H_2}} \equiv \mathrm{SFR}/M_{\mathrm{H_2}}$. In principle, there is no contradiction between the detected strong cosmic evolution of $\mathrm{SFE_{HI}}$ and the weak evolution of $\mathrm{SFE_{H_2}}$ – these empirical findings could simply imply that the H_2/HI-mass ratios $R_{\mathrm{mol}}^{\mathrm{galaxy}}$ of galaxies increase substantially with z.

In this letter, we show that there is indeed strong theoretical support for such an increase of $R_{\mathrm{mol}}^{\mathrm{galaxy}}$ with z in regular galaxies. This evolution is driven by the approximate scaling of galaxy sizes as $(1+z)^{-1}$ predicted by dark matter theory (Gunn & Gott, 1972) and confirmed by observations in the Ultra Deep Field (Bouwens et al., 2004). Hence, the cold gas disks at high redshift must, on average, be denser than today. Combining this prediction with the relation between gas pressure and H_2/HI-ratios in nearby galaxies (e.g. Blitz & Rosolowsky, 2006), leads to the conclusion that $R_{\mathrm{mol}}^{\mathrm{galaxy}}$ must increase dramatically with z. Our quantitative predictions of this evolution rely on a recently presented semi-analytic

numerical simulation of HI and H_2 in $\sim 3 \cdot 10^7$ simulated galaxies (Obreschkow et al., 2009a), based on the Millennium Simulation (Springel et al., 2005).

Section 4.2 overviews our simulation method and the model for the H_2/HI-ratio in galaxies. In Section 4.3, we present and interpret the predicted evolution of galactic HI and H_2 and their relation to star formation. Section 4.4 compares these predictions to empirical data, and Section 4.5 summarizes our key conclusions.

4.2 Simulating HI and H_2 in galaxies

4.2.1 Physical model for galactic H_2/HI-ratios

In virtually all regular galaxies in the local Universe, whether spirals (e.g. Leroy et al., 2008) or ellipticals (e.g. Young, 2002), the cold gas resides in a flat disk. Some observations of CO at $z \approx 2$ (Tacconi et al., 2006) suggest that even at high redshift most cold gas lies in disks. Based on this evidence, we have recently introduced a model for the distributions of HI and H_2 in regular galaxies (Obreschkow et al., 2009a), assuming that all cold gas resides in a flat symmetric disk with an exponential surface density profile and that the local H_2/HI-ratio is dictated by the kinematic gas pressure (Blitz & Rosolowsky, 2006, Leroy et al., 2008). Within these assumptions, we could show that the H_2/HI-mass ratio $R_{\rm mol}^{\rm galaxy}$ of an entire galaxy is given by

$$R_{\rm mol}^{\rm galaxy} = \left(3.44\, {R_{\rm mol}^{\rm c}}^{-0.506} + 4.82\, {R_{\rm mol}^{\rm c}}^{-1.054}\right)^{-1}, \tag{4.1}$$

where $R_{\rm mol}^{\rm c}$ represents the H_2/HI-ratio at the galaxy center. $R_{\rm mol}^{\rm c}$ can be approximated as

$$R_{\rm mol}^{\rm c} = \left[11.3\,{\rm m^4 kg^{-2}} r_{\rm disk}^{-4} M_{\rm gas}\left(M_{\rm gas} + 0.4\, M_{\rm stars}^{\rm disk}\right)\right]^{0.8}, \tag{4.2}$$

where $r_{\rm disk}$ is the exponential scale radius of the disk, $M_{\rm gas}$ is the total cold gas mass, and $M_{\rm stars}^{\rm disk}$ is the stellar mass in the disk. Eqs. (4.1,4.2) constitute a physical

model to estimate $R_{\rm mol}^{\rm galaxy}$ in regular galaxies based on $M_{\rm stars}^{\rm disk}$, $M_{\rm gas}$, and $r_{\rm disk}$. In order to predict the cosmic evolution of $R_{\rm mol}^{\rm galaxy}$, we therefore require a model for the co-evolution of $M_{\rm stars}^{\rm disk}$, $M_{\rm gas}$, and $r_{\rm disk}$ in galaxies. To this end, we adopted the virtual galaxy catalog of the Millennium Simulation described in Section 4.2.2. The limitations of the model of Eqs. (4.1,4.2) and their impact on the predicted H_2/HI-ratios are discussed in (Obreschkow et al., 2009a).

4.2.2 HI and H_2 in the Millennium Simulation

The Millennium Simulation (Springel et al., 2005) is an N-body simulation within the ΛCDM cosmology of $\sim 10^{10}$ gravitationally interacting particles in a periodic box of comoving volume $(500\ h^{-1}\ {\rm Mpc})^3$, where $H_0 = 100\,h\,{\rm km\,s^{-1}\,Mpc^{-1}}$ and $h = 0.73$. The evolving large-scale structure generated by this simulation served as the skeleton for the simulation of $\sim 3 \cdot 10^7$ galaxies at the halo centers. In the "semi-analytic" approach adopted by De Lucia & Blaizot (2007), galaxies were considered as simplistic objects with a few global properties that are evolved stepwisely using a list of physical prescriptions. For example, the total amount of cold hydrogen (HI+H_2) in a galaxy is defined by the history of the net accretion, which in the model consists of (i) the infall of gas from the hot halo, (ii) the loss of gas by star formation, and (iii) outflows driven by supernovae and active galactic nuclei. Star formation in each galaxy is tackled using a law, where all cold gas above a critical surface density is transformed into stars on a timescale proportional to the dynamical time of the disk (for details see Croton et al., 2006).

In Obreschkow et al. (2009a), we applied the model of Section 4.2.1 to the simulated galaxies in the catalog of De Lucia & Blaizot (2007) ("DeLucia-catalog"), to split their cold hydrogen masses into HI and H_2. Our simulation successfully reproduced many local observations of HI and H_2, such as mass functions (MFs), mass–diameter relations, and mass–velocity relations. Yet, the high-redshift predictions are inevitably limited by the semi-analytic recipes of the DeLucia-catalog. The most uncertain recipes are those related to mergers (e.g. feedback of black

hole coalescence and starbursts), but they have a minor effect on the cosmic space densities of HI and H_2, since most cold gas in the simulation is found in regular disk galaxies[1] with at most minor merger histories. However, inaccurate prescriptions for isolated galaxies could significantly affect the space densities of HI and H_2, and it may well become necessary to refine our simulation as improved semi-analytic methods come on line.

4.3 Results

4.3.1 Predicted evolution of HI and H_2

Fig. 4.1 shows the predicted evolution of the HI-MF and H_2-MF, i.e. the comoving space densities of sources per logarithmic mass interval. The predictions at $z = 0$ roughly agree with available observational data, but the obvious differences, such as the spurious bumps around $M_{\rm HI} \approx 10^{8.5}$ and $M_{\rm H_2} \approx 10^8$ (a mass resolution limit), have been discussed in Obreschkow et al. (2009a).

The predicted HI-masses remain roughly constant from $z = 0$ to $z = 2$, while H_2-masses increase dramatically. These different evolutions are also reflected in the comoving space densities $\Omega_{\rm HI} \equiv \rho_{\rm HI}/\rho_{\rm c}$ and $\Omega_{\rm H_2} \equiv \rho_{\rm H_2}/\rho_{\rm c}$, where $\rho_{\rm c}(z) = 3H^2(z)/(8\pi G)$ is the critical density for closure. Here, $\Omega_{\rm HI}$ and $\Omega_{\rm H_2}$ only account for gas in galaxies, excluding unbound HI between the first galaxies (Becker et al., 2001) or possible H_2 in haloes (Pfenniger & Combes, 1994). The simulated functions $\Omega_{\rm HI}(z)$ and $\Omega_{\rm H_2}(z)$ are shown in Figs. 4.2a, b, while Fig. 4.2c represents their ratio $R_{\rm mol}^{\rm universe}(z) \equiv \Omega_{\rm H_2}(z)/\Omega_{\rm HI}(z)$, which is closely described by the power-law

$$R_{\rm mol}^{\rm universe}(z) \approx 0.3 \cdot (1+z)^{1.6}. \tag{4.3}$$

The simulation yields $R_{\rm mol}^{\rm universe}(0) \approx 0.3$ and finds the crossover, $R_{\rm mol}^{\rm universe}(z) = 1$, at $z \approx 1.4$. Our model predicts that Eq. (4.3) extends to epochs, where the first galaxies formed, but this prediction is likely to breakdown at the highest

[1] By contrast, a significant fraction of the *stars* at $z = 0$ is in massive elliptical galaxies with violent merger histories, but even those galaxies formed most stars in their spiral progenitors.

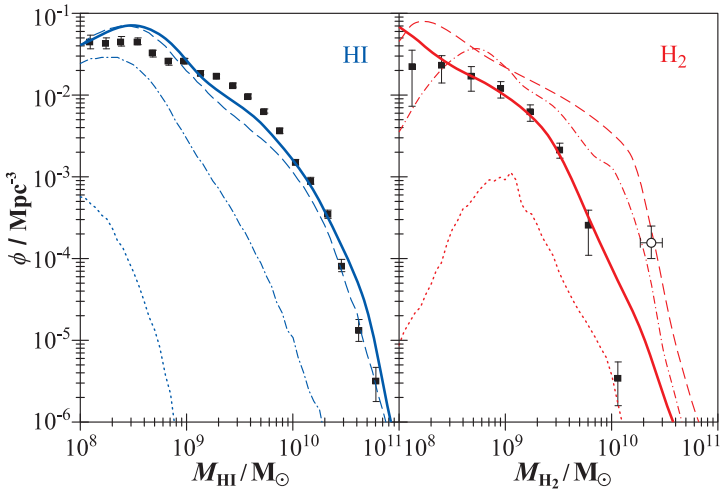

Figure 4.1. MFs of HI and H_2. Lines show the simulation results at $z = 0$ (solid), $z = 2$ (dashed), $z = 5$ (dash-dotted), $z = 10$ (dotted). Square dots represent the empirical data and 1-σ scatter at $z = 0$ (Obreschkow & Rawlings, 2009c, Zwaan et al., 2005a), and the open circle represents our density estimate at $z = 1.5$ (Section 4.4) based on Daddi et al. (2008).

redshifts, where the formation of H_2 was inhibited by the lack of metals (Abel & Haiman, 2000).

Physically, the strong evolution of H_2/HI is essentially driven by the size-evolution of galaxies and their haloes. The Millennium Simulation assumes that the virial radius $r_{\rm vir}$ of a spherical halo always encloses a mass with an average density 200-times above the critical density $\rho_{\rm c} \propto H^2$ (Croton et al., 2006). Hence, for a fixed halo mass, $r_{\rm vir} \propto H^{-2/3}$. In a flat Universe this implies

$$r_{\rm vir} \propto \left[\Omega_{\rm m}(1+z)^3 + \Omega_\Lambda\right]^{-1/3}, \tag{4.4}$$

which asymptotically tends to $r_{\rm vir} \propto (1+z)^{-1}$ for high z. By virtue of the theory of Fall & Efstathiou (1980), this cosmic scaling of $r_{\rm vir}$ results in a similar scaling of the disk radius, i.e. $r_{\rm disk} \propto (1+z)^{-1}$, consistent with observations in the Ultra Deep Field (Bouwens et al., 2004).

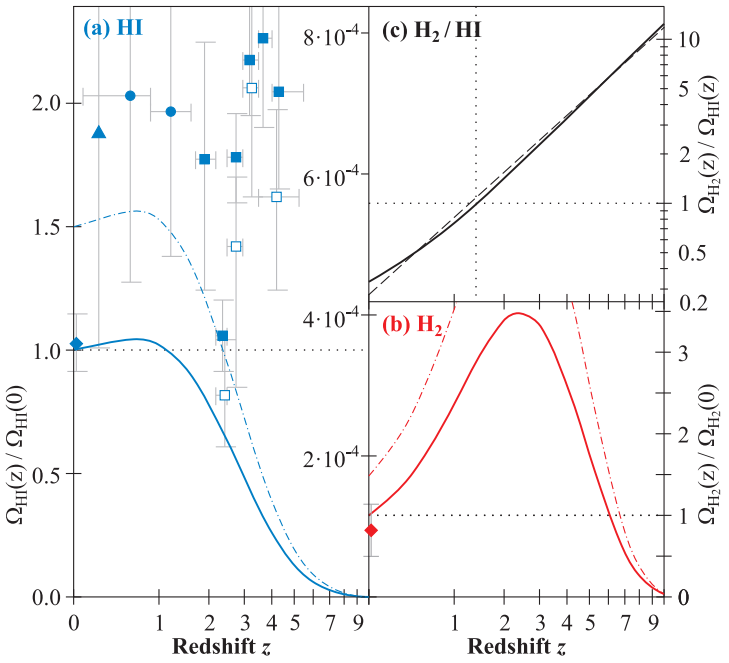

Figure 4.2. Cosmic evolution of the fractional space densities of HI and H_2. Solid lines represent the simulated evolution of $\Omega_{\rm HI}$ (a), $\Omega_{\rm H_2}$ (b), and $\Omega_{\rm H_2}/\Omega_{\rm HI}$ (c). The dashed line in panel (c) is the power-law fit for $\Omega_{\rm H_2}/\Omega_{\rm HI}$ given in Eq. (4.3). The points represent the observations described in Section 4.4. The dash-dotted lines in panels (a) and (b) represent the evolution of $\Omega_{\rm HI}$ and $\Omega_{\rm H_2}$, if the correction factor ζ in Obreschkow et al. (2009a) is set to $\zeta = 1$, i.e. the total cold gas mass of the DeLucia-catalog is not corrected. We originally introduced this correction to fit the sum of the local space densities of HI and H_2 (shown as diamonds).

For the gas-dominated galaxies in the early Universe, Eq. (4.2) reduces to $R^{\rm c}_{\rm mol} \propto r_{\rm disk}^{-3.2} M_{\rm gas}^{1.6}$. Yet, the cold gas masses $M_{\rm gas}$ of individual galaxies in the simulation evolve weakly with cosmic time, due to a self-regulated equilibrium between the net inflow of gas and star formation. In fact, most of the evolution of $\Omega_{\rm HI+H_2}$ in the redshift range $z \approx 3-10$ is due to the build-up of new galaxies. Therefore, $R^{\rm c}_{\rm mol} \propto r_{\rm disk}^{-3.2} \propto (1+z)^{3.2}$. At redshifts $z \approx 1-10$, $R^{\rm c}_{\rm mol}$ typically takes values between 10 and 10^4, such that Eq. (4.1) can be approximated as $R^{\rm galaxy}_{\rm mol} \propto {R^{\rm c}_{\rm mol}}^{0.5}$. Hence, $R^{\rm galaxy}_{\rm mol} \propto (1+z)^{1.6}$, which supports Eq. (4.3).

The cosmic evolution of $\Omega_{\rm H_2}$ shown in Fig. 4.2 can be divided in two epochs: The *early epoch* ($z \gtrsim 3$), where $\Omega_{\rm H_2}$ increases with cosmic time, and the *late epoch* ($z \lesssim 3$), where $\Omega_{\rm H_2}$ decreases with time. In the early epoch, $R_{\rm mol}^{\rm galaxy} > 1$ implies $\Omega_{\rm H_2} \approx \Omega_{\rm HI+H_2}$, and hence the growth of $\Omega_{\rm H_2}$ reflects the general increase of $\Omega_{\rm HI+H_2}$ due to the intense assembly of new galaxies. In the late epoch, $R_{\rm mol}^{\rm galaxy} \lesssim 1$ implies that $\Omega_{\rm H_2} \approx R_{\rm mol}^{\rm universe}\Omega_{\rm HI+H_2}$. At this epoch the formation of the massive galaxies in the simulation is completed, i.e. $\Omega_{\rm HI+H_2}(z) \approx$ const and $\Omega_{\rm H_2} \propto R_{\rm mol}^{\rm universe}$. Thus the decrease of $\Omega_{\rm H_2}$ in this late epoch is driven by cosmic decline in $R_{\rm mol}^{\rm universe}$ or, physically, by the cosmic evolution of pressure.

4.3.2 Link between HI, H_2, and star formation

To discuss the global cosmic evolution of the efficiencies $\rm SFE_{HI}$ and $\rm SFE_{H_2}$ (Section 4.1), we shall define

$$\langle \rm SFE_{HI} \rangle \equiv \rho_{\rm SFR}/\rho_{\rm HI}\,, \quad \langle \rm SFE_{H_2} \rangle \equiv \rho_{\rm SFR}/\rho_{\rm H_2}, \tag{4.5}$$

where $\rho_{\rm HI} \propto \Omega_{\rm HI}$, $\rho_{\rm H_2} \propto \Omega_{\rm H_2}$, and $\rho_{\rm SFR}$ denote the comoving space densities of HI, H_2, and SFR.

In the semi-analytic recipes of the DeLucia-catalog, SFRs are estimated from the gas density and the dynamical time scale of the disk (Section 4.2.2). This Schmidt–Kennicutt law (Kennicutt, 1998, Schmidt, 1959) for star formation makes similar predictions to models based on cold gas pressure(e.g. Blitz & Rosolowsky, 2006), and therefore the SFRs in the DeLucia-catalog are, by default, approximately consistent with our model to split cold hydrogen into HI and H_2. The evolutions of $\langle \rm SFE_{HI} \rangle$ and $\langle \rm SFE_{H_2} \rangle$ predicted by the simulation again reflect the marked difference between HI and H_2. They are approximated ($\sim$20% relative error) by the power-laws,

$$\langle \rm SFE_{HI} \rangle / [Gyr^{-1}] = 0.23\,(1+z)^{2.2}, \tag{4.6}$$

$$\langle \rm SFE_{H_2} \rangle / [Gyr^{-1}] = 0.75\,(1+z)^{0.6}, \tag{4.7}$$

out to $z \approx 8$.

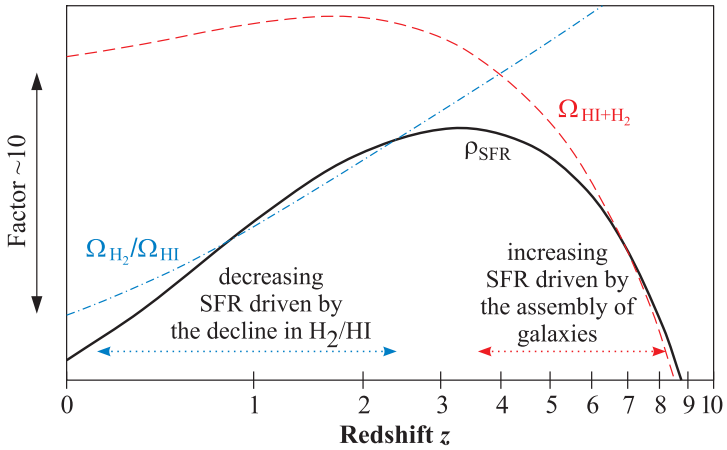

Figure 4.3. A simplistic model for the cosmic history of star formation.

Due to the low power in Eq. (4.7) $\rho_{\rm SFR}(z)$ is approximately proportional to $\Omega_{\rm H_2}(z)$. We can therefore apply the two cosmic epochs of $\Omega_{\rm H_2}(z)$ introduced in Section 4.3.1 to the history of star formation (see Fig. 4.3): In the *early epoch* ($z \gtrsim 3$), $\rho_{\rm SFR}$ increases with cosmic time, proportionally to $\Omega_{\rm HI+H_2}$. This increase traces the dramatic assembly of new galaxies. In the *late epoch* ($z \lesssim 3$), $\rho_{\rm SFR}$ decreases roughly proportionally to $\Omega_{\rm H_2}/\Omega_{\rm HI}$. This epoch is driven by the cosmic evolution of pressure (or density) in galactic disks. This interpretation of the history of star formation does not, in fact, conflict with the picture that star formation is ultimately defined by the accreted cold gas mass (see Section 4.2.2) and a Schmidt–Kennicutt law for transforming this gas into stars. Our H_2/HI-based interpretation simply adds another layer to the causal chain, by suggesting that cold gas mass and density ultimately dictate the amount of molecular material available for star formation.

The simulation also includes star formation via merger-driven starbursts, associated with the creation of the stellar spheroids of early-type spiral or elliptical galaxies. However, the cosmic star formation density caused by mergers only accounts for about 1% of $\rho_{\rm SFR}$ in the semi-analytic simulation of the DeLucia-catalog. (This fraction should not be confused with the fraction of gas-rich or "wet" mergers, since only some of the cold gas involved in these mergers is efficiently turned into stars in the form of a starburst.)

4.4 Comparison with observations

The DeLucia-catalog and our post-processing to assign HI and H_2, rely on established data of the local Universe. Our simulated HI- and H_2-properties at $z = 0$ are consistent with all available observations, i.e. MFs (see Fig. 4.1), disk sizes, and velocity profiles (Obreschkow et al., 2009a). In particular, the simulated values $\Omega_{\rm HI}(0) = 3.5 \cdot 10^{-4}$ and $\Omega_{\rm H_2}(0) = 1.2 \cdot 10^{-4}$ are consistent with the values (diamonds in Fig. 4.2) derived from the MFs observed in HI- and CO-emission at $z \approx 0$ (Obreschkow & Rawlings, 2009c, Zwaan et al., 2005a). At $z > 0$, the currently available data are sparse, especially in emission.

The only measurement of $\Omega_{\rm HI}$ in emission at intermediate redshift is based on the stacking of 121 galaxies at $z = 0.24$ (Lah et al., 2007, triangle in Fig. 4.2). The detection is speculative (see Fig. 7 in Lah et al., 2007), but roughly consistent with our simulation. All other measurements of $\Omega_{\rm HI}$ at $z > 0$ rely on absorption detections of damped Lyman-α systems (DLAs). Respective data points from Rao et al. (2006) (circles in Fig. 4.2) and Prochaska et al. (2005) (filled squares) are, taken together, inconsistent with the predicted values of $\Omega_{\rm HI}$. By contrast, Zwaan et al. (2005b) demonstrated that the population of HI-galaxies in the local Universe can fully explain the column density distributions of DLAs out to $z = 1.5$, consistent with the nearly absent evolution of $\Omega_{\rm HI}$ from $z = 0$ to $z = 1.5$ predicted by our simulation. At present it is therefore difficult to judge, whether the simulation is inconsistent with empirical data at these low redshifts covering 2/3 of the age of the Universe. At higher redshifts, however, the measurements of $\Omega_{\rm HI}$ seem not reconcilable with the simulated result, and even accounting for gravitational lensing by the DLAs only corrects the empirical values of $\Omega_{\rm HI}$ by about 30% (open squares in Fig. 4.2, Prochaska et al., 2005). The simulated values of $\Omega_{\rm HI}$ are likely to underestimate the real values by about a factor 2 – a plausible offset given the long list of simplifying approximations required from the N-body Millennium Simulation to our final post-processing of hydrogen in galaxies. Much progress could be expected from treating HI-masses and H_2-

masses as separate quantities directly in the semi-analytic galaxy simulation. This would allow, for example, to refine the feedback-mechanisms for suppression of gas infall (explained in Croton et al., 2006), such that HI can still be accreted, while the formation of H_2 and stars is inhibited. Such a semi-analytic setting would also allow the implementation of a recipe for the large-scale dissociation of molecular gas by the radiation of newly formed stars (Allen et al., 1986). Both examples would effectively increase the amount of HI in high-redshift galaxies.

The most representative high-redshift observations of molecular gas to-date rely on two *normal* galaxies (*BzK*-4171 and *BzK*-21000) at $z \approx 1.5$, reliably detected in CO(2–1) emission by Daddi et al. (2008). Unlike other CO-sources at similar or higher z, these objects are ordinary massive galaxies with FIR-luminosities of $L_{\rm FIR} \approx 10^{12}$ $L_\odot$, selected only due to the availability of precise spectroscopic redshifts. From these two detections, we estimated the H_2-space density (empty circle in Fig. 4.1) as follows: The mass interval spans between the masses $M_{H_2} \approx 2 \cdot 10^{10} M_\odot$ and $M_{H_2} \approx 3 \cdot 10^{10}$, respectively obtained for *BzK*-4171 and *BzK*-21000 by applying the CO-to-H_2 conversion of $\alpha = 1\ M_\odot (\mathrm{K\ km\ s^{-1}\ pc^{-2}})^{-1}$ (Daddi et al., 2008). The space density of these CO-sources was approximated as the space density of FIR-sources at $L_{\rm FIR} \approx 10^{12}$ $L_\odot$, based on the fact that all (both) targeted galaxies with $L_{\rm FIR} \approx 10^{12}$ $L_\odot$ revealed similar CO-luminosities $L_{\rm CO}$. We estimate their space density to be $1 - 2 \cdot 10^{-4}$ Mpc^{-3} per unit of $\log(L_{\rm FIR})$ by extrapolating the FIR-luminosity functions (LFs) of Huynh et al. (2007). Since $L_{\rm FIR} \propto L_{\rm CO} \propto M_{H_2}$, we find roughly the same space density per unit $\log(M_{H_2})$. These result is consistent with the simulated H_2-MF at $z = 2$ (Fig. 4.1).

Considering H_2-absorption studies, Curran et al. (2004) and Noterdaeme et al. (2008) have determined H_2/HI-ratios in DLAs that showed H_2-absorption. They found H_2/HI-ratios of $\sim 10^{-6}$ to $\sim 10^{-2}$ at $z \approx 2 - 3$, clearly much smaller than our prediction for $\Omega_{H_2}/\Omega_{\rm HI}$. We argue that measurements of H_2/HI in DLAs do not trace $\Omega_{H_2}/\Omega_{\rm HI}$ since DLAs are by definition HI-selected objects and H_2 has

a much smaller space coverage than HI. In fact, H_2-disks in galaxies are much smaller than HI-disks, especially at high z (Obreschkow & Rawlings, 2009a), and even inside the H_2-disks the coverage of H_2 is small compared to HI (e.g. Ferrière, 2001). A more detailed explanation of why H_2-searches in DLAs are expected to be difficult was given by Zwaan & Prochaska (2006) based on the analysis of CO-emission maps of local galaxies.

4.5 Conclusions

In this letter, we have predicted the cosmic evolution of HI- and H_2-masses in $\sim 3 \cdot 10^7$ simulated galaxies based on the Millennium Simulation. The predicted cosmic decline in the H_2/HI-ratio is consistent with the weak cosmic evolution of $\Omega_{\rm HI}$ inferred from DLA-studies and recent observations revealing a significantly enhanced space density of H_2 at $z = 1.5$ (Daddi et al., 2008).

Perhaps the most important conclusion is that HI- and H_2-masses evolve very differently with cosmic time and therefore cannot be used as proportional tracers of one another, especially not for the purpose of high-redshift predictions. There is no contradiction between the large H_2-masses detected at high z, which imply values of $\mathrm{SFE}_{\mathrm{H_2}}$ similar to those in the local Universe, and the weak evolution of HI, implying massively increased values of $\mathrm{SFE}_{\rm HI}$ at high z.

Acknowledgements

This work is supported by the European Community Framework Programme 6, Square Kilometre Array Design Studies (SKADS), contract no 011938. The Millennium Simulation databases and the web application providing online access to them were constructed as part of the German Astrophysical Virtual Observatory. We also thank the anonymous referee for the helpful suggestions.

Chapter 5

Compactness of cold gas in high-redshift galaxies

D. Obreschkow and S. Rawlings

"Compactness of Cold Gas in High-Redshift Galaxies"

MNRAS, submitted (2009)

Galaxies in the early Universe were more compact and contained more molecular gas than today. In this letter, we revisit the relation between these empirical findings, and we quantitatively predict the cosmic evolution of the surface densities of atomic (HI) and molecular (H_2) hydrogen in regular galaxies. Our method uses a pressure-based model for the H_2/HI-ratio of the Interstellar Medium, applied to $\sim 3 \cdot 10^7$ virtual galaxies in the Millennium Simulation. We predict that, on average, the HI-surface density of these galaxies saturates at $\Sigma_{\rm HI} < 10\ {\rm M}_\odot\,{\rm pc}^{-2}$ at all redshifts (z), while H_2-densities evolve dramatically as $\Sigma_{\rm H_2} \propto (1+z)^{2.4}$. This scaling is dominated by a $\propto (1+z)^2$ surface brightness scaling originating from the $\propto (1+z)^{-1}$ size scaling of galaxies at high z. Current measurements of $\Sigma_{\rm H_2}$ at high z, derived from CO-observations, tend to have even higher values, perhaps due to a selection bias towards merging systems. As a case study, we investigate the evolution of simulated galaxies, which resemble the Milky Way at $z = 0$. We explicitly predict their HI- and H_2-distribution at $z = 1.5$, corresponding to the CO-detected galaxy BzK-21000, and at $z = 3$, corresponding to the primary science goal of the Atacama Large Millimeter/submillimeter Array (ALMA).

5.1 Introduction

Galaxies were more compact in the early Universe than today (Bouwens et al., 2004, Buitrago et al., 2008, Trujillo et al., 2006). This empirical feature is probably driven by an increase in the volume-to-mass ratio of dark haloes with cosmic time (Gunn & Gott, 1972), which dictates the density evolution of galaxies by the transfer of angular momentum (Fall & Efstathiou, 1980). We have recently argued (Obreschkow & Rawlings, 2009b) that the density evolution of galactic disks implies a systematic pressure change, which causes a dramatic decline in the mass ratio between molecular (H_2) and atomic (HI) hydrogen with cosmic time. Using the Millennium Simulation, we showed that this decline in the H_2/HI-ratio simultaneously explains (i) the observations of large molecular masses in ordinary galaxies at $z = 1.5$ (Daddi et al., 2008), (ii) the weak cosmic evolution of the HI-density $\Omega_{\rm HI}$ inferred from damped Lyman-α systems (Prochaska et al., 2005), and (iii) the history of star formation inferred from ultraviolet, far-infrared, submillimeter, and radio continuum observations (Hopkins & Beacom, 2006).

In this letter, we quantitatively predict the cosmic evolution of the surface densities of HI and H_2 in a large sample of regular galaxies. Section 5.2 explains our physical model and the numerical simulation. Section 5.3 presents our predictions for the average cosmic evolution of the HI- and H_2-distributions in a broad sample of galaxies, while Section 5.4 specifically focusses on the evolution of HI- and H_2-distributions in Milky Way (MW)-type galaxies. Section 5.5 gives a brief summary and outlook.

5.2 Simulation of $\Sigma_{\rm HI}$ and $\Sigma_{\rm H_2}$ in galaxies

Several computational studies (e.g. Combes et al., 1999, Dobbs, 2008, Greve & Sommer-Larsen, 2008, Robertson & Kravtsov, 2008) have investigated the distribution of molecular gas in regular galaxies and revealed pivotal connections between the distribution of molecules and star formation. In particular, Robertson

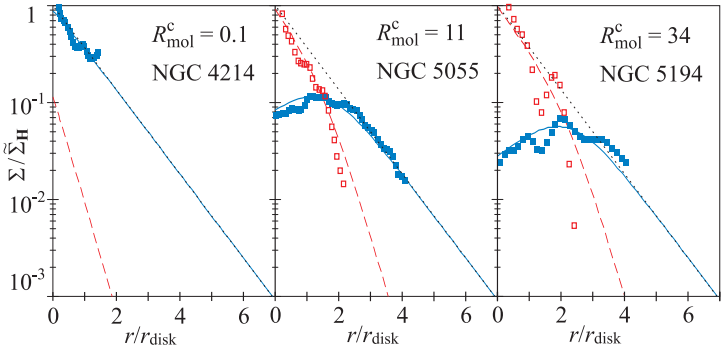

Figure 5.1. Surface densities of galactic cold gas as a function of galactic radius. Lines show the predictions of Eqs. (5.1, 5.2) for $\Sigma_{\rm HI}(r)$ (solid), $\Sigma_{\rm H_2}(r)$ (dashed), and $\Sigma_{\rm HI}(r)+\Sigma_{\rm H_2}(r)$ (dotted) for different values of $R^{\rm c}_{\rm mol}$. Dots represent the observed counterparts (Leroy et al., 2008) for $\Sigma_{\rm HI}(r)$ (filled) and $\Sigma_{\rm H_2}(r)$ (empty), inferred from CO(2–1) observations.

& Kravtsov (2008) and Krumholz et al., 2009 (see also Elmegreen, 1993) demonstrated that the empirical relation between the local H_2/HI-ratios and cold gas pressure, measured by Blitz & Rosolowsky (2006) and Leroy et al. (2008), can be approximately reproduced by SPH/N-body simulations, which include a model for interstellar radiation.

While those simulations are effective tools for the study of the cold gas in individual galaxies, they are computationally too expensive to be included in "cosmological simulations", i.e. simulations of representative samples of galaxies with resolved merger histories in an expanding model-universe. However, cosmological simulations of HI- and H_2-distributions are required for the design and analysis of high-z cold gas surveys possible with future telescopes, such as the Square Kilometer Array (SKA) and the Atacama Large Millimeter/submillimeter Array (ALMA). To circumvent the current computational bottleneck, we decided (Obreschkow et al., 2009a) to adopt a semi-analytic simulation of millions of galaxies and to estimate the HI- and H_2-distributions of these galaxies using an analytic model. We shall first explain this model and then the semi-analytic simulation.

Our model for the distributions of HI and H_2 in regular galaxies represents a ramification of the H_2/HI–pressure relation measured by Leroy et al. (2008), combined with two assumptions for the distribution of cold hydrogen. The first assumption is that all galaxies carry their cold gas in flat disks, such as is observed in virtually all regular galaxies (see Leroy et al. (2008) for spiral galaxies at low z, Young (2002) for elliptical galaxies at low z, and e.g. Tacconi et al. (2006) for galaxies at high z). The second assumption is that the surface density of cold hydrogen, $\Sigma_{\rm HI}(r)+\Sigma_{\rm H_2}(r)$, follows an exponential profile in the radial coordinate r (e.g. Leroy et al., 2008). Based on these assumptions we have shown (Obreschkow et al., 2009a) that the surface densities of HI and H_2 are

$$\Sigma_{\rm HI}(r) = \frac{\tilde{\Sigma}_{\rm H}\,\exp(-r/r_{\rm disk})}{1+R^{\rm c}_{\rm mol}\exp(-1.6\,r/r_{\rm disk})}\,, \tag{5.1}$$

$$\Sigma_{\rm H_2}(r) = \frac{\tilde{\Sigma}_{\rm H}\,R^{\rm c}_{\rm mol}\,\exp(-2.6\,r/r_{\rm disk})}{1+R^{\rm c}_{\rm mol}\exp(-1.6\,r/r_{\rm disk})}\,, \tag{5.2}$$

where $r_{\rm disk}$ is the exponential scale radius of the cold gas disk, $\tilde{\Sigma}_{\rm H} = (M_{\rm HI}+M_{\rm H_2})/(2\pi r^2_{\rm disk})$ is a normalization factor, and $R^{\rm c}_{\rm mol}=\Sigma_{\rm H_2}(0)/\Sigma_{\rm HI}(0)$ is the central H_2/HI-ratio. $R^{\rm c}_{\rm mol}$ can be approximated (Obreschkow et al., 2009a) from $r_{\rm disk}$, the disk stellar mass $M^{\rm disk}_{\rm stars}$, and the total (HI+H_2+He) cold gas mass $M_{\rm gas}$ as,

$$R^{\rm c}_{\rm mol} = \left[K\,r^{-4}_{\rm disk}M_{\rm gas}\left(M_{\rm gas}+0.4\,M^{\rm disk}_{\rm stars}\right)\right]^{0.8}, \tag{5.3}$$

where $K = 11.3\,{\rm m}^4\,{\rm kg}^{-2}$ is an empirical constant.

If the radii and surface densities in Eqs. (5.1, 5.2) are normalized to $r_{\rm disk}$ and $\tilde{\Sigma}_{\rm H}$, then $\Sigma_{\rm HI}(r)$ and $\Sigma_{\rm H_2}(r)$ become unique functions of $R^{\rm c}_{\rm mol}$. Fig. 5.1 shows $\Sigma_{\rm HI}(r)$ and $\Sigma_{\rm H_2}(r)$ in these normalized coordinates for three different values of $R^{\rm c}_{\rm mol}$, chosen to match those of nearby galaxies with measured HI- and CO-densities (Leroy et al., 2008): NGC 4214, a star-forming, HI-rich, dwarf galaxy; NGC 5055, a massive spiral galaxy with similar HI- and H_2-masses; NGC 5194, a barred, H_2-rich spiral galaxy. The scale lengths $r_{\rm disk}$ and the densities $\tilde{\Sigma}_{\rm H}$ of these

galaxies were estimated by fitting exponential functions to $\Sigma_{\rm HI}(r) + \Sigma_{\rm H_2}(r)$ for each galaxy (NGC 4214/5055/5194: $R_{\rm mol}^{\rm c} = 0.1/11/34$, $r_{\rm disk} = 2.3/5.1/2.6$ kpc, $\tilde{\Sigma}_{\rm H} = 10/56/139\ {\rm M}_\odot\,{\rm pc}^{-2}$). The good fit between the model and the observations demonstrates the validity of the pressure-based model for the H_2/HI-ratio.

To evaluate $\Sigma_{\rm HI}(r)$ and $\Sigma_{\rm H_2}(r)$ using Eqs. (5.1–5.3), we require an estimate of $r_{\rm disk}$, $M_{\rm stars}^{\rm disk}$, and $M_{\rm gas}$. In Obreschkow et al. (2009a), we therefore adopted the cosmological galaxy simulation performed by De Lucia & Blaizot (2007) on the dark-matter skeleton of the Millennium Simulation (Springel et al., 2005). In this "semi-analytic" simulation, galaxies were represented by a list of global properties, such as position and total masses of gas, stars, and black holes. These properties were evolved using simplistic formulae for mechanisms, such as gas accretion by infall and mergers, star formation, gas heating by supernovae, and feedback from black holes. The free parameters in this model were tuned mostly to optical observations in the local universe (see Croton et al., 2006), such as the joint luminosity/colour/morphology distribution of optically observed low-redshift galaxies. However, no measurements of HI and H_2 were used to adjust the free parameters.

The semi-analytic simulation resulted in a catalog listing the properties of $\sim 3 \cdot 10^7$ model-galaxies at 64 cosmic time steps. In these galaxies, the cold gas was treated as a single component, hence masking the complexity of atomic and molecular phases. We therefore post-processed this simulation using Eqs. (5.1–5.3) to evaluate HI- and H_2-distributions for every galaxy. The results of the emerging HI and H_2 simulations were presented in Obreschkow et al. (2009a). They well match the HI- and H_2-mass functions, mass–diameter relations, and mass–velocity relations observed in the local Universe. The high-z predictions are roughly consistent with the sparse cold gas detections at $z > 0$ (Obreschkow & Rawlings, 2009b).

The limitations and uncertainties of this model for HI and H_2 at low z and high z were discussed in detail in Section 6 of Obreschkow et al. (2009a).

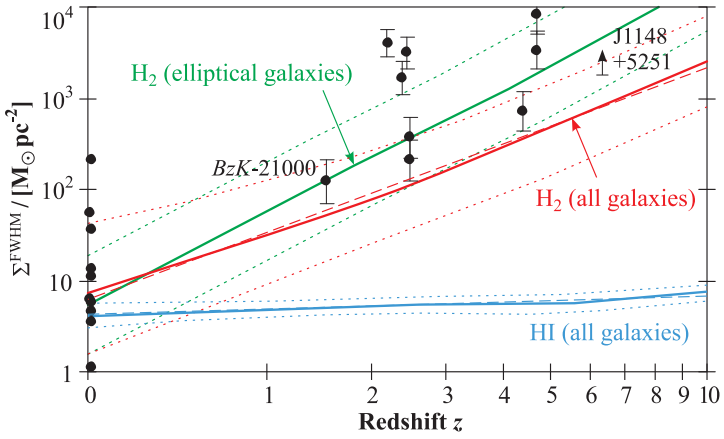

Figure 5.2. Solid and dotted lines show the simulated cosmic evolution of the surface densities $\langle\Sigma_{\rm HI}^{\rm FWHM}\rangle$ and $\langle\Sigma_{\rm H_2}^{\rm FWHM}\rangle$ with 1-σ scatter. These lines represent interpolations between 51 discrete redshifts between $z = 0$ and $z = 10$. At each redshift, the average value relies on $\sim 10^6 - 3 \cdot 10^7$ galaxies (the precise number depends on z). Dashed lines are the power law fits of Eqs. (5.4, 5.5). Points show the empirical data of Table 5.1.

5.3 Cosmic evolution of $\Sigma_{\rm HI}$ and $\Sigma_{\rm H_2}$

In this section, we shall investigate the average cosmic evolution of the surface densities of HI and H_2 in the simulated galaxies (see Section 5.2). We define the "average" $\langle ... \rangle$ as the $(M_{\rm HI} + M_{\rm H_2})$-weighted geometric average over all galaxies with $M_{\rm HI} + M_{\rm H_2} \geq 10^8 {\rm M}_\odot$. The threshold $M_{\rm HI} + M_{\rm H_2} = 10^8 {\rm M}_\odot$ approximately marks the completeness limit of the simulation and the mass-weighting ensures that massive galaxies with low space densities contribute significantly to the average.

For each, galaxy we define the Full-Width-Half-Maximum (FWHM) surface densities, $\Sigma_{\rm HI}^{\rm FWHM}$ and $\Sigma_{\rm H_2}^{\rm FWHM}$, as the average surface densities inside the radii r, where $\Sigma_{\rm HI}(r)$ and $\Sigma_{\rm H_2}(r)$ reach 50% of their maximal value. The simulated cosmic evolution of $\langle\Sigma_{\rm HI}^{\rm FWHM}\rangle$ and $\langle\Sigma_{\rm H_2}^{\rm FWHM}\rangle$ is displayed in Fig. 5.2 as solid lines. Both $\langle\Sigma_{\rm HI}^{\rm FWHM}\rangle(z)$ and $\langle\Sigma_{\rm H_2}^{\rm FWHM}\rangle(z)$ are well fitted by power-laws (dashed lines in

Fig. 5.2),

$$\langle \Sigma_{\rm HI}^{\rm FWHM}/[{\rm M}_\odot\,{\rm pc}^{-2}]\rangle(z) = 4.7\,(1+z)^{0.2}, \quad (5.4)$$

$$\langle \Sigma_{\rm H_2}^{\rm FWHM}/[{\rm M}_\odot\,{\rm pc}^{-2}]\rangle(z) = 7.1\,(1+z)^{2.4}. \quad (5.5)$$

The simulated HI-density remains roughly constant reaching maximal values around $8-9$ ${\rm M}_\odot\,{\rm pc}^{-2}$, consistent with the observed HI-saturation level in nearby galaxies (Bigiel et al., 2008). The simulated H_2-densities can be compared to CO-data. The data points in Fig. 5.2 (see also Table 5.1) represent 12 local and 11 distant galaxies with observational estimates of $\Sigma_{\rm H_2}^{\rm FWHM}$ derived from resolved CO-maps[1]. To our knowledge, none of these galaxies are gravitationally lensed.

At $z = 0$, the observed average of $\Sigma_{\rm H_2}^{\rm FWHM}$, weighted by the cold gas masses and the space densities drawn from the cold gas mass function (Obreschkow & Rawlings, 2009c), is $\langle\Sigma_{\rm H_2}^{\rm FWHM}\rangle = 7 \pm 1$ ${\rm M}_\odot\,{\rm pc}^{-2}$, consistent with the simulated value of $\langle\Sigma_{\rm H_2}^{\rm FWHM}\rangle = 7.9$ ${\rm M}_\odot\,{\rm pc}^{-2}$. However, at $z > 0$, the empirical densities $\Sigma_{\rm H_2}^{\rm FWHM}$ systematically exceed the simulated average values. This is perhaps a selection effect, since the CO-detected galaxies at $z > 0$ seem to be heavily biased towards systems subjected to major mergers (Tacconi et al., 2006). On average, major mergers decrease the specific angular momentum, hence decreasing $r_{\rm disk}$ and increasing $\Sigma_{\rm H_2}^{\rm FWHM}$.

This explanation can be tested by comparing the CO-measurements at $z > 0$ exclusively with the simulated galaxies with major mergers in their evolution. In the semi-analytic model, the evolution of the angular momentum during a merger is directly computed from the underlying N-body Millennium Simulation. We can therefore expect that, on average, mergers decrease the specific angular momentum, and hence increase the cold gas densities towards the high observed densities shown in Fig. 5.2. Within the semi-analytic model (Croton et al., 2006),

[1]The adopted CO-to-H_2 conversion is $X_{\rm CO} = 4\,{\rm K\,km\,s^{-1}\,pc^2}$ at $z = 0$ (Table 5.1, top), consistent with observations in local quiescent galaxies (Leroy et al., 2008); and $X_{\rm CO} = 1\,{\rm K\,km\,s^{-1}\,pc^2}$ for sources at $z > 0$ (Table 5.1, bottom), consistent with observations in Ultra Luminous Infrared Galaxies (Downes & Solomon, 1998).

Object	**Type**	**z**	**CO-line**	$\log(\mathbf{\Sigma}_{\mathrm{H_2}}^{\mathrm{FWHM}}/[\mathrm{M_\odot\,pc^{-2}}])$
NGC0628	Sc	0.0	2–1	$-0.4 \pm 0.1^{(a)}$
NGC3198	SBc	0.0	2–1	$0.7 \pm 0.1^{(a)}$
NGC3184	SBc	0.0	2–1	$0.6 \pm 0.1^{(a)}$
NGC4736	Sab	0.0	2–1	$1.2 \pm 0.1^{(a)}$
NGC3351	SBb	0.0	2–1	$0.1 \pm 0.1^{(a)}$
NGC6946	SBc	0.0	2–1	$2.4 \pm 0.1^{(a)}$
NGC3627	SBb	0.0	2–1	$1.6 \pm 0.1^{(a)}$
NGC5194	SBc	0.0	2–1	$1.1 \pm 0.1^{(a)}$
NGC3521	SBbc	0.0	2–1	$0.8 \pm 0.1^{(a)}$
NGC2841	Sb	0.0	2–1	$-0.1 \pm 0.1^{(a)}$
NGC5055	Sbc	0.0	2–1	$1.8 \pm 0.1^{(a)}$
NGC7331	SAb	0.0	2–1	$0.8 \pm 0.1^{(a)}$
BzK-21000	Galaxy	1.5	2–1	$2.1 \pm 0.2^{(b)}$
SMM J123549+6215	SMG	2.2	3–2	$3.6 \pm 0.1^{(c)}$
SMM J163650+4057	SMG	2.4	3–2	$3.3 \pm 0.2^{(c)}$
SMM J163658+4105	SMG	2.5	3–2	$3.5 \pm 0.2^{(c)}$
SMM J123707+6214SW	SMG	2.5	3–2	$2.4 \pm 0.2^{(c)}$
SMM J123707+6214NE	SMG	2.5	3–2	$2.6 \pm 0.2^{(c)}$
BRI 1335 0417	QSO	4.4	2–1	$2.9 \pm 0.2^{(d)}$
BRI 1202-0725 north	QSO	4.7	2–1	$3.6 \pm 0.2^{(d)}$
BRI 1202-0725 south	QSO	4.7	2–1	$4.0 \pm 0.2^{(d)}$
J1148+5251	QSO	6.4	3–2	$> 3.6^{(f)}$

Table 5.1. Local (top) and distant (bottom) galaxies with spatially resolved CO-detections, and corresponding estimated H_2-surface densities $\Sigma_{\mathrm{H_2}}^{\mathrm{FWHM}}$. (*a*) From radial H_2-density profiles given in Leroy et al. (2008); (*b*) from CO-fluxes and velocity peak separation measured by Daddi et al. (2008); (*c*) from Table 1 in Tacconi et al. (2006), for the submillimeter galaxy (SMG) SMM J163650+4057 the radius was averaged between semi-major and semi-minor axis, for SMM J123549+6215 the CO-flux was determined from CO(3–2) and the radius from CO(6–5); (*d*) from Carilli et al. (2002), BRI 1335 0417 probably has two non-resolved subcomponents; (*f*) Walter et al. (2004).

where stellar bulges arise during mergers, galaxies resulting from major mergers are "elliptical" galaxies, defined as the objects with a bulge-to-total mass ratio larger than 0.4 (see eq. 18 in Obreschkow et al., 2009a). The average $\langle \Sigma_{\mathrm{H_2}}^{\mathrm{FWHM}} \rangle$ and

the corresponding 1-σ scatter of the simulated elliptical galaxies are represented by the green lines in Fig. 5.2 and provide a much better fit to the observational data. The residual difference between the observations and the simulation may be related to uncertainties in the disk sizes in the simulation.

What are the reasons for the different cosmic evolutions of $\Sigma_{\rm HI}$ and $\Sigma_{\rm H_2}$? According to Eqs. (5.1–5.3), these evolutions can be understood from the average cosmic evolution of $r_{\rm disk}$, $M_{\rm gas}$, and $M_{\rm stars}$. Most of the massive galaxies in the semi-analytic simulation are gas-dominated at $z > 1$ and their cold gas masses remain roughly constant with cosmic time due to a self-regulated equilibrium between the net cold gas accretion and star formation. Thus, for any given galaxy, the cosmic evolution of the value $R^{\rm c}_{\rm mol}$ and the functions $\Sigma_{\rm HI}(r)$ and $\Sigma_{\rm H_2}(r)$ is essentially dictated by the evolution of the scale radius $r_{\rm disk}$. Assuming a similar specific angular momentum for the galaxy and its halo (Fall & Efstathiou, 1980), $r_{\rm disk}$ is expected to evolve proportionally to the virial radius $r_{\rm vir}$ of the halo. For a spherical halo of mass $M_{\rm vir}$, the latter scales as $r^3_{\rm vir} \propto M_{\rm vir}/\left[\Omega_{\rm m}(1+z)^3 + \Omega_\Lambda\right]$ (flat universe, Gunn & Gott, 1972), and hence for a fixed $M_{\rm vir}$,

$$r_{\rm disk} \propto \left[\Omega_{\rm m}(1+z)^3 + \Omega_\Lambda\right]^{-1/3}, \tag{5.6}$$

where $\Omega_{\rm m}$ (here 0.25) and Ω_Λ (here 0.75) denote the normalized space densities of matter and vacuum energy.

At high z, Eq. (5.6) reduces to $r_{\rm disk} \propto (1+z)^{-1}$, consistent with observations in the Hubble Ultra Deep Field (Bouwens et al., 2004). If the cosmic evolution of $M_{\rm gas}$ and $M_{\rm stars}$ is neglected, then $r_{\rm disk} \propto (1+z)^{-1}$ implies $R^{\rm c}_{\rm mol} \propto (1+z)^{3.2}$ (see Eq. 5.3) and $\tilde{\Sigma}_{\rm H} \propto (1+z)^2$. Yet, for $R^{\rm c}_{\rm mol} > 5/3$, the maximum of $\Sigma_{\rm HI}(r)$ is given by $\Sigma^{\rm max}_{\rm HI} = 0.516\,\tilde{\Sigma}_{\rm H}\,{R^{\rm c}_{\rm mol}}^{-5/8}$ (see Obreschkow et al., 2009a) and hence $\Sigma^{\rm max}_{\rm HI} \propto (1+z)^2\,(1+z)^{-2} = {\rm const}$. In other words, the surface density of HI is expected to show little evolution with redshift, consistent with the numerical fit for $\langle\Sigma^{\rm FWHM}_{\rm HI}\rangle(z)$ of Eq. (5.4). On the other hand, $\Sigma_{\rm H_2}(r)$ in Eq. (5.2) reduces to $\tilde{\Sigma}_{\rm H}\,\exp(-r/r_{\rm disk})\;\forall\, r > 0$, if $R^{\rm c}_{\rm mol} \gg 1$ (i.e. $z \gg 1$). Hence, if the cosmic evolution

of $M_{\rm gas}$ is negligible, $\Sigma_{\rm H_2}^{\rm max}$ and $\Sigma_{\rm H_2}^{\rm FWHM}$ are predicted to scale as $\propto \tilde{\Sigma}_{\rm H} \propto (1+z)^2$. A comparison to Eq. (5.5) confirms that, within our model, the cosmic evolution of $\Sigma_{\rm H_2}$ is largely explained by the size-evolution of galaxies, while the evolution of $M_{\rm gas}$ plays a minor role, accounting for an additional $\propto (1+z)^{0.4}$ scaling.

5.4 Evolution Scenario for the Milky Way

We shall now investigate the cosmic evolution of the HI- and H_2-distributions in MW-type galaxies. By definition, a simulated galaxy at $z = 0$ is called a "MW-type" galaxy, if its morphological type is Sb–Sc and if it matches the stellar mass $M_{\rm stars}$, the HI-mass $M_{\rm HI}$, the H_2-mass $M_{\rm H_2}$, the HI-half-mass radius $r_{\rm HI}^{\rm half}$, and the H_2-half-mass radius $r_{\rm H_2}^{\rm half}$ of the MW within a factor 1.3. This factor roughly matches the empirical uncertainties of the MW data in Table 5.2. Within this definition, the simulation contains $2{\cdot}10^3$ MW-type galaxies at $z = 0$. At $z > 0$, we define MW-type galaxies as those objects, which are the most massive progenitors of a MW-type galaxy at $z = 0$. Most MW-type galaxies accrete about half of their mass in a time-interval corresponding to the redshift range $z = 2-10$. They typically undergo a series of minor mergers, allowing the build-up of small bulges.

To accommodate the nature of the empirical data (e.g. poor data for gas at the MW center), we here consider the half-mass radii $r_{\rm HI}^{\rm half}$ and $r_{\rm H_2}^{\rm half}$, and the enclosed average surface densities $\Sigma_{\rm HI}^{\rm half}$ and $\Sigma_{\rm H_2}^{\rm half}$, rather than FWHM values.

In Table 5.2, we explicitly present the predicted average gas masses, gas radii, and gas densities of the $2 \cdot 10^3$ MW-type galaxies at three specific redshifts: $z = 0$, corresponding to the MW itself; $z = 1.5$, corresponding to the galaxy BzK-21000, which is the only ordinary (i.e. non-ultra luminous) galaxy at higher z detected and spatially resolved in CO-emission to-date; $z = 3$, corresponding to the primary science goal of ALMA, i.e. the detection of MW-type galaxies at $z = 3$ in less than 24 hours observation. Fig. 5.3 illustrates the average density profiles $\Sigma_{\rm HI}(r)$ and $\Sigma_{\rm H_2}(r)$ at these three redshifts.

The cosmic evolution of the average HI- and H_2-properties of the simulated

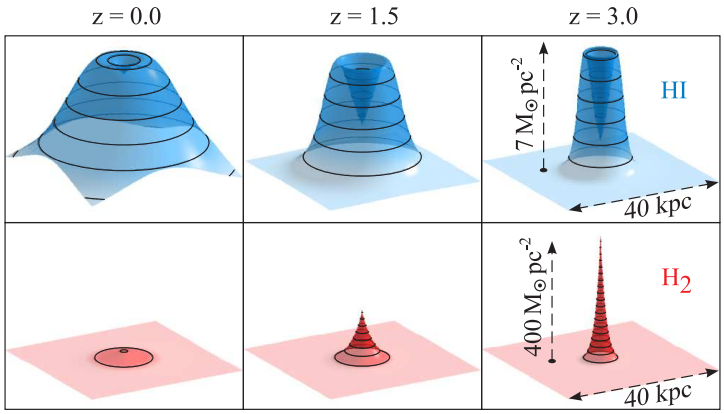

Figure 5.3. Cosmic evolution of the average profiles $\Sigma_{\rm HI}(r)$ and $\Sigma_{\rm H_2}(r)$ calculated from $2 \cdot 10^3$ simulated MW-type galaxies. The contours are spaced by $1\,{\rm M}_\odot\,{\rm pc}^{-2}$ for HI and $20\,{\rm M}_\odot\,{\rm pc}^{-2}$ for H_2, with the bottom contour corresponding to the separation value. The redshifts $z = 1.5$ and $z = 3$ respectively correspond to the galaxy BzK-21000 (Daddi et al., 2008) and to the primary science goal of ALMA, i.e. the detection of MW-type galaxies at $z = 3$ in less than 24 hours observation.

MW-type galaxies can be characterized as follows: (i) the mass ratio $M_{\rm H_2}/M_{\rm HI}$ approximately varies as $(1+z)^{1.6}$, identical to the space density evolution $\Omega_{\rm H_2}/\Omega_{\rm HI} \propto (1+z)^{1.6}$ predicted in Obreschkow & Rawlings (2009b); (ii) the surface density of HI remains approximately constant, while the density of H_2 increases by a factor 30 from $z = 0$ to $z = 3$; (iii) both the HI-radius and the H_2-radius shrink by a factor $4 - 5$ from $z = 0$ to $z = 3$; (iv) the HI-distribution is more annular at high z (see Fig. 5.3), resembling the central HI-deficiency seen in H_2-rich local galaxies.

The comparison of the galaxy BzK-21000 (Daddi et al., 2008) and the MW-type galaxies at $z = 1.5$ (see Table 5.2) suggests that the H_2-density of BzK-21000 is consistent with that of a typical MW progenitor, while the total H_2-mass of BzK-21000 may be a few times higher. Considering that the MW lies at the lower end of intermediate mass spiral galaxies (stellar masses $M_{\rm stars}$ in the range $3 \cdot 10^{10} - 3 \cdot 10^{11}$ $M_\odot$; Flynn et al., 2006), the H_2-distribution of BzK-21000 appears to be typical for the progenitors of intermediate mass disk galaxies.

	Sim/MW	Sim/BzK	Sim
Redshift z	0.0	1.5	3.0
Type	Sb-c/SBbc	Sc/S?	Sc-d
$M_{\rm stars}/[10^{10}{\rm M}_\odot]$	$5^{+0.3}_{-0.2}/5^{+1}_{-1}$(a)	$1.7^{+0.2}_{-0.2}/6^{+1}_{-1}$	$0.5^{+0.1}_{-0.1}$
$M_{\rm HI}/[10^{9}{\rm M}_\odot]$	$7.8^{+0.4}_{-0.3}/8^{+2}_{-2}$(b)	$2.3^{+0.9}_{-0.5}/?$	$0.7^{+0.3}_{-0.2}$
$r_{\rm HI}^{\rm half}/[{\rm kpc}]$	$16^{+0.5}_{-0.4}/15^{+5}_{-5}$(b)	$7.3^{+1.2}_{-0.8}/?$	$3.9^{+0.7}_{-0.5}$
$\Sigma_{\rm HI}^{\rm half}/[{\rm M}_\odot{\rm pc}^{-2}]$	$4.5^{+0.1}_{-0.1}/6^{+3}_{-3}$(b)	$5.4^{+0.3}_{-0.3}/?$	$5.5^{+0.4}_{-0.4}$
$M_{\rm H_2}/[10^{9}{\rm M}_\odot]$	$3.5^{+0.2}_{-0.2}/3.5^{+1}_{-1}$(c)	$4.6^{+0.7}_{-0.5}/17^{+5}_{-5}$	$2.9^{+0.7}_{-0.4}$
$r_{\rm H_2}^{\rm half}/[{\rm kpc}]$	$6.8^{+0.2}_{-0.2}/7^{+1}_{-1}$(c)	$2.9^{+0.5}_{-0.4}/4^{+1}_{-1}$	$1.4^{+0.3}_{-0.2}$
$\Sigma_{\rm H_2}^{\rm half}/[{\rm M}_\odot{\rm pc}^{-2}]$	$12^{+1}_{-1}/11^{+3}_{-3}$(c)	$130^{+50}_{-20}/150^{+50}_{-50}$	360^{+190}_{-70}

Table 5.2. Average value and 1-σ scatter of the cold gas and stellar properties of $2 \cdot 10^3$ simulated MW-type galaxies (Sim) at $z = 0$, $z = 1.5$, and $z = 3$. The actual measurements of the MW with 1-σ uncertainties were adopted from: (a) Flynn et al. (2006); (b) from analytic fits to $\Sigma_{\rm HI}(r)$ in Kalberla & Dedes (2008); (c) from $\Sigma_{\rm H_2}(r)$ in Table 3 in Sanders et al. (1984). The properties of the simulated MW-type galaxies at $z = 1.5$ are compared to those of the CO-detected galaxy BzK-21000 (Daddi et al., 2008).

5.5 Conclusion

We have studied the cosmic evolution of the surface densities of HI and H_2 in regular galaxies using theoretical models combined with the Millennium Simulation.

A key result is that the surface density of HI remains approximately constant and close to saturation at all redshifts, while the mean surface density of H_2 changes dramatically as $\propto (1+z)^{2.4}$, mainly due to the size evolution of galaxies. These predictions will become testable with future telescopes such as ALMA and the SKA. The few CO-detected high-z galaxies available today seem to have even higher H_2-surface densities than predicted by the $\propto (1+z)^{2.4}$ scaling (see Fig. 5.2). This could result from a selection bias towards systems, which have lost some of their angular momentum in major mergers.

We also studied the cosmic evolution of the cold gas in a sample of MW-type galaxies. We predicted that at $z = 3$ the H_2-mass of a MW-type galaxy is

$M_{\mathrm{H_2}} \approx 3 \cdot 10^9\,\mathrm{M}_\odot$ with the denser 50% of this mass reaching an average surface density of $\Sigma_{\mathrm{H_2}}^{\mathrm{half}} \approx 300 - 500\,\mathrm{M}_\odot\mathrm{pc}^{-2}$.

Acknowledgements

This effort/activity is supported by the European Community Framework Programme 6, Square Kilometre Array Design Studies (SKADS), contract no 011938. The Millennium Simulation databases and the web application providing online access to them were constructed as part of the activities of the German Astrophysical Virtual Observatory.

Chapter 6

A heuristic model for CO-emission lines

D. Obreschkow, I. Heywood, H.-R. Klöckner, and S. Rawlings

"A Heuristic prediction of the cosmic evolution of the CO-luminosity functions"

ApJ, accepted (2009)

We predict the emission line luminosity functions (LFs) of the first 10 rotational transitions of $^{12}C^{16}O$ in galaxies at redshift $z = 0$ to $z = 10$. This prediction relies on a recently presented simulation of the molecular cold gas content in $\sim 3 \cdot 10^7$ evolving galaxies based on the Millennium Simulation. We combine this simulation with a model for the conversion between molecular mass and CO-line intensities, which incorporates the following mechanisms: (i) molecular gas is heated by the CMB, starbursts (SBs), and active galactic nuclei (AGNs); (ii) molecular clouds in dense or inclined galaxies can overlap; (iii) compact gas can attain a smooth distribution in the densest part of disks; (iv) CO-luminosities scale with metallicity changes between galaxies; (v) CO-luminosities are always detected against the CMB. We analyze the relative importance of these effects and predict the cosmic evolution of the CO-LFs. The most notable conclusion is that the detection of regular galaxies (i.e. no AGN, no massive SB) at high $z \gtrsim 7$ in CO-emission will be dramatically hindered by the weak contrast against the CMB, in contradiction to earlier claims that CMB-heating will ease the detection of high-redshift CO. The full simulation of extragalactic CO-lines and the predicted CO-LFs at any redshift can be accessed online[1] and they should be useful for the modeling of CO-line surveys with future telescopes, such as ALMA, the LMT, or the SKA.

[1] http://www.g-vo.org/Millennium/, prior registration required

6.1 Introduction

An increasing body of evidence suggests that molecular hydrogen (H_2) widely dominated over atomic hydrogen (HI) in the regular galaxies of the early universe (e.g. Obreschkow & Rawlings, 2009b). Empirical corner stones towards this conclusion were the measurement of strong CO-line emission in distant regular galaxies (Daddi et al., 2008), the detection of HI via Lyman-α absorption against distant quasars (e.g. Prochaska et al., 2005), the observational confirmation of a correlation between the interstellar gas pressure and H_2/HI-ratios (Blitz & Rosolowsky, 2006), and the observational confirmation that galaxy sizes increase significantly with cosmic time (e.g. Bouwens et al., 2004).

In light of future millimeter/submillimeter telescopes, such as the Atacama Large Millimeter/submillimeter Array (ALMA) or the Large Millimeter Telescope (LMT), much attention is directed towards the possibility of detecting the suspected molecular gas (mostly H_2) at high redshift via the characteristic emission lines of the CO-molecule. However, the case for frequent CO-detections in regular high-redshift galaxies is by no means secure, since neither the cosmic evolution of the H_2-mass function (MF), nor the evolution of the relationship between H_2-masses and CO-line luminosities is well constrained to-date. An elucidation of this situation seems nevertheless within reach, owing to a long list of specific discoveries over the past two decades (Section 6.3), based on which computer simulations could already predict the CO-line emission of individual high-redshift galaxies in some detail (e.g. Combes et al., 1999, Greve & Sommer-Larsen, 2008). Moreover, Blain et al. (2000) and Carilli et al. (2002) predicted the number of detectable CO-sources in various frequency ranges. They assumed that the CO-line luminosities evolve with the far-IR (FIR) luminosity, and they tackled the cosmic evolution of the FIR-luminosity function by considering a pure density evolution. While this approach is perhaps justified at low redshifts, it probably oversimplifies the physical complexity of CO-emission at high redshift ($z > 1$) as we shall show in this paper.

A missing jigsaw piece in the bigger picture is a physical prediction of the cosmic evolution of the galaxy luminosity functions (LFs) for different CO-emission lines. In this paper, we will attempt such a prediction by concatenating many specific empirical and theoretical findings about H_2 and CO. The two main steps towards our prediction of the CO-LFs are (i) a model for the cosmic evolution of the H_2-MF and (ii) a model for the conversion between H_2-masses and CO-line luminosities. In this paper, we shall focus on the latter, while adopting the H_2-masses of a sample of $\sim 3 \cdot 10^7$ galaxies (Obreschkow et al., 2009a), simulated based on the Millennium dark matter simulation (Springel et al., 2005).

In Section 6.2, we summarize the galaxy simulation producing the H_2-masses and various other galaxy-properties related to CO-line emission. Our model for CO-line luminosities is developed in Section 6.3. Section 6.5 presents the prediction of the cosmic evolution of the CO-LFs and discusses their dependence on the mechanisms listed at the beginning of Section 6.3. Section 6.6 ranks the relative importance of these mechanisms and discusses the limitations of their implementation. A brief summary is given in Section 6.7.

6.2 Simulation of the H_2-MF

This section summarizes the cold gas simulation presented in Obreschkow et al. (2009a). Main results and limitations were discussed in detail by Obreschkow et al. (2009a) and Obreschkow & Rawlings (2009b).

The simulation has three consecutive layers. The first layer is the Millennium Simulation (Springel et al., 2005), an N-body dark matter simulation in a periodic box of comoving volume $(500\,h^{-1}\,\mathrm{Mpc})^3$, where $H_0 = 100\,h\,\mathrm{km\,s^{-1}\,Mpc^{-1}}$ and $h = 0.73$. The second simulation layer uses the evolving mass skeleton of the Millennium Simulation to tackle the formation and cosmic evolution of galaxies in a semi-analytic fashion (Croton et al., 2006, De Lucia & Blaizot, 2007). This is a global approach, where galaxies are represented by a list of global properties, such as position, velocity, and total masses of gas, stars, and black holes.

These properties were evolved using simplistic formulae for mechanisms, such as gas cooling, reionization, star formation, gas heating by supernovae, starbursts, black hole accretion, black hole coalescence, and the formation of stellar bulges via disk instabilities. The resulting virtual galaxy catalog (hereafter the "DeLucia-catalog") contains the positions, velocities, merger histories, and intrinsic properties of $\sim 3 \cdot 10^7$ galaxies at 64 cosmic time steps. At redshift $z = 0$, galaxies as low in mass as the Small Magellanic Cloud are resolved. The free parameters in the semi-analytic model were tuned to various observations in the local universe (see Croton et al., 2006). Therefore, despite the simplistic implementation and the possible incompleteness of this model, the simulated galaxies nonetheless provide a good fit to the joint luminosity/colour/morphology distribution of observed low-redshift galaxies (Cole et al., 2001, Huang et al., 2003, Norberg et al., 2002), the bulge-to-black hole mass relation (Häring & Rix, 2004), the Tully–Fisher relation (Giovanelli et al., 1997), and the cold gas metallicity as a function of stellar mass (Tremonti et al., 2004).

The cold gas masses of the simulated galaxies are the net result of gas accretion by cooling from a hot halo (dominant mode) and galaxy mergers, gas losses by star formation and feedback from supernovae, and cooling flow suppression by feedback from accreting black holes. The DeLucia-catalog does not distinguish between molecular and atomic cold gas, but simplistically treats all cold gas as a single phase. Therefore, the third simulation layer, explained by Obreschkow et al. (2009a), consists of post-processing the DeLucia-catalog to split the cold gas masses of each galaxy into HI, H_2, and He. Our model for this subdivision mainly relies on three empirical findings: (i) Most cold gas in regular spiral (Leroy et al., 2008) and elliptical galaxies (Young, 2002) in the local universe resides in flat disks, and there is evidence that this feature extends to higher redshifts (e.g. Tacconi et al., 2006). (ii) The surface density of the total hydrogen component (HI+H_2) is approximately described by an axially symmetric exponential profile

(Leroy et al., 2008),

$$\Sigma_{\rm H}(r) = \tilde{\Sigma}_{\rm H}\, \exp(-r/r_{\rm disk})\,, \tag{6.1}$$

where $r_{\rm disk}$ is the exponential scale length and the normalization factor $\tilde{\Sigma}_{\rm H}$ can be calculated as $\tilde{\Sigma}_{\rm H} \equiv M_{\rm H}/(2\pi r_{\rm disk}^2)$, where $M_{\rm H}$ is the total mass of cold hydrogen in the disk. (iii) The local H_2/HI-mass ratio closely follows the gas pressure of the interstellar medium outside molecular clouds over at least four orders of magnitude in pressure and for various galaxy types (Blitz & Rosolowsky, 2006, Leroy et al., 2008). Based on those findings, we (Obreschkow et al., 2009a) derived an analytic expression of the HI- and H_2-surface density profiles,

$$\Sigma_{\rm HI}(r) = \frac{\tilde{\Sigma}_{\rm H}\, \exp(-r/r_{\rm disk})}{1 + R^{\rm c}_{\rm mol} \exp(-1.6\, r/r_{\rm disk})}\,, \tag{6.2}$$

$$\Sigma_{\rm H_2}(r) = \frac{\tilde{\Sigma}_{\rm H}\, R^{\rm c}_{\rm mol}\, \exp(-2.6\, r/r_{\rm disk})}{1 + R^{\rm c}_{\rm mol} \exp(-1.6\, r/r_{\rm disk})}\,, \tag{6.3}$$

where $R^{\rm c}_{\rm mol}$ is the H_2/HI-mass ratio at the galaxy center. This model was applied to the galaxies in the DeLucia-catalog to characterize their HI and H_2 content (masses, diameters, and circular velocities). The resulting hydrogen simulation successfully reproduces many local observations of HI and H_2, such as MFs, mass–diameter relations, and mass–velocity relations (Obreschkow et al., 2009a). This success is quite surprising, since our model for HI and H_2 only introduced one additional free parameter to match the observed average space density of cold gas in the local universe (Obreschkow et al., 2009a). A key prediction of this simulation is that the H_2/HI-ratio of most regular galaxies increases dramatically with redshift, hence causing a clear signature of cosmic "downsizing" in the H_2-MF (Obreschkow & Rawlings, 2009b), i.e. a negative shift in the mass scale with cosmic time.

The simulated H_2-MF at $z = 0$ approximately matches the local H_2-MF inferred from the local CO(1–0)-LF (Keres et al., 2003, Obreschkow & Rawlings, 2009c), and the few measurements of CO-line emission from regular galaxies at $z \approx 1.5$ (Daddi et al., 2008) are consistent with the predicted H_2-MF at this

redshift (Obreschkow & Rawlings, 2009b). Furthermore, the predicted comoving space density of H_2 evolves proportionally to the observed space density of star formation rates (e.g. Hopkins, 2007) within a factor 2 out to at least $z = 3$. For those reasons, we expect the simulated H_2-MF to scale reasonably well with redshift. Yet, at $z \gtrsim 5$ the simulation becomes very uncertain because the geometries and matter content of regular galaxies are virtually unconstrained from an empirical viewpoint. The young age and short merger intervals of these galaxies compared to their dynamical time scales, may have caused them to deviate substantially from the simplistic disk-gas model. An extended discussion of these and other limitations at low and high redshift is given in Section 6.3 of Obreschkow et al. (2009a).

6.3 Model for the CO/H_2 conversion

Most detections of H_2 rely on emission lines originating from the relaxation of the rotational J-levels of the $^{12}C^{16}O$-molecule (hereafter "CO"). Appendix 6.9 provides background information on the inference of H_2-masses from CO-line measurements and highlights the justification and drawbacks of this method.

To predict the CO-line luminosities associated with the molecular gas masses of the simulated galaxies (Section 6.2), we shall now introduce a simplistic, but physically motivated model for the conversion between H_2-masses and CO-luminosities at any redshift. This model aims to respect the following theoretical and empirical constraints:

1. The temperature of molecular gas depends on the temperature of the CMB and on the radiative feedback from starbursts (SBs) and active galactic nuclei (AGNs).

2. Molecular clumps can shield each other if they overlap along the line-of-sight and in velocity space. This effect may not be negligible in the dense galaxies at high redshift, especially if observed edge-on.

3. While locally observed molecular gas is organized in Giant Molecular Clouds (GMCs), the dense gas in compact luminous galaxies, such as Ultra Luminous Infrared Galaxies (ULIRGs), is predicted to follow a smooth distribution.

4. The CO-line emission of molecular gas is correlated with the CO/H_2-mass ratio, i.e. to the metallicity of the galaxy.

5. The CMB presents an observing background. The absorption of CO-lines against the CMB may significantly reduce the effectively detectable luminosities of CO-emission lines.

These mechanisms will be modeled one by one over the Sections 6.3.1–6.3.5.

6.3.1 Gas temperature and the CO-ladder

To model the luminosity-ratios of different CO-lines, we analyzed the CO-spectral energy distributions (SEDs) of nine galaxies drawn from the literature (see Fig. 6.1 and references therein). This sample includes local regular galaxies, local and distant SBs, and distant quasi stellar objects (QSOs). Four of these sources (SMM J16359+6612, F10214+4724, APM 08279+5255, Cloverleaf H1413+135) are known to be strongly magnified by gravitational lensing. We assume that this has no major effect on the flux-ratios between different CO-lines. This assumption relies on the fact that the lensed galaxies are far-infrared-bright objects, which makes it likely that the strongly lensed regions include the star-bursting ones. Those are also the high-excitation regions, which seem to dominate the CO-emission of most CO-lines (see discussion of M 82 in this Section).

Surprisingly, all nine CO-SEDs are well fitted by a model for a single gas component in local thermodynamic equilibrium (LTE). In Appendix 6.10, we show that the frequency-integrated line luminosities (= power) of such a model

scales with the upper level J of the transition as

$$L_{\rm J} \propto [1 - \exp(-\tau_{\rm J})] \cdot \frac{J^4}{\exp\left(\frac{h_{\rm p}\,\nu_{\rm CO}\,J}{k_{\rm b}\,T_{\rm ex}}\right) - 1}, \tag{6.4}$$

where $T_{\rm ex}$ is the excitation temperature, $\nu_{\rm CO} = 115\,{\rm GHz}$ is the rest-frame frequency of the CO(1–0)-transition, and $\tau_{\rm J}$ is the optical depth. The latter scales with J as

$$\tau_{\rm J} = 7.2\,\tau_{\rm c}\,\exp\!\left(-\frac{h_{\rm p}\,\nu_{\rm CO}\,J^2}{2\,k_{\rm b}\,T_{\rm ex}}\right)\sinh\!\left(\frac{h_{\rm p}\,\nu_{\rm CO}\,J}{2\,k_{\rm b}\,T_{\rm ex}}\right), \tag{6.5}$$

where $\tau_{\rm c}$ is a constant. The factor 7.2 in Eq. (6.5) was introduced in order for $\tau_{\rm c}$ to correspond to the optical depth of the CO(1–0) line (i.e. $\tau_1 = \tau_{\rm c}$) at the excitation temperature $T_{\rm ex} \approx 17\,{\rm K}$, which is the lowest temperature of our model (see end of this Section).

If normalized to the CO(1–0)-luminosity L_1, the LTE-model of Eqs. (6.4, 6.5) has two free parameters $\tau_{\rm c}$ and $T_{\rm ex}$. In order to apply this model to the velocity-integrated fluxes $S^{\rm V}_{\rm J}$ shown in Fig. 6.1, we use the relation $L_{\rm J} \propto J\,S^{\rm V}_{\rm J}$ (see Appendix 6.8, Eq. 6.33).

We first fitted the LTE-model to the observed CO-SEDs individually via χ^2-minimization. The resulting 1-σ confidence intervals of the temperatures $T_{\rm ex}$ equal $10 - 20\%$ of their best-fit values. Despite this uncertainty, a clear dependence of $T_{\rm ex}$ on the galaxy types (regular, SB, QSO) can de detected (see below). By contrast, the parameters $\tau_{\rm c}$ are poorly constrained. Their best-fit values range from 0.5 to 5 with no clear trend amongst the different galaxy types, and their confidence intervals are such that a single parameter $\tau_{\rm c}$ for all CO-SEDs seems to provide a consistent solution. We therefore tested a second model, where all nine SEDs share the same parameter $\tau_{\rm c}$, and found that the Bayesian evidence (e.g. Sivia & Skilling, 2006) of this 10-parameter model ($1 \times \tau_{\rm c}$, $9 \times T_{\rm ex}$) against the 18-parameter model ($9 \times \tau_{\rm c}$, $9 \times T_{\rm ex}$) is "strong" with odds of order $10^5 : 1$. We therefore assume a single parameter $\tau_{\rm c}$ for all galaxies, emphasizing, however, that the actual optical depth $\tau_{\rm J}$ varies considerably as a function of J and $T_{\rm ex}$ by

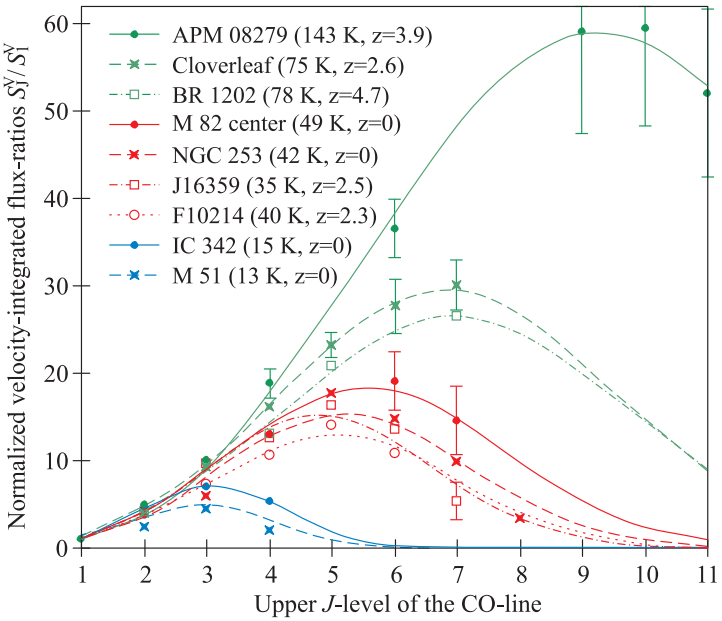

Figure 6.1. CO-SEDs of nine nearby and distant galaxies: APM 08279+5255 (Weiss et al., 2007), Cloverleaf H1413+117 (Barvainis et al., 1997), BR 1202-0725 (Kawabe et al., 1999, Omont et al., 1996), the central region of M 82 (Weiss et al., 2005b), NGC 253 (Güsten et al., 2006), SMM J16359+6612 (Weiss et al., 2005a), IRAS F10214+4724 (Ao et al., 2008), IC 342 (Israel & Baas, 2003), M 51 (Nieten et al., 1999, Wielebinski et al., 1999). Symbols and error bars represent the measurements, but to avoid confusion, only some error bars are displayed. The lines represent fits of our model for thermalized gas with finite optical depth, and the corresponding excitation temperatures $T_{\rm ex}$ are indicated for each galaxy. Different colors are used for regular galaxies (blue), SBs (red), QSOs (green).

virtue of Eq. (6.5). The best fit to all nine SEDs yields $\tau_{\rm c} = 2$, consistent with the moderate optical depths for different CO-lines found by Barvainis et al. (1997) in the Cloverleaf quasar. The excitation temperatures $T_{\rm ex}$ corresponding to $\tau_{\rm c} = 2$ are listed in Fig. 6.1. The individual reduced χ^2's for each galaxy range from 0.5 to 1.2, hence demonstrating that the LTE-model with a single parameter $\tau_{\rm c}$ provides an excellent fit to all observed CO-line-ratios.

This conclusion justifies the use of the single component LTE-model as a *working model*, but it does not imply that this model describes the *physical reality* of molecular gas. In fact, it seems that neither the assumption of LTE-conditions, nor that of a single gas component are fully satisfied in reality.

Firstly, the density of molecular gas is often too low to collisionally excite the higher rotational levels to thermal equilibrium. In this case, the LTE-conditions are not met. A more accurate description of the excitation state is then provided by so-called large velocity gradient (LVG) models (de Jong et al., 1975), which are more complex than the LTE-model. A plausible explanation for the surprising success of the LTE-model is that the suppression of high-J emission by sub-thermal excitation can be approximately mimicked by a thermalized gas with a slightly underestimated optical depth, or a temperature $T_{\rm ex}$ slightly below the kinetic temperature of the gas. Another explanation is that in real clouds the sub-thermal excitation of high-J states could be compensated by a minor fraction of much warmer ($\sim$100 K) and denser molecular gas, such as is seen next to the star-forming cores in nearby molecular clouds (e.g. the "ridge" in the Orion molecular cloud, Lis & Schilke, 2003). In any case, we stress that the temperatures $T_{\rm ex}$ identified by our LTE-analysis should not be considered as very accurate. Better models, albeit more complex, can be found in the references of Fig. 6.1.

Secondly, the assumption of a single component seems to work because in most galaxies one component widely dominates the total CO-SED. A good example to illustrate this conclusion and its limitations is the nearby starburst M 82, for which the CO-SED up to the CO(7–6)-transition has been presented by Weiss et al. (2005b). The CO-SED of the center of M 82 is displayed in Fig. 6.1 and is reasonably well described by a LTE-model (reduced $\chi^2 = 1.1$). Yet, an in-depth LVG-analysis (Fig. 7 in Weiss et al., 2005b) revealed that the center of M 82 exhibits a low-excitation (LE) and a high-excitation (HE) component with kinetic temperatures of $\sim$ 50 K (perhaps higher for the LE component), consistent with the single temperature of the LTE-model of 49 K (see Fig. 6.1). In terms of

velocity-integrated fluxes, the CO-SED of the LE component peaks around the upper level $J = 3-4$, while the HE component peaks around $J = 6-7$. However, the flux from the HE component completely dominates the combined CO-SED, such that the latter still peaks around $J = 6 - 7$. This domination of the HE component justifies the use of a single component as a working model. Moreover, the domination of the HE component, in which the excitation conditions are close to LTE, adds another reason for the aforementioned success of the LTE-model. The limitations of the single component model become obvious, when considering the CO-SED of the entire galaxy M 82 (Weiss et al., 2005b). The exceptionally strong gas outflows from the star-bursting center add an additional LE component, which dominates the total CO-SED up to the CO(3–2)-transition or perhaps the CO(4–3)-transition. The success of the single component model for the other three SBs in Fig. 6.1 suggests that the strongly CO-luminous outflows of M 82 are rather anomalous.

Despite the above limitations of the single component LTE-model, we shall use this model for the rest of this paper for three reasons: (i) given current computational resources, applying an LVG-model to $\sim 10^9$ galaxies (i.e. up to $\sim 3{\cdot}10^7$ galaxies per discrete time step) is highly impractical; (ii) as demonstrated above (e.g. Fig. 6.1), the LTE-model is a reasonable working model in the sense that it can approximately fit most observed CO-SEDs; (iii) the differences between the LTE-model and the LVG-model are often much smaller than the uncertainties associated with other mechanisms, such as cloud overlap in high-z galaxies, metallicity, or gas heating by SBs (see Section 6.6.2).

Fig. 6.1 demonstrates that the characteristic excitation temperatures $T_{\rm ex}$ increase from regular galaxies to SBs, and more so to QSOs. This supports the interpretation of gas-heating by radiation from SBs and AGNs (see also observations of Weiss et al., 2007 and theoretical work of Maloney & Black, 1988). On the other hand, $T_{\rm ex}$ must also depend on the temperature of the CMB at the redshift of the source (Combes et al., 1999, Silk & Spaans, 1997).

We assume that in regular galaxies the molecular gas is heated by a constant specific power (i.e. power per unit gas mass), representing the intra-cloud radiative heating by massive stars and supernovae associated with regular star formation efficiencies. This specific power implies a minimal temperature T_0 for the bulk of the molecular gas. In addition, the CMB represents a background temperature of $T_{\rm CMB}(z) = (1+z) \cdot 2.7\,{\rm K}$. If the radiative heating of molecular gas happens via absorption by optically thick dust, then the resulting gas temperature or the CO-excitation temperature is $T_{\rm ex}^4 \approx T_0^4 + T_{\rm CMB}(z)^4$, as can be seen from combining the Stefan-Boltzmann law with the conservation of energy. Following the same argument, we can also include the heating of SBs and AGNs via

$$T_{\rm ex}^4 = T_0^4 + T_{\rm CMB}^4(z) + T_{\rm SB}^4 + T_{\rm AGN}^4, \tag{6.6}$$

where $T_{\rm SB}$ and $T_{\rm AGN}$ are galaxy-dependent parameters characterizing the estimated temperatures of the molecular gas, if respectively SB-feedback or AGN-feedback were the only sources of radiative heating. Combes et al. (1999) pointed out that, if the radiative transfer is mediated by optically thin dust with an optical depth proportional to λ^{-2}, the exponents in Eq. (6.6) should be increased from 4 to 6. In reality the exponents in Eq. (6.6) are therefore likely to be somewhat higher than 4. Yet, Eq. (6.6) only depends on the precise value of the exponents in the few cases where the highest temperatures on the right-hand-side are comparable, while otherwise the highest temperature predominates $T_{\rm ex}$.

In the following, we require that the specific radiation power ($\propto T_{\rm SB}^4$) acquired by the molecular gas from SBs, increases proportionally to the surface density of the star formation rate (SFR) $\Sigma_{\rm SF}$ for small values of $\Sigma_{\rm SF}$, while saturating at an upper limit, characterized by the temperature $T_{\rm SB}^{\rm max}$. This saturation level encodes all possible self-regulation mechanisms, preventing further heating, such as the suppression of star formation by photo-dissociation of molecular gas. To parameterize the efficiency of SB-heating, we define the characteristic SFR-density $\Sigma_{\rm SF}^{\rm c}$, at which the specific radiation power reaches 50% of the saturation level. A

minimal parametrization of these requirements is given by the function

$$T_{\rm SB}^4 = T_{\rm SB}^{\rm max4}\,\Sigma_{\rm SF}/(\Sigma_{\rm SF} + \Sigma_{\rm SF}^{\rm c}), \tag{6.7}$$

which reduces to the linear relation $T_{\rm SB}^4 \approx T_{\rm SB}^{\rm max4}\,\Sigma_{\rm SF}/\Sigma_{\rm SF}^{\rm c}$ for $\Sigma_{\rm SF} \ll \Sigma_{\rm SF}^{\rm c}$. To compute $\Sigma_{\rm SF} = {\rm SFR}/(\pi\, r_{\rm SF}^2)$ for the galaxies in our simulation, we approximate the characteristic length $r_{\rm SF}$ with the half-mass radius $r_{\rm H_2}^{\rm half}$ of molecular gas and we use the SFRs computed by the semi-analytic model (see Croton et al., 2006). In this model stars can form via two mechanisms: (i) quiescent continual star formation in the disk, which depends on the cold gas surface density; (ii) star-bursting activity in the bulge, which is driven by galaxy mergers. We shall use the combined SFRs of both modes to calculate $\Sigma_{\rm SF}$, since, in principle, both modes are likely to cause inter-cloud radiative heating, if the corresponding SFR densities are high enough, i.e. of order $\Sigma_{\rm SF}^{\rm c}$.

In analogy to SBs, we parameterize the heating from AGNs via

$$T_{\rm AGN}^4 = T_{\rm AGN}^{\rm max\,4}\,\dot{M}_{\rm BH}/(\dot{M}_{\rm BH} + \dot{M}_{\rm BH}^{\rm c}), \tag{6.8}$$

where $T_{\rm AGN}^{\rm max}$ is the maximal CO-excitation temperature that can be achieved by AGN-heating, $\dot{M}_{\rm BH}$ is the black hole mass accretion rate, and $\dot{M}_{\rm BH}^{\rm c}$ is the critical accretion rate, where the specific heating power is half the maximum value. In the semi-analytic model of the DeLucia-catalog (Croton et al., 2006), black holes can grow via two mechanisms: (i) a quiescent mode, whereby black holes continually accrete material from a static hot halo; (ii) a merger mode, where the black holes of merging galaxies coalesce, while accreting additional material from the cold gas disks. The free parameters in this model, were adjusted such that the predicted relation between black hole mass and bulge mass matches the local observations by Häring & Rix (2004). Since our model for CO-heating only depends on $\dot{M}_{\rm BH}$, we have implicitly assumed that all growing black holes have the same heating efficiency, independent of their growth mode and physical parameters, such as

the black hole mass – a simplistic assumption, which may well require a more careful treatment as large samples of CO-detected AGN become available.

To finalize our model, we need to estimate the five parameters T_0, $T_{\rm SB}^{\rm max}$, $T_{\rm AGN}^{\rm max}$, $\Sigma_{\rm SF}^{\rm c}$, and $\dot{M}_{\rm BH}^{\rm c}$. To fix T_0, we consider regular galaxies (no SB, no AGN) in the local universe ($T_{\rm CMB}(z=0) = 2.7\,K$), where Eq. (6.6) implies that $T_{\rm ex}$ is nearly identical to T_0. From simultaneous CO(2–1) and CO(1–0) detections in 35 regular galaxies in the local universe, Braine et al. (1993) concluded that the ratio between the brightness temperature luminosities is $L_2^{\rm T}/L_1^{\rm T} = 0.89$ with a scatter of only 0.06. According to Eq. (6.31), this is equivalent to $L_2/L_1 = 2^3 \cdot 0.89$, which, by virtue of Eqs. (6.4, 6.5), implies a one-to-one correspondence between $T_{\rm ex} \approx T_0$ and $\tau_{\rm c}$. If we impose $\tau_{\rm c} = 2$ (see above), then $T_0 \approx 17\,{\rm K}$, which roughly agrees with the excitation temperatures of the regular galaxies M 51 and IC 342 for the same depth parameter (see Fig. 6.1). We therefore fix $T_0 \equiv 17\,{\rm K}$.

We further set the critical star-formation density to $\Sigma_{\rm SF}^{\rm c} \equiv 500\,{\rm M}_\odot\,{\rm yr}^{-1}\,{\rm kpc}^{-2}$, consistent with observations of the nuclear SBs of M 82 (de Grijs, 2001) and NGC 253 (Beck & Beckwith, 1984). For those galaxies Eq. (6.7) then implies that $T_{\rm SB}^{\rm max4} = T_{\rm SB}^4/2$, where $T_{\rm SB} \approx T_{\rm ex} = 40 - 50\,{\rm K}$ (see Fig. 6.1), hence $T_{\rm SB}^{\rm max} = 50 - 60\,{\rm K}$. We therefore choose $T_{\rm SB}^{\rm max} \equiv 60\,K$. Our chosen value for $\Sigma_{\rm SF}^{\rm c}$ also compares well to the star-formation density $\sim 10^3\,{\rm M}_\odot\,{\rm yr}^{-1}\,{\rm kpc}^{-2}$ predicted by Thompson et al. (2005) for the optically thick, dense regions of star forming disks.

For AGN heating, we choose $T_{\rm AGN}^{\rm max} \equiv 150\,{\rm K}$, assuming that APM 08279+5255 represents an object close to the maximal possible heating. The critical black hole accretion rate $\dot{M}_{\rm BH}^{\rm c}$ is assumed to be $\dot{M}_{\rm BH}^{\rm c} \equiv 10\,{\rm M}_\odot\,{\rm yr}^{-1}$, consistent with the higher Eddington accretion rates in the sample of 121 radio-loud quasars studied by Bao et al. (2008). Assuming a standard radiative accretion efficiency of 10%, this value for $\dot{M}_{\rm BH}^{\rm c}$ corresponds to a black hole mass of $5 \cdot 10^8\,{\rm M}_\odot$, which is on the order of a typical progenitor of the supermassive black holes found in the massive galaxies in the local universe.

6.3.2 Overlap of molecular clumps

A reason, why CO-radiation can be used as a *linear* tracer of molecular mass in nearby galaxies despite its optical thickness is that most lines-of-sight to the molecular clumps in nearby galaxies do not cross other clumps, and hence CO behaves as if it were optically thin (see Appendix 6.9). However, at high redshift, galaxies are denser (e.g. Bouwens et al., 2004) and carry more molecular gas (Obreschkow & Rawlings, 2009b), and thus the overlap (in space and velocity) of molecular clumps may become significant. Such overlap will (i) reduce the directly visible surface area per unit molecular mass, and (ii) increase the effective optical depth of the CO-radiation.

Bally et al. (1987; see also Genzel & Stutzki, 1989) identified and analyzed more than 100 clumps in the Orion molecular cloud. Based on these data, we assume that the diameters and masses of clumps are approximately $r_{\rm clump} = 1\,{\rm pc}$ and $M_{\rm clump} = 500\,{\rm M}_\odot$. Given a total molecular mass $M_{\rm H_2}$, the number of clumps is approximated by

$$N = \frac{M_{\rm H_2}}{M_{\rm clump}} \tag{6.9}$$

and the "fractional filling factor" of a single clump can be approximated as

$$\kappa = \frac{0.1\, r_{\rm clump}^2}{q_{\rm H_2}\, r_{\rm H_2}^2}, \tag{6.10}$$

where $q_{\rm H_2}$ is the axes-ratio of the inclined galaxy-disk[2] as seen by the observer and $r_{\rm H_2}$ is the radius of molecular gas in this disk, which we take as the galactocentric radius, where $\Sigma_{\rm H_2}(r)$ given in Eq. (6.3) equals 10% of the maximal surface density. The factor 0.1 accounts for the fact that clouds are only considered to "overlap", if they have comparable radial velocities, as otherwise they become mutually transparent to CO-line radiation. The value of 0.1 is a rough estimate based on the velocity dispersion of each clump ($1 - 10\,{\rm km\,s^{-1}}$, Bally et al., 1987 and

[2]The simulated DeLucia-catalog does not provide galaxy orientations. We therefore assign inclinations randomly between 0 deg (face-on) and 90 deg (edge-on) according to a sine-distribution.

Maddalena et al., 1986) and the fact that the relative velocities between two clumps can vary from $10\,\mathrm{km\,s^{-1}}$ (if in the same cloud-complex) up to the circular velocity of the disk of several $100\,\mathrm{km\,s^{-1}}$ (if in different parts of the galaxy). In a more accurate model, the value 0.1 would have to be altered with the inclination of the galaxy.

Assuming that the clumps are randomly distributed in space and frequency, we find that the fractional volume of the position–velocity space covered by the N clumps, counting overlapping regions only once, is

$$F = 1 - (1 - \kappa)^{\mathrm{N}}. \tag{6.11}$$

$F \in [0, 1]$ is here called the "filling factor" (although other definitions of this term exist) and its expression of Eq. (6.11) can be derived iteratively by realizing that the filling factor of i clumps, $i > 1$, is $\kappa_{\mathrm{i}} = \kappa_{\mathrm{i}-1} + \kappa \cdot (1 - \kappa_{\mathrm{i}-1})$ with $\kappa_1 \equiv \kappa$. Since the summed volume occupied by all clumps in the position–velocity space equals $N\,\kappa$, we find that any line-of-sight crossing at least one clump, must on average cross

$$B = \frac{N\,\kappa}{1 - (1 - \kappa)^{\mathrm{N}}}. \tag{6.12}$$

clumps, which also overlap in velocity space. If clumps do not overlap (i.e. $B = 1$), the emergent CO-line luminosities are proportional to the number of clumps N, and hence proportional to the molecular mass $M_{\mathrm{H_2}}$ (see Eq. 6.9). However, if the clumps overlap (i.e. $B > 1$), the directly visible surface area of the molecular gas is proportional to $M_{\mathrm{H_2}}/B$ and the optical depth increases from τ_{J} to $B\,\tau_{\mathrm{J}}$.

6.3.3 Clumpy and smooth molecular gas

Measurements of CO-emission lines in distant ULIRGs revealed that the use of CO-luminosity-to-H_2-mass conversion factors known from local galaxies leads to H_2-masses on the order of or larger than the dynamical masses inferred from the circular velocities (Scoville et al., 1991, Solomon & Vanden Bout, 2005). This con-

tradiction and high-resolution CO-maps of ULIRGs led to the new understanding that the densely packed GMCs at the center of massive compact galaxies are unstable against the tidal shear and therefore disintegrate into a smooth blend of gas and stars. Detailed observations and geometrical models of Downes et al. (1993) and Downes & Solomon (1998) uncovered that the smooth gas is about 5-times more CO-luminous per unit molecular mass. Multiple line observations of the two nearby ULIRGs Arp 220 and NGC 6240 (Greve et al., 2009, and references therein) seem to confirm this model, but they also demonstrate that gas in the dense phase may coexist with less dense gas enveloping the dense nuclear disk.

To account for the possibility of smooth molecular gas, we assume that CO-luminosities per unit molecular mass scale proportionally to the efficiency

$$\varepsilon = f_{\rm clumpy} + 5 \cdot (1 - f_{\rm clumpy}), \tag{6.13}$$

where $f_{\rm clumpy}$ is the H_2-mass fraction in the regular clumpy phase (i.e. in GMCs) and $(1 - f_{\rm clumpy})$ is the H_2-mass fraction in the regular phase. We define the transition between the clumpy and the smooth gas phase at the H_2-surface density threshold $\Sigma_{\rm c} = 10^3\,{\rm M}_\odot\,{\rm pc}^{-2}$, which is between the highest H_2-densities observed in the local universe ($\sim 10^2\,{\rm M}_\odot\,{\rm pc}^{-2}$, e.g. NGC 6946, Leroy et al., 2008) and the most extreme H_2-surface densities of ULIRGs ($\sim 10^4\,{\rm M}_\odot\,{\rm pc}^{-2}$, e.g. Arp 220 and NGC 6240, Greve et al., 2009). Assuming a thickness of the nuclear disk of a few 10 pc, consistent with the nuclear disk model of Downes & Solomon (1998), the adopted value of value of $\Sigma_{\rm c}$ corresponds to a volume density of $\gtrsim 10^3\,{\rm cm}^{-3}$. This value falls in between the two volume densities found by Greve et al. (2009) for the smooth and dense gas phases of Arp 220 and NGC 6240.

In the smooth phase, the H_2/HI-mass ratio is much larger than unity, so that the H_2-surface density $\Sigma_{\rm H_2}(r)$ can be safely approximated by the total hydrogen density $\Sigma_{\rm H}(r)$ given in Eq. (6.1). The H_2-mass fraction in regions less dense than

$\Sigma_{\rm c}$, can then be calculated as

$$f_{\rm clumpy} = \begin{cases} \frac{\Sigma_{\rm c}}{\tilde{\Sigma}_{\rm H}} \left[1 + \ln \left(\frac{\tilde{\Sigma}_{\rm H}}{\Sigma_{\rm c}} \right) \right] & \text{if } \tilde{\Sigma}_{\rm H} > \Sigma_{\rm c}, \\ 1 & \text{otherwise.} \end{cases} \tag{6.14}$$

We shall assume that the overlap factor B is calculated in the same way for the smooth component as for the clumpy one, which corresponds to approximating the self-shielding of the smooth region by the self-shielding of a densely packed distribution of clumps with the same total volume and mass[3]. Fig. 6.2 shows the simulated global fraction of H_2-mass in the smooth phase and the fraction of CO-power from this phase as a function of cosmic time. The predicted monotonic increase of both fractions with redshift clearly reflects the strong density and size evolution of cold gas disks predicted by the simulation (e.g. Obreschkow & Rawlings, 2009a).

At $z = 2$, the H_2-mass fraction in the smooth phase is about 0.3% (corresponding to a fractional CO-power of $\sim 1\%$), roughly consistent with the fact that the space density of ULIRGs is $\sim 1\%$ of the space density of normal galaxies at this redshift (Daddi et al., 2008). The remaining 99% of CO-power at $z = 2$ in the simulation stems from clumpy gas, i.e. from GMCs. This result seems consistent with recent observational evidence that star formation in many active star forming galaxies at $z \approx 2$ is distributed on significantly larger scales than in ULIRGs (Daddi et al., 2008, Genzel et al., 2008) and that star formation properties in high-z galaxies are similar to those in GMCs (e.g. Gao, 2009).

At $z = 5$, the CO-power from the smooth gas phase is predicted to make up $\sim 10\%$ of the total CO-power of all galaxies. One might argue that such small fractions can be neglected. However, in Section 6.5.3, we will show that the contribution of CO-radiation from smooth molecular gas at $z = 5$ will change the space density of the brightest objects in the CO-LFs by an order of magnitude.

[3]The filling factor F of the smooth component turns out to be very close to 1, and hence $B \approx N\,\kappa$.

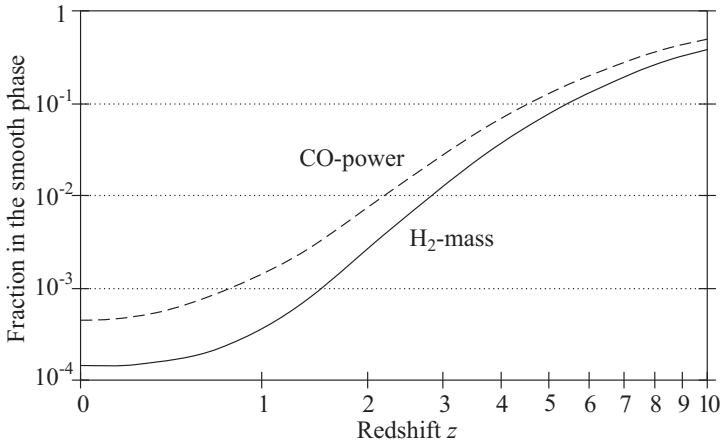

Figure 6.2. Cosmic evolution of the H_2-mass fraction in the smooth gas phase summed over all galaxies in the simulation (solid line), and the corresponding fraction of CO-line power (dashed line).

6.3.4 Metallicity

Various recent observations revealed significant variations of the CO-luminosity-to-H_2-mass conversion factor within and amongst the Milky Way (MW) and several nearby galaxies (Arimoto et al., 1996, Boselli et al., 2002, Israel, 2000, Paglione et al., 2001, Wilson, 1995). In general, the CO-luminosity per unit molecular mass turned out to be roughly proportional to the mass-fraction of metals (Obreschkow & Rawlings, 2009c). Such a dependence may naively be expected for radiation emitted by a metallic[4] molecule like CO, but considering the optical thickness of this radiation, one could also conclude that the CO-luminosity per unit molecular mass is nearly independent of the metallicity (Kutner & Leung, 1985). However, lower metallicities imply a lower dust-to-gas ratio and hence a more efficient destruction of CO by ultra violet (UV) radiation, which can restore a positive correlation between metallicities and the CO-luminosities (see Maloney & Black, 1988, and references therein).

Based on these quantitative measurements and qualitative theoretical con-

[4]Here, all elements other than hydrogen and helium are referred to as "metals".

siderations, we decided to scale the luminosity of all CO-lines proportionally to $Z \equiv M_{\rm Z}/M_{\rm gas}$, where $M_{\rm Z}$ is the metal mass in cold gas and $M_{\rm gas}$ is the total cold gas mass (including He).

6.3.5 Effective luminosity against the CMB

The CMB power per unit frequency has its maximum within the frequency band covered by the CO-lines. For example, at $z = 0$ the CMB peaks between the CO(1–0)-line and the CO(2–1)-line, and at $z = 5$ the CMB peaks between the CO(8–7)-line and the CO(9–8)-line. Therefore, the absorption of CO-lines against the CMB may significantly reduce the detectable luminosities of CO-emission lines.

Within our assumption that clouds are in local thermal equilibrium, Kirchhoff's law of thermal radiation globally predicts that the absorptivity of the clouds equals their emissivity. Explicitly, if a cloud emitting thermal radiation with a power per unit frequency equal to $\epsilon(\nu)\, u(\nu, T_{\rm ex})$, where $\epsilon(\nu) \in [0, 1]$ is the emissivity at the frequency ν and $u(\nu, T_{\rm ex})$ is the power per unit frequency of a black body, then the absorbed CMB power per unit frequency equals $\epsilon(\nu)\, u(\nu, T_{\rm CMB})$. The effective CO-line luminosity measured against the CMB is the difference between the intrinsic luminosity emitted by the source and the luminosity absorbed from the CMB. If the intrinsic luminosity of the source is given by Eq. (6.4), the effective luminosity against the CMB can be obtained by replacing the second factor (i.e. the black body factor) in Eq. (6.4) by

$$\ell(J, T_{\rm ex}, z) \equiv \frac{J^4}{\exp\left(\frac{h_{\rm p}\,\nu_{\rm CO}\,J}{k_{\rm b}\,T_{\rm ex}}\right) - 1} - \frac{J^4}{\exp\left(\frac{h_{\rm p}\,\nu_{\rm CO}\,J}{k_{\rm b} T_{\rm CMB}(z)}\right) - 1}. \tag{6.15}$$

In particular, this expression ensures that no radiation can be detected from molecular gas in thermal equilibrium with the CMB, since $\ell(J, T_{\rm CMB}(z), z) = 0$. Alternatively, Eq. 6.15 could also be expressed in terms of brightness temperatures (e.g. Eq. (14.46) of Rohlfs & Wilson, 2004).

6.4 Combined model for CO-line luminosities

A priori, we departed from the idea that CO-line fluxes $L_{\rm J}$ scale with the total mass of molecular hydrogen $M_{\rm H_2}$. Combining this assumption with the models of Sections 6.3.1–6.3.5, we heuristically suggest that the CO-line luminosity (power) of the transitions $J \rightarrow J-1$ is given by

$$L_{\rm J} = M_{\rm H_2} \cdot \frac{k\, Z\, \varepsilon}{B} \cdot \left[1 - e^{-B\,\tau_{\rm J}}\right] \cdot \ell(J, T_{\rm ex}, z), \tag{6.16}$$

where k is an overall normalization factor. Consistent with common practice, we shall define k in such a way that $L_{\rm J}$ is the line-power, obtained by integrating the power per unit solid angle emitted along the line-of-sight over all directions, even though the emission need not be isotropic. In fact, our model is explicitly non-isotropic, since the parameter B depends on the inclination of the galaxy via the axes-ratio $q_{\rm H_2}$.

To estimate the value of k, we note that in local regular galaxies all molecular gas is in the clumpy phase (i.e. $\varepsilon = 1$), molecular clumps barely overlap (i.e. $B = 1$), and the excitation temperatures are given by $T_{\rm ex} \approx T_0$, hence $\tau_{\rm J} = \tau_{\rm c} = 2$ and $\ell(1, T_{\rm ex}, 0) = 2.45$. Therefore, Eq. (6.16) for $J = 1$ reduces to

$$L_1 = 2.12\, k\, Z\, M_{\rm H_2}. \tag{6.17}$$

According to Eq. (6.17), k is proportional to the standard $\rm CO/H_2$ conversion factor α_1 (Appendix 6.9); in fact, combining Eq. (6.17) with Eqs. (6.38, 6.31), yields $k = 11.9\, k_{\rm b}\, fco^3\, Z^{-1}\, c^{-3}\, \alpha_1^{-3}$. Adopting the value $\alpha_1 = 4.6\, {\rm M_\odot (K\,km\,s^{-1}\,pc^2)^{-1}}$, typical for the MW (Solomon & Vanden Bout, 2005), and a cold gas metallicity of $Z = 0.01 - 0.02$, yields $k = 5 - 10 \cdot 10^{-8}\, {\rm W\,kg^{-1}}$.

Here, we shall fix the parameter k such that Eq. (6.16) applied to the $\rm H_2$-masses of our simulated galaxies (Section 6.2) at $z = 0$ reproduces the observed CO(1–0)-luminosity function (LF) of the local universe as measured by Keres et al. (2003) (see Fig. 6.3). A χ^2-minimization for the luminosity range $L_1 >$

$10^{5.5}\,\mathrm{Jy\,km\,s^{-1}\,Mpc^2}$, i.e. the range where our simulated H_2-MF is complete, yields

$$k = 8 \cdot 10^{-8}\,\mathrm{W\,kg^{-1}}, \tag{6.18}$$

which is indeed consistent with the aforementioned value predicted from the CO/H_2 conversion of the MW.

6.5 Results

We have applied the model of Eq. (6.16) to the galaxies of the hydrogen simulation described in Section 6.2. The predicted CO-LFs for the first 10 rotational transitions in the redshift range $z = 0 - 10$ are displayed in Fig. 6.3. For consistency with observer's practice, the luminosity scales refer to velocity-integrated luminosities L^{V}, as opposed to the frequency-integrated luminosities L (= power) used in Section 6.3. The conversion between those luminosities depends on the wavelength of the emission line as explained in Appendix 6.8.

The good match (reduced $\chi^2 = 0.7$) between the simulated CO(1–0)-LF at $z = 0$ and the local CO(1–0)-LF, inferred by Keres et al. (2003) from FIR-selected sample of IRAS galaxies, is due to our tuning of the constant k and the reasonably accurate H_2-mass distribution of our hydrogen simulation (Section 6.2).

The simulation shows a clear signature of cosmic downsizing from $z = 2$ to $z = 0$ for all CO-transitions. This feature reflects the predicted downsizing of H_2-masses (Obreschkow & Rawlings, 2009b). For the particular case of the CO(2–1)-LF at $z = 2$, the simulation result is roughly consistent with the space density (open circle in Fig. 6.3) inferred from two recent CO(2–1)-emission measurements in normal galaxies at $z = 1.5$ by Daddi et al. (2008). We note that the offset of this empirical data point from our simulation is larger in Fig. 6.3 than in Fig. 1 of Obreschkow & Rawlings (2009b). In the latter, we have compared the empirical data point of Daddi et al. (2008) to our simulated H_2-MF at $z = 2$. To this end we converted the measured CO(2–1)-luminosities into H_2-masses using the

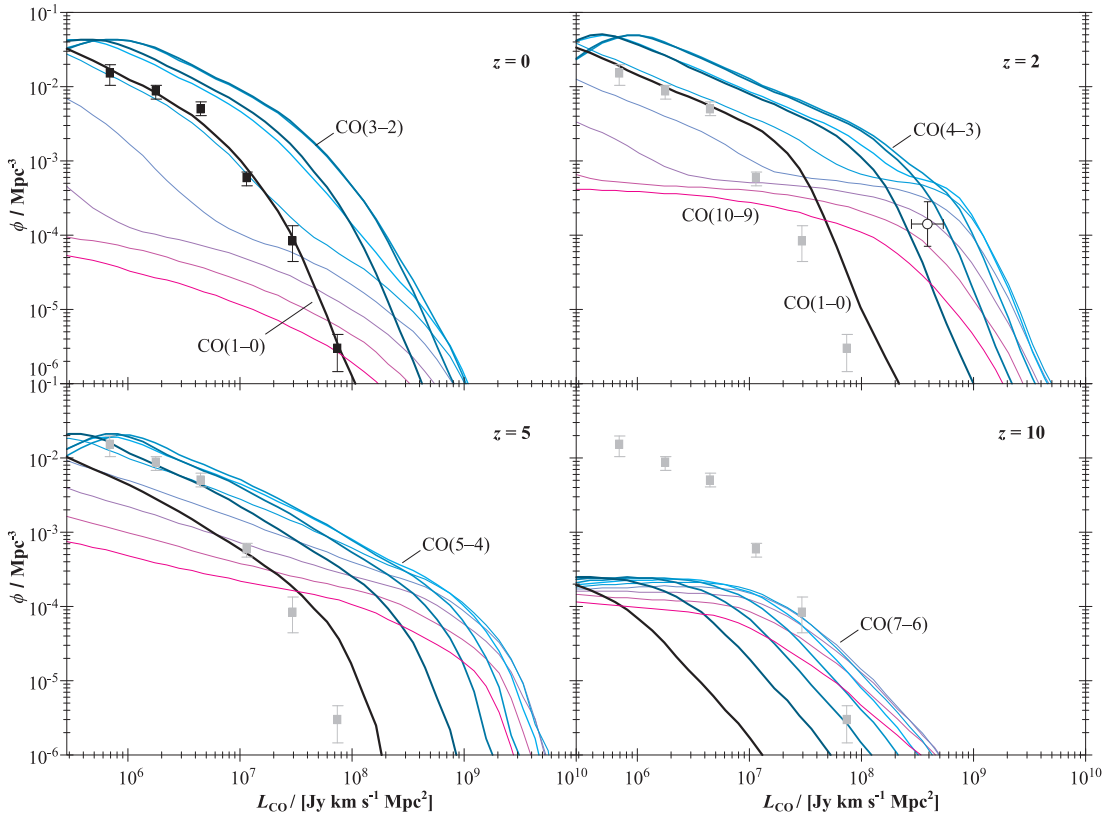

Figure 6.3. Predicted cosmic evolution of the CO-LFs in the redshift range $z = 0 - 10$. The thick black line represents the CO(1–0) transition, while increasingly thin and red lines represent the increasingly higher order transitions up to CO(10–9). Filled points and error bars represent the observed CO(1–0)-LF of the local universe (Keres et al., 2003). The open circle with error bars corresponds to the CO(2–1) density estimate based on two detections in regular galaxies at $z \approx 1.5$ by Daddi et al. (2008) (see Obreschkow & Rawlings, 2009b for further explanations). The differential space density $\phi(L^{\rm V})$ is defined as the number of sources per unit comoving volume and unit $\log_{10}(L^{\rm V})$ with a velocity-integrated luminosity $L^{\rm V}$.

standard CO/H_2 conversion factor for ULIRGs, $\alpha_2 = 1\ {\rm M}_\odot({\rm K\ km\ s^{-1}\,pc^{-2}})^{-1}$ (Daddi et al., 2008; see definition of α_2 in Appendix 6.9). However, the model for the CO/H_2 conversion of this paper yields higher values of α_2 for regular high-redshift galaxies, such as those found by Daddi et al. (2008).

For higher order transitions ($J > 5$), the predicted downsizing even extends out to $z \approx 5$, due to the strong dependence of these transitions on SBs and AGNs (Section 6.5.1). In Fig. 6.3, the "dominant" transition, i.e. the one with the maximal velocity-integrated luminosity per unit cosmic volume, is indicated at each redshift. The upper J-level of this transition increases with redshift due to the combined radiative heating by SBs and AGNs. We shall now analyze the dependence of the CO-LFs on the individual mechanisms modeled in Section 6.3.

6.5.1 Effects of radiative heating by SBs and AGNs

Fig. 6.4 compares the simulated CO(1–0)-LF and CO(6–5)-LF at $z = 0$ and $z = 8$ to the corresponding LFs, if either AGN-heating or SB-heating is suppressed. At low redshift, both SBs and AGNs have nearly no observable effect on the CO(1–0)-LF, consistent with the conclusion of Keres et al. (2003) that only the highest luminosity-bin of the measured CO(1–0)-LF could indicate a deviation from a Schechter-function distribution, perhaps due to SBs in the sample.

By contrast, the CO(6–5)-LF appears to be significantly boosted by AGNs at $z = 0$. In fact, this simulated LF deviates from a Schechter function and exhibits two "knees", respectively corresponding to a "normal" galaxy population (left knee) and a more luminous population heated by AGNs (right knee). Since the luminous end of the CO(6–5)-LF is entirely dominated by AGN-heating, we expect the local space density of the most CO(6–5)-luminous objects to match the space density of local AGNs. To test the simulation, we therefore overlayed the simulated local CO(6–5)-LF with the most recent empirical determination of the local hard ($2 - 8\,\mathrm{keV}$) X-ray-LF (HX-LF) obtained by Yencho et al. (2009) (data points in Fig. 6.4, top). This HX-LF relies on a galaxy sample studied by the X-ray *Chandra* observatory. In order to map the HX-luminosity scale onto the CO(6–5)-luminosity scale, we crudely assumed a proportional relation between the two, tuned to the empirical data from the Cloverleaf quasar. We evaluated the lensed HX-luminosity (at $2 - 8\,\mathrm{keV}$ rest-frame) of the Cloverleaf quasar di-

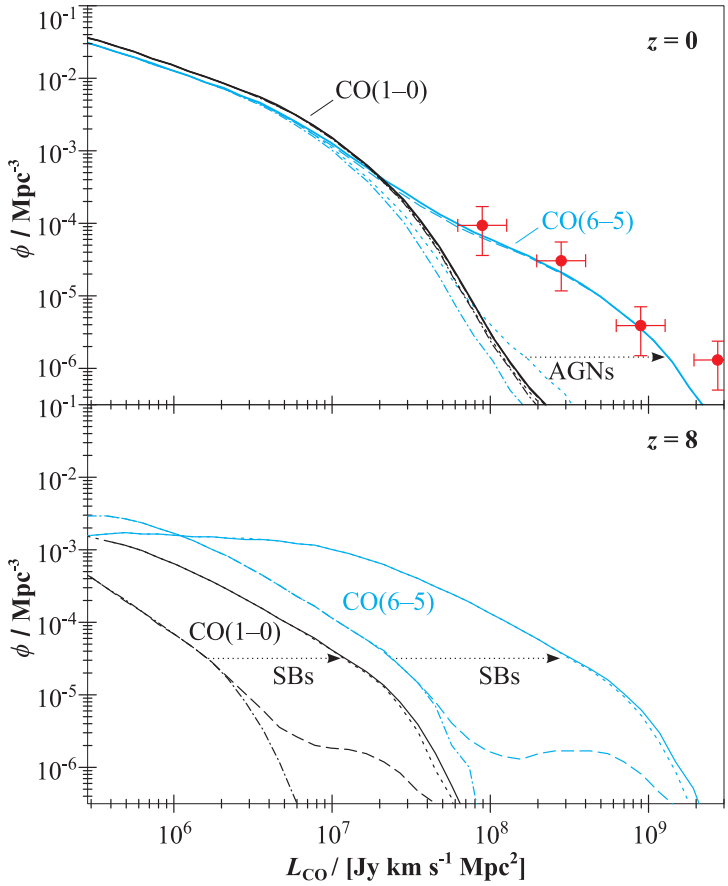

Figure 6.4. Effects of SB- and AGN-heating on the CO(1–0)-LF (black) and CO(6–5)-LF (blue) at redshifts $z = 0$ and $z = 8$. The solid lines represent the CO-LFs of the full model, such as shown in Fig. 6.3, while the other lines represent the cases where either SBs (dashed), AGNs (dotted), or both (dash-dotted) were suppressed in the simulation. The red dots with error bars represent the local HX-LF (Oshima et al., 2001), mapped onto the CO(6–5)-luminosity scale as explained in Section 6.5.1.

rectly from the X-ray SED measured and corrected for Galactic absorption by Oshima et al. (2001). For the cosmology of this paper, this HX-luminosity is $L_{\mathrm{HX}} = (1 \pm 0.5) \cdot 10^{45}\,\mathrm{erg\,s^{-1}}$. On the other hand, the lensed CO(6–5)-line luminosity of the Cloverleaf quasar, interpolated from the CO(5–4) and CO(7–6) line fluxes presented by Barvainis et al. (1997) and corrected for the standard cosmology of this paper, amounts to $L_{\mathrm{J=6}} \approx 5 \cdot 10^{10}\,\mathrm{Jy\,km\,s^{-1}\,Mpc^2}$. Assuming that the

$L_{\rm HX}/L_{\rm J=6}$-ratio of the Cloverleaf quasar is not affected by differential magnification and that it mimics the $L_{\rm HX}/L_{\rm J=6}$-ratio of local AGNs, the HX-LF (Yencho et al., 2009) transforms into the data points shown in Fig. 6.4. The vertical error bars represent the statistical density uncertainties given for the HX-LF, while the horizontal error bars represent the 50% uncertainty of $L_{\rm HX}$. The good fit between the space densities of local AGNs and those predicted for the luminous CO(6–5)-sources supports our prediction.

At very high redshift ($z \gtrsim 7$), where the predicted space density of AGNs in the DeLucia-catalog is extremely low (see Croton et al., 2006), SBs become the dominant source of CO-heating as shown in Fig. 6.4 (bottom). This analysis predicts that SB-heated molecular gas disks are the most likely objects to be detected in CO-line emission at $z \gtrsim 7$. The optimal transitions are CO(8–7) and CO(6–5) in terms of velocity-integrated luminosities or surface-brightness temperatures, respectively.

The effects of gas heating by the CMB will are discussed together with the effects of the CMB as an observing background in Section 6.5.5.

6.5.2 Effects of overlapping molecular gas

The effect of overlapping clumps (Section 6.3.2) exhibits a modest dependence on the upper J-level of the CO-transitions, although minor differences may occur due to the dependence of the optical depths on J (see Eq. 6.5). Our model predicts that the effect of overlapping clouds becomes increasingly important with redshift, as a direct consequence of the predicted increase in the surface densities of galaxies with redshift. Between $z = 0$ and $z = 1$, the effect is negligible (i.e. < 0.1 dex luminosity change), while at $z = 5$ CO-luminosities are predicted to be reduced by a factor 2–3 due to cloud overlap. The dashed line in Fig. 6.5 illustrates the effect of ignoring the overlap of clumps (by forcing $B = 1$) at $z = 5$.

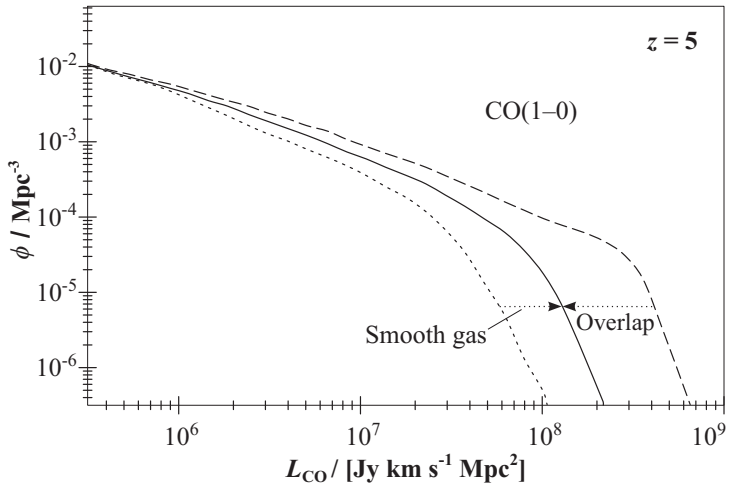

Figure 6.5. Effects of overlapping clumps and smoothly distributed gas on the CO(1–0)-LF at $z = 5$. The solid line represents the CO-LF of the full model, such as shown in Fig. 6.3. The other lines correspond to the suppression of overlap effects (dashed) and smoothly distributed gas (dotted). Note the different scale of the axes compared to the other figures.

6.5.3 Effects of smooth molecular gas

In our model (see Section 6.3.3), we assumed that molecular gas in very dense galaxy-parts is smoothly distributed, rather than organized in gravitationally bound GMCs. Within our simplistic treatment (Eqs. 6.13, 6.16), this effect is independent of the J-level of the CO-transition. The effect of smooth gas becomes increasingly important with redshift, as a direct consequence of the predicted increase in the surface densities of galaxies with redshift. Between $z = 0$ and $z = 1$ the effect is negligible (i.e. < 0.1 dex luminosity change), but at $z = 5$ its importance is comparable to that of heating by strong SBs and massive AGNs. The dotted line in Fig. 6.5 shows the effect of ignoring the possibility of smooth gas (by forcing $f_{\rm clumpy} = 1$) at $z = 5$.

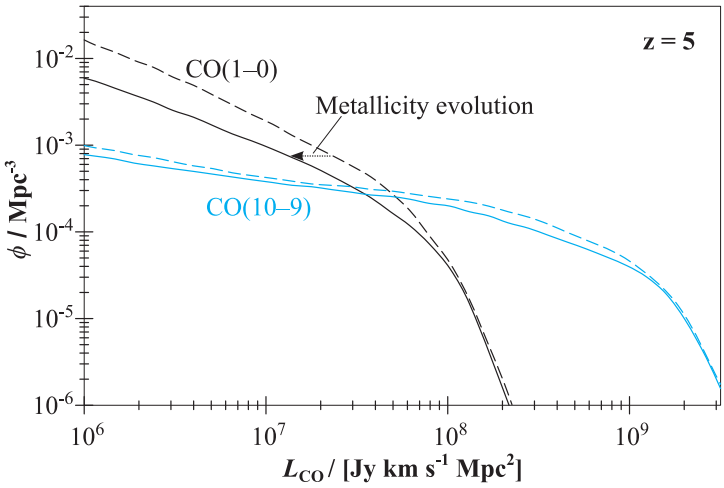

Figure 6.6. Effects of the cosmic evolution of cold gas metallicity on the LFs of CO(1–0) (black) and CO(10–9) (blue) at $z = 5$. Solid lines represent the CO-LFs of the full model, such as shown in Fig. 6.3, while dashed lines represent the CO-LFs, where the cosmic evolution of metals has been suppressed in the simulation.

6.5.4 Effects of metallicity

Fig. 6.6 shows the effect of neglecting the cosmic evolution of cold metals in galaxies, by illustrating the effects at $z = 5$ of suppressing this evolution. In general, the effect of metallicity appears to be relatively weak, since the cosmic evolution of the cold gas metallicity from $z = 5$ to $z = 0$ is relatively weak as discussed in more detail in Section 6.3 of Obreschkow et al. (2009a).

We also note that the cosmic evolution of the cold gas metallicity has a stronger effect on weak CO-sources than on the luminous ones. In fact, galaxies more luminous than the "knee" of the CO-LFs are nearly unaffected by the cosmic evolution of metals at $z = 5$ compared to $z = 0$. The reason for this feature is that the more CO-luminous galaxies are, on average, more massive and older, and hence they have already formed the bulk of their metals at $z > 5$.

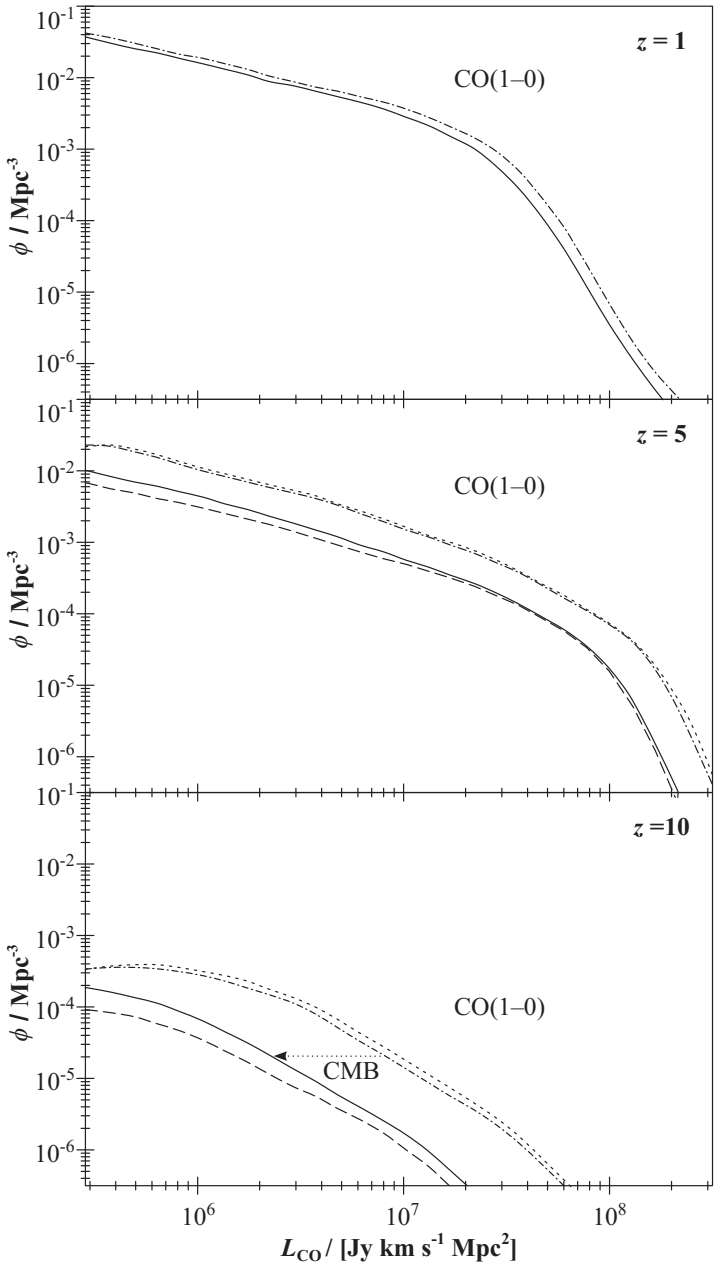

Figure 6.7. Effects of the CMB on the CO(1–0)-LF at $z = 1$, $z = 5$, and $z = 10$. The solid lines represent the CO-LFs corresponding to the full model, such as shown in Fig. 6.3. The other lines represent the cases, where either the gas-heating by the CMB (dashed), the CMB as an observing background (dotted), or both effects (dash-dotted) have been suppressed in the simulation.

6.5.5 Effects of the CMB

The CMB as an observing background already becomes noticeable at $z \approx 1$, where its effective reduction of the CO(1–0)-luminosities amounts to about 0.1 dex (less for higher order transition) according to Eq. (6.15). This effect increases steeply with redshift and reaches 1 dex at $z \approx 5$ for the CO(1–0) line, such as shown in Fig. 6.7. The increase of the CO-excitation temperature by the heating effect of the CMB appears to be a minor effect, which only becomes noticeable around $z \approx 5$. This effect acts against the loss of detectable luminosity by the CMB as an observing background by about 10% at $z \approx 5$ for the CO(1–0) line (slightly more for higher order transitions).

Our model generally predicts that the effect of the CMB as an observing background always dominates the opposite effect of the CMB as a source of heating. Hence, the combined effect of the CMB always reduces the detectable luminosities of CO-sources, at all redshifts and for all rotational transitions. This effect is most pronounced for lower order transitions, since emission from higher order transitions originates mostly from SBs and AGNs, whose heating effect can mask the comparatively low temperature of the CMB (e.g. $T_{\rm CMB} \ll T_{\rm SB}$ and $T_{\rm CMB} \ll T_{\rm AGN}$). For regular galaxies (no SBs, no AGNs), the combined effect of the CMB increases with redshift in such a way that these galaxies become virtually invisible in CO-line emission against the CMB at $z \gtrsim 7$.

This result contradicts the claims of Silk & Spaans (1997) and Gnedin et al. (2001) that the higher excitation temperatures caused by the warm CMB of the early universe will ease the detection of CO-emission lines. This conclusion only accounts for gas heating by the CMB, but ignores the CMB as an inevitable observing background as already noted by Combes et al. (1999).

6.6 Discussion

6.6.1 Ranking of various mechanisms

The analysis of Section 6.5 can be summarized in a ranking list of the different mechanisms affecting the CO/H_2 conversion. This ranking naturally depends on the redshift, the considered part of the CO-LF, and the J-level of the CO-transition. Here we consider the source population around the "knee" of the CO-LFs for the levels $J = 3-6$ at redshift $z \approx 3$. This case corresponds to using the fully funded (Maiolino, 2008) ALMA-bands 3 and 4 for the first ALMA-science goal, i.e. the detection of a MW-type galaxy in CO-line emission at $z \approx 3$ (De Breuck, 2005). For this particular setting the predicted ranking (from most important to least important) is

1. Gas heating by AGNs (+)
2. Gas heating by SBs (+)
3. Overlap of clumps (−)
4. Smooth gas (+)
5. CMB as an observing background (−)
6. Cosmic evolution of the cold gas metallicity (−)
7. Gas heating by the CMB (+)

The signs in parentheses indicate whether the effect increases (+) or decreases (−) the CO-line luminosities. Although this ranking may change considerably with redshift and with J (e.g. Fig. 6.4), the above ranking can be considered as a rule of thumb for estimating the relative importance of various effects. For example, if a simulation of CO-LFs includes a model for the smooth gas in high-redshift galaxies, then it should also account for the heating by SBs and AGNs and self-shielding by overlapping clumps.

6.6.2 Model limitations

The predictions presented is this paper are approximate ramifications of a semi-empirical model, which potentially suffers from simplifications and uncertainties on each of the four successive simulation-layers: (i) the Millennium dark matter simulation, (ii) the semi-analytic galaxy simulation of the DeLucia-catalog, (iii) our post-processing to assign extended HI- and H_2-properties to each galaxy, (iv) the model for CO-line emission introduced in this paper. It is beyond the scope of this paper to discuss the limitations related to the simulation-layers (i)–(iii), but extensive discussions were provided by Springel et al. (2005), Croton et al. (2006), and Obreschkow et al. (2009a), respectively.

All four simulation-layers were widely constrained by a broad variety of observations: (i) the cosmological parameters for the Millennium simulation were adopted from 2dFGRS (Colless et al., 2001) and WMAP (Bennett et al., 2003, Spergel et al., 2003); (ii) the semi-analytic recipes are motivated by various references given in Croton et al. (2006) and the free parameters were tuned to fit the luminosity/colour/morphology distribution of low-redshift galaxies (Cole et al., 2001, Huang et al., 2003, Norberg et al., 2002), the bulge-to-black hole mass relation (Häring & Rix, 2004), the Tully–Fisher relation (Giovanelli et al., 1997), the cold gas metallicity as a function of stellar mass (Tremonti et al., 2004); (iii) our model to assign HI- and H_2-properties is motivated by various studies of HI and H_2 in local galaxies (e.g. Blitz & Rosolowsky, 2006, Elmegreen, 1993, Leroy et al., 2008, Young, 2002) and the free parameter was tuned to the local space density of cold gas (Keres et al., 2003, Obreschkow & Rawlings, 2009c, Zwaan et al., 2005a); (iv) our CO-model was constrained as described in Section 6.3 of this paper. Since this empirical basis is widely dominated by observations in the local universe, we expect our low-redshift predictions for CO, such as the CO-LFs for higher order transitions, to be more accurate than the high-redshift predictions.

With regard to our model for CO-line emission, the most reliably modeled effects are those of the CMB, since they could be assessed from global consider-

ations, with no strong dependence on free parameters (see Sections 6.3.5, 6.5.1). Also the effects of cold gas metallicity are relatively unproblematic: firstly, these effects are relatively small (e.g. Fig. 6.6); secondly, the correlation between metallicity and the CO/H_2 conversion is empirically supported (see Section 6.3.4); thirdly, the metallicities predicted by the DeLucia-catalog seem reliable as they reproduce the mass–metallicity relation inferred from 53,000 star forming galaxies in the Sloan Digital Sky Survey (Croton et al., 2006, De Lucia et al., 2004, Tremonti et al., 2004).

The effects of inter-cloud heating by high density star formation (or SBs) and heating by AGNs are much less certain. Our temperature model relies on the CO-SEDs of only 7 galaxies (4 SBs and 3 QSOs) with poorly constrained star formation densities and black hole accretion rates. It is further possible that the molecular material in some of these galaxies is simultaneously heated by both a SB and an AGN. The relations of Eqs. (6.6–6.8) are simplistic parameterizations of our limited knowledge on gas heating by SBs and AGNs, but they may require a revision as larger galaxy samples with simultaneous CO-SEDs, SFRs, and black hole accretions rates come on line. Given the present-day uncertainties of SB- and AGN-heating, the use of the LTE-model for CO-SEDs (Section 6.5.1) seems sufficient. In fact, the offset of the LTE-model model from the more complex LVG-models is small (Combes et al., 1999) compared to the systematic uncertainties of radiative heating by SBs and AGNs.

Surprisingly, we found that self-shielding by overlapping clumps is perhaps the most subtle effect to model at $z > 3$, because it seems to be a very significant effect (see Fig. 6.5) and yet its physical complexity is considerable. Especially in the case of galaxies with heavily overlapping clumps (i.e. $B \gg 1$), the value of the overlap parameter B sensibly depends on the radius and mass of molecular clumps. If we also consider that clumps are not randomly distributed, but organized in cloud-complexes, and that their geometries are far from spherical, the predicted CO-line luminosities of galaxies with heavily overlapping clumps could differ from our

current prediction by nearly an order of magnitude. Similar uncertainties should be assumed for the effects of smooth gas in high-redshift galaxies. In fact, the critical surface density Σ_c, at which gas transforms from clouds to smooth disks, is very uncertain and may vary as a function of the mass and size of the galaxy.

6.7 Conclusion

We have predicted the cosmic evolution of the galaxy LFs for the first 10 rotational transitions of the CO-molecule. This prediction relies on a combination of a recently presented simulation of H_2-masses in $\sim 3 \cdot 10^7$ evolving galaxies with a model for the conversion between H_2-masses and CO-line luminosities. The latter model accounts for radiative heating by AGNs, SBs, and the CMB, for smooth and overlapping gas, for the cosmic evolution of metallicity, and for the CMB as an observing background.

The main outcome of this study is two-fold. Firstly, the predicted CO-LFs are probably the most robust basis to-date towards predicting the CO-line detections of high-redshift surveys with future telescopes, such as ALMA (see Blain et al., 2000), the LMT, or phase-3 of the Square Kilometre Array (SKA). Secondly, this study revealed that the most serious uncertainties of the CO-LFs at high redshifts originate from the poorly understood self-shielding of overlapping clouds, from the smooth gas in luminous galaxies, and from the heating by SBs and AGNs. Hence, any serious progress in predicting the CO-LFs must address these mechanisms in more detail. By contrast, the widely cited effects of the CMB and the cosmic evolution of metallicity seem to be relatively well modeled.

This study makes some explicit predictions, which could be tested in future CO-surveys; e.g.:

1. The CO-LFs should show a strong signature of "downsizing" in the redshift range $z = 0 - 2$. Explicitly, the total power of each CO-line per comoving volume increases from $z = 0$ to $z = 2$ by a factor 2 to more than 10, depending on the CO-transition (see Fig. 6.3).

2. On average, the relative CO-line power in higher order transitions, i.e. the excitation temperature $T_{\rm ex}$, increases monotonically with redshift z. This is a consequence of more heating at high z, mainly due to SBs and AGNs (see Fig. 6.3).

3. Some CO-LFs (e.g. CO(6–5) and CO(7–6) at $z = 0$, and CO(5–4), CO(6–5) and CO(7–6) at $z = 2$) significantly deviate from a Schechter function. They are predicted to have two "knees", respectively corresponding to a "normal" galaxy population and a more CO-luminous population, where the gas is heated mostly by AGNs (e.g. Fig. 6.4 top).

4. Out to the most distant galaxies, most of the cosmic CO-luminosity is predicted to stem from regular clumpy gas, i.e. from GMCs, rather than a hypothetical dense phase, which is believed to dominate some ULIRGs (Downes & Solomon, 1998, Downes et al., 1993).

5. The CMB will significantly suppress the apparent CO-line flux of galaxies at high z (see Fig. 6.7). In particular, galaxies at $z \gtrsim 7$ with no strong source of internal heating, such as a SB or an AGN, will not be detectable in CO-line emission.

Acknowledgements

This effort/activity is supported by the European Community Framework Programme 6, Square Kilometre Array Design Studies (SKADS), contract no 011938. The Millennium Simulation databases and the web application providing online access to them were constructed as part of the activities of the German Astrophysical Virtual Observatory. We thank W. F. Wall and the anonymous referee for helpful suggestions.

6.8 Appendix A : Luminosities and fluxes of lines

This section overviews the concepts used in relation with line fluxes and line luminosities with an emphasis on connecting the terminology and units of observers to those of theoreticians.

6.8.1 Terminology and definitions

Any continuous isotropic electromagnetic radiation from a point-source is completely characterized by the luminosity density (or monochromatic luminosity) $l(\nu)$, an intrinsic quantity measured in units proportional to $1\,\mathrm{W\,Hz^{-1}} \equiv 1\,\mathrm{J}$. The corresponding observable quantity is the flux density (or monochromatic flux) $s(\nu)$, measured in units proportional to $1\,\mathrm{W\,Hz^{-1}\,m^{-2}} \equiv 1\,\mathrm{kg\,s^{-2}}$ ($1\,\mathrm{Jy} = 10^{-26}\,\mathrm{W\,Hz^{-1}\,m^{-2}}$).

The luminosity distance D_L is defined in such a way, that the conservation of energy applied to $l(\nu)$ and $s(\nu)$ takes the standard form of the continuity equation,

$$\int l(\nu)\mathrm{d}\nu = 4\pi D_\mathrm{L}^2 \int s(\nu)\mathrm{d}\nu. \tag{6.19}$$

By definition a source is at redshift z, if electromagnetic radiation emitted by this source at a rest-frame frequency ν_e is observed at a frequency $\nu_\mathrm{o} = \nu_\mathrm{e}\,(1+z)^{-1}$; or, in terms of wave-lengths, $\lambda_\mathrm{o} = \lambda_\mathrm{e}\,(1+z)$. A frequency interval $\mathrm{d}\nu$ around ν_e will be compressed to $\mathrm{d}\nu(1+z)^{-1}$, when observed at ν_o; therefore,

$$l(\nu_\mathrm{e}) = 4\pi D_\mathrm{L}^2 s(\nu_\mathrm{o})\,(1+z)^{-1}. \tag{6.20}$$

If the source presents an emission line centered at a rest-frame frequency ν_e, one often considers the integrated luminosity and flux from the whole line. However, at least three definitions of these integrated quantities are commonly used. The most physically meaningful choices are the frequency-integrated quantities,

$$L \equiv \int_{\nu_\mathrm{e}-\Delta\nu_\mathrm{e}}^{\nu_\mathrm{e}+\Delta\nu_\mathrm{e}} l(\nu)\mathrm{d}\nu, \quad S \equiv \int_{\nu_\mathrm{o}-\Delta\nu_\mathrm{o}}^{\nu_\mathrm{o}+\Delta\nu_\mathrm{o}} s(\nu)\mathrm{d}\nu, \tag{6.21}$$

where $\Delta\nu_{\rm e}$ and $\Delta\nu_{\rm o}$ represent the half-widths of the line in rest-frame frequency and observer-frame frequency, respectively. The precise definition of these half-widths (i.e. the definition of where the line ends) depends on the observer's choice. L represents the actual power of the emission line and is measured in units proportional to $1\,{\rm W}$ ($1\,{\rm L}_\odot = 3.839\cdot10^{26}\,{\rm W}$). S represents the power per unit area received by the observer, measured in units proportional to $1\,{\rm W\,m^{-2}} \equiv 1\,{\rm kg\,s^{-3}}$.

An alternative definition to the frequency-integrated quantities are the velocity-integrated analogues, often preferred by observers,

$$L^{\rm V} \equiv \int_{-\Delta V}^{+\Delta V} l(\nu){\rm d}V, \quad S^{\rm V} \equiv \int_{-\Delta V}^{+\Delta V} s(\nu){\rm d}V, \tag{6.22}$$

where V is the rest-frame velocity, projected on the line-of-sight, of the emitting material relative to the center of the observed galaxy, and ΔV is the maximal velocity (rotation+dispersion) of the emitting material. $L^{\rm V}$ is measured in units proportional to $1\,{\rm kg\,m^3\,s^{-3}}$ ($1\,{\rm Jy\,km\,s^{-1}\,Mpc^2} = 9.521\cdot10^{21}\,{\rm kg\,m^3\,s^{-3}}$), and $S^{\rm V}$ is measured in units proportional to $1\,{\rm kg\,m\,s^{-3}}$ ($1\,{\rm Jy\,km\,s^{-1}} = 10^{-23}\,{\rm kg\,m\,s^{-3}}$).

Confusion sometimes arises in the definition of the velocity V in Eqs. (6.22), since several definitions of velocity are commonly used in the context of emission and absorption lines (see Fig. 6.8): (i) the standard recession velocity $V_{\rm opt}(\nu) = c(\nu_{\rm e}-\nu)/\nu$, traditionally used by optical astronomers; (ii) the variation $V_{\rm radio}(\nu) = c(\nu_{\rm e}-\nu)/\nu_{\rm e}$, sometimes employed by radio-astronomers; (iii) the "intrinsic rest-frame velocity" W, representing the rest-frame velocity, projected on the line-of-sight, of the emitting material relative to the center of the observed galaxy. For the investigation of emission (or absorption) lines at high redshift, it is critical to specify, which definition of the velocity V is used in the definition of velocity-integrated quantities like $L^{\rm V}$ and $S^{\rm V}$. The most natural choice, which we adopted in Eqs. (6.22), is $V = W$. This is the only choice, which makes $L^{\rm V}$ an intrinsic property, that does not depend on the observer's distance.

In the rest-frame of the observed galaxy, the center of the emission line is at

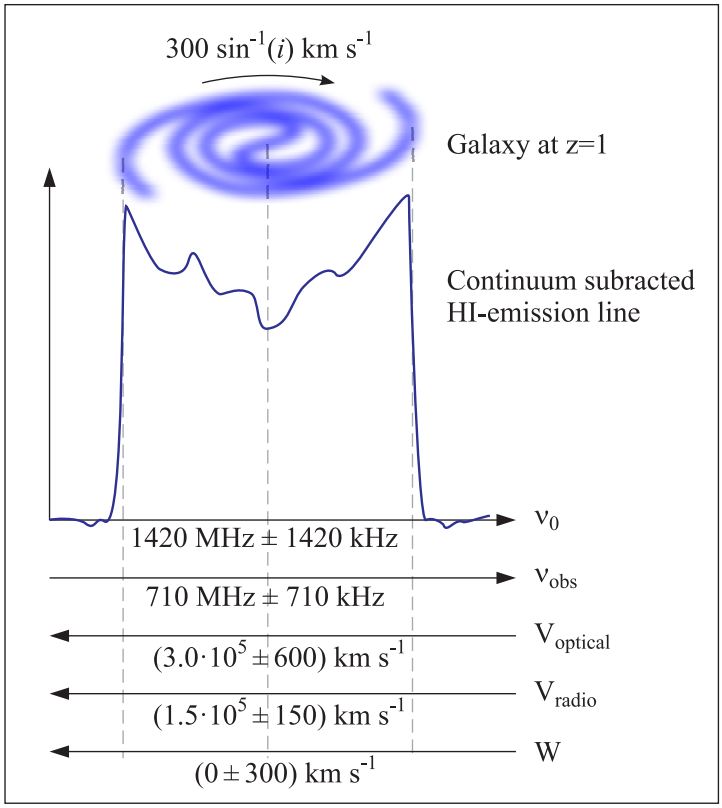

Figure 6.8. Different velocity measures used in relation to emission lines from galaxies.

the frequency $\nu_{\rm e}$ and V is computed as $V = c(\nu - \nu_{\rm e})/\nu_{\rm e}$. Hence,

$$\frac{{\rm d}V}{{\rm d}\nu} = \lambda_{\rm e} \quad \text{if } \nu \text{ is in the rest-frame.} \tag{6.23}$$

In the observer's frame, the center of the emission line is at the frequency $\nu_{\rm o}$ and and V is computed as $V = c(\nu - \nu_{\rm o})/\nu_{\rm o}$. Hence,

$$\frac{{\rm d}V}{{\rm d}\nu} = \lambda_{\rm o} \quad \text{if } \nu \text{ is in the observer-frame.} \tag{6.24}$$

Sometimes, line luminosities are defined with respect to the surface brightness temperature $T_{\rm B}$, which is defined as the (frequency-dependent) temperature of a black-body with the physical size of the observed source and providing an identical

flux density $s(\nu_\mathrm{o})$. In radio astronomy the energy distribution of a black body is commonly approximated by the Rayleigh-Jeans law, i.e. the power radiated per unit of surface area, frequency, and solid angle equals $u(\nu) = 2\nu^2 k T_\mathrm{B} c^{-2}$, where k_b is the Boltzmann constant. For isotropic line emission at rest-frame frequency ν_e this implies $l(\nu_\mathrm{e}) = 4\pi D_\mathrm{A}^2 \Omega\, u(\nu_\mathrm{e}) = 8\pi \nu_\mathrm{e}^2 k_\mathrm{b} T_\mathrm{B} c^{-2} D_\mathrm{A}^2 \Omega$, where $D_\mathrm{A} = D_\mathrm{L}(1+z)^{-2}$ is the angular diameter distance and Ω is the solid angle subtended by the source. Using Eq. (6.20), we then obtain

$$T_\mathrm{B}(\nu_\mathrm{o}) = \frac{c^2}{2\,k_\mathrm{b}} \frac{s(\nu_\mathrm{o})\,\nu_\mathrm{e}^{-2}\,(1+z)^3}{\Omega}. \tag{6.25}$$

T_B is an intrinsic quantity, which does not change with redshift z, as can be seen from $s(\nu_\mathrm{o})/\Omega \propto (1+z)^{-3}$. Often the brightness temperature intensity I of an emission line source is defined as the velocity-integrated brightness temperature,

$$I \equiv \int_{-\Delta V}^{+\Delta V} T_\mathrm{B}(\nu) \mathrm{d}V, \tag{6.26}$$

giving units proportional to $1\,\mathrm{K\,m\,s^{-1}}$ ($1\,\mathrm{K\,km\,s^{-1}} = 10^3\,\mathrm{K\,m\,s^{-1}}$). Alternatively, observers sometimes define the intensity I as the velocity-integral of the "beam-diluted" brightness temperature T_mb, which is smaller than T_B if the source does not cover the whole beam. We also note that some authors use the symbol I for fluxes, which we label S (e.g. Weiss et al., 2007). The brightness temperature luminosity L^T is defined as the product of the intensity and the source area (Solomon et al., 1997),

$$L^\mathrm{T} \equiv D_\mathrm{A}^2 \Omega \int_{-\Delta V}^{+\Delta V} T_\mathrm{B}(\nu) \mathrm{d}V. \tag{6.27}$$

This implies that L^T is measured in units proportional to $1\,\mathrm{K\,m^3\,s^{-1}}$ ($1\,\mathrm{K\,km\,s^{-1}\,pc^2} = 9.521 \cdot 10^{35}\,\mathrm{K\,m^3\,s^{-1}}$).

6.8.2 Basic relations

From the conservation law of Eq. (6.19), we directly find the flux-to-luminosity relations

$$L = 4\pi D_{\mathrm{L}}^2 \, S. \tag{6.28}$$

The velocity-integrated flux S^{V} can be expressed in terms of the frequency-integrated flux S by using the Jacobian of Eq. (6.24),

$$S^{\mathrm{V}} = \lambda_{\mathrm{o}} \, S. \tag{6.29}$$

Similarly, the velocity-integrated luminosities L^{V} can be expressed in terms of the frequency-integrated luminosity L (i.e. intrinsic power of the emission line) by using the Jacobian of Eq. (6.23),

$$L^{\mathrm{V}} = \lambda_{\mathrm{e}} \, L, \tag{6.30}$$

Finally, from Eqs. (6.25, 6.27, 6.28, 6.29),

$$L^{\mathrm{T}} = (8\pi k_{\mathrm{b}})^{-1} \lambda_{\mathrm{e}}^3 \, L. \tag{6.31}$$

Using the four basic relations of Eqs. (6.28–6.31), we can express any of the quantities L, S, L^{V}, S^{V}, and L^{T} as a function of any other. For example, Eqs. (6.28, 6.29, 6.30) imply that

$$L^{\mathrm{V}} = (1+z)^{-1} \, 4\pi D_{\mathrm{L}}^2 \, S^{\mathrm{V}}. \tag{6.32}$$

Note that this relation differs from Eq. (6.28) by a redshift-factor. Eqs. (6.28, 6.30) imply that

$$L = \frac{4\pi}{c} \, D_{\mathrm{L}}^2 \nu_{\mathrm{o}} S^{\mathrm{V}}, \tag{6.33}$$

or, using typical observer-units,

$$\frac{L}{\mathrm{L}_\odot} = 1.040 \cdot 10^{-3} \left(\frac{D_\mathrm{L}}{\mathrm{Mpc}}\right)^2 \frac{\nu_\mathrm{o}}{\mathrm{GHz}} \frac{S^\mathrm{V}}{\mathrm{Jy\,km\,s^{-1}}} \,. \tag{6.34}$$

This is equivalent to Eq. (1) in Solomon & Vanden Bout (2005). Similarly, Eqs. (6.28, 6.29, 6.31) imply that

$$L^\mathrm{T} = \frac{c^2}{2\,k_\mathrm{b}}\,\nu_\mathrm{o}^{-2}\,D_\mathrm{L}^2(1+z)^{-3}S^\mathrm{V}, \tag{6.35}$$

or, in observer units,

$$\begin{aligned}\frac{L^\mathrm{T}}{\mathrm{K\,km\,s^{-1}\,pc^2}} = 3.255 \cdot 10^7 \left(\frac{\nu_\mathrm{o}}{\mathrm{GHz}}\right)^{-2} \left(\frac{D_\mathrm{L}}{\mathrm{Mpc}}\right)^2 \\ \times (1+z)^{-3} \frac{S^\mathrm{V}}{\mathrm{Jy\,km\,s^{-1}}} \,.\end{aligned} \tag{6.36}$$

which is identical to Eq. (3) in Solomon & Vanden Bout (2005).

6.9 Appendix B : Background of the CO/H_2 conversion

To-date, most estimates of molecular gas masses in galaxies rely on radio and (sub-)millimeter emission lines of trace molecules, especially on emission lines associated with the decay of rotational excitations of the CO molecule.

It is not obvious that the CO-lines trace H_2, and this method has indeed a long history of controversy. From local observations in the MW, it has become obvious that molecular gas resides in loosely connected giant ($\sim 10 - 100\,\mathrm{pc}$) "clouds", which are generally composed of hundreds of dense "clumps" ($\sim 1\,\mathrm{pc}$), hosting even denser "cores" ($\sim 0.1\,\mathrm{pc}$), where new stars are born (see e.g. the Orion Molecular Cloud, Maddalena et al., 1986, Tatematsu et al., 1993). CO-line emission cannot be used as mass tracer of individual clumps and cores, since they are *optically thick* to rotational CO-emission lines as can be inferred from the intensity-ratios between different rotational levels (Binney & Merrifield, 1998

Chapter 8). However, if averaged over entire clouds or galaxies (typically 10^4-10^7 clouds), CO behaves as if it were *optically thin*, in a sense that individual clumps and cores do not significantly overlap (in space and frequency) (Wall, 2006), and hence on these large scales CO-line luminosities are expected to become suitable tracers of the molecular mass. Compelling empirical support for this conclusion was provided by the very tight correlation between the virial masses, estimated from sizes and velocity dispersions, and the CO(1–0)-luminosities of 273 molecular clouds in the MW analyzed by Solomon et al. (1987).

To convert CO-line luminosities into H_2-masses, it is common to define the X-factors as

$$X_{\rm J} \equiv \frac{N_{\rm H_2}}{I_{\rm J}}, \tag{6.37}$$

where J is the upper rotational transition $J \rightarrow J-1$, $N_{\rm H_2}$ is to column number-density of H_2-molecules (here, we exclude Helium), and $I_{\rm J}$ is the brightness temperature intensity [see definition in Eq. (6.26)] of the CO($J \rightarrow J-1$)-emission line. Alternatively, the CO/H_2 conversion factors are sometimes defined as (Solomon & Vanden Bout, 2005)

$$\alpha_{\rm J} \equiv \frac{M_{\rm H_2}}{L^{\rm T}_{\rm J}}, \tag{6.38}$$

where $L^{\rm T}_{\rm J}$ is the brightness temperature luminosity [see definition in Eq. (6.27)] of the CO($J \rightarrow J-1$)-emission line. Note that the definitions of $N_{\rm H_2}$ and $M_{\rm H_2}$ in Eqs. (6.37, 6.38) do not include a Helium fraction, but some authors (e.g. Downes et al., 1993) include a Helium fraction of $\sim 36\%$ in $N_{\rm H_2}$ and $M_{\rm H_2}$, which makes their values of $X_{\rm J}$ and $\alpha_{\rm J}$ 1.36-times larger.

Since $M_{\rm H_2} = D_{\rm A}^2 \Omega N_{\rm H_2} m_{\rm H_2}$, where $m_{\rm H_2}$ is the mass of a H_2-molecule, and $L^{\rm T}_{\rm J} = D_{\rm A}^2 \Omega I_{\rm J}$ for all $J \geq 1$, we find that the two conversion factors are related by

$$\alpha_{\rm J} = X_{\rm J}\, m_{\rm H_2}\,, \tag{6.39}$$

or, in typical observer units,

$$\frac{\alpha_{\rm J}}{\mathrm{M}_\odot(\mathrm{K\,km\,s^{-1}\,pc^2})^{-1}} = \frac{1.6\cdot10^{-20}\,X_{\rm J}}{(\mathrm{K\,km\,s^{-1}\,cm^2})^{-1}}. \tag{6.40}$$

From Eqs. (6.30, 6.31, 6.38, 6.39) it follows that

$$M_{\rm H_2} = \frac{m_{\rm H_2}\,c^2}{8\pi\,k\,\nu_{\rm J}^2}\,X_{\rm J}\,L_{\rm J}^{\rm V}, \tag{6.41}$$

where $L_{\rm J}^{\rm V}$ and $\nu_{\rm J}$ respectively denote the velocity-integrated luminosity and the rest-frame frequency of the CO($J\rightarrow J-1$)-emission line. $\nu_{\rm J}$ can be calculated as $\nu_{\rm J} = J\,\nu_{\rm CO}$ where $\nu_{\rm CO} = 115\,\mathrm{GHz}$ is the rest-frame frequency of the CO(1–0)-line. Eq. (6.41) can then be expressed in typical observer units as

$$\frac{M_{\rm H_2}}{\mathrm{M}_\odot} = \frac{313\,J^{-2}\,X_{\rm J}}{10^{20}(\mathrm{K\,km\,s^{-1}\,cm^2})^{-1}}\cdot\frac{L^{\rm V}_{\rm CO(J\rightarrow J-1)}}{\mathrm{Jy\,km\,s^{-1}\,Mpc^2}}. \tag{6.42}$$

Other mass–luminosity and mass–flux relations for H_2 commonly found in the standard literature can be derived from Eq. (6.42) and the basic relations in Section 6.8.2.

Both the theoretical and the empirical determination of this conversion have a long history in radio astronomy, and are still considered highly challenging problems at the present day (see overviews in Maloney & Black, 1988, Wall, 2007, Dickman et al., 1986). Different methods to measure $\alpha_{\rm J}$ (or $X_{\rm J}$) were summarized by Downes et al. (1993), Arimoto et al. (1996), and Solomon & Vanden Bout (2005). The latter suggest that a sensible average value for the MW is $\alpha_1 = 3.4\mathrm{M}_\odot(\mathrm{K\,km\,s^{-1}\,pc^2})^{-1}$, or $\alpha_1 = 4.8\mathrm{M}_\odot(\mathrm{K\,km\,s^{-1}\,pc^2})^{-1}$, if helium is included in the definition of α_1.

6.10 Appendix C : Line emission of CO in LTE

The rotational states of a diatomic molecule, such as CO, can be represented in the basis $\{|J,m\rangle\}$, where $J \geq 0$ is the angular quantum number and $m \in \{-J,...,J\}$

is the magnetic quantum number. In the absence of external fields, the energy only depends on J via $E_{\rm J} = h_{\rm p}\,\nu_{\rm CO}\,J(J+1)/2$, where $\nu_{\rm CO} = 115\,{\rm GHz}$ and is the rest-frame frequency of the transition $J = 1 \to 0$. In local thermal equilibrium (LTE), the occupation probabilities of these energy-levels are therefore given by

$$n_{\rm J} = \frac{g_{\rm J}}{\mathcal{Z}(T_{\rm ex})}\,\exp\left[-\frac{h_{\rm p}\,\nu_{\rm CO}\,J(J+1)}{2\,k_{\rm b}\,T_{\rm ex}}\right], \tag{6.43}$$

where $g_{\rm J} = 2\,J+1$ are the degeneracies lifted by the quantum number m, $T_{\rm ex}$ is the excitation temperature, and $\mathcal{Z}(T)$ is the canonical partition function, which ensures the normalization condition $\sum n_{\rm J} = 1$. The partition function is approximated to $< 1\%$ for all $T > 10\,{\rm K}$ by

$$\mathcal{Z}(T_{\rm ex}) = \frac{2\,k_{\rm b}\,T_{\rm ex}}{h_{\rm p}\,\nu_{\rm CO}} - \frac{2}{3}. \tag{6.44}$$

The interaction between a state $|J,m\rangle$ and the electromagnetic field only permits transitions simultaneously changing J by ± 1 and m by $-1, 0, 1$. To determine the electromagnetic emission emerging from the three transitions $|J,m\rangle \to |J-1,m'\rangle$, where $m' \in \{m, m\pm 1\}$, we require a measure of the rates of spontaneous emission from $|J,m\rangle$, induced emission from $|J,m\rangle$, and absorption by $|J-1,m'\rangle$. These rates are effectively described by the Einstein coefficients $A_{\rm J,J-1}$, $B_{\rm J,J-1}$, and $B_{\rm J-1,J}$ (defined in Binney & Merrifield, 1998, Chapter 8), which can be calculated directly from the interaction Hamiltonian between the rotational states and the electromagnetic-field. From considerations of a gas in LTE it follows that these coefficients are related via $A_{\rm J,J-1} \propto J^3 B_{\rm J,J-1}$ and $g_{\rm J-1} B_{\rm J-1,J} = g_{\rm J} B_{\rm J,J-1}$. Rieger (1974) showed that $A_{\rm J,J-1}$ scales with J as

$$A_{\rm J,J-1} \propto \frac{J^4}{2\,J+1}, \tag{6.45}$$

and hence

$$B_{\rm J,J-1} \propto \frac{J}{2\,J+1} \quad \text{and} \quad B_{\rm J-1,J} \propto \frac{J}{2\,J-1}. \tag{6.46}$$

Following Binney & Merrifield (1998), the "source function" $l_{\rm J}$, which is proportional to the power radiated per unit frequency from the transition $J \rightarrow J-1$ (i.e. the sum of the power from all the transitions $|J,m\rangle \rightarrow |J-1,m'\rangle$) in an optically thick medium, is then given by

$$l_{\rm J} \propto \frac{n_{\rm J}\, A_{\rm J,J–1}}{n_{\rm J–1}\, B_{\rm J–1,J} - n_{\rm J}\, B_{\rm J,J–1}} \propto \frac{J^3}{\exp\left(\frac{h_{\rm p}\,\nu_{\rm CO}\,J}{k_{\rm b}\,T_{\rm ex}}\right) - 1}, \tag{6.47}$$

and hence the *frequency-integrated* power in a medium with arbitrary optical depth $\tau_{\rm J}$ is given by

$$\begin{aligned} L_{\rm J} &\propto J\, l_{\rm J}\, [1 - \exp(-\tau_{\rm J})] \\ &\propto [1 - \exp(-\tau_{\rm J})] \cdot \frac{J^4}{\exp\left(\frac{h_{\rm p}\,\nu_{\rm CO}\,J}{k_{\rm b}\,T_{\rm ex}}\right) - 1}, \end{aligned} \tag{6.48}$$

where

$$\begin{aligned} \tau_{\rm J}(T_{\rm ex}) &\propto J^{-1}\,(n_{\rm J–1}\, B_{\rm J–1,J} - n_{\rm J}\, B_{\rm J,J–1}) \\ &\propto \exp\left(-\frac{h_{\rm p}\,\nu_{\rm CO}\,J^2}{2\,k_{\rm b}\,T_{\rm ex}}\right)\, \sinh\left(\frac{h_{\rm p}\,\nu_{\rm CO}\,J}{2\,k_{\rm b}\,T_{\rm ex}}\right). \end{aligned} \tag{6.49}$$

From Eq. (6.31) the brightness temperature luminosity is given by $L_{\rm J}^{\rm T} \propto L_{\rm J} J^{-3}$. In the particular case of an optically thick medium ($\tau_{\rm J} \rightarrow \infty$) and high temperatures ($k_{\rm b}\,T_{\rm ex} \gg h_{\rm p}\,\nu_{\rm CO}\,J$), Eq. (6.48) then implies that $L_{\rm J}^{\rm T}$ is independent of J, which is indeed one of the essential properties of brightness temperature luminosities.

Chapter 7

Mock observing cone of HI and CO out to $z = 10$

D. Obreschkow, I. Heywood, H.-R. Klöckner, F. Levrier, and S. Rawlings

"A Virtual Sky with Extragalactic HI- and CO-Lines for the SKA and ALMA"

ApJ, submitted (2009)

We presents a sky simulation[1] of the HI-emission line and the first ten $^{12}C^{16}O$-emission lines of gas in galaxies beyond the Milky Way. The simulated sky field has a comoving diameter of $500\,h^{-1}\,\mathrm{Mpc}$, hence the actual field-of-view depends on the (user-defined) maximal redshift. For all galaxies, we estimate the line fluxes, line profiles, and angular sizes of the HI and CO emission lines. The galaxy sample is complete for galaxies with cold hydrogen masses above $10^8\,\mathrm{M}_\odot$. This sky simulation builds on a semi-analytic model of the cosmic evolution of galaxies in a Λ-cold dark matter (ΛCDM) cosmology. The evolving CDM-distribution was adopted from the Millennium Simulation, an N-body CDM-simulation in a cubic box with a side length of $500\,h^{-1}\,\mathrm{Mpc}$. This side length limits the coherence scale of our sky simulation: it is long enough to allow the extraction of the baryon acoustic oscillations (BAOs) in the galaxy power spectrum, yet the position and amplitude of the first acoustic peak are poorly defined. This sky simulation is a tangible product aiding the design and operation of future telescopes like the SKA and ALMA. The results presented in this paper have been restricted to a graphical representation of the simulated sky and fundamental $\mathrm{d}N/\mathrm{d}z$-analyzes for peak flux density limited and total flux limited surveys of HI and CO. A key prediction is that HI will be harder to detect at high redshift than predicted by a no-evolution model.

[1] http://s-cubed.physics.ox.ac.uk/, go to "S^3-SAX-Sky"

7.1 Introduction

The interstellar medium (ISM) is the bridge between the environment of galaxies and their newborn stars. Its atomic and molecular phases can be detected via emission lines. Typically studied lines include the HI-radio line (1.420 GHz rest-frame) and the rotational CO-lines in the (sub)millimeter spectrum (multiples of 115.27 GHz). These lines characterize both the composition and the dynamical state of the ISM, and their apparent frequency measures the redshift of the source. If the object sits at a cosmological distance, the redshift is dominated by the expansion of the Universe and hence provides a distance measure. Therefore, observations of HI and CO at high redshift are currently discussed as a means of localizing billions of galaxies (Carilli & Blain, 2002, Carilli & Rawlings, 2004), thus unveiling an unprecedented image of cosmic structure.

However, due to current sensitivity limitations, no HI-emission has yet been found beyond redshift $z = 0.25$ (Catinella et al., 2008, Verheijen et al., 2007). In contrast, CO-emission lines have been detected in different systems out to $z \approx 6.4$ (Walter et al., 2004), yet all these lines originate from atypical objects, such as ultra luminous infrared galaxies (ULIRGs) or quasi stellar objects (QSOs), with the exception of two ordinary galaxies recently detected in CO(2–1)-emission at $z \approx 1.5$ (Daddi et al., 2008). Both HI (Prochaska et al., 2005) and H_2 (Noterdaeme et al., 2008) have also been measured via absorption of their respective Lyman lines against distant QSOs. Yet, the nature of the absorbing galaxies remains unknown.

The discrepancy between the primordial astrophysical importance of cold gas in galaxies and its gravely limited detectability at high z is a main driver for the design of many future radio and (sub)millimeter telescopes. Prominent examples are the Square Kilometre Array (SKA), the Large Millimeter Telescope (LMT), and the Atacama Large Millimeter/submillimeter Array (ALMA), which are expected to respectively detect HI and CO at high z. The optimization of these instruments and the planning of their surveys require robust predictions of the

detectable signatures. Such predictions are available for the continuum radiation of a large sample of galaxies (e.g. Wilman et al., 2008). By contrast, high-redshift line emission of HI and CO has only been simulated for single galaxies (Boomsma et al., 2002, Combes et al., 1999, Greve & Sommer-Larsen, 2008) or simplistically extrapolated for a population of regular galaxies (Abdalla & Rawlings, 2005, Blain et al., 2000, Braun, 2006, Carilli & Blain, 2002). All these models ignore the implications of galaxy mergers, cooling flow suppression mechanisms, and other complex phenomena. Moreover, most line simulations exclusively consider either the atomic or the molecular gas phase of the ISM. This approach implicitly assumes that the other phase is negligible or that the masses in both phases evolve proportionally. Both of these assumptions contradict recent studies of the co-evolution of HI and H_2 in regular galaxies (Obreschkow & Rawlings, 2009b). Finally, the line simulations cited above neglect cosmic large-scale structure. The time seems ripe for joint predictions of atomic and molecular emission lines in a sample of galaxies large enough to probe cosmic structure.

In this paper, we present a simulation of a sky field with a comoving diameter of $500\,h^{-1}\,\mathrm{Mpc}$. The actual field-of-view depends on the (user-defined) maximal redshift. This simulation is obtained by constructing a mock observing cone from a previously presented galaxy simulation. The latter relies on the large-scale structure computed by the Millennium Simulation (Springel et al., 2005) and an enhanced semi-analytic galaxy model (Croton et al., 2006, De Lucia & Blaizot, 2007, Obreschkow et al., 2009a).

Section 7.2 explains the simulation methods. In Section 7.3, we provide a graphical illustration of the simulated sky field and extract $\mathrm{d}N/\mathrm{d}z$-estimates for peak flux density limited surveys. Section 7.4 discusses some important limitations of the presented simulation. A list of possible applications is provided in Section 7.5 along with a brief conclusion. The appendix shows additional illustrations, lists the parameters describing the analytic fits to the predicted $\mathrm{d}N/\mathrm{d}z$-functions, and describes the on-line access to the simulation data.

7.2 Methods

In this section, we describe the multiple simulation steps required to progress from a simulation of the *evolution* of cosmic structure to a *static* sky simulation. We have grouped this description into four steps, corresponding to four successive simulation steps. The first step (Section 7.2.1) contains all the simulation work presented in earlier studies. This work resulted in a catalog of $\sim 3 \cdot 10^7$ evolving galaxies with detailed cold gas properties. In the second step (Section 7.2.2), this catalog is transformed into a mock observing cone, which represents a virtual sky field. In the third step (Section 7.2.3), the intrinsic properties of the galaxies in this virtual sky field are converted into apparent line fluxes. In the fourth step (Sections 7.2.4 and 7.2.5), the line emission is refined by the evaluation of line profiles and angular sizes of the line-emitting gas.

7.2.1 Simulation of the ISM in $\sim 3 \cdot 10^7$ evolving galaxies

Here, we recapitulate the galaxy simulation presented in earlier studies. This simulation relies on three consecutive layers: (i) a simulation of the cosmic evolution of dark matter (Springel et al., 2005); (ii) a semi-analytic simulation of the evolution of galaxies on the dark matter skeleton (Croton et al., 2006, De Lucia & Blaizot, 2007); and (iii) a post-processing to split the cold hydrogen masses associated with each galaxy into HI and H_2 (Obreschkow et al., 2009a).

For the dark matter simulation, we adopted the Millennium Simulation (Springel et al., 2005), an N-body dark matter simulation within the standard Λ-cold dark matter (ΛCDM) cosmology. This simulation uses a cubic simulation box with periodic boundary conditions and a comoving volume of $(500\,h^{-1}\,\mathrm{Mpc})^3$. The Hubble constant was fixed to $H_0 = 100\,h\,\mathrm{km\,s^{-1}\,Mpc^{-1}}$ with $h = 0.73$. The other cosmological parameters were chosen as $\Omega_{\mathrm{matter}} = 0.25$, $\Omega_{\mathrm{baryon}} = 0.045$, $\Omega_\Lambda = 0.75$, and $\sigma_8 = 0.9$. The simulation-box contains $\sim 10^{10}$ particles with individual masses of $8.6 \cdot 10^8\,\mathrm{M_\odot}$. This mass resolution allows the identification of structures as low in mass as the Small Magellanic Cloud.

For the second simulation-layer, i.e. the cosmic evolution of the galaxies distributed on the dark matter skeleton, we adopt the semi-analytic model of De Lucia & Blaizot (2007) (see also Croton et al., 2006). In this macroscopic model all galaxies are represented by a list of global properties, such as position, velocity, and total masses of gas, stars, and black holes. These properties are evolved using empirically or theoretically motivated formulae for mechanisms, such as gas cooling, reionization, star formation, gas heating by supernovae, starbursts, black hole accretion, black hole coalescence, and the formation of stellar bulges via disk instabilities. The resulting virtual galaxy catalog (hereafter the "DeLucia-catalog") contains the positions, velocities, merger histories, and intrinsic properties of $\sim 3 \cdot 10^7$ galaxies at 64 cosmic time steps. The free parameters in the semi-analytic model were tuned to various observations in the local universe (see Croton et al., 2006). Therefore, despite the simplistic implementation and the possible incompleteness of this model, the DeLucia-catalog nonetheless provides a good fit to the joint luminosity/colour/morphology distribution of observed low-redshift galaxies (Cole et al., 2001, Huang et al., 2003, Norberg et al., 2002), the bulge-to-black hole mass relation (Häring & Rix, 2004), the Tully–Fisher relation (Giovanelli et al., 1997), and the cold gas metallicity as a function of stellar mass (Tremonti et al., 2004).

In this paper, we are particularly interested in the cold gas masses of the galaxies in the DeLucia-catalog. These cold gas masses are the net result of (i) gas accretion by cooling from a hot halo (dominant mode) and galaxy mergers, (ii) gas losses by star formation and feedback from supernovae, (iii) and cooling flow suppression by feedback from accreting black holes. The DeLucia-catalog does not distinguish between molecular and atomic cold gas, but simplistically treats all cold gas as a single phase. The atomic and molecular phases are therefore dealt with in the third simulation layer.

The third simulation-layer, i.e. the subdivision of the cold hydrogen mass of each galaxy into HI- and H_2-distributions (Obreschkow et al., 2009a), relies on an

analytic model for the mass-distributions of HI and H_2 within regular galaxies. In this model, the column densities of HI and H_2, $\Sigma_{\rm HI}$ and $\Sigma_{\rm H_2}$ respectively, are given by

$$\Sigma_{\rm HI}(r) = \frac{\tilde{\Sigma}_{\rm H}\, \exp(-r/r_{\rm disk})}{1 + R^{\rm c}_{\rm mol} \exp(-1.6\, r/r_{\rm disk})}\,, \tag{7.1}$$

$$\Sigma_{\rm H_2}(r) = \frac{\tilde{\Sigma}_{\rm H}\, R^{\rm c}_{\rm mol}\, \exp(-2.6\, r/r_{\rm disk})}{1 + R^{\rm c}_{\rm mol} \exp(-1.6\, r/r_{\rm disk})}\,, \tag{7.2}$$

where r denotes the galactocentric radius, $r_{\rm disk}$ is a scale length, $R^{\rm c}_{\rm mol}$ is the H_2/HI-mass ratio at the galaxy center, and $\tilde{\Sigma}_{\rm H}$ is a normalization factor. We derived Eqs. (7.1,7.2) based on a list of empirically supported assumptions, the most important of which are: (i) the cold gas of regular galaxies resides in a flat disk (see Leroy et al., 2008 for local spiral galaxies, Young, 2002 for local elliptical galaxies, Tacconi et al., 2006 for galaxies at higher redshifts); (ii) the surface density of the total hydrogen component (HI+H_2) is well described by an axially symmetric exponential profile (Leroy et al., 2008); (iii) the local H_2/HI-mass ratio scales as a power of the gas pressure of the ISM outside molecular clouds (Blitz & Rosolowsky, 2006).

Using Eqs. (7.1,7.2), we can characterize the HI- and H_2-content of every simulated galaxy in the DeLucia-catalog. The resulting hydrogen simulation successfully reproduces many local observations of HI and H_2, such as mass functions (MFs), mass–diameter relations, and mass–velocity relations (Obreschkow et al., 2009a). This success is quite surprising, since our model for HI and H_2 only introduced one additional free parameter to match the observed average space density of cold gas in the local Universe (Obreschkow et al., 2009a). A key prediction of this simulation is that the H_2/HI-ratio of most regular galaxies increases dramatically with redshift, hence causing a clear signature of cosmic downsizing in the H_2-MF (Obreschkow & Rawlings, 2009b).

Despite its consistency with existing observations, we emphasize that the presented model for the cosmic of HI and H_2 is simplistic and uncertain. In particular

at high z, the model assumptions may significantly differ from the reality. For example, high-z galaxies are likely to be more disturbed due to higher merger rates and long dynamic time scales compared to their age. There is also evidence that cold gas disks become more turbulent with redshift (e.g. Förster Schreiber et al., 2006, Genzel et al., 2008). Uncertainties from these and other model limitations are discussed briefly in Section 7.4 and in depth in Section 6 of Obreschkow et al. (2009a).

7.2.2 Building a mock observing cone

We shall now describe how the cubic simulation-box is transformed into a virtual sky field. This procedure can be regarded as a fourth simulation-layer on top of the hierarchical simulation described in Section 7.2.1.

The method adopted here closely follows the one described by Blaizot et al. (2005), namely the building of a chain of replicated simulation-boxes along the line-of-sight, as shown in Fig. 7.1. At any position in this chain, the galaxies are drawn from the cosmic time in the simulation, which corresponds to the look-back time, at which the galaxy is seen by the observer $\mathcal{O}$. Since our galaxy simulation uses 64 discrete time steps, we describe each galaxy in the cone by its properties at the closest available time step[2], in terms of redshift. This defines the spherical shells of identical cosmic time, which are separated by dashed lines in Fig. 7.1. The relatively narrow redshift-separation of these shells ensures that the assigned galaxy properties cannot differ significantly from the properties at their exact look-back time.

The same galaxy can appear once in every box in Fig. 7.1, but with different intrinsic properties due to the cosmic evolution. However, the position of the repeated galaxy in comoving coordinates will be very similar, which can result in spurious radial features for the observer $\mathcal{O}$ (see Fig. 1 in Blaizot et al., 2005). To suppress this effect, we randomize the galaxy positions by applying random

[2]The galaxy properties cannot readily be interpolated between two successive time steps, since a galaxy at any time step may have several progenitors.

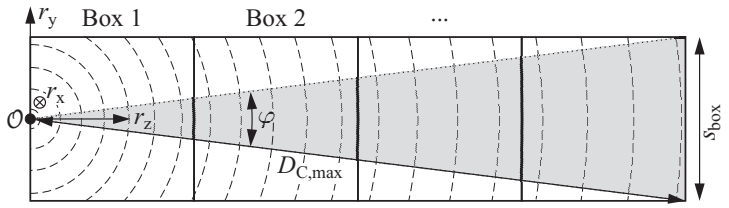

Figure 7.1. Schematic illustration of the construction of a mock observing cone (shaded region) from a chain of replicated simulation boxes (solid square boxes). The galaxies in the replicated boxes are drawn from the discrete cosmic-time step of the simulation, which best corresponds to their cosmological redshift relative to the observer $\mathcal{O}$. Galaxies from the same discrete time step therefore lie within spherical shells around the observer (indicated by the dashed-lines).

symmetry operations to each box in the chain. These operations consist of 90 deg-rotations, inversions, and continuous translations[3]. Applying these symmetry operations also removes the non-physical periodicity of $500\,h^{-1}$ Mpc associated with the side length of the periodic simulation-box. But we emphasize that applying the symmetry operations does not provide information on scales larger than the simulation-box. Symmetry operations can, however, introduce unwanted small-scale density variations at the interface of two neighboring boxes. These and other limitations of this method are discussed by Blaizot et al. (2005).

From the randomized chain of replicated simulation-boxes, an observing cone can be extracted (shaded region in Fig. 7.1). Each galaxy in this cone is projected onto the celestial sphere centered about the vernal point (RA = 0, Dec = 0). The Euclidian projection formulas for arbitrary large angles are

[3]Translations can be applied because of the periodic boundary conditions imposed on the simulation box of the Millennium Simulation.

$$\mathrm{RA} = \arctan\left(\frac{r_\mathrm{x}}{r_\mathrm{z}}\right), \tag{7.3}$$

$$\mathrm{Dec} = \arctan\left(\frac{r_\mathrm{y}}{\sqrt{r_\mathrm{x}^2 + r_\mathrm{z}^2}}\right), \tag{7.4}$$

where r_x, r_y, and r_z are the comoving coordinates of the galaxy relative to the observer (see Fig. 7.1). The "cosmological redshift" z of each galaxy is computed directly from its comoving distance $D_\mathrm{C} = (r_\mathrm{x}^2 + r_\mathrm{y}^2 + r_\mathrm{z}^2)^{1/2}$, while the Doppler-shift corrected "apparent redshift" is computed as $\tilde{z} = z + V_\mathrm{r}/c$, where V_r is the peculiar recession velocity of the galaxy relative to the Hubble flow.

Fig. 7.1 shows that the opening angle φ of the virtual sky field is set by the maximal comoving distance $D_\mathrm{C,max}$ via

$$\varphi = 2 \arcsin \frac{s_\mathrm{box}}{2\, D_\mathrm{C,max}}, \tag{7.5}$$

where s_box is the comoving side length of the simulation-box. Given a value of s_box and a choice of cosmological parameters, Eq. (7.5) implies a one-to-one relation between φ and the maximal redshift z_max.

Fig. 7.2 displays the relation between φ, $D_\mathrm{C,max}$, and z_max for the cosmological parameters of the Millennium Simulation (Section 7.2.1) and three different side lengths s_box. The choice $s_\mathrm{box} = 500\,h^{-1}\,\mathrm{Mpc}$ (solid line) corresponds to the box of the Millennium Simulation. $s_\mathrm{box} = 62.5\,h^{-1}\,\mathrm{Mpc}$ (dashed line) corresponds to the "Milli-Millennium" Simulation, a small test version of the Millennium Simulation. $s_\mathrm{box} = 2\,h^{-1}\,\mathrm{Gpc}$ (dash-dotted line) corresponds to the giant simulation-box of the Horizon-4π Simulation, a dark matter stimulation with 10-times less mass resolution than the Millennium Simulation (Prunet et al., 2008, Teyssier et al., 2008; see also Section 7.4.4).

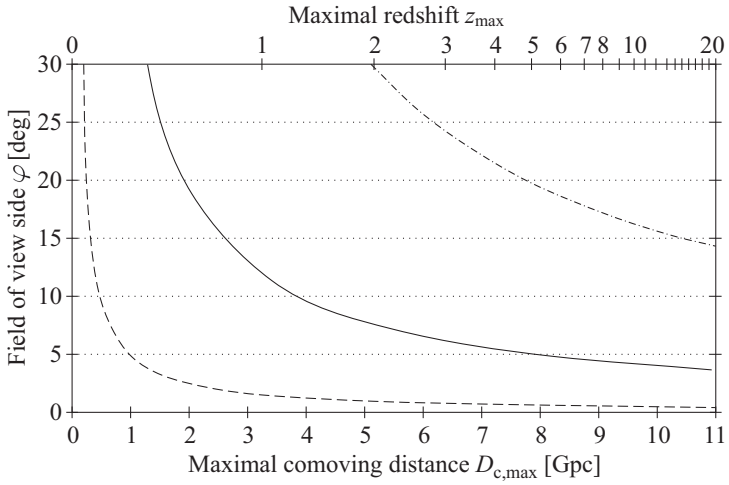

Figure 7.2. Relation between the maximal comoving distance $D_{\mathrm{C,max}}$ or maximal redshift z_{max} and the opening angle φ of the mock observing cone. The different lines correspond to the box sizes of the Millennium Simulation (solid), the Milli-Millennium Simulation (dashed), and the Horizon-4π Simulation (dash-dotted).

7.2.3 Assigning apparent line fluxes

We shall now assign apparent line fluxes to each galaxy in the mock observing cone constructed in Section 7.2.2. In general, the frequency-integrated line flux S of any emission line, can be computed from the frequency-integrated luminosity (= intrinsic power) via

$$S = \frac{L}{4\pi D_{\mathrm{L}}^2}, \tag{7.6}$$

where $D_{\mathrm{L}} = (1 + z)\, D_{\mathrm{C}}$ is the luminosity distance to the source. We note that Eq. (7.6) takes a different form for velocity-integrated fluxes and brightness temperatures. For reference, a summary of all relations between frequency-integrated and velocity-integrated fluxes, luminosities, and brightness temperatures has been compiled in Appendix A of Obreschkow et al. (2009b).

In Sections 7.2.3 and 7.2.3, we shall now summarize the models used to estimate the frequency-integrated luminosities L (hereafter simply "luminosities") of different emission lines.

Conversion of HI-mass into HI-line luminosities

We evaluate the HI-luminosities $L_{\rm HI}$ from the HI-masses $M_{\rm HI}$ of the simulated galaxies via the standard conversion (e.g. Meyer et al., 2004)

$$\frac{L_{\rm HI}}{\rm L_\odot} = 6.27 \cdot 10^{-9} \cdot \frac{M_{\rm HI}}{\rm M_\odot}. \tag{7.7}$$

The HI-line or "21 cm-line" at a rest-frame frequency of 1.420 GHz originates from the photon-mediated transition between the two spin states of the proton-electron system in the electronic ground state. The upper spin state has a low spontaneous decay rate of $f = 2.9 \cdot 10^{-15}\,\rm Hz$. This frequency is about 5 orders of magnitude smaller than that of HI-HI collisions (Binney & Merrifield, 1998). Hence, the two spin states are in thermal equilibrium with the kinetic state of the gas, which implies a spin-temperature far above the spin excitation temperature $T_{\rm ex} \approx 0.07\,K$. Therefore, the spin systems are in the high-temperature limit, where 3/4 of all systems are in the upper (three-fold degenerate) state. The radiative power emitted per atom can therefore be calculated as $L_{\rm HI} = 0.75\,f\,h_{\rm p}\,1.4\,\rm GHz$ ($h_{\rm p}$ is the Planck constant), which readily reduces to Eq. (7.7).

We have neglected HI-self absorption, since this seems to affect only massive spiral galaxies when observed almost edge-on (Ferrière, 2001, Wall, 2006). This assumption should also be valid for high-redshift galaxies, since their HI-masses were not much larger than today, as can be inferred from Lyman-α absorption measurements against distant quasars (Lah et al., 2007) and as is predicted by our simulation (Obreschkow & Rawlings, 2009b).

HI in collapsed structures, i.e. in galaxies, is generally warm enough ($\gtrsim 50\,K$) that the Cosmic Microwave Background (CMB) can be safely neglected as an observing background for all galaxies at $z < 10$. Only in the intergalactic medium (IGM) during the cosmic Epoch of Reionization (EoR) can HI appear in 21 cm-absorption against the CMB (e.g. Iliev et al., 2002).

Conversion of H_2-mass into CO-line luminosities

We derive the CO-line luminosities $L_{\rm CO}$ from the H_2-masses of the simulated galaxies. We only consider the radiation emitted by the most abundant CO-isotopomer, $^{12}C^{16}O$, when relaxing from one of the rotational states $J = 1, ..., 10$ to the state $J - 1$. The radiation frequency of such a decay is $J \cdot \nu_{\rm CO}$, where $\nu_{\rm CO} = 115.27\,{\rm GHz}$ is the rest-frame frequency of the transition $J = 1 \rightarrow 0$.

The conversion between H_2-masses and CO-luminosities is a highly nuanced affair with a long history in millimeter astronomy. We therefore presented an in-depth analysis of this conversion in Obreschkow et al. (2009b) and introduced a model to estimate the different luminosities $L_{\rm CO,J}$ of the galaxies in our simulation. This model respects the following physical mechanisms: (i) molecular gas is heated by the CMB, starbursts (SBs), and active galactic nuclei (AGNs); (ii) molecular clouds in dense or inclined galaxies can overlap; (iii) very dense gas is smooth instead of clumpy; (iv) the metallicity varies amongst galaxies and changes with redshift; (v) CO-luminosities are always detected against the CMB. We shall apply this model in the present paper. Limitations and uncertainties are discussed in Section 7.4.3.

7.2.4 Emission line profiles

Having assigned an integrated line flux to each galaxy in the simulation, we can now refine their attributes, by characterizing each line with a profile. To this end we depart from the *edge-on* line profiles evaluated in Obreschkow et al. (2009a) for each galaxy in the simulation. We represented those profiles by normalized flux densities $\Psi(V)$, where V is the velocity measured in the rest-frame of the center of the observed galaxy. The normalization condition, $\int_{\rm V} \Psi(V){\rm d}V = 1$, implies that $\Psi(V)$ only needs to be multiplied by the velocity-integrated flux (in units of Jy km/s) in order to obtain actual flux densities (in units of Jy). For each galaxy we calculated two profiles $\Psi(V)$, one for the HI-component and one for

the H_2-component (associated with CO)[4]. This calculation relied on a detailed mass model based on the halo, disk, and bulge of the galaxies, combined with our model for the HI- and H_2-surface densities given in Eqs. (7.1,7.2). For practical reasons, the resulting line profiles were reduced to five parameters (see Fig. 7.8): the normalized flux density at the line center Ψ_0; the normalized peak flux density $\Psi_{\rm max}$, usually corresponding to the two peaks of a double-horn profile; the line width $w_{\rm peak}$ between the two peaks of the double-horn profile; the line width w_{50} at the 50-percentile level of the peak flux density; and the line width w_{20} at the 20-percentile level. The original normalized line profile can be approximately recovered from these parameters using the formulas in Appendix 7.6.

The remaining task consists of correcting the line profiles for the inclination i of each galaxy[5]. i is defined as the angle between the line-of-sight and the galaxy's rotation axis; hence $i = 0\,$deg corresponds to face-on galaxies and $i = 90\,$deg corresponds to edge-on galaxies. In the absence of a random gas velocity dispersion, apparent line widths $w^{\rm obs}$ could be computed from the edge-on line widths w, via $w^{\rm obs} = w \cdot \sin i$, while apparent normalized flux densities would scale as $\Psi^{\rm obs} = \Psi / \sin i$.

Here, we assume that the cold gas has a random, isotropic velocity dispersion characterized by a Gaussian velocity distribution in each space dimension. The observed line profile of a face-on galaxy ($i = 0\,$deg) then takes the shape of a Gaussian function. Under no inclination can the line profile become more narrow than this Gaussian function or can the normalized line flux densities become higher than the peak of this Gaussian function. Let $\sigma_{\rm gas}$ be the standard-deviation of the Gaussian velocity dispersion. Then the minimum line widths are given by $w_{20}^{\rm obs} = 2\sqrt{-2\,\ln(0.2)} \approx 3.6\,\sigma_{\rm gas}$, $w_{50}^{\rm obs} = 2\sqrt{-2\,\ln(0.5)} \approx 2.4\,\sigma_{\rm gas}$, and $w_{\rm peak}^{\rm obs} = 0$, and the maximum normalized flux densities are $\Psi_0 = (\sigma_{\rm gas}\sqrt{2\pi})^{-1}$ and $\Psi_{\rm max} = (\sigma_{\rm gas}\sqrt{2\pi})^{-1}$.

[4]In Obreschkow et al. (2009a), we called these two profiles $\Psi_{\rm HI}$ and $\Psi_{\rm CO}$, respectively.

[5]The simulated DeLucia-catalog does not provide galaxy orientations. We therefore assign inclinations randomly between 0 deg (face-on) and 90 deg (edge-on) according to a sine-distribution.

In addition, the maximal normalized flux density $\Psi_{\rm max}$ cannot differ from the central normalized flux density Ψ_0 by an arbitrarily large amount, due to the line profile smoothing. Explicitly, the slope in the emission line between the points Ψ_0 and $\Psi_{\rm max}$ cannot exceed the maximal slope of the Gaussian velocity function, which is equal to $0.24\,\sigma_{\rm gas}^{-2}$. This requirement translates into an upper bound for $\Psi_{\rm max}$ equal to $\Psi_0^{\rm obs} + 0.12\,\sigma_{\rm gas}^{-2}\,w_{\rm peak}^{\rm obs}$. A set of equations respecting all of these conditions is given by

$$w_{20}^{\rm obs} = (w_{20} - 3.6\,\sigma_{\rm gas}) \cdot \sin i + 3.6\,\sigma_{\rm gas}, \tag{7.8}$$

$$w_{50}^{\rm obs} = (w_{50} - 2.4\,\sigma_{\rm gas}) \cdot \sin i + 2.4\,\sigma_{\rm gas}, \tag{7.9}$$

$$w_{\rm peak}^{\rm obs} = w_{\rm peak} \cdot \sin i, \tag{7.10}$$

$$\Psi_0^{\rm obs} = \min\left(\frac{\Psi_0}{\sin i}, \frac{1}{\sigma_{\rm gas}\sqrt{2\pi}}\right), \tag{7.11}$$

$$\Psi_{\rm max}^{\rm obs} = \min\left(\frac{\Psi_{\rm max}}{\sin i}, \frac{1}{\sigma_{\rm gas}\sqrt{2\pi}}, \Psi_0^{\rm obs} + \frac{0.12 w_{\rm peak}^{\rm obs}}{\sigma_{\rm gas}^2}\right). \tag{7.12}$$

For all the line profiles, we here adopt $\sigma_{\rm gas} = 8\,{\rm km\,s^{-1}}$ to remain consistent with Obreschkow et al. (2009a). We note, however, that high-redshift galaxies may have higher velocity dispersions (Förster Schreiber et al., 2006) perhaps due to an intense ongoing accretion of gas. Another limitation of the presented line model is that all CO-lines have by definition the same line shape. This assumption nevertheless approximately agrees with simultaneous observations of different emission lines (e.g. Greve et al., 2009, Weiss et al., 2007).

7.2.5 Angular sizes

We shall finalize our simulation of line-emitting galaxies by ascribing an angular distribution in the sky to each line. To this end we assume that the HI-line flux density per unit solid angle is proportional to the HI-column density and that the CO-line flux densities per unit solid angle are proportional to the H_2-column density. While this assumption might fail in some galaxies where strong central

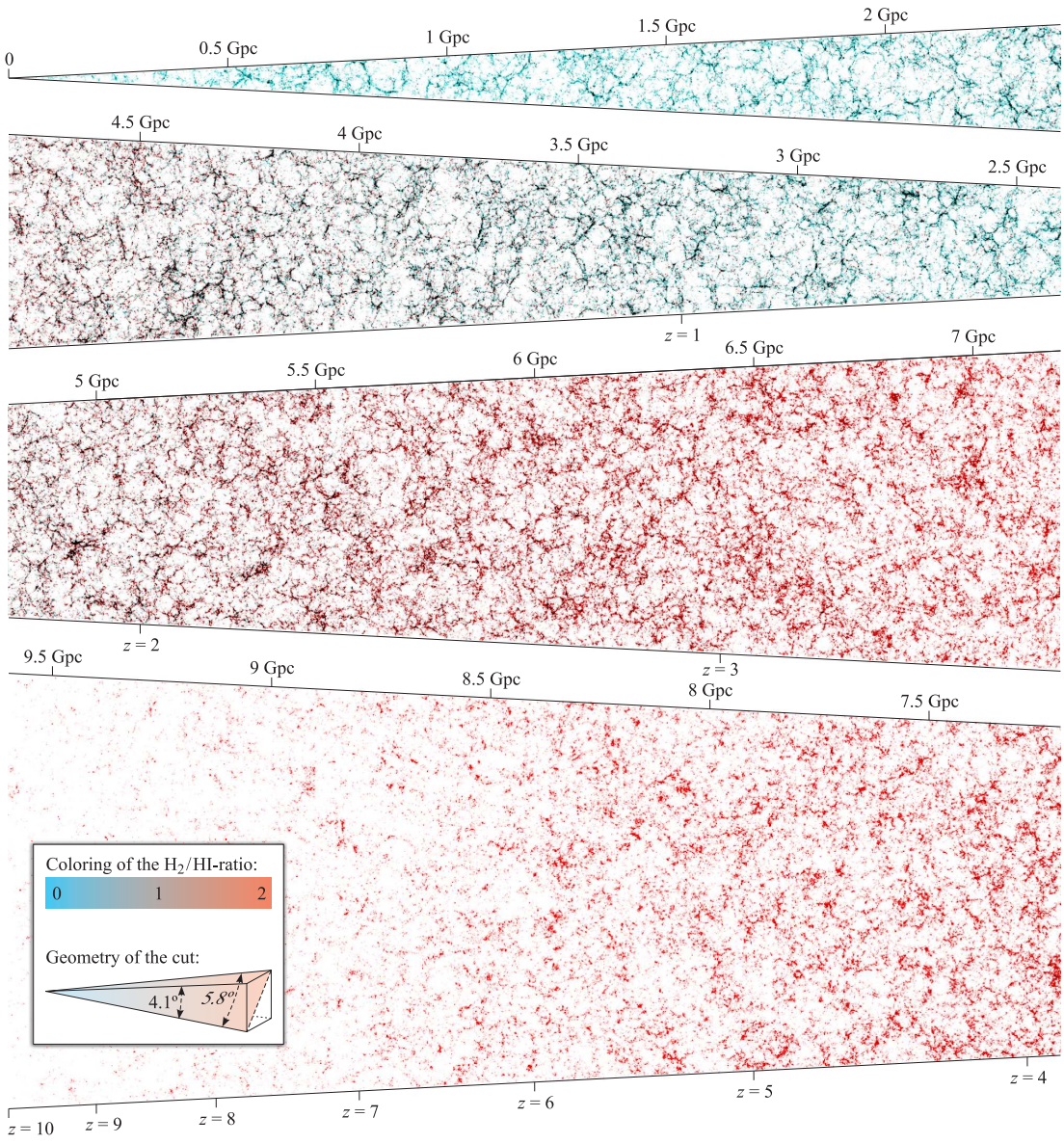

Figure 7.3. Longitudinal cut through the simulated mock observing cone. The cut slice has a thickness of 10 Mpc and is represented in comoving coordinates. For illustration purposes, the slice has been wrapped in four parts, which variably read from the left to the right and vice versa. The dots represent gas-rich galaxies and the coloring shows their H_2/HI-ratio, from 0 (blue) to 2 (red).

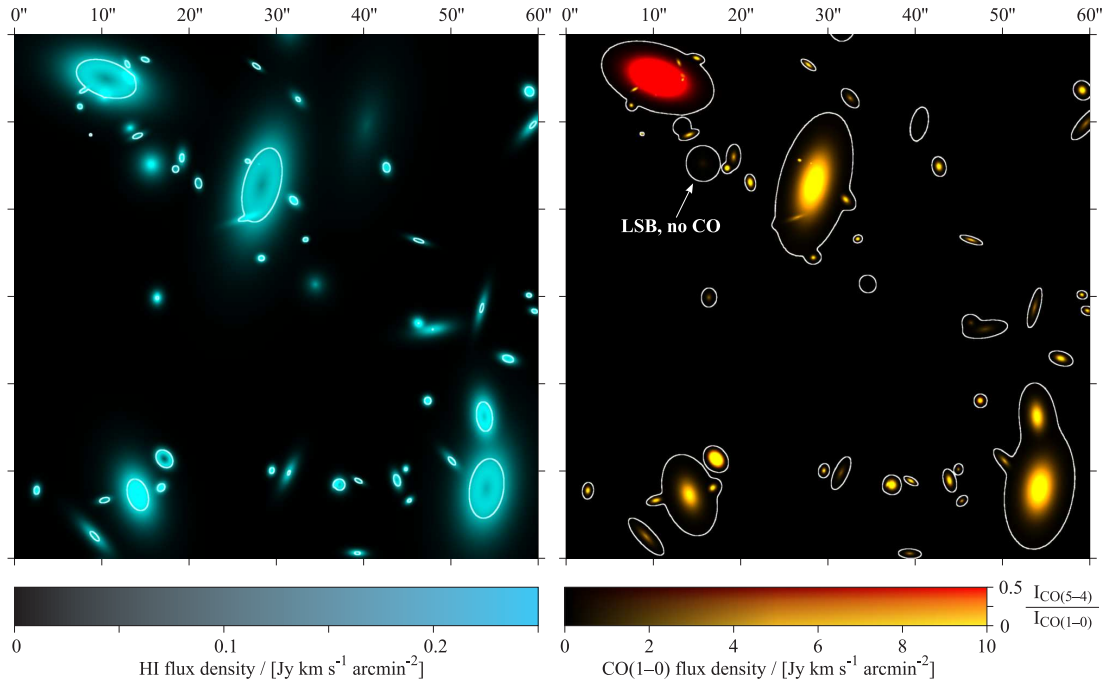

Figure 7.4. Illustration of the galaxies in the redshift range $z = 1.0 - 1.1$ in a small field of 1 arcmin^2. The full field of view of the observing cone is 60,000-times larger than this example. The gradual coloring represents integrated line fluxes per unit solid angle for HI (left) and CO(1–0) (right). The different color tones for CO represent the brightness temperature intensity ratio $I_{\mathrm{CO}(5-4)}/I_{\mathrm{CO}(1-0)}$. The white contours around HI-sources represent iso-density curves of CO at the 50-percentile level of the full CO density scale and vise versa.

heating or significant CO-self absorption occurs, it nonetheless provides a useful estimate of the size of the line-emitting regions. Within this assumption, the line flux densities per unit solid angle can be inferred from the surface densities $\Sigma_{\mathrm{HI}}(r)$ and $\Sigma_{\mathrm{H_2}}(r)$ given in Eqs. (7.1,7.2). We only need to normalize these densities to the respective line fluxes and replace the scale radius r_{disk} by the apparent scale radius $r_{\mathrm{disk}}/D_{\mathrm{A}}$, where $D_{\mathrm{A}} = (1+z)^{-1}\, D_{\mathrm{C}}$ is the angular diameter distance.

The shapes of the line-emitting regions need to be corrected for the inclinations i. If $q_{\mathrm{HI},0}$ and $q_{\mathrm{H_2},0}$ respectively denote the intrinsic axis ratios of the atomic and

molecular gas in galaxies, then the apparent axis ratios are given by (Eq. (1) in Kannappan et al., 2002)

$$q_{\rm HI}^2 = \cos^2 i + q_{\rm HI,0}^2 \sin^2 i, \tag{7.13}$$

$$q_{\rm H_2}^2 = \cos^2 i + q_{\rm H_2,0}^2 \sin^2 i. \tag{7.14}$$

These relations satisfy $q_{\rm HI} = q_{\rm H_2} = 1$, if $i = 0\,{\rm deg}$ (face-on), and $q_{\rm HI} = q_{\rm HI,0}$ and $q_{\rm H_2} = q_{\rm H_2,0}$, if $i = 90\,{\rm deg}$ (edge-on).

We assume that all galaxies have the same values for respectively $q_{\rm HI,0}$ and $q_{\rm H_2,0}$. In local spiral galaxies, we typically find $q_{\rm HI,0} = 0.1$, as can be seen from high-resolution maps of the edge-on spiral galaxies NGC 891 and NGC 4565 (Rupen, 1991). To our knowledge, no reliable estimate of $q_{\rm H_2,0}$ for disk galaxies is available. However, simultaneous CO(1–0) and optical observations revealed that the density of stars in nearby galaxies strongly correlates with the density of molecular gas (Leroy et al., 2008, Richmond & Knapp, 1986), probably as a natural consequence of the formation of stars from molecular gas. Therefore, we shall assume that the intrinsic aspect ratio of molecular gas $q_{\rm H_2,0}$ is identical to that of stellar disks. The latter is ~ 0.1, as can be seen in the sample of 34 nearby edge-on spiral galaxies studied by Kregel et al. (2002). We therefore adopt $q_{\rm H_2,0} = 0.1$. We stress that $q_{\rm HI,0} = q_{\rm H_2,0}$ does not contradict the fact that characteristic scale radii and scale heights of HI-distributions are generally larger than those of H_2-distributions (Leroy et al., 2008).

The assumption of constant values for $q_{\rm HI,0}$ and $q_{\rm H_2,0}$ may not be verified at high redshifts due to time-scale arguments. In fact, a significant fraction of the galaxies at $z > 5$ may have an age comparable to their dynamical time-scale. Their cold gas distribution might therefore be bulkier than the flat gas disks seen today. However, no reliable estimates of $q_{\rm HI,0}$ and $q_{\rm H_2,0}$ beyond the local Universe are available today.

7.3 Results

The simulated mock observing cone can be accessed on-line as described in Appendix 7.7. This section starts with a graphical illustration of the simulated mock observing cone. As a second step, we analyze the predicted number of galaxies detected in an idealized line-survey with a constant peak flux density limit. Specific predictions for particular surveys with radio and (sub)millimeter telescopes, such as the SKA, the LMT, and ALMA, shall follow in forthcoming studies.

7.3.1 Graphical overview

By successively applying the simulation steps described in Section 7.2, we have constructed an observing cone of line emitting galaxies. Fig. 7.3 shows a longitudinal slice of this cone with a thickness of 10 Mpc. This slice corresponds to a diagonal cut, as illustrated in Fig. 7.3 and has an opening angle of 5.8 deg. Each pixel inside this slice corresponds to a galaxy. The structure of the cosmic web appears clearly, as well as the increasing filamentarity of this structure with decreasing redshift. The color scales represents the H_2/HI-mass ratios of the galaxies. We can clearly recognize the pressure-driven cosmic decline of this ratio (see Obreschkow & Rawlings, 2009b).

The mock observing cone translates into a virtual sky field when projected onto a sphere using Eqs. (7.3,7.4). Fig. 7.4 displays the HI- and CO-flux densities of galaxies between $z = 1$ and $z = 1.1$ in a small extract of this virtual sky. The surface densities of the galaxies have been modeled using Eqs. (7.1,7.2) in the manner described in Section 7.2.5. The more massive galaxies in the field reveal ring-like HI-distributions with CO-rich central regions. By contrast, some of the smaller galaxies with low surface brightness (LSB), have most of their HI in the center, with nearly no detectable CO. In general, CO (and hence H_2) is more compact than HI. All these simulated features compare well to observed HI- and CO-distributions in nearby galaxies (Leroy et al., 2008) as demonstrated in Obreschkow et al. (2009a) and Obreschkow & Rawlings (2009a).

The coloring of the CO-surface densities in Fig. 7.4 (right) represents the CO(5–4)/CO(1–0) line ratio in terms of brightness temperatures. For normal galaxies, without a particular source of heating, this ratio is much smaller than unity (yellow coloring), however for some galaxies with strong heating by an ongoing SB or AGN, the higher order lines can get excited (red coloring). These mechanisms and our model to assess them are discussed in Obreschkow et al. (2009b).

Fig. 7.9 in Appendix 7.8 shows a 3-times larger sky field than Fig. 7.4 at the three redshifts $z \approx 1$, $z \approx 3$, and $z \approx 6$. The progression from $z \approx 1$ to $z \approx 6$ in Fig. 7.9 reveals two notable features. Firstly, galaxy sizes decrease with redshift. In fact, the angular diameter distances at $z \approx 1$ and $z \approx 3$ are virtually identical according to the cosmology adopted in this paper (Section 7.2.1). Therefore, the galaxy sizes of these two virtual sky maps can be compared directly. The angular diameter distance at $z \approx 6$ is about 25% smaller, hence the same physical scales appear slightly oversized. The size evolution of the galaxies reflects the cosmic evolution of the volume/mass-ratio of the dark matter haloes (Gunn & Gott, 1972). We discussed the impact of this evolution on the surface densities of HI and H_2 in Obreschkow & Rawlings (2009a).

Secondly, the CO(5–4)/CO(1–0) line ratios of CO-detectable galaxies increases with redshift. In fact, at $z \approx 6$ no galaxy with a line ratio significantly below unity (i.e. with yellow coloring) can be seen. This feature relies partially on the compactness of the galaxies, which, according to our model for CO-lines (Obreschkow et al., 2009b), allows an efficient heating by star formation. An additional reason for the absence of low CO(5–4)/CO(1–0) line ratios at $z \gtrsim 6$ is that molecular gas in galaxies with no significant star formation and no AGN will be hardly detectable in CO due to its near thermal equilibrium with the CMB.

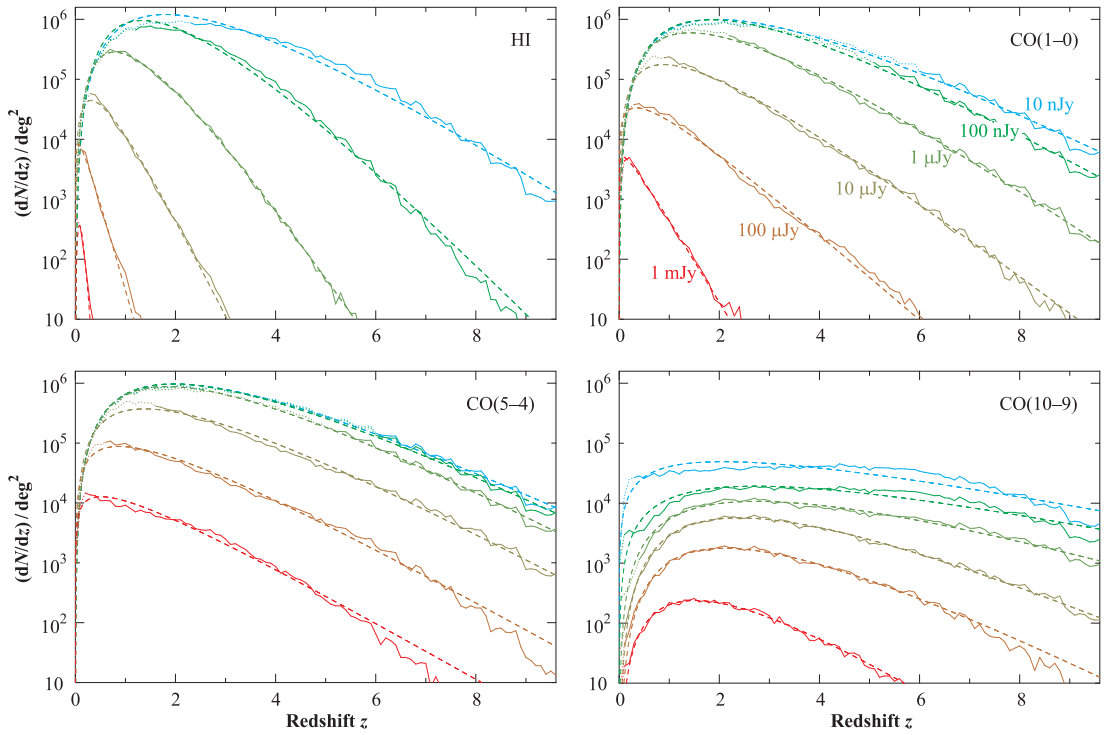

Figure 7.5. dN/dz-plots for the emission lines of HI, CO(1–0), CO(5–4), and CO(10–9) at different peak flux density limits. Solid lines represent the simulated data in the regime where the simulated galaxy sample is complete. Dotted lines represent the cases where the flux density limit is low enough to detect sources in the incomplete parts of the galaxy mass function (see Section 7.3.2). These lines should be considered as lower limits. All simulated functions (solid and dotted) use a redshift bin size of $\Delta z = 0.1$ and a sky field of 4×4 deg^2. Dashed lines represent analytic fits of Eq. (7.15). The respective fitting parameters are listed in table 7.1. Colors correspond to the peak flux density limits shown in the panel for CO(1–0).

7.3.2 dN/dz for a peak flux density limited survey

In the simulated observing cone, we can readily count the number of galaxies per redshift interval with line fluxes above a certain threshold. This dN/dz-analysis is a key step towards a prediction of the number of sources detectable with any particular telescope and survey strategy. In this section, we focus on the number

of sources detected in a peak flux density limited survey, and we restrict the presented results to the HI, CO(1–0), CO(5–4), and CO(10–9) emission lines. Results for other CO emission lines and/or for integrated flux limited surveys are presented in Appendix 7.9.

Fig. 7.5 shows the $\mathrm{d}N/\mathrm{d}z$-functions for six different peak flux density limits, logarithmically spaced between 1 mJy and 10 nJy. Peak flux densities for each source and emission line are calculated in the way described in Section 7.2.4. This method accounts for the different gas distributions, rotation curves, and inclinations of the galaxies. Every source with a peak flux density above the peak flux density limit is considered as detected, while all other sources are considered as non-detected. Different aspects of Fig. 7.5 will be discussed in detail over the following paragraphs.

Cosmic variance

The simulated $\mathrm{d}N/\mathrm{d}z$-functions shown in Fig. 7.5 (solid and dotted lines) correspond to a bin size of $\Delta z = 0.1$ and a sky field of 4×4 deg^2, extracted from *one particular* realization of the mock observing cone, that is one random choice of symmetry operations for the replicated simulation boxes (see Section 7.2.2). The wiggles visible in the simulated $\mathrm{d}N/\mathrm{d}z$-functions are physical. Similar wiggles can be expected for a real sky survey of a sky field of 4×4 deg^2 with a redshift bin size of $\Delta z = 0.1$. The fact that the amplitude of those wiggles does not decrease as $1/\sqrt{\mathrm{d}N/\mathrm{d}z}$ clearly uncovers the presence of the cosmic large-scale structure, also visible in Fig. 7.3.

To quantify the effects of cosmic variance, we now consider the $\mathrm{d}N/\mathrm{d}z$-functions extracted from five different random realizations of the mock observing cone. Fig. 7.6 shows the corresponding $\mathrm{d}N/\mathrm{d}z$-functions for a peak flux limited HI-survey with a peak flux limit of 1 μJy. Each function uses a bin size of $\Delta z = 0.1$ and a small sky field of 1×1 deg^2 in order to make the effects of cosmic structure obvious. As a rough estimate the log-scatter between the different $\mathrm{d}N/\mathrm{d}z$-

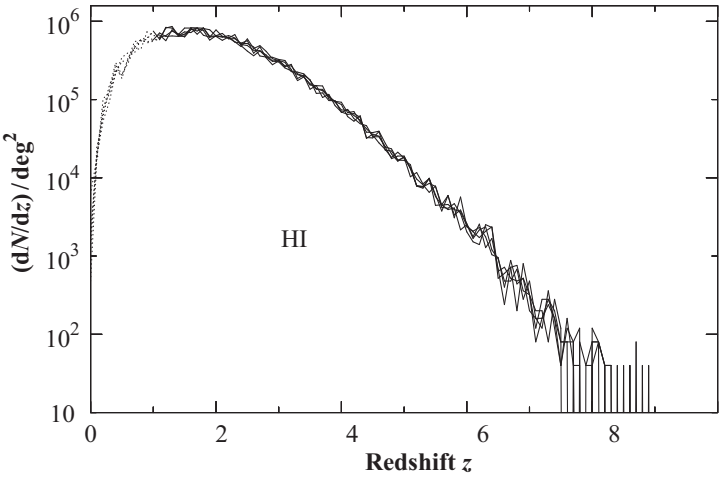

Figure 7.6. Effects of cosmic variance on a peak flux limited HI-survey with a flux limit of 1 μJy. The five lines show the dN/dz-functions extracted from five distinct random realizations of the mock observing cone (see Section 7.2.2). Each function uses a bin size of $\Delta z = 0.1$ and a small sky field of 1×1 deg^2 in order to illustrate the effects of cosmic variance.

functions is about 0.1 dex. From this small scatter we conclude that cosmic variance is, in most cases, negligible compared to the uncertainties of the semi-analytic galaxy model.

However, the comoving volume per unit solid angle and unit redshift varies as a function of redshift. Therefore, the scatter due to cosmic variance varies with redshift. It is largest at the lowest redshifts ($z < 0.5$), where the comoving surface per unit solid angle is small, and at the highest redshifts ($z > 5$), where the radial comoving distance per unit of redshift is small. In these redshift regimes effects of cosmic variance should therefore be estimated, when comparing simulated data to observations.

Completeness

Our simulation is complete for galaxies with total hydrogen masses (HI+H_2) above 10^8 $M_\odot$. Galaxies with smaller hydrogen masses typically sit at the centers

of halos with less than 20 particles in the Millennium Simulation, which cannot be reliably identified. In some cases, the peak flux density limit in Fig. 7.5 is sufficiently low, such that sources in the incomplete regime can be detected. To highlight these cases, we have represented the $\mathrm{d}N/\mathrm{d}z$-functions in Fig. 7.5 as dotted lines, wherever more than 1% of the detected galaxies have total hydrogen masses below $10^8\,\mathrm{M}_\odot$. The number of missing galaxies in these parts of the $\mathrm{d}N/\mathrm{d}z$-functions can be much larger than 1%, since only a fraction of the expected galaxies with hydrogen masses below $10^8\,\mathrm{M}_\odot$ is present in the simulation. The dotted lines in Fig. 7.5 should therefore be taken as strict lower limits for $\mathrm{d}N/\mathrm{d}z$.

Parametrization of the dN/dz-plots

The simulated $\mathrm{d}N/\mathrm{d}z$-functions can easily be recovered from the on-line database of the sky simulation (see Appendix 7.7). Alternatively, we also approximated the $\mathrm{d}N/\mathrm{d}z$-functions by analytic fits of the form

$$\frac{\mathrm{d}N}{\mathrm{d}z\ \mathrm{deg}^2} = 10^{c_1} \cdot z^{c_2} \cdot \exp(-c_3 \cdot z), \tag{7.15}$$

where c_1, c_2, and c_3 are free parameters. The best parameters in terms of an rms-minimization are shown in Table 7.1 for various emission lines detected with different limits for the peak flux densities and integrated fluxes. Analytic $\mathrm{d}N/\mathrm{d}z$-functions for intermediate flux limits can be approximately inferred by linearly interpolating the parameters c_1, c_2, and c_3.

Basic conclusions

An important conclusion from Fig. 7.5 is that HI-surveys at high redshift ($z \gtrsim 4$) will be difficult compared to CO-surveys. In order to detect the same number of sources in this redshift range, an HI-survey will need to be approximately 10-times more sensitive than a CO(1–0)-survey and approximately 100-times more sensitive than a CO(5–4)-survey.

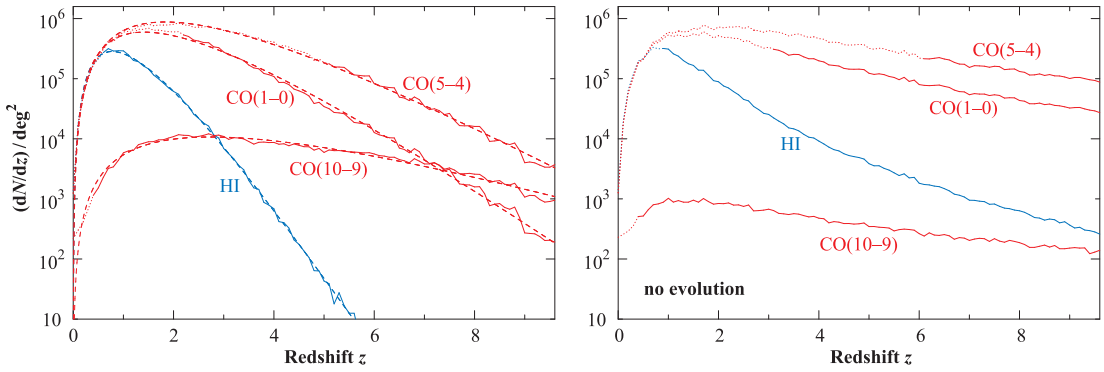

Figure 7.7. Comparison of the dN/dz-plots for different emission lines observed with an identical peak flux density limit of 1 μJy. The left panel shows our simulation presented in this paper. For comparison, the right panel represents the case of a simulation with no galaxy evolution, as obtained by using only the local galaxy simulation-box for the construction of the mock observing cone. The line types are as explained in Fig. 7.5, and colors have been used to distinguish HI (blue) from CO (red). All simulated functions (solid and dotted) use a redshift bin size of $\Delta z = 0.1$ and a sky field of 4×4 deg^2.

Fig. 7.7 (left) shows a comparison of the simulated dN/dz-functions for different emission lines observed with an identical peak flux density limit of 1 μJy. The flat slope of the dN/dz-function for CO(10–9) reflects that this line is boosted by SBs, which were more abundant and effective (more compact galaxies) at high z (see Obreschkow et al., 2009b). CO(1–0) reveals the steepest slope of all the CO-lines in the dN/dz-plot. On one hand, this feature indicates that local galaxies are dominated by low-order excitations of the CO-molecule, consistent with empirical data (Braine et al., 1993). On the other hand, CO(1–0) becomes nearly invisible in normal galaxies at high redshift ($z > 7$) due to a near thermal equilibrium between the molecular gas and the CMB (see Obreschkow et al., 2009b). The even steeper slope of the dN/dz-function for HI originates from the cosmic decline of the H_2/HI-ratio in galaxies described in Obreschkow & Rawlings (2009b).

Fig. 7.7 (right) shows the same $\mathrm{d}N/\mathrm{d}z$-functions as Fig. 7.7 (left), but for the case of no galaxy evolution. These functions were obtained by constructing a mock observing cone using only the simulation-box at $z = 0$. The comparison of Fig. 7.7 (left) to Fig. 7.7 (right) reveals that HI at high redshifts will be much harder to detect than predicted by a no-evolution model. Qualitatively, the same conclusion applies to low-order CO-emission lines, but the effect is less significant. In contrast, our simulation predicts that the high-order CO-emission lines will be easier to detect than suggested by a no-evolution model, since these lines will be strongly boosted by SBs at high redshift.

7.4 Discussion

7.4.1 Limitations of the galaxy simulation

Our simulation is inevitably bound to the ΛCDM cosmology with the cosmological parameters given in Section 7.2. The empirical uncertainty of these parameters may be a source of systematic errors in our predictions. To analyze the errors associated with the uncertainty of the Hubble constant, we can study the change of our predictions in the linear expansion[6] of h. This analysis shows that varying h between 0.6 and 0.8 does not significantly affect the $\mathrm{d}N/\mathrm{d}z$-functions, i.e. not more than a factor 2. Additionally, Wang et al. (2008) showed that the lower value for the fluctuation amplitude σ_8 found by WMAP-3 compared to the value used in the Millennium simulation is almost entirely compensated by an increase in halo bias. Caution should nevertheless be applied when relying on predictions from a single cosmological model.

An additional limitation of the Millennium Simulation is the mass resolution of $8.6 \cdot 10^8\,\mathrm{M}_\odot$ per particle. This mass scale sets the completeness limit in our hydrogen simulation to $M_{\mathrm{HI}} + M_{\mathrm{H_2}} \approx 10^8\,\mathrm{M}_\odot$ (Section 7.3.2; Obreschkow et al., 2009a). Moreover, galaxies with $M_{\mathrm{HI}} + M_{\mathrm{H_2}} \lesssim 10^9\,\mathrm{M}_\odot$ normally sit a the centers of dark matter halos with poorly resolved merger histories. Therefore, their

[6] In the simulation, both masses and lengths scale as h^{-1} (Springel et al., 2005).

properties may not have converged in the semi-analytic simulation (Croton et al., 2006, Obreschkow et al., 2009a).

A long list of limitations associated with the semi-analytic galaxy simulation and our post-processing to assign extended HI- and H_2-properties has been considered in Obreschkow et al. (2009a). The bottom line of this discussion is that, at $z \gtrsim 5$, the simulation becomes very uncertain because the geometries and matter content of regular galaxies are virtually unconstrained from an empirical viewpoint. The young age and short merger intervals of these galaxies may, in fact, have caused them to deviate substantially from the simplistic disk-gas model. At $z \lesssim 5$, the predictions of our HI- and H_2-properties are more certain, as they are consistent with available observations. For example, two measurements of CO(2–1)-line emission in regular galaxies at $z \approx 1.5$ (Daddi et al., 2008) are consistent with the H_2-MF at this redshift (Obreschkow & Rawlings, 2009b). Furthermore, the predicted comoving space density of H_2 evolves proportionally to the observed space density of star formation (e.g. Hopkins, 2007) within a factor 2 out to at least $z = 3$. At $z = 0$, the simulated HI-mass function and CO(1–0)-luminosity function are consistent with the observations of Zwaan et al. (2005a) and Keres et al. (2003). Additionally, the local sizes and line widths of HI and CO match the local observations (Obreschkow et al., 2009a, and references therein).

We shall now highlight some specific limitations associated with the emission lines considered in this paper.

7.4.2 Limitations specific to the HI-line

We emphasize that at high redshift, the simulated cosmic HI-space density $\Omega_{\rm HI}$ falls below the inferences from Lyman-α absorption against distant QSOs by a factor ~ 2. As mentioned in Obreschkow & Rawlings (2009b), this could reflect a serious limitations of the semi-analytic models implied by the treatment of all cold hydrogen (HI+H_2) as a single phase. Consequently, our $\mathrm{d}N/\mathrm{d}z$-predictions for HI could be slightly pessimistic. If we believe the empirical estimations of

$\Omega_{\rm HI}$, the offset of our HI-masses by a factor ~ 2 can be readily accounted for by artificially decreasing the flux limit of the simulated survey by a factor 2. For typical HI-surveys in the redshift range $z = 0.5 - 10$, this would increase the number of detectable sources by a factor $2 - 4$.

We have limited our predictions for HI to HI-emission from galaxies. However, in the EoR, the IGM was not completely ionized and therefore acted as an additional source of HI-emission or -absorption (Iliev et al., 2002). It may therefore be necessary to analyze the implications of intergalactic HI on the detectability of galactic HI at $z \gtrsim 6$ (Becker et al., 2001). On a theoretical level, such an analysis could result from combining the simulation presented in this paper with a simulation of the EoR (e.g. Baek et al., 2009, Santos et al., 2008).

7.4.3 Limitations specific to the CO-lines

The main discussion of these limitations is given in Obreschkow & Rawlings (2009b), where we introduced our model for the conversion between H_2 and CO. The most serious sources of uncertainty appear to be the heating of molecular gas by SBs and AGNs, the overlap of molecular clouds at high redshift, and the possible presence of nuclear molecular disks in high-redshift galaxies. By contrast, the often discussed effects of the CMB and the cosmic evolution of the metallicity seem relatively well understood today. Overall, the uncertainty in the predicted CO-luminosities increases with redshift and with the J-level of the CO-transition.

The highest uncertainties, i.e. those for the higher order CO-lines at high redshift, can be close to a factor 10. The $\mathrm{d}N/\mathrm{d}z$-functions in this regime are therefore expected to deviate significantly from our predictions. Such deviations will uncover much of the physics of CO-line emission. In fact, in Obreschkow & Rawlings (2009b) we have explained in detail how different deviations of the CO-luminosity functions from our predictions can be translated into physical interpretations.

7.4.4 Is the simulation large enough to probe the BAOs?

The largest coherence-scale of our sky simulation is defined by the size of the periodic simulation box of the underlying dark matter simulation (Millennium Simulation, Springel et al., 2005). The side length of this box is $s_{\rm box} = 500\,h^{-1}\,{\rm Mpc}$, which sets the smallest extractable wave number to $k = 2\pi/s_{\rm box} \approx 0.013\,h$. This value is comparable to the wave number of the first peak in the CDM power spectrum (e.g. Springel et al., 2005). Therefore, the presented simulation allows us to study the power spectrum of HI- and CO-lines and to extract the baryon acoustic oscillations (BAOs); however the position and the amplitude of the first peak of the BAOs will be very poorly constrained.

By contrast, the SKA will have the potential to improve on present measurements of the baryonic power spectrum by at least an order of magnitude in amplitude, and it will detect power in spatial frequencies far below the first acoustic peak. Such a detection could set a primordial constraint on cosmological parameters, especially on the equation of state of dark energy (Blake et al., 2004). Therefore, a simulation of such a detection is regarded as a necessary step in designing the SKA. Yet, this requirement represents a major challenge since no current simulation of cosmic structure is large enough to accurately follow the largest acoustic oscillations, while simultaneously resolving structures small enough to allow the assembly of typical galaxies.

A circumvention of this numerical predicament could result from merging two simulations with different length-scales (see e.g. Angulo et al., 2008). For example, we could adopt the Horizon-4π dark matter simulation (Prunet et al., 2008, Teyssier et al., 2008), which has a giant box side length of $s_{\rm box} = 2\,h^{-1}\,{\rm Gpc}$, yet 10-times less mass resolution than the Millennium Simulation. Each dark matter halo of the Horizon-4π Simulation could then be populated with the resolved dark matter substructure and the galaxies contained in comparable haloes of the Millennium Simulation.

7.5 Conclusion

With this paper we release a simulation of the HI-emission line and the first ten $^{12}C^{16}O$-emission lines of galaxies in a sky field with a comoving diameter of $500\,h^{-1}\,\mathrm{Mpc}$. The actual field-of-view depends on the (user-defined) maximal redshift z_{max} according to the relation displayed in Fig. 7.2 (see also Eq. 7.5). This simulation represents the first quantitative attempt to compare the detectability of HI and CO at high redshift. Despite the limitations and uncertainties of this simulation (Section 7.4), its underlying galaxy simulation is nonetheless consistent with currently available observations (see Obreschkow et al., 2009a, Obreschkow & Rawlings, 2009b, Obreschkow et al., 2009b).

While this paper focussed on the simulation techniques and directly accessible results, the list of possible applications of the presented simulation is extensive. Some examples are:

- a $\mathrm{d}N/\mathrm{d}z$-analysis for particular surveys with the SKA, the LMT, and ALMA or their pathfinders;
- a combined study of HI-emission from galaxies and HI-emission from the IGM during the EoR (Santos et al., 2008) to quantify confusion issues;
- an optimization of the survey time allocated to different ALMA bands based on the CO-line ratios predicted at various redshifts;
- first quantitative predictions of the SKA's and ALMA's abilities to probe the galaxy power spectrum;
- predictions of the absorption signatures of HI and CO against distant QSOs;
- a study of line stacking experiments at redshifts where the detection of individual galaxies becomes impossible.

Such predictions can assist the design and optimized use of telescopes like the SKA, ALMA, and their pathfinders. Moreover, in light of forthcoming observations with the SKA and ALMA, the predictions made *prior* to these observations are the safest and perhaps the only way to test the predictive power of our current theories. This feature accentuates the necessity of extensive predictions, whether they will be verified or not by the empirical data.

Acknowledgements

This effort/activity is supported by the European Community Framework Programme 6, Square Kilometre Array Design Studies (SKADS), contract no 011938. The Millennium Simulation databases and the web application providing online access to them were constructed as part of the activities of the German Astrophysical Virtual Observatory.

7.6 Appendix A : Parametrization of emission line profiles

In Section 7.2.4, the normalized profiles of the HI- and CO-emission lines have been parameterized using the five parameters $\Psi_0^{\rm obs}$, $\Psi_{\rm max}^{\rm obs}$, $w_{\rm peak}^{\rm obs}$, $w_{50}^{\rm obs}$, and $w_{20}^{\rm obs}$ (see Fig. 7.8). From these parameters, the original normalized velocity profiles $\Psi(V)$ can be approximately recovered using the analytic function

$$\Psi_{\rm approx}(V) = \begin{cases} k_3 \, \exp\left[-\frac{(|V|-k_1)^2}{k_2}\right] & \text{if } |V| \geq w_{\rm peak}^{\rm obs}/2, \\ \frac{k_5}{\sqrt{k_4 - V^2}} & \text{if } |V| < w_{\rm peak}^{\rm obs}/2, \end{cases} \tag{7.16}$$

where k_i, $i \in \{1, ..., 5\}$, are free parameters. Eq. (7.16) combines the the functional form of Eq. (42) in Obreschkow et al. (2009a) for the center of the emission line with a Gaussian for the tails of the emission line. The five parameters k_i can be inferred from the parameters $\Psi_0^{\rm obs}$, $\Psi_{\rm max}^{\rm obs}$, $w_{\rm peak}^{\rm obs}$, $w_{50}^{\rm obs}$, and $w_{20}^{\rm obs}$. The analytic solution is

$$k_1 = \frac{1}{4} \frac{\ln(0.5)\,({w_{\rm peak}^{\rm obs}}^2 - {w_{20}^{\rm obs}}^2) + \ln(0.2)\,({w_{50}^{\rm obs}}^2 - {w_{\rm peak}^{\rm obs}}^2)}{\ln(0.5)\,(w_{\rm peak}^{\rm obs} - w_{20}^{\rm obs}) + \ln(0.2)\,(w_{50}^{\rm obs} - w_{\rm peak}^{\rm obs})}, \tag{7.17}$$

$$k_2 = \frac{0.25\,({w_{\rm peak}^{\rm obs}}^2 - {w_{50}^{\rm obs}}^2) + k_1\,(w_{50}^{\rm obs} - w_{\rm peak}^{\rm obs})}{\ln(0.5)}, \tag{7.18}$$

$$k_3 = \Psi_{\rm max}^{\rm obs} \exp\left[\frac{(2\,k_1 - w_{\rm peak}^{\rm obs})^2}{4\,k_2}\right], \tag{7.19}$$

$$k_4 = \frac{1}{4} \frac{{w_{\rm peak}^{\rm obs}}^2 \, {\Psi_{\rm max}^{\rm obs}}^2}{{\Psi_{\rm max}^{\rm obs}}^2 - {\Psi_0^{\rm obs}}^2}, \tag{7.20}$$

$$k_5 = \Psi_0^{\rm obs} \sqrt{k_4}. \tag{7.21}$$

Fig. 7.8 compares a simulated normalized HI-emission line with the emission line recovered using Eqs. (7.16–7.21).

We note that some emission lines, especially those of galaxies seen face-on, peak at the line center. These lines have $w_{\rm peak}^{\rm obs} = 0$, and therefore Eq. (7.16) reduces to the Gaussian tails.

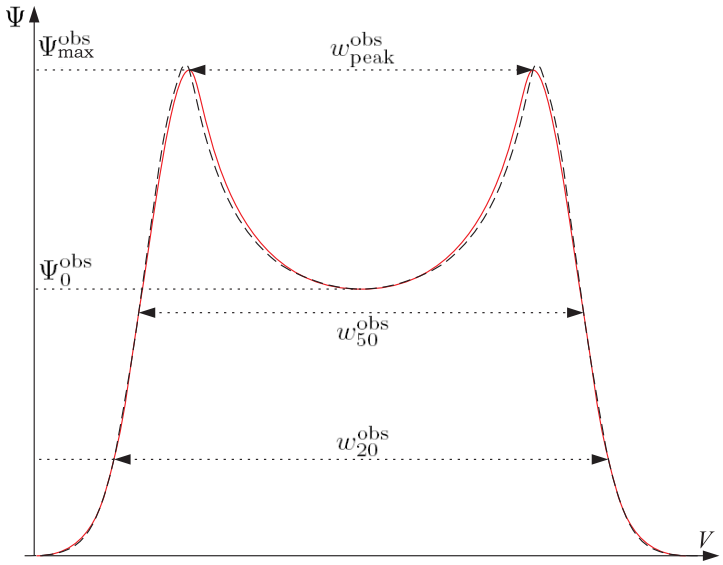

Figure 7.8. Comparison of a simulated normalized emission line $\Psi(V)$ (solid line) with the emission line $\Psi_{\rm approx}(V)$ (dashed line), recovered from the five parameters $\Psi^{\rm obs}_0$, $\Psi^{\rm obs}_{\rm max}$, $w^{\rm obs}_{\rm peak}$, $w^{\rm obs}_{50}$, and $w^{\rm obs}_{20}$.

7.7 Appendix B : Online-access to the sky simulation

One particular realization of the mock observing cone, i.e. one choice of random symmetry operations for the replicated simulation boxes (see Section 7.2.2), can be access on-line via http://s-cubed.physics.ox.ac.uk/ (go to "S^3-SAX-Sky"). Each galaxy in the virtual observing cone is specified by a list of properties, including its position, its attributes for the HI- and CO-emission lines, as well as its intrinsic properties of the DeLucia-catalog, such as optical magnitudes, masses, star formation rates, clustering properties, or merger histories.

The accessible database contains two subsets, a full sky simulation ($\sim 2.8 \cdot 10^8$ galaxies), associated with the Millennium Simulation ($s_{\rm box} = 500\,h^{-1}\,{\rm Mpc}$), and a small sky simulation ($\sim 4.5 \cdot 10^6$ galaxies), associated with the Milli-Millennium Simulation ($s_{\rm box} = 62.5\,h^{-1}\,{\rm Mpc}$). The solid angle subtended by the small sky simulation is 64-times smaller than of the full sky simulation. However, the small simulation can be useful for testing purposes.

The maximal opening angle φ of the sky field depends on the maximal comoving distance $D_{\rm C,max}$ (or the maximal redshift $z_{\rm max}$) via Eq. 7.5 (see also Fig. 7.2). The user must be aware that there are no galaxies outside this maximal opening angle, i.e. galaxies only exist, where |RA| and |Dec| are smaller than $\varphi/2$.

The database can be queried using the structured query language (SQL) interface. The latter not only allows the user to download a particular galaxy sample, but it also offers ways to directly calculate dN/dz-functions and luminosity-functions or to retrieve all the galaxies of a particular cluster. Samples of such advanced queries are given on the web-page.

7.8 Appendix C : Illustration of a larger sky field

Fig. 7.9 shows the HI and CO of the galaxies in a mock sky field of 3×1 arcmin^2 at three different redshifts. Each redshift slice has the same comoving thickness of 240 Mpc, such that the number of galaxies is proportional to the comoving space density of galaxies. Note, however, that the flux scales differ between the three panels of Fig. 7.9. The main features of the galaxies in Fig. 7.9 are discussed in Section 7.3.1.

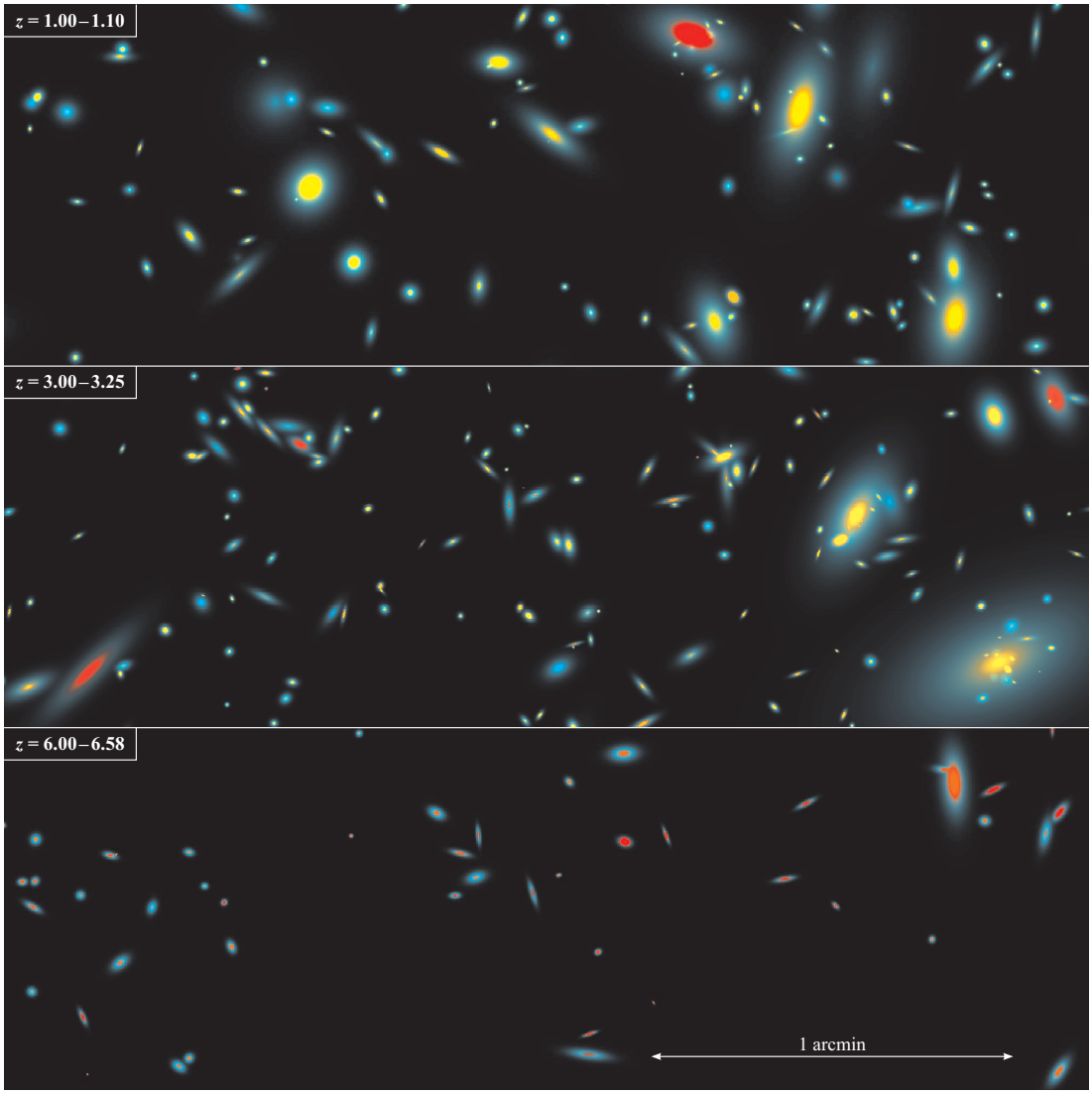

Figure 7.9. Simulated sky field covering 3×1 arcmin^2. The three panels correspond to three different redshift slices, with an identical comoving depth of 240 Mpc. The coloring is identical to Fig. 7.4, but the flux scales are 10-times smaller at $z = 3$ and 100-times smaller at $z = 6$.

7.9 Appendix D : Analytic fits for $\mathrm{d}N/\mathrm{d}z$-functions

Table 7.1 lists the values of the parameters c_1, c_2, and c_3 for the analytic $\mathrm{d}N/\mathrm{d}z$-fit of Eq. (7.15). The parameters are given for both peak flux density limited and integrated flux limited surveys, although the functions have only been displayed for the peak flux density limited case. Since apparent line widths are typically of order $100\,\mathrm{km\,s^{-1}}$, surveys limited by a flux density s_{lim} and those limited by a velocity-integrated flux $S^{\mathrm{V}}_{\mathrm{lim}} = s_{\mathrm{lim}} \times 100\,\mathrm{km\,s^{-1}}$ have indeed similar $\mathrm{d}N/\mathrm{d}z$-functions.

In some cases the flux limits are low enough that galaxies can be detected, for which the galaxy mass function in the simulation is incomplete. The corresponding parts of the $\mathrm{d}N/\mathrm{d}z$-functions must be considered as lower limits, as emphasized in Section 7.3.2. these parts have been represented as dotted lines in Fig. 7.5 and Fig. 7.7.

Parameters		**Limiting peak flux density** [Jy]						**Limiting integrated flux** [Jy km s^{-1}]					
		10^{-8}	10^{-7}	10^{-6}	10^{-5}	10^{-4}	10^{-3}	10^{-6}	10^{-5}	10^{-4}	10^{-3}	10^{-2}	10^{-1}
HI	c_1	6.54	6.89	6.77	5.87	4.57	6.90	6.60	6.95	6.53	5.75	5.03	6.35
	c_2	2.58	2.93	2.43	1.29	0.38	2.87	2.70	2.98	2.13	1.32	1.04	2.58
	c_3	1.43	2.20	3.13	4.17	7.10	34.28	1.52	2.37	2.86	3.85	7.95	29.65
CO(1–0)	c_1	6.31	6.40	6.37	5.93	5.06	4.07	6.30	6.36	6.30	5.92	5.25	5.06
	c_2	2.20	2.32	2.10	1.40	0.59	0.23	2.18	2.27	2.01	1.51	0.99	1.26
	c_3	1.12	1.27	1.48	1.58	1.74	3.29	1.11	1.24	1.39	1.50	1.69	4.95
CO(2–1)	c_1	6.28	6.34	6.42	6.23	5.63	4.63	6.28	6.32	6.37	6.19	5.66	4.88
	c_2	2.13	2.24	2.31	1.83	1.12	0.38	2.13	2.21	2.22	1.85	1.29	0.77
	c_3	1.08	1.16	1.35	1.50	1.59	1.94	1.07	1.15	1.29	1.45	1.51	1.85
CO(3–2)	c_1	6.27	6.31	6.39	6.31	5.80	4.86	6.27	6.30	6.36	6.25	5.82	5.09
	c_2	2.12	2.20	2.31	2.00	1.30	0.52	2.12	2.18	2.25	1.94	1.44	0.94
	c_3	1.07	1.12	1.28	1.45	1.51	1.59	1.06	1.12	1.23	1.37	1.46	1.58
CO(4–3)	c_1	6.27	6.30	6.36	6.25	5.75	4.83	6.27	6.29	6.33	6.19	5.76	5.00
	c_2	2.11	2.17	2.26	1.92	1.26	0.57	2.12	2.16	2.21	1.84	1.38	0.88
	c_3	1.06	1.11	1.22	1.33	1.39	1.39	1.06	1.10	1.19	1.26	1.34	1.34
CO(5–4)	c_1	6.27	6.29	6.31	6.04	5.44	4.53	6.27	6.29	6.29	5.99	5.52	4.71
	c_2	2.12	2.16	2.17	1.59	1.01	0.59	2.11	2.15	2.12	1.56	1.24	0.83
	c_3	1.06	1.10	1.18	1.15	1.16	1.16	1.06	1.09	1.15	1.10	1.18	1.12
CO(6–5)	c_1	6.27	6.28	6.16	5.61	4.95	4.17	6.27	6.27	6.12	5.61	5.07	4.31
	c_2	2.11	2.12	1.85	1.08	0.84	0.96	2.11	2.12	1.79	1.15	1.06	1.09
	c_3	1.06	1.10	1.07	0.90	0.94	1.09	1.06	1.09	1.04	0.88	0.97	1.01
CO(7–6)	c_1	6.26	6.21	5.71	5.00	4.45	3.89	6.26	6.19	5.69	5.07	4.54	4.03
	c_2	2.10	2.00	1.18	0.74	1.19	1.59	2.09	1.97	1.22	0.85	1.21	1.71
	c_3	1.06	1.06	0.80	0.66	0.90	1.21	1.06	1.05	0.80	0.67	0.86	1.11
CO(8–7)	c_1	6.21	5.75	4.99	4.42	4.13	3.66	6.20	5.73	5.07	4.48	4.18	3.77
	c_2	2.01	1.29	0.71	1.08	1.90	2.27	1.99	1.31	0.84	1.02	1.84	2.38
	c_3	1.04	0.79	0.52	0.63	1.05	1.45	1.03	0.78	0.56	0.59	0.96	1.28
CO(9–8)	c_1	5.70	4.94	4.34	4.10	3.85	3.33	5.68	5.02	4.42	4.11	3.93	3.40
	c_2	1.28	0.79	1.09	1.85	2.46	2.34	1.31	0.91	1.07	1.74	2.48	2.32
	c_3	0.74	0.47	0.49	0.82	1.19	1.48	0.74	0.52	0.49	0.74	1.12	1.19
CO(10–9)	c_1	4.80	4.28	4.02	3.88	3.52	2.94	4.88	4.34	4.06	3.91	3.65	2.99
	c_2	0.90	1.31	1.83	2.36	2.43	2.20	1.00	1.28	1.78	2.28	2.59	2.13
	c_3	0.43	0.48	0.67	0.99	1.15	1.46	0.48	0.48	0.64	0.90	1.13	1.09

Table 7.1. Parameters for the analytic fit formula of Eq. (7.15) for $\mathrm{d}N/\mathrm{d}z$ peak flux density limited and integrated flux limited surveys.

Chapter 8

Conclusion

In compiling this section, I decided to omit a repetition of a summary since the thesis and the individual chapters were summarized in their respective abstracts. Instead, this conclusion will shed light on the most important outcomes of this thesis and position the latter in a broader framework.

8.1 Contributions of this thesis

The tangible products of this thesis are two simulated databases. The first database (Chapters 3 and 6) lists the *intrinsic* cold gas properties of $\sim 3 \cdot 10^7$ galaxies in a cubic volume of $(500\,h^{-1}\,\mathrm{Mpc})^3$ at 64 discrete redshifts, covering the whole time-line of the star forming Universe. This database represents an extension of the DeLucia-catalog (De Lucia & Blaizot, 2007), which contains the comoving coordinates, velocities, merger histories, and various intrinsic properties of the same $\sim 3 \cdot 10^7$ evolving galaxies. Our second database (Chapter 7) represents a virtual observing cone and lists the *apparent* HI- and CO-line properties of millions of galaxies in a sky field with a comoving diameter of $500\,h^{-1}\,\mathrm{Mpc}$. Both databases will be publicly released as part of the SKA design studies (SKADS), an international effort to investigate SKA-related technologies, supported by the European Community Sixth Framework Programme. The prime intent of these databases is to assist the development of the future SKA and ALMA in the multiple ways described in Section 1.3.

In the following, I shall highlight what I consider the most significant scientific contributions of this thesis.

- *Perhaps the most important prediction is the dramatic cosmic evolution of the H_2/HI-ratio in the bulk of regular galaxies* (Chapter 4). We showed that this evolution is a direct consequence of (i) the relation between H_2/HI-ratios and pressure (Blitz & Rosolowsky, 2006, Elmegreen, 1993, Leroy et al., 2008) and (ii) the size evolution of galaxies (Bouwens et al., 2004, Buitrago et al., 2008, Trujillo et al., 2006). The size evolution itself is driven by the increase in the volume/mass-ratio of dark haloes with cosmic time (Gunn & Gott, 1972), which translates into increasing disk sizes by transfer of angular momentum (Fall & Efstathiou, 1980). Although this empirical evolution of galaxy sizes is not well understood to-date, it can be used to predict the cosmic evolution of the H_2/HI-ratio in galaxies. The magnitude of this evolution, i.e. $\Omega_{\rm HI}(z)/\Omega_{\rm H_2}(z) \propto (1+z)^{1.6}$, and its robustness against the details of the semi-analytic galaxy model leave little doubt about its reality. Moreover, this prediction offers a unified explanation for (i) the weak evolution of the cosmic HI-density inferred from Lyman-α absorption against distant quasars (e.g. Prochaska et al., 2005), (ii) the strong molecular emission lines recently detected in normal galaxies at $z = 1.5$ (Daddi et al., 2008), and (iii) the strong evolution of the cosmic star formation density (Hopkins & Beacom, 2006).

  To the best of my knowledge, no explicit prediction of such a cosmic evolution of the H_2/HI-ratio has been published prior to this work. It will be very exciting to confront this prediction with the results of future high-redshift surveys of HI and H_2 with powerful telescopes like the SKA and ALMA.

  As a consequence of the evolving H_2/HI-ratio, the large H_2-masses suspected in high-redshift galaxies (Daddi et al., 2008) do not imply that those galaxies carry large amounts of HI. In particular, the assumption (e.g. Wilkinson, 1991) that HI-rich galaxies at high redshift ($z \gtrsim 3$) will reach HI-masses in the range of $10^{12}\,{\rm M}_\odot - 10^{13}\,{\rm M}_\odot$ is not supported by this thesis. According to our simulation, at any redshift, galaxies with HI-masses larger than $10^{11}\,{\rm M}_\odot$ have comoving space densities below $10^{-6}\,{\rm Mpc}^{-3}$ and are therefore very rare.

- A related prediction is that the physical sizes of the HI- and H_2-disks in regular galaxies increase with cosmic time (Chapter 5). Consequently, neutral gas in distant galaxies can be expected to be more compact than in local ones, such as confirmed by several resolved CO-line detections at high redshift (see Chapter 5 and references therein). Combining the predicted size-evolution with the mass-evolution of HI, we find that the maximal surface density of HI in regular galaxies remains constant over cosmic time at a value of $\sim 10\,\mathrm{M}_\odot\,\mathrm{pc}^{-2}$. This value matches the saturation level of HI observed in local galaxies (Leroy et al., 2008). By contrast, H_2 does not saturate, and we predict that its surface density decreased by two orders of magnitude from $z = 5$ to $z = 0$, roughly paralleling the cosmic evolution of the star formation densities.

- Potentially useful analytical results are the radial surface density profiles $\Sigma_{\mathrm{HI}}(r)$ and $\Sigma_{\mathrm{H_2}}(r)$ derived in Chapter 3 (Eqs. 3.11, 3.12). By construction, these profiles reproduce the empirical relation between H_2/HI-ratios and ISM pressure measured by (Leroy et al., 2008, see also Blitz & Rosolowsky, 2006, Elmegreen, 1993). They can also be regarded as the simplest implementation of a model combining an exponential profile for the total hydrogen density, $\Sigma_{\mathrm{HI}}(r) + \Sigma_{\mathrm{H_2}}(r)$, with a second exponential profile with a different scale length for the local H_2/HI-ratio, $\Sigma_{\mathrm{H_2}}(r)/\Sigma_{\mathrm{HI}}(r)$. Moreover, the analytic expressions for $\Sigma_{\mathrm{HI}}(r)$ and $\Sigma_{\mathrm{H_2}}(r)$ make a list of specific predictions expanded in Chapter 5. For example, H_2-rich galaxies, i.e. those with central H_2/HI-ratios $R_{\mathrm{mol}}^{\mathrm{c}} \gtrsim 10$, have annular HI-distributions with a marked density drop towards the center. Another example is that if $\Sigma_{\mathrm{HI}}(r)$ and $\Sigma_{\mathrm{H_2}}(r)$ cross, they do so close to the maximum of $\Sigma_{\mathrm{HI}}(r)$.

  Our analytic model for $\Sigma_{\mathrm{HI}}(r)$ and $\Sigma_{\mathrm{H_2}}(r)$ is consistent with the observed surface density maps of the nearby galaxies studied as part of The HI Nearby Galaxy Survey (THINGS, Leroy et al., 2008, Walter et al., 2008). Examples for four galaxies were shown in Figs. 3.1 and 5.1.

- I believe that our prediction of the CO-luminosity functions will be significant in light of the first detections with ALMA. The use of this prediction relies not only in the specific CO-LFs presented in Chapter 6, but, perhaps more importantly, on our analysis of the effect of different physical mechanisms on the CO-to-H_2 conversion. This analysis will permit inferences on the physics in high-redshift galaxies, once CO-detections become available for a statistically significant sample.

8.2 Broader frame and outlook

The frame of the hydrogen simulation presented in this thesis is fixed by the limits adopted for the length-scales, the cosmic epoch, and the physical processes.

The largest accessible length-scale is defined by the size of the simulation box of the underlying dark matter simulation (Millennium Simulation, Springel et al., 2005). The side length of this box is $s_{\rm box} = 500\,h^{-1}\,$Mpc, which falls short regarding a solid prediction of the SKA's ability to probe cosmic structure. The largest baryonic oscillations that can be measured from this simulation, albeit with a big uncertainty, correspond to the wave number $k = 2\pi/s_{\rm box} \approx 0.013\,h$. This value is comparable to the expected wave number of the first peak in the power spectrum of galaxies (e.g. Springel et al., 2005), and hence this peak is poorly defined in the simulation. By contrast, the SKA will improve on present measurements of the baryonic power spectrum by at least an order of magnitude in amplitude, and it will detect power in space frequencies far below the first acoustic peak Blake et al. (2004). Such a detection could set a primordial constraint on cosmological parameters, in particular, on the equation of state of dark energy (details in Blake et al., 2004). Therefore, a simulation of such a detection is regarded as a necessary step in designing the SKA. Yet, this requirement represents a major challenge since no current simulation of cosmic structure is large enough to include the largest acoustic oscillations, while simultaneously resolving structures small enough to allow the assembly of typical galaxies. A circumvention of this

hindrance could result from merging our present hydrogen simulation with a less resolved dark matter simulation of the very largest structures. Within SKADS this idea resulted in the concrete plan to use the Horizon-4π simulation (Prunet et al., 2008, Teyssier et al., 2008) – a dark matter simulation with a box side of $s_{\rm box} = 2\,{\rm Gpc}\,h^{-1}$, but with 10 times less mass resolution than the Millennium Simulation – and populate its dark matter haloes with the dark matter substructure and galaxies resolved in comparable haloes in the Millennium Simulation.

The minimal length-scales considered in our hydrogen simulation are set by the working assumption that the cold gas in galaxies can be approximated as axially symmetric disks. For galaxies in the local Universe this assumption becomes spurious on scales on the order of 1 kpc, where substructures like spiral arms, warps, and central bars become relevant. Both the SKA and ALMA will achieve subarcsecond resolution, hence allowing the mapping of the cold gas in local galaxies with great detail. These observational perspectives premise accurate simulations of HI- and H_2-distributions on sub-galactic scales. A straightforward way to meet this requirement consists in post-processing the global HI- and H_2-properties simulated in this work. The option currently investigated within SKADS consists in stamping 3-dimensional "pictures" of realistic HI-distributions onto each galaxy in our simulation (Boomsma et al., 2002).

Another boundary is set by our restriction to neutral hydrogen in galactic disks. This setting translates into limiting the considered time span to the cosmic era of galaxy formation. During the preceding era, i.e. the cosmic "dark ages", and the early era of galaxy formation, i.e. the "epoch of reionization" (EoR), most hydrogen existed as HI in the IGM before it became completely ionized by the radiation from the first stars and massive black holes. Probing this neutral IGM in HI-emission and -absorption constitutes the core of the SKA key science project V, "Probing the dark ages". To optimize the SKA towards such a detection, Santos et al. (2008) have simulated the signature of HI in the EoR in much detail. When combined with the hydrogen simulation presented in this thesis,

the full cosmic time span, where neutral hydrogen can potentially be detected by the SKA, is covered by the SKADS simulations.

Perhaps the most significant and poorly characterized limitations of our simulations are those associated with the physical modeling of galaxies. For example, the simulated values of $\Omega_{\rm HI}(z)$ at $z > 2$ (Chapter 4) underestimate the inferences from damped Lyman-α systems by a factor 2. No definite explanation for this discrepancy could be found so far. It is nevertheless fair to mention that much of the inaccuracy in our simulation is intrinsically given by the multi-layer approach, in which we successively evaluate (i) the growth of cosmic structure, (ii) the cosmic evolution of galaxies, and (iii) the co-evolution of HI and H_2 in galaxies. Much progress could be expected by treating HI-masses and H_2-masses as separate entities directly in the semi-analytic galaxy simulation. As mentioned in Chapter 4, this would allow a refinement of the feedback-mechanisms for the suppression of gas infall (explained in Croton et al., 2006), such that HI can still be accreted, while the formation of H_2 and stars is inhibited. Such a semi-analytic setting would also allow us to implement a recipe for the large-scale dissociation of molecular gas by the radiation field of newly formed stars (Allen et al., 1986). Both examples would effectively increase the amount of HI in high-redshift galaxies and thereby bring our prediction of $\Omega_{\rm HI}(z)$ in alignment with the observations.

In light of these limitations, I would like to end with an emphasis on modesty. Galaxy evolution is a vastly more nuanced affair than our simplistic models would suggest. In the attempt to predict the "unknown", we do not claim accuracies beyond first approximations in our simulations. Therefore, emerging predictions with a significance level on orders of magnitude, such as the cosmic decline in the H_2/HI-ratio (Chapter 4), constitute perhaps the most exciting contribution of this work.

Chapter 9

Excursion

In this final chapter, I briefly summarize some extracurricular research projects I have been involved with during my doctoral studies.

9.1 An original approach to the Tully-Fisher relation

Collaborators: S. Rawlings

References: "The HI-Tully-Fisher relation", D. Obreschkow, SKA Conference, Perth, April 2008

Abstract: The empirical determination of the circular velocity-to-mass relation (Tully-Fisher relation) of spiral galaxies normally requires information about the inclinations of the observed galaxies. Hence, the studied galaxies need to be spatially resolved – a serious limitation, especially for investigations at high redshift. To address this issue, we developed a mathematical method to extract the Tully-Fisher relation for a galaxy sample with no or limited information about the inclinations. Applying this method to the galaxies in the HIPASS catalog (Meyer et al., 2004) results in a Tully-Fisher relation, which almost perfectly matches the one derived using photographic inclinations from the optical cross-match catalog (HOPCAT). However, the scatter of this second relation is larger, hence revealing an addition of spurious scatter when strictly imposing the (uncertain) photographic inclinations.

9.2 An eccentric core-collapse in Cassiopeia A?

Collaborators: P. Podsiadlowski, B. Fitzpatrick

References: "The Cas A Supernova Remnant: Evidence for an Asymmetric Implosion?", D. Obreschkow, Stellar Coffee Talk, Oxford, March 2007

Abstract: The morphology of the supernova remnant Cas A has a striking resemblance to high-speed visualizations of an eccentric cavitation bubble collapsing inside a spherical water ball (see Section 9.4). This led us to investigate the scenario of an eccentric core collapse as a possible origin of the peculiar jet structure of Cas A. Surprisingly, this scenario turned out to be consistent with various other observations of Cas A. Moreover, B. Fitzpatrick (doctoral student in Oxford Astrophysics) used an SPH-simulation to demonstrate that a gravitational collapse onto an eccentric stellar core results in two jets, which are, at least qualitatively, similar to those of Cas A. I consider this a very interesting project to be followed up.

9.3 Planets at the Lagrangian Points of Binary Stars?

Collaborators: J. Bell Burnell, S. Mohamed

References: D. Obreschkow, Stellar Coffee Talk, Oxford, September 2007

Abstract: 90 % of the 300 or so extrasolar planets known today (Schneider, 2008) orbit around single stars as opposed to binary systems. In fact, planetary orbits around binary stars are only considered stable if the distance between two of the three bodies is much smaller than their distance to the third one. In contradiction to this classical conclusion, we found moderate observational evidence for planet-sized compact objects at the triangular Lagrangian points (L4, L5) of dozens of binary stars in the Large Magellanic Cloud. These planetary objects were detected statistically as transiting absorbers in a sample of eclipsing binary stars from the Observational Gravitational Lensing Experiment (OGLE). Our detection method exploits the precise synchronization of the Lagrangian

point transits with the stellar eclipse cycles. Stacking the precalculated transit phases of many light curves significantly reduces the measurement uncertainties, thus permitting the statistical identification of absorbers or groups of absorbers smaller than Jupiter. The detected moderate evidence for absorbers is particularly surprising as the triangular Lagrangian points of binary stars are, in fact, unstable equilibrium points.

9.4 The collapse of cavitation bubbles in microgravity

Collaborators: P. Kobel, N. Dorsaz, A. de Bosset, C. Nicollier, and M. Farhat
References: Obreschkow et al. (2006), Farhat et al. (2006), Kobel et al. (2009), www.flashandsplash.ch

Abstract: Hydrodynamic cavitation is the field associated with the study of unstable vapor bubbles in liquids. Uncontrolled cavitation is a major source of erosion damage in many industrial systems, such as fast ship propellers, cryogenic pumps, pipelines, and turbines. To-date this damaging process is only partially understood and a broad consensus seems established that detailed time-resolved studies of single cavitation bubbles are required as a basis for further theoretical progress. In a proposal to the European Space Agency (ESA) in 2004, we have pointed out the potential use of studying single cavitation bubbles inside spherical water drops stabilized in microgravity. ESA subsequently selected the proposed experiment to fly aboard the Airbus A300 zero-g – a sub-orbital platform to generate intervals of 24 s of nearly perfect weightlessness ($\ll 0.01\,g$). The total microgravity time allocated to our experiment was 1 hour, corresponding to 150 individual flight maneuvers. The high-speed visualizations of collapsing cavitation bubbles obtained during microgravity revealed several unknown implications of isolated, finite liquid volumes and spherical free surfaces for the bubble collapse and subsequent phenomena. In particular, bubble lifetimes in drops are shorter than in extended volumes – an observation which led us to a correction of the Rayleigh-Plesset equation for finite volumes. In the case of eccentrically

placed bubbles, the toroidal collapse induces two liquid jets, consistent with theoretical predictions. These jets escaped from the drop in antipodal directions and represent the first direct, simultaneous visualization of both collapse-induced jets in a steady liquid volume.

9.5 Face statistics of irregular dice

Collaborators: N. Jones, N. Johnson

References: "The Many Surprises of Irregular Dice", D. Obreschkow and N. Jones, in preparation, http://www.physics.ox.ac.uk/cm/cmt/cuboid/

Abstract: You roll a six-sided die with parallel faces but non-equal edge lengths. What is the probability of landing on a particular face? Very little is known about the outcome statistics of these objects. We have addressed this problem with three different approaches: (i) an experimental approach consisting of tossing a custom-made irregular dice hundreds of times; (ii) an analytical approach based on the assumption of thermodynamic equilibrium; (iii) a sophisticated computer simulation[1], which we used to analyze $5.3 \cdot 10^9$ tosses using 578 processors. Quite surprisingly the combined result of these three approaches is that the face statistics of irregular dice is highly complex. In fact, the outcome statistics depends on the elasticity and friction between the surface and the die, as well as on the initial energy. The latter is particularly surprising since it demonstrates that irregular dice possess a long-term memory of their initial conditions in a statistical sense.

9.6 A non-orthogonal theory for quantum dot polarons

Collaborators: M.-A. Dupertuis, S. Dalessi, F. Michelini

References: Obreschkow et al. (2007)

Abstract: This work represents a follow-up of my master thesis on the interaction

[1] A Windows version of this simulation can be downloaded on http://www.physics.ox.ac.uk/cm/cmt/cuboid/.

between electrons captured in quantum dots (QDs) and optical lattice vibrations. Understanding this interaction is considered an important step towards a broad variety of technological applications (see introduction of Obreschkow et al., 2007). Usually the interaction between optical lattice vibrations and QD electrons is described by the Fröhlich Hamiltonian, which, in the particular case of QDs, cannot be treated as a perturbation (Verzelen et al., 2000). We found that the use of non-commuting phonon creation/annihilation operators associated with a set of non-orthogonal optical modes is an effective way to deal with this situation. In fact, the non-orthogonal setting simplifies the mathematical treatment and reveals a nested coupling structure of the Frölich interaction – a physical interpretation, which cannot be seen using a standard orthogonal basis. We developed the concept of a non-orthogonal basis for the Frölich interaction into a minimal model, which we used to compute the energy levels and geometries of the lower polaronic excitations in a pyramidal QD in a non-perturbative setting.

Glossary of variables

α_{J}	CO-to-H_2 conversion factor α for the CO-transition $J \rightarrow J-1$
B	Overlap factor of molecular clumps (in space and velocity)
$\mathcal{B}$	Mass ratio between bulge and disk+bulge
β	Mass fraction of hydrogen (HI+H_2) in non-metallic cold gas ($\beta = 0.75$)
c_{bulge}	Concentration parameter of the bulge
c_{disk}	Concentration parameter of the disk
c_{halo}	Concentration parameter of the halo
D_{A}	Angular diameter distance
D_{C}	Comoving distance
$D_{\mathrm{C,max}}$	Maximal comoving distance of the simulated observing cone
D_{L}	Luminosity distance
ε	Correction-factor of CO-luminosities due to H_2 in a smooth phase
F	Filling factor of H_2 (in space and velocity)
f_{clumpy}	Fraction of the H_2-mass in the clumpy (i.e. GMC-like) phase
f_σ	Average ratio between $\sigma_{\mathrm{gas,z}}$ and $\sigma_{\mathrm{stars,z}}$ in galaxies
f_σ^0	Ratio between $\sigma_{\mathrm{gas,z}}$ and $\sigma_{\mathrm{stars,z}}$ at the center of galactic disks
H	Neutral hydrogen (HI+H_2)
HI	Neutral atomic hydrogen (without helium)
H_2	Neutral molecular hydrogen (without helium)
h	Hubble parameter ($h = 0.73$ in the simulation of this thesis)
h_{gas}	Exponential scale height of cold gas (perpendicular to the disk)

h_p	Plank constant ($h_\mathrm{p} \approx 6.626 \cdot 10^{-34}\ \mathrm{m^2\,kg\,s^{-1}}$)
h_stars	Exponential scale height of stars (perpendicular to the disk)
k_b	Boltzmann constant ($k_\mathrm{b} \approx 1.381 \cdot 10{-}23\ \mathrm{m^2\,kg\,s^{-2}\,K^{-1}}$)
κ	Fractional filling factor (in space and velocity) of a single H_2 clump
L	Frequency-integrated luminosity (= power) of an emission line
$\mathrm{L}_\odot$	Solar luminosity
L_CO	Luminosity of a specific CO-emission line
L_HI	Luminosity of the HI-emission line
L^T	Brightness temperature luminosity of an emission line
L^V	Velocity-integrated luminosity of an emission line
λ_e	Intrinsic wave length in the rest frame of the source
λ_o	Apparent wave length in the observer frame
M	Mass
$\mathrm{M}_\odot$	Solar mass
M^*	Characteristic turn-over mass in the Schechter function
M_B	Absolute blue band magnitude
M_bary	Baryon mass of a galaxy
$\dot{M}_\mathrm{BH}$	Black hole mass accretion rate
$\dot{M}^\mathrm{c}_\mathrm{BH}$	Value of $\dot{M}_\mathrm{BH}$, where the AGN-heating starts saturating
M^bulge	Mass of the bulge of a galaxy
M^disk	Mass of the disk of a galaxy
M_gas	Cold gas mass of a galaxy
M_H	Mass of cold hydrogen (HI+H_2, without helium)
M_HI	HI-mass of a galaxy

$M_{\mathrm{H_2}}$	H_2-mass of a galaxy
M_{halo}	Mass of the galaxy halo
M_{He}	Helium mass in the cold gas of a galaxy
M_{stars}	Stellar mass of a galaxy
$M_{\mathrm{stars}}^{\mathrm{bulge}}$	Stellar mass in the bulge of a galaxy
$M_{\mathrm{stars}}^{\mathrm{disk}}$	Stellar mass in the disk of a galaxy
M_{vir}	Virial mass of the halo of a galaxy
M_{x}	Mass of the component x
M_{Z}	Mass of the metals in the cold gas of a galaxy
$N_{\mathrm{H_2}}$	Column number-density of H_2-molecules in a galactic disk
ν	Frequency of electromagnetic radiation
ν_{CO}	Rest-frame frequency of the CO(1–0)-line ($\nu_{\mathrm{CO}} \approx 115.27$ GHz)
ν_{e}	Intrinsic frequency in the rest frame of the source
ν_{HI}	Rest-frame frequency of the HI-line ($\nu_{\mathrm{HI}} \approx 1.420$ GHz)
ν_{o}	Apparent frequency in the observer frame
$\Omega_{\mathrm{gas}}(z)$	Normalized cosmic space density of cold gas in galactic disks
$\Omega_{\mathrm{HI}}(z)$	Normalized cosmic space density of HI in galactic disks
$\Omega_{\mathrm{H_2}}(z)$	Normalized cosmic space density of H_2 in galactic disks
$\Omega_{\mathrm{HI+H_2}}(z)$	Normalized cosmic space density of HI+H_2 in galactic disks
P_{c}	External ISM pressure at the center of a galactic disk
P_{CO}	Power of a specific CO-emission line
P_{HI}	Power of the HI-emission line
φ_{disk}	Gravitational potential of a galactic disk
ϕ_{HI}	Differential space density of HI used in the HI-MF

$\phi_{\mathrm{H_2}}$	Differential space density of H_2 used in the H_2-MF
ϕ_{x}	Differential space density of component x, typically used in MFs
$\Psi(V_{\mathrm{obs}})$	Normalized luminosity density of an emission line (edge-on)
$\Psi_{\mathrm{CO}}(V_{\mathrm{obs}})$	Normalized luminosity density of a molecular emission line
Ψ^{0}_{CO}	Normalized luminosity density at the center of a molecular emission line
$\Psi^{\mathrm{max}}_{\mathrm{CO}}$	Normalized maximal luminosity density of a molecular emission line
$\Psi_{\mathrm{HI}}(V_{\mathrm{obs}})$	Normalized luminosity density of the HI-emission line
Ψ^{0}_{HI}	Normalized luminosity density at the center of the HI-emission line
$\Psi^{\mathrm{max}}_{\mathrm{HI}}$	Normalized maximal luminosity density of the HI-emission line
$\Psi^{\mathrm{obs}}(V_{\mathrm{obs}})$	Normalized luminosity density of an emission line (inclined)
q_{HI}	Apparent axes-ratio of the inclined HI-disk
$q_{\mathrm{HI},0}$	Intrinsic (edge-on) axes-ratio of the HI-disk
$q_{\mathrm{H_2}}$	Apparent axes-ratio of the inclined H_2-disk
$q_{\mathrm{H_2},0}$	Intrinsic (edge-on) axes-ratio of the H_2-disk
r_{bulge}	Exponential scale radius of the stellar bulge projected onto the disk
$\tilde{r}_{\mathrm{bulge}}$	Plummer-scale radius of the bulge of a galaxy
r_{disk}	Exponential scale radius of the cold gas disk
$\tilde{r}_{\mathrm{disk}}$	Exponential scale radius of the stellar disk
r_{eq}	Galaxy radius, where the surface densities of HI and H_2 are equal
r_{HI}	Radius of the HI-disk, where $\Sigma_{\mathrm{HI}}(r_{\mathrm{HI}}) = \Sigma_0$
$r^{\mathrm{half}}_{\mathrm{HI}}$	Half mass radius of HI in a galactic disk
$r^{\mathrm{HWHM}}_{\mathrm{HI}}$	Galaxy radius, where the HI-surface density is at 50% of its maximum
$r^{\mathrm{max}}_{\mathrm{HI}}$	Galaxy radius, where the surface density of HI peaks
$r_{\mathrm{H_2}}$	Radius of the H_2-disk, where $\Sigma_{\mathrm{H_2}}(r_{\mathrm{H_2}}) = \Sigma_0$

$r_{\mathrm{H_2}}^{\mathrm{half}}$	Half mass radius of H_2 in a galactic disk
$r_{\mathrm{H_2}}^{\mathrm{HWHM}}$	Galaxy radius, where the H_2-surface density is at 50% of its maximum
$r_{\mathrm{H_2}}^{\mathrm{max}}$	Galaxy radius, where the surface density of H_2 peaks
R_{mol}	H_2/HI mass ratio
$R_{\mathrm{mol}}^{\mathrm{c}}$	H_2/HI surface density ratio at the center of a galactic disk
$R_{\mathrm{mol}}^{\mathrm{galaxy}}$	Total H_2/HI mass ratio of a galaxy
$R_{\mathrm{mol,i}}^{\mathrm{galaxy}}$	Model i for the H_2/HI mass ratio of a galaxy
$R_{\mathrm{mol,th}}^{\mathrm{galaxy}}$	Theoretical model for the H_2/HI mass ratio of a galaxy
$R_{\mathrm{mol}}^{\mathrm{universe}}(z)$	H_2/HI density ratio of the Universe at a given redshift z
r	Galactocentric radius
r_{s}	Scale radius of a galaxy halo
r_{vir}	Virial radius of the galaxy halo
r_{x}	x-coordinate of a galaxy in the mock observing cone
r_{y}	y-coordinate of a galaxy in the mock observing cone
r_{z}	z-coordinate of a galaxy in the mock observing cone
$\rho_{\mathrm{bulge}}(r)$	Spherical space density distribution of a galactic bulge
ρ_{c}	Critical space density for closure
$\rho_{\mathrm{gas}}(z)$	Comoving cosmic space density of cold gas in galactic disks
$\rho_{\mathrm{HI}}(z)$	Comoving cosmic space density of HI in galactic disks
$\rho_{\mathrm{H_2}}(z)$	Comoving cosmic space density of H_2 in galactic disks
$\rho_{\mathrm{halo}}(r)$	Spherical space density distribution of a galactic halo
$\rho_{\mathrm{SFR}}(z)$	Comoving cosmic star formation rate density ($\mathrm{M_\odot\,yr^{-1}\,Mpc^{-3}}$)
$\rho_{\mathrm{stars}}(z)$	Comoving cosmic space density of stars in galactic disks
$\rho_{\mathrm{x}}(z)$	Comoving space density of component x at redshift z

S	Frequency-integrated flux of an emission line
s_{box}	Comoving side length of the simulation box
$\mathrm{SFE}_{\mathrm{HI}}$	HI-star formation efficiency (= depletion time of HI into stars)
$\mathrm{SFE}_{\mathrm{H_2}}$	H_2-star formation efficiency (= depletion time of H_2 into stars)
S^{V}	Velocity-integrated flux of an emission line
Σ_0	Selected detection limit for the surface density of HI or H_2
$\Sigma^{\mathrm{bulge}}(r)$	Column density of a galactic bulge
Σ_{c}	Surface density of H, above which H_2 is assumed in a smooth phase
$\Sigma_{\mathrm{gas}}(r)$	Surface density of cold gas in a galactic disk
$\Sigma_{\mathrm{H}}(r)$	Surface density cold hydrogen (HI+H_2) in a galactic disk
$\tilde{\Sigma}_{\mathrm{H}}$	Surface density of HI+H_2 at the center of a galactic disk (see Eq. 3.5)
$\Sigma_{\mathrm{HI}}(r)$	Surface density of HI in a galactic disk
$\Sigma_{\mathrm{HI}}^{\mathrm{FWHM}}$	Average surface density of HI inside the radius $r_{\mathrm{HI}}^{\mathrm{HWHM}}$
$\Sigma_{\mathrm{HI}}^{\mathrm{half}}$	Average surface density of HI inside the radius $r_{\mathrm{HI}}^{\mathrm{half}}$
$\Sigma_{\mathrm{HI}}^{\mathrm{max}}$	Maximal surface density of HI
$\Sigma_{\mathrm{H_2}}(r)$	Surface density of H_2 in a galactic disk
$\Sigma_{\mathrm{H_2}}^{\mathrm{FWHM}}$	Average surface density of H_2 inside the radius $r_{\mathrm{H_2}}^{\mathrm{HWHM}}$
$\Sigma_{\mathrm{H_2}}^{\mathrm{half}}$	Average surface density of H_2 inside the radius $r_{\mathrm{H_2}}^{\mathrm{half}}$
$\Sigma_{\mathrm{H_2}}^{\mathrm{max}}$	Maximal surface density of H_2
$\Sigma_{\mathrm{SF}}(r)$	Surface density of the star formation rate
$\Sigma_{\mathrm{SF}}^{\mathrm{c}}$	Value of Σ_{SF}, where the SB-heating starts saturating
$\Sigma_{\mathrm{stars}}^{\mathrm{bulge}}(r)$	Surface density of stars in a galactic bulge
$\Sigma_{\mathrm{stars}}^{\mathrm{disk}}(r)$	Surface density of stars in a galactic disk
σ_{data}	Standard deviation of observed data relative to some model

σ_{gas}	Isotropic velocity dispersion of cold gas
$\sigma_{\mathrm{gas,z}}$	Vertical velocity dispersion of cold gas
σ_{obs}	Measurement-related scatter of observed data
σ_{phy}	Intrinsic (physical) scatter of observed data relative to some model
$\sigma_{\mathrm{phy,i}}$	Intrinsic (physical) scatter of observed data relative to model i
σ_{stars}	Isotropic velocity dispersion of stars
$\sigma_{\mathrm{stars,z}}$	Vertical velocity dispersion of stars
σ_{X}	Intrinsic scatter of $\log(X)$ in the metallicity-dependent model for X
T_{AGN}	Temperature of the molecular gas acquired from an AGN
$T_{\mathrm{AGN}}^{\mathrm{max}}$	Maximal value of T_{AGN}
T_{B}	Surface brightness temperature
$T_{\mathrm{CMB}}(z)$	Temperature of the cosmic microwave background
T_{ex}	Excitation temperature of CO in a galaxy
T_{SB}	Temperature of the molecular gas acquired from a starbust
$T_{\mathrm{SB}}^{\mathrm{max}}$	Maximal value of T_{SB}
τ	Optical depth
τ_{c}	Optical depth parameter (see Chapter 6.3.1)
τ_{J}	Optical depth of the CO-transition $J \rightarrow J-1$
V	Velocity
V_{c}	Circular velocity
$V_{\mathrm{c}}^{\mathrm{bulge}}$	Circular velocity contribution of the bulge of a galaxy
$V_{\mathrm{c}}^{\mathrm{disk}}$	Circular velocity contribution of the disk of a galaxy
$V_{\mathrm{c}}^{\mathrm{halo}}$	Circular velocity contribution of the halo of a galaxy
V_{obs}	Observable velocity

$V_{\rm vir}$	Virial velocity of the halo of a galaxy
$w_{\rm CO}^{20}$	Molecular line width at 20% of the peak flux density
$w_{\rm CO}^{50}$	Molecular line width at 50% of the peak flux density
$w_{\rm CO}^{\rm peak}$	Molecular line width between the two horns of the line
$w_{\rm HI}^{20}$	HI-line width at 20% of the peak flux density
$w_{\rm HI}^{50}$	HI-line width at 50% of the peak flux density
$w_{\rm HI}^{\rm peak}$	HI-line width between the two horns of the HI-line
X	CO-to-H_2 conversion factor ("X-factor")
$X_{\rm c}$	Constant model for X
$X_{\rm J}$	CO-to-H_2 conversion factor X for the CO-transition $J \rightarrow J-1$
$X_{\rm v}$	Variable model for X
$\mathcal{Z}$	Canonical partition function
z	Redshift
$z_{\rm max}$	Maximal redshift of the simulated observing cone
ζ	Global cold gas mass correction factor

Bibliography

Abdalla F., Blake C., Rawlings S., 2009, MNRAS, submitted

Abdalla F. B., Rawlings S., 2005, MNRAS, 360, 27

Abel T., Haiman Z., 2000, Molecular Hydrogen in Space, Combes F., Pineau Des Forets G., eds.

Adelman-McCarthy J. K., et al., 2008, ApJS, 175, 297

Allen R. J., Atherton P. D., Tilanus R. P. J., 1986, Nat, 319, 296

Andreani P., Casoli F., Gerin M., 1995, A&A, 300, 43

Andredakis Y. C., Peletier R. F., Balcells M., 1995, MNRAS, 275, 874

Angulo R. E., Baugh C. M., Frenk C. S., Lacey C. G., 2008, MNRAS, 383, 755

Ao Y., Weiß A., Downes D., Walter F., Henkel C., Menten K. M., 2008, A&A, 491, 747

Arimoto N., Sofue Y., Tsujimoto T., 1996, PASJ, 48, 275

Arnett D., 1996, Supernovae and nucleosynthesis. an investigation of the history of matter, from the Big Bang to the present. Princeton University Press

Baek S., di Matteo P., Semelin B., Combes F., Revaz Y., 2009, A&A, 495, 389

Balcells M., Domínguez-Palmero L., Graham A., Peletier R. F., 2001, Astronomical Society of the Pacific Conference Series, Vol. 249, The Central Kiloparsec of Starbursts and AGN: The La Palma Connection, Knapen J. H., Beckman J. E., Shlosman I., Mahoney T. J., eds.

Bally J., Stark A. A., Wilson R. W., Langer W. D., 1987, ApJL, 312, L45

Bao Y.-Y., Zhang X., Chen L.-E., Zhang H.-J., Peng Z.-Y., Zheng Y.-G., 2008, Chinese Astronomy and Astrophysics, 32, 351

Barnes D. G., et al., 2001, MNRAS, 322, 486

Barvainis R., Maloney P., Antonucci R., Alloin D., 1997, ApJ, 484, 695

Beck S. C., Beckwith S. V., 1984, MNRAS, 207, 671

Becker R. H., et al., 2001, AJ, 122, 2850

Bennett C. L., et al., 2003, ApJS, 148, 1

Bertone S., De Lucia G., Thomas P. A., 2007, MNRAS, 379, 1143

Bertsch D. L., Dame T. M., Fichtel C. E., Hunter S. D., Sreekumar P., Stacy J. G., Thaddeus P., 1993, ApJ, 416, 587

Bigiel F., Leroy A., Walter F., Brinks E., de Blok W. J. G., Madore B., Thornley M. D., 2008, AJ, 136, 2846

Binney J., Merrifield M., 1998, Galactic astronomy. Princeton University Press

Blain A. W., Frayer D. T., Bock J. J., Scoville N. Z., 2000, MNRAS, 313, 559

Blaizot J., Wadadekar Y., Guiderdoni B., Colombi S. T., Bertin E., Bouchet F. R., Devriendt J. E. G., Hatton S., 2005, MNRAS, 360, 159

Blake C. A., Abdalla F. B., Bridle S. L., Rawlings S., 2004, New Astronomy Review, 48, 1063

Blitz L., Fukui Y., Kawamura A., Leroy A., Mizuno N., Rosolowsky E., 2007, Protostars and Planets V, Reipurth B., Jewitt D., Keil K., eds.

Blitz L., Rosolowsky E., 2004, ApJL, 612, L29

—, 2006, ApJ, 650, 933

Boomsma R., van der Hulst J. M., Oosterloo T. A., Sancisi R., 2002, Bulletin of the American Astronomical Society, Vol. 34

Boselli A., Lequeux J., Gavazzi G., 2002, Ap&SS, 281, 127

Bottema R., 1993, A&A, 275, 16

Boulanger F., Viallefond F., 1992, A&A, 266, 37

Bouwens R. J., Illingworth G. D., Blakeslee J. P., Broadhurst T. J., Franx M., 2004, ApJL, 611, L1

Bower R. G., Benson A. J., Malbon R., Helly J. C., Frenk C. S., Baugh C. M., Cole S., Lacey C. G., 2006, MNRAS, 370, 645

Braine J., Combes F., Casoli F., Dupraz C., Gerin M., Klein U., Wielebinski R., Brouillet N., 1993, AAPS, 97, 887

Braine J., Wiklind T., 1993, A&A, 267, L47

Braun R., 1991, Early Universe Radio Observatory (EURO). http://www.skatelescope.org

—, 2006

Buitrago F., Trujillo I., Conselice C. J., 2008, ArXiv e-prints

Bullock J. S., Kolatt T. S., Sigad Y., Somerville R. S., Kravtsov A. V., Klypin A. A., Primack J. R., Dekel A., 2001, MNRAS, 321, 559

Burton W. B., 1971, A&A, 10, 76

Carilli C. L., Blain A. W., 2002, ApJ, 569, 605

Carilli C. L., Gnedin N., Furlanetto S., Owen F., 2004, New Astronomy Review, 48, 1053

Carilli C. L., et al., 2002, AJ, 123, 1838

Carilli C. L., Rawlings S., 2004, New Astronomy Review, 48, 979

Carruthers G. R., 1970, ApJL, 161, L81

Catinella B., Haynes M. P., Giovanelli R., Gardner J. P., Connolly A. J., 2008, ApJL, 685, L13

Cole S., et al., 2001, MNRAS, 326, 255

—, 2005, MNRAS, 362, 505

Colless M., et al., 2001, MNRAS, 328, 1039

Combes F., Maoli R., Omont A., 1999, A&A, 345, 369

Comerford J. M., Natarajan P., 2007, MNRAS, 379, 190

Courteau S., de Jong R. S., Broeils A. H., 1996, ApJL, 457, L73

Crosthwaite L. P., Turner J. L., 2007, AJ, 134, 1827

Croton D. J., et al., 2006, MNRAS, 365, 11

Curran S. J., Murphy M. T., Pihlström Y. M., Webb J. K., Bolatto A. D., Bower G. C., 2004, MNRAS, 352, 563

Daddi E., Dannerbauer H., Elbaz D., Dickinson M., Morrison G., Stern D., Ravindranath S., 2008, ApJL, 673, L21

Dalgarno A., 2000, Molecular Hydrogen in Space, Combes F., Pineau Des Forets G., eds.

Davies J. I., 1990, MNRAS, 244, 8

Davis M., et al., 2003, Society of Photo-Optical Instrumentation Engineers (SPIE) Conference Series, Guhathakurta P., ed., Vol. 4834

De Breuck C., 2005, ESA Special Publication, Vol. 577, ESA Special Publication, Wilson A., ed.

de Grijs R., 2001, Astronomy and Geophysics, 42, 4

de Jong T., Dalgarno A., Chu S.-I., 1975, ApJ, 199, 69

De Lucia G., Blaizot J., 2007, MNRAS, 375, 2

De Lucia G., Kauffmann G., White S. D. M., 2004, MNRAS, 349, 1101

de Ravel L., et al., 2008, ArXiv e-prints

de Vaucouleurs G., de Vaucouleurs A., Corwin H. G., 1976, 2nd reference catalogue of bright galaxies. University of Texas Press

Dickey J. M., Hanson M. M., Helou G., 1990, ApJ, 352, 522

Dickman R. L., Snell R. L., Schloerb F. P., 1986, ApJ, 309, 326

Dobbs C. L., 2008, MNRAS, 391, 844

Dolag K., Bartelmann M., Perrotta F., Baccigalupi C., Moscardini L., Meneghetti M., Tormen G., 2004, A&A, 416, 853

Downes D., Solomon P. M., 1998, ApJ, 507, 615

Downes D., Solomon P. M., Radford S. J. E., 1993, ApJL, 414, L13

Doyle M. T., et al., 2005, MNRAS, 361, 34

Drapatz S., Zinnecker H., 1984, MNRAS, 210, 11P

Eisenstein D. J., et al., 2005, ApJ, 633, 560

Elmegreen B. G., 1989, ApJ, 338, 178

—, 1993, ApJ, 411, 170

Ewen H. I., Purcell E. M., 1951, Nat, 168, 356

Faber S. M., Jackson R. E., 1976, ApJ, 204, 668

Fall S. M., Efstathiou G., 1980, MNRAS, 193, 189

Fang F., et al., 2005, Bulletin of the American Astronomical Society, Vol. 37

Farhat M., Obreschkow D., Kobel P., Dorsaz N., De Bosset A., 2006, Sixth International Symposium on Cavitation (CAV2006)

Ferrière K. M., 2001, Reviews of Modern Physics, 73, 1031

Flynn C., Holmberg J., Portinari L., Fuchs B., Jahreiß H., 2006, MNRAS, 372, 1149

Förster Schreiber N. M., et al., 2006, ApJ, 645, 1062

Fukugita M., Hogan C. J., Peebles P. J. E., 1998, ApJ, 503, 518

Fukui Y., et al., 1999, IAU Symp., Vol. 190, New Views of the Magellanic Clouds, Chu Y.-H., Suntzeff N., Hesser J., Bohlender D., eds.

Gao Y., 2009, American Astronomical Society Meeting Abstracts, Vol. 214

Genzel R., et al., 2008, ApJ, 687, 59

Genzel R., Stutzki J., 1989, ARA&A, 27, 41

Georgakakis A., Hopkins A. M., Caulton A., Wiklind T., Terlevich A. I., Forbes D. A., 2001, MNRAS, 326, 1431

Gilli R., et al., 2003, ApJ, 592, 721

Giovanelli R., Haynes M. P., da Costa L. N., Freudling W., Salzer J. J., Wegner G., 1997, ApJL, 477, L1

Gnedin N. Y., Silk J., Spaans M., 2001, ArXiv Astrophysics e-prints

Goldsmith P. F., Li D., Krčo M., 2007, ApJ, 654, 273

Greve T. R., Papadopoulos P. P., Gao Y., Radford S. J. E., 2009, ApJ, 692, 1432

Greve T. R., Sommer-Larsen J., 2008, A&A, 480, 335

Guelin M., Zylka R., Mezger P. G., Haslam C. G. T., Kreysa E., Lemke R., Sievers A. W., 1993, A&A, 279, L37

Gunn J. E., Gott J. R. I., 1972, ApJ, 176, 1

Güsten R., Philipp S. D., Weiß A., Klein B., 2006, A&A, 454, L115

Häring N., Rix H.-W., 2004, ApJL, 604, L89

Helfer T. T., Thornley M. D., Regan M. W., Wong T., Sheth K., Vogel S. N., Blitz L., Bock D. C.-J., 2003, ApJS, 145, 259

Hennawi J. F., Dalal N., Bode P., Ostriker J. P., 2007, ApJ, 654, 714

Heyer M. H., Corbelli E., Schneider S. E., Young J. S., 2004, ApJ, 602, 723

Heyer M. H., Dame T. M., Thaddeus P., 2000, Proc. 232. WE-Heraeus Seminar, Berkhuijsen E. M., Beck R., Walterbos R. A. M., eds.

Hoekstra H., Franx M., Kuijken K., van Dokkum P. G., 2002, MNRAS, 333, 911

Hopkins A. M., 2007, Astronomical Society of the Pacific Conference Series, Vol. 380, Deepest Astronomical Surveys, Afonso J., Ferguson H. C., Mobasher B., Norris R., eds.

Hopkins A. M., Beacom J. F., 2006, ApJ, 651, 142

Hoyle F., 1946, MNRAS, 106, 343

Huang J.-S., Glazebrook K., Cowie L. L., Tinney C., 2003, ApJ, 584, 203

Hunter S. D., et al., 1997, ApJ, 481, 205

Huynh M. T., Frayer D. T., Mobasher B., Dickinson M., Chary R.-R., Morrison G., 2007, ApJL, 667, L9

Iliev I. T., Shapiro P. R., Ferrara A., Martel H., 2002, ApJL, 572, L123

Israel F., 2000, Molecular Hydrogen in Space, Combes F., Pineau Des Forets G., eds.

Israel F. P., 1997, A&A, 328, 471

Israel F. P., Baas F., 2003, A&A, 404, 495

Jeffreys H., 1961, Theory of Probability; 3 edition. Oxford University Press

Kalberla P. M. W., Dedes L., 2008, A&A, 487, 951

Kannappan S. J., Fabricant D. G., Franx M., 2002, AJ, 123, 2358

Kassin S. A., et al., 2007, ApJL, 660, L35

Kauffmann G., Colberg J. M., Diaferio A., White S. D. M., 1999, MNRAS, 303, 188

Kaufmann T., Mayer L., Wadsley J., Stadel J., Moore B., 2007, MNRAS, 375, 53

Kawabe R., Kohno K., Ohta K., Carilli C., 1999, Astronomical Society of the Pacific Conference Series, Vol. 156, Highly Redshifted Radio Lines, Carilli C. L., Radford S. J. E., Menten K. M., Langston G. I., eds.

Kennicutt R. C. J., 1998, ApJ, 498, 541

Kennicutt R. C. J., et al., 2003, PSPS, 115, 928

Keres D., Yun M. S., Young J. S., 2003, ApJ, 582, 659

Kobel P., Obreschkow D., Dorsaz N., De Bosset A., Farhat M., 2009, Experiments in Fluids, 47, 3948

Kobulnicky H. A., Zaritsky D., 1999, ApJ, 511, 118

Kregel M., van der Kruit P. C., de Grijs R., 2002, MNRAS, 334, 646

Krumholz M. R., McKee C. F., Tumlinson J., 2009, ApJ, 693, 216

Kutner M. L., Leung C. M., 1985, ApJ, 291, 188

Lah P., et al., 2007, MNRAS, 376, 1357

Lauberts A., Valentijn E. A., 1989, The surface photometry catalogue of the ESO-Uppsala galaxies. Garching: European Southern Observatory

Lavezzi T. E., Dickey J. M., 1998, AJ, 115, 405

Ledoux C., Petitjean P., Srianand R., 2003, MNRAS, 346, 209

Lees J. F., Knapp G. R., Rupen M. P., Phillips T. G., 1991, ApJ, 379, 177

Leroy A., Bolatto A., Walter F., Blitz L., 2006, ApJ, 643, 825

Leroy A. K., Walter F., Brinks E., Bigiel F., de Blok W. J. G., Madore B., Thornley M. D., 2008, AJ, 136, 2782

Lis D. C., Schilke P., 2003, ApJL, 597, L145

Maddalena R. J., Morris M., Moscowitz J., Thaddeus P., 1986, ApJ, 303, 375

Maiolino R., 2008, New Astronomy Review, 52, 339

Maloney P., Black J. H., 1988, ApJ, 325, 389

Matthews L. D., Gao Y., Uson J. M., Combes F., 2005, AJ, 129, 1849

McGaugh S. S., Bothun G. D., Schombert J. M., 1995, AJ, 110, 573

McGaugh S. S., de Blok W. J. G., 1997, ApJ, 481, 689

McGaugh S. S., Schombert J. M., Bothun G. D., de Blok W. J. G., 2000, ApJL, 533, L99

Meyer M. J., et al., 2004, MNRAS, 350, 1195

Milliard B., et al., 2007, ApJS, 173, 494

Mo H. J., Mao S., White S. D. M., 1998, MNRAS, 295, 319

Morganti R., Sadler E. M., Oosterloo T. A., Pizzella A., Bertola F., 1997, Publications of the Astronomical Society of Australia, 14, 89

Navarro J. F., Frenk C. S., White S. D. M., 1995, MNRAS, 275, 720

—, 1996, ApJ, 462, 563

—, 1997, ApJ, 490, 493

Nieten C., Dumke M., Beck R., Wielebinski R., 1999, A&A, 347, L5

Noordam J., Braun R., de Bruyn G., 1991, Euro16: Proposal for an Array of 16 Low Cost 100 Meter Radio Telescopes. http://www.skatelescope.org

Norberg P., et al., 2002, MNRAS, 336, 907

Noterdaeme P., Ledoux C., Petitjean P., Srianand R., 2008, A&A, 481, 327

Obreschkow D., Croton D., DeLucia G., Khochfar S., Rawlings S., 2009a, ApJ, 698, 1467

Obreschkow D., Kobel P., Dorsaz N., De Bosset A., Nicollier C., Farhat M., 2006, Physical Review Letters

Obreschkow D., Michelini F., Dalessi S., Kapon E., Dupertuis M.-A., 2007, Phys. Rev., B 76, 35329

Obreschkow D., Rawlings S., 2009a, MNRAS, submitted

—, 2009b, ApJL, 696, L129

—, 2009c, MNRAS, 394, 1857

Obreschkow D., Rawlings S., Heywood I., Klöckner H.-R., 2009b, ApJ, accepted

—, 2009c, ApJ, submitted

Omont A., Petitjean P., Guilloteau S., McMahon R. G., Solomon P. M., Pécontal E., 1996, Nat, 382, 428

Oshima T., et al., 2001, ApJL, 563, L103

Paglione T. A. D., et al., 2001, ApJS, 135, 183

Panter B., Jimenez R., Heavens A. F., Charlot S., 2008, MNRAS, 391, 1117

Paturel G., Petit C., Prugniel P., Theureau G., Rousseau J., Brouty M., Dubois P., Cambrésy L., 2003, A&A, 412, 45

Pfenniger D., Combes F., 1994, Particle Astrophysics, Atomic Physics and Gravitation, Tran Thanh van J., Fontaine G., Hinds E., eds.

Plummer H. C., 1911, MNRAS, 71, 460

Pontzen A., Pettini M., 2009, MNRAS, 70

Prochaska J. X., Herbert-Fort S., Wolfe A. M., 2005, ApJ, 635, 123

Prunet S., Pichon C., Aubert D., Pogosyan D., Teyssier R., Gottloeber S., 2008, ApJS, 178, 179

Rao S. M., Turnshek D. A., Briggs F. H., 1995, ApJ, 449, 488

Rao S. M., Turnshek D. A., Nestor D. B., 2006, ApJ, 636, 610

Regan M. W., Thornley M. D., Helfer T. T., Sheth K., Wong T., Vogel S. N., Blitz L., Bock D. C.-J., 2001, ApJ, 561, 218

Reynolds R. J., 2004, Advances in Space Research, 34, 27

Richmond M. W., Knapp G. R., 1986, AJ, 91, 517

Rieger T. J., 1974, Journal of Quantitative Spectroscopy and Radiative Transfer, 14, 59

Righi M., Hernández-Monteagudo C., Sunyaev R. A., 2008, A&A, 489, 489

Robertson B. E., Kravtsov A. V., 2008, ApJ, 680, 1083

Rohlfs K., Wilson T. L., 2004, Tools of radio astronomy, 4th rev. and enl. ed. Springer

Rubio M., Garay G., Montani J., Thaddeus P., 1991, ApJ, 368, 173

Rupen M. P., 1991, AJ, 102, 48

Sage L. J., 1993, A&A, 272, 123

Sage L. J., Welch G. A., 2006, ApJ, 644, 850

Sanders D. B., Solomon P. M., Scoville N. Z., 1984, ApJ, 276, 182

Santos M. G., Amblard A., Pritchard J., Trac H., Cen R., Cooray A., 2008, ApJ, 689, 1

Sauty S., et al., 2003, A&A, 411, 381

Schechter P., 1976, ApJ, 203, 297

Schmidt M., 1959, ApJ, 129, 243

—, 1968, ApJ, 151, 393

Schneider J., 2008, Interactive Extra-solar Planets Catalog. http://exoplanet.eu/catalog.php

Schuster K. F., Kramer C., Hitschfeld M., Garcia-Burillo S., Mookerjea B., 2007, A&A, 461, 143

Scoville N. Z., Sargent A. I., Sanders D. B., Soifer B. T., 1991, ApJL, 366, L5

Sersic J. L., 1968, Atlas de galaxias australes. Cordoba, Argentina: Observatorio Astronomico

Shostak G. S., van der Kruit P. C., 1984, A&A, 132, 20

Silk J., Spaans M., 1997, ApJL, 488, L79

Sivia D., Skilling J., 2006, Data Analysis: A Bayesian Tutorial; 2 edition. Oxford University Press

Solomon P. M., Downes D., Radford S. J. E., Barrett J. W., 1997, ApJ, 478, 144

Solomon P. M., Rivolo A. R., Barrett J., Yahil A., 1987, ApJ, 319, 730

Solomon P. M., Vanden Bout P. A., 2005, ARA&A, 43, 677

Spergel D. N., et al., 2003, ApJS, 148, 175

Springel V., Frenk C. S., White S. D. M., 2006, Nat, 440, 1137

Springel V., et al., 2005, Nat, 435, 629

Storrie-Lombardi L. J., McMahon R. G., Irwin M. J., 1996, MNRAS, 283, L79

Swarup G., 1991, CURRENT SCIENCE V.60, NO.2/JAN25, P.106, 1991, 60, 106

Tacconi L. J., et al., 2006, ApJ, 640, 228

Tatematsu K., et al., 1993, ApJ, 404, 643

Teyssier R., et al., 2008, ArXiv e-prints

Thompson T. A., Quataert E., Murray N., 2005, ApJ, 630, 167

Thronson H. A. J., Tacconi L., Kenney J., Greenhouse M. A., Margulis M., Tacconi-Garman L., Young J. S., 1989, ApJ, 344, 747

Tremonti C. A., et al., 2004, ApJ, 613, 898

Trujillo I., et al., 2006, ApJ, 650, 18

Tully R. B., Fisher J. R., 1977, A&A, 54, 661

Valentijn E. A., van der Werf P. P., 1999, ApJL, 522, L29

van de Hulst H. C., 1945, Ned. tijd. natuurkunde, 11, 210

Verheijen M., van Gorkom J. H., Szomoru A., Dwarakanath K. S., Poggianti B. M., Schiminovich D., 2007, ApJL, 668, L9

Verheijen M. A. W., 2001, Astronomical Society of the Pacific Conference Series, Vol. 240, Gas and Galaxy Evolution, Hibbard J. E., Rupen M., van Gorkom J. H., eds.

Verzelen O., Ferreira R., Bastard G., 2000, Phys. Rev. B, 62, R4809

von Ditfurth H., 1972, Im Anfang war der Wasserstoff, first edition edn. Hoffmann u Campe Vlg GmbH

Wagoner R. V., 1973, ApJ, 179, 343

Wall W. F., 2006, Rev. Mex. Astron. Astrofis., 42, 117

—, 2007, MNRAS, 379, 674

Walter F., Brinks E., de Blok W. J. G., Bigiel F., Kennicutt R. C., Thornley M. D., Leroy A., 2008, AJ, 136, 2563

Walter F., Carilli C., Bertoldi F., Menten K., Cox P., Lo K. Y., Fan X., Strauss M. A., 2004, ApJL, 615, L17

Wang J., De Lucia G., Kitzbichler M. G., White S. D. M., 2008, MNRAS, 384, 1301

Weinzirl T., Jogee S., Khochfar S., Burkert A., Kormendy J., 2009, ApJ, 696, 411

Weiss A., Downes D., Neri R., Walter F., Henkel C., Wilner D. J., Wagg J., Wiklind T., 2007, A&A, 467, 955

Weiss A., Downes D., Walter F., Henkel C., 2005a, A&A, 440, L45

Weiss A., Walter F., Scoville N. Z., 2005b, A&A, 438, 533

Welch G. A., Sage L. J., 2003, ApJ, 584, 260

White S. D. M., Rees M. J., 1978, MNRAS, 183, 341

Wielebinski R., Dumke M., Nieten C., 1999, A&A, 347, 634

Wild W., Harris A. I., Eckart A., Genzel R., Graf U. U., Jackson J. M., Russell A. P. G., Stutzki J., 1992, A&A, 265, 447

Wilkinson P., 1991, The Hydrogen Array. http://www.skatelescope.org

Wilman R. J., et al., 2008, MNRAS, 388, 1335

Wilson C. D., 1995, ApJL, 448, L97

Wong T., Blitz L., 2002, ApJ, 569, 157

Yencho B., Barger A. J., Trouille L., Winter L. M., 2009, ArXiv e-prints

Young J. S., Knezek P. M., 1989, ApJL, 347, L55

Young J. S., Scoville N. Z., 1991, ARA&A, 29, 581

Young J. S., Xie S., Kenney J. D. P., Rice W. L., 1989, ApJS, 70, 699

Young J. S., et al., 1995, ApJS, 98, 219

Young L. M., 2002, AJ, 124, 788

Yun M. S., Reddy N. A., Condon J. J., 2001, ApJ, 554, 803

Zavala J., Okamoto T., Frenk C. S., 2008, MNRAS, 387, 364

Zwaan M., 2006

Zwaan M. A., Meyer M. J., Staveley-Smith L., Webster R. L., 2005a, MNRAS, 359, L30

Zwaan M. A., et al., 2004, MNRAS, 350, 1210

Zwaan M. A., Prochaska J. X., 2006, ApJ, 643, 675

Zwaan M. A., van der Hulst J. M., Briggs F. H., Verheijen M. A. W., Ryan-Weber E. V., 2005b, MNRAS, 364, 1467